AGH

AKADEMIA GÓRNICZO-HUTNICZA IM. STANISŁAWA STASZICA W KRAKOWIE

DZIEDZINA NAUK INŻYNIERYJNO-TECHNICZNYCH

DYSCYPLINA: INŻYNIERIA ŚRODOWISKA, GÓRNICTWO I ENERGETYKA

ROZPRAWA DOKTORSKA

Wpływ dynamicznych właściwości porosprężystych piaskowca tumlińskiego na stateczność otworu wiertniczego

Autor: mgr Mohammad Zamani Ahmad Mahmoudi

Promotor rozprawy: Dr hab. inż. Dariusz Knez

Praca wykonana: Akademia Górniczo-Hutnicza w Krakowie
Wydział Wiertnictwa, Nafty i Gazu

Kraków, 2024

AGH

AGH UNIVERSITY OF SCIENCE AND TECHNOLOGY

FIELD OF ENGINEERING AND TECHNICAL SCIENCES

DISCIPLINE: ENVIRONMENTAL ENGINEERING, MINING AND ENERGY

DOCTORAL DISSERTATION

Influence of Dynamic Poro-elastic Properties of Tumlin Sandstone on Wellbore Stability

Author: Mohammad Zamani Ahmad Mahmoudi

Supervisor: Dr hab. eng. Dariusz Knez

Completed at: AGH University of Krakow
Faculty of Drilling, Oil and Gas

Kraków, 2024

Abstract

This PhD research investigated the effects of dynamic poro-elastic parameters on wellbore stability in Tumlin sandstone formation located north of Kielce, Poland. To conduct the research, firstly, laboratory tests were executed to measure the rock’s physical, mechanical, and dynamic poro-elastic parameters. The rock’s dynamic poro-elastic parameters including bulk modulus, Biot's coefficient, Biot's modulus, Skempton’s coefficient, shear modulus, Young's modulus, Poisson's ratio, and unconstrained specific storage coefficient were measured using an acoustic velocity measurement apparatus. Those poro-elastic parameters were measured as functions of hydrostatic stress applied on the sandstone samples.

Then, numerical simulations were executed via FLAC3D software. In the numerical models, two scenarios were simulated to conduct coupled rock-fluid wellbore stability analysis. The first scenario was the start of drilling where the rock quickly reacts to the drilling operation, and the pore pressure suddenly increases in the rock. This condition corresponds to undrained loading conditions. The second scenario occurs shortly after the first scenario, when the loading condition shifts from undrained to drained conditions.

The results showed that as Tumlin sandstone transitions to undrained conditions, Poisson's ratio increases, indicating reduced compressibility and higher lateral strain, which can cause wellbore instability. Moreover, a decrease in Young's modulus and shear modulus under undrained conditions further suggests reduced stiffness and increased deformation, leading to critical risk of wellbore failure.

Furthermore, it was found that as the hydrostatic level is below the half of the rock’s uniaxial compressive strength (UCS), the differences in dynamic poro-elastic parameters between drained and undrained conditions increase progressively, making rock behavior more predictable. Above this threshold, Biot's coefficient stabilizes, and Biot modulus increases, indicating that Tumlin sandstone becomes stiffer and less sensitive to pore pressure changes.

It was also revealed that at any drilling depth, the safety factor is higher under undrained conditions compared to drained conditions. Moreover, the disparity in safety factors between drained and undrained conditions is directly related to the depth. Specifically, this difference gets more noticeable when the drilling depth exceeds 1400 m. At depths shallower than 1400 m, safety factors for both undrained and drained conditions remain above 1, indicating a stable wellbore. However, at depths below 1400 m, the safety factor under undrained conditions falls below 1, suggesting an increased risk of wellbore failure.

Overall, the findings emphasize the importance of managing drilling pressures and mud properties carefully to mitigate risks associated with undrained conditions and varying hydrostatic stress levels. Implementing controlled drilling rates and pressures is crucial for maintaining wellbore stability, especially in deeper depths in Tumlin sandstone formation.

Acknowledgements

I would like to begin by extending my heartfelt thanks to my highly respected advisor, Professor Dariusz Knez, for granting me this invaluable opportunity and for providing me with insightful and constructive guidance throughout the various stages of this research. His unwavering support and dedication have been instrumental in the completion of this PhD research.

I also genuinely offer my sincere appreciation to Dr. Albert Złotkowski and Dr. Herimitsinjo Rajaoalison, whose invaluable advice and instruction have been pivotal in carrying out this research. Their guidance has been greatly appreciated.

Finally, I sincerely thank my dear friends Piotr Mytnik and Mitra Khalilidermani, for their collaboration and support, which has been immensely helpful and constructive in the completion of this research.

List of Contents

List of Figures:

Introductory

Chapter 2

Chapter 4

Chapter 5

Chapter 6

Chapter 7

Chapter 8

List of Tables

Chapter 6

Chapter 7

Chapter 8

Introductory

Wellbore stability is a common concern in the drilling of hydrocarbon wellbores, water wells, exploratory boreholes, geothermal boreholes, etc. The underground rocks contain miscellaneous pore liquids like water, brine, oil, etc., in their void spaces. Hence, it can be said that porous rocks are systems combined from dry rock matrix (skeleton) and pore fluids. Figure 1 shows a porous sandstone rock containing water as pore fluid.

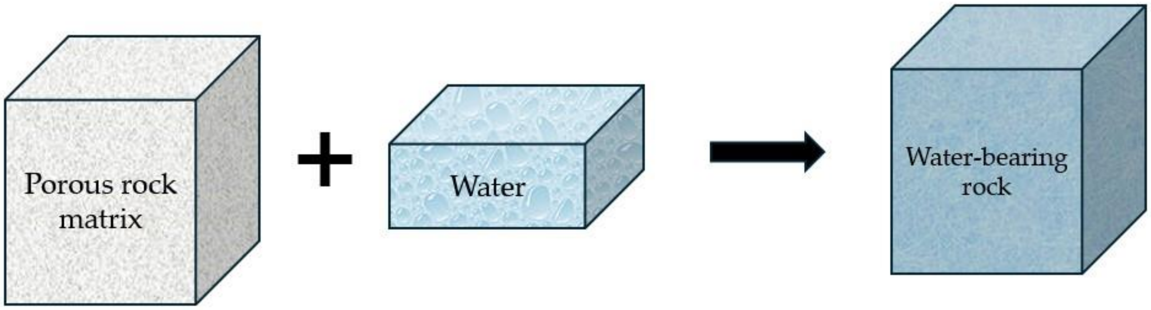

Figure 1. A porous sandstone rock as a system of solid matrix and water.

In nature, rocks are imposed to different loadings derived from the overburden weight, tectonics forces, seismic shocks, etc. The mechanical behavior of porous rocks under those loading conditions relies on both solid matrix and pore fluid. Hence, it can be expressed that porous rocks have a hydro-mechanical behavior when they are subjected to external pressures [1].

The influence of pore fluid pressure on the rocks' mechanical response was initially formulated by Terzaghi who developed the effective stress law [2]. Terzaghi's effective stress law had been established for water-containing soils. This law helped civil engineers to explain and formulate many geotechnics problems such as foundation settlement, deformation of soil embankments, instability of soil slopes, etc. However, regarding the rocks, the law was incapable of explaining some engineering phenomena [3].

The early incapability of the effective stress law was discovered within the hydrogeology scope. In 1892, King stated that water table in a well close to a rail station in Whitewater, Wisconsin, USA, fluctuated with the trains passage through the area [4]. As the train approached the station, the water table rose. Conversely, when the train departed from the station, the water table in the well decreased. Moreover, in a report by the United States Geological Surveys in 1902, a coincidence between the ocean tide and water table fluctuations in the wells was observed in Atlantic city, New Jersey, USA. At high tide condition, when the sea's weight increased, the water level within the coastal water wells rose, and vice versa [5].

Except hydrogeology, the coupled rock-fluid problems also arose in petroleum engineering. For instance, minor and major seismic problems were reported in many global oil fields. In Galveston, Texas, USA, oil production caused a remarkable land subsidence that led to the submergence of the near-coast lands [3]. The state claimed that the submerged lands possessed to it while the landowners filed a complaint against the state's claim. Finally, in 1926, a geologic investigation corroborated that the submergence had been the outcome of the oil production activities in the region.

The interaction between rocks and pore fluids was characterized by the poroelasticity theory. The basics of this theory were developed by Biot in 1941 [6]. The two abovementioned problems in hydrogeology scope were successfully explained by this theory. The poroelasticity theory couples the pore pressure and applied stresses to the rock deformation and fluid exchange, thereby delivering realistic results. Through this coupling, if pore pressure changes, it causes mechanical strain in the rock's matrix, and reversely, such a change in mechanical strain disturbs the pore pressure within the voids.

The primary aim of the current PhD research is to discover the impact of rock's poro-elastic parameters on wellbore instability potential in the study area. In other words, it aims to reveal how the stability of a wellbore drilled in Tumlin sandstone is influenced by poro-elastic parameters. Using both experimental tests and numerical simulations, the influence of dynamic poro-elastic parameters including Skempton's coefficient, Biot's coefficient, bulk modulus, Young's modulus, Biot modulus, shear modulus, Poisson's ratio, and unconstrained specific storage coefficient on wellbore stability was investigated.

The second target of this research is to establish empirical correlations between the rock's dynamic poro-elastic parameters and hydrostatic stress. The extracted correlations will contribute to better understanding the interaction between the dynamic poro-elastic parameters and the failure potential of the drilled wellbore. Moreover, those empirical correlations can be utilized in numerical modelling or analytical solutions of stability of wellbores drilled in other geologically same sandstones.

After conducting the research, it was proved that dynamic poro-elastic parameters of Tumlin sandstone play a significant role in wellbore stability. Particularly, it was demonstrated that those dynamic poro-elastaic parameters are highly determining at the early stages of drilling when the rock is under undrained condition. During this condition, the bulk modulus and shear modulus of the rock around the wellbore decline while Poisson's ratio increases. Such a reduction in Young's modulus and shear modulus proves that the stiffness and shear strength of the rock decline. Moreover, the increase in

Poisson’s ratio demonstrates that the rock is more likely to undergo severe lateral strains. Consequently, the wellbore failure may occur.

Additionally, it was confirmed that at any given drilling depth, the safety factor for wellbore stability in undrained conditions is lower than drained conditions. The difference in safety factors between undrained and drained conditions directly relies on the drilling depth. Specifically, when the drilling depth exceeds 1400 m, this difference becomes more severe.

The research also proved that dynamic poro-elastic parameters of Tumlin sandstone are dependent on applied hydrostatic stress. Dynamic poro-elastic parameters including Skempton’s coefficient, Biot’s coefficient, and unconstrained specific storage coefficient demonstrate a decreasing trend with increasing hydrostatic stress. Nevertheless, while the Skempton’s coefficient decreases linearly, the Biot’s coefficient and the unconstrained specific storage coefficient follow a logarithmic decline. Other dynamic poro-elastic parameters including Young’s modulus, bulk modulus, shear modulus, Poisson’s ratio, and Biot modulus escalate with hydrostatic stress. These findings proved that a hydro-mechanical wellbore stability analysis is more reliable if the poro-elastic parameters are imported as stress-dependent functions to the numerical models. If a consistent value is chosen for a poro-elastic value for the entire vertical profile of the formation, the accuracy of the numerical results will be affected.

In the past, there were only some partial studies on the effect of one or two certain poro-elastic parameters on the rocks’ mechanical response in geomechanics applications. Nevertheless, no comprehensive investigation was dedicated to examining the effects of a complete set of poro-elastc parameters on wellbore stability. This research strives to address this research gap, delivering new findings applicable in WSA.

This research attempts to achieve new findings and empirical correlations useful for WSA applications. Wellbore instability is a crucial concern in all above-mentioned anthropogenic initiatives. In better words, water extraction or oil production are inevitably implemented through drilling of wells. Similarly, to sequestrate the supercritical CO_2, there is need to drill injection boreholes through which the liquefied CO_2 is injected to the subsurface formations. In the same way, to store pressurized liquid gases such as natural gas or natural hydrogen, drilling the injection boreholes is required. In all these initiatives, the stability of the drilled wellbores is affected by the rocks’ poro-elastic characteristics. Hence, the findings of this dissertation are applicable in wellbore stability analysis of those engineering projects.

In this research, the effect of rock's dynamic poro-elastic parameters on wellbore stability was assessed. The study area from which the rock specimens were taken was the Tumlin sandstone formation located in the north part of Kielce city in Poland. The Tumlin sandstone formation has undergone geological investigations since 1920 [7,8]. From the geological perspective, this formation is situated on the border of the Paleozoic Holly cross mountains and the lower Triassic (Buntsandstein) sediments [8].

Up to now, there have been several mines exploiting Tumlin sandstone for construction purposes. The geological data related to Tumlin sandstone formation was mainly obtained through those mines. The dip of the Tumlin sandstone layer is nearly about 10°; however, it can vary as ±2° in different spots of the layer [8]. The length (extension) of the sandstone layer exceeds several ten kilometers [8].

The compositional structure of Tumlin sandstone rock consists of 79-88% polycrystal Quartz. Moreover, Micas and Feldspars constitute about 0.3% of the composition. Furthermore, a very minor percentage of iron oxides are present in the rock matrix. For instance, Hematite consists of 1.07% of the composition. In addition, carbonate minerals such as CaO and MgO encompass small fractions around 0.05% and 0.22%, respectively. Pawlica studied the presence of heavy minerals in Tumlin sandstone formation [7]. It was reported that the rock contains very low amounts of heavy minerals [8].

In the past, the grain size distribution of Tumlin sandstone had been also measured using photographs of a dozen thin sections of rock samples. Nearly 200 grains were analyzed. It was found that the Tumlin sandstone is medium- or fine-grained, moderately well sorted. The grains were chiefly less than 2 mm in diameter [8].

During this PhD research program, rock samples taken from Tumlin sandstone formation were analyzed in the laboratory of Faculty of Drilling, Oil, and Gas at AGH university of Kraków. The rock's average porosity and density were respectively measured as 15.70%, and 2530 kg/m^3. Furthermore, the physical, mechanical, and dynamic poro-elastic characteristics of rock samples were measured using a triaxial compression test machine, and an acoustic wave propagation apparatus (AVS).

Previous studies in literature analyzed the wellbore instability problems mainly through elastic and poro-elastic solutions. The elastic solutions may not deliver reliable results since they do not consider the pivotal coupling between pore fluid, mud, and rock matrix. Some examples of those elastic solutions are Kirsch [9], Hubbert and Willis [10], Fairhurst [11], and Bradley [12]. Moreover, several researchers tried to perform WAS using rock-fluid coupling analysis [13-19]. However, their works had some drawbacks.

The main drawback was that the rock’s poro-elastic parameters were assumed constant [20].

In the current PhD research, the dynamic poro-elastic parameters of Tumlin sandstone were measured by an AVS apparatus. As those poro-elastic parameters are dynamic, the term "dynamic" will be implied throughout the dissertation and often omitted to prevent repetition. Moreover, all dynamic poro-elastic parameters were measured as functions of hydrostatic stress. Those dynamic poro-elastic parameters included Skempton’s coefficient, bulk modulus, Biot's coefficient, Biot's modulus, shear modulus, Young's modulus, Poisson's ratio, and unconstrained specific storage coefficient.

Afterwards, numerical simulations were executed via FLAC3D, and the measured sandstone properties were imported to the models. Then, a wellbore was drilled within the numerical model, and the influence of dynamic poro-elastic parameters on wellbore stability was evaluated. The maximum radial displacements at wellbore wall together with a defined safety factor were utilized to quantify the wellbore failure potential.

In numerical simulations, the wellbore stability was analyzed through two scenarios: 1) at the early beginning of the drilling operation when the loading condition is undrained, and 2) shortly after the drilling initiation when the loading condition transitions from undrained to drained. Considering this point, the current research provides a novel wellbore stability analysis in which the impacts of both undrained and drained conditions have been included.

Based on the conducted research, the following new achievements were obtained regarding the influence of dynamic poro-elastic parameters on wellbore stability in Tumlin sandstone formation:

1. Several empirical correlations were established between dynamic poro-elastic parameters of Tumlin sandstone formation and hydrostatic stress. The corresponding correlations are presented in Eqs. (6.2-6.13).
2. A failure mathematical relationship was experimentally extracted for Tumlin sandstone. The relevant relationship is presented in Eq. (6.1).
3. Safety factor values of wellbore failure were obtained for both undrained and drained loading conditions using the data assumed in the dissertation.
4. The potential of wellbore wall failure at the early stages of the drilling was quantitatively compared with the later stages of the drilling operation.

Chapter 1: Introduction to Fluid-Rock interaction and Wellbore Stability

1.1. Fluid-rock interaction

Assume a fluid, e.g. water or oil, within a deep porous rock. Such a porous rock may represent an aquifer or reservoir, respectively. How can an anthropogenic activity change the fluid pore pressure in the rock?

Of course, there are several engineering techniques that may come to somebody's mind. When the pore fluid is oil, a potential solution is to inject a pressurized liquid into the reservoir; this is the mechanism widely utilized in Enhanced Oil Recovery (EOR) techniques. As an example, in USA, the injection of CO_2, natural gas, and Nitrogen into the depleted oil reservoirs improves oil production roughly from 30% to 60%. When the trapped oil is subjected to the injected liquid, the pressure gradient pushes the oil towards the production wellbores [21]. During this process, the pore pressure increases within the porous rock.

Now, consider the second scenario in which a tower is built on a loose sand layer with a near-surface water table. The construction of the tower started in 1173 AM; however, as the construction of upper floors proceeded, the tower leant more and more. In other words, as the weight of the tower increased, the sand layer underwent a non-uniform vertical subsidence. Although the construction process finished in 1350 AM, the tower's foundation experienced a large subsidence. This is the story of Leaning Tower of Pisa in the city of Pisa, Italy. In this case, the tower weight led to water drainage from the sand layer, thereby causing foundation subsidence [3].

The above examples were two typical illustrations of fluid-rock interaction. In the first case, the injection-induced pressure pushes the oil within the reservoir, and then, the oil transmits this induced pressure to the rock matrix (skeleton). In the second case, the weight force of the tower acted on the porous sand layer, and then, that force was transmitted to the pore water. Consequently, the water was gradually drained, and subsequent ground subsidence occurred. From the above examples, it is simply turned out that fluid injection (or fluid drainage) together with the mechanical loading (or unloading) can induce new stresses within the whole "fluid-rock" medium. Consequently, it affects the in-situ pore fluid volume, or the rock layer's thickness.

This fluid-rock interaction can be explained through the poroelasticity theory introduced by Maurice Anthony Biot in 1941 [6]. Biot developed his works as a theoretical extension for three-dimensional (3D) calculation of the foundation subsidence occurred in water-saturated, loose soils. Although the early fundamental equations of fluid-rock interaction were established by Biot, the "poroelasticity" word was initially utilized by

Geertsma in 1966 [22]. He had referred to the Biot's equations as the *poroelasticity theory* in the footprint of his paper entitled *"Problems of rock mechanics in petroleum production engineering"* [22]. Furthermore, he had remarked that the mathematical method for extraction of Biot's poroelasticity equations is identical to the procedure applied in thermoelasticity theory.

1.2. Contributing parameters on wellbore stability

Wellbore instability is a problematic issue observed in many petroleum, mining and civil engineering projects. It imposes financial costs estimated to reach up to several billion dollars per year in the world [23-25]. Furthermore, it is a time-dependent phenomenon. In fact, from the drilling initiation time to the production phase, the impact of contributing parameters on wellbore failure may reduce or increase with time. The most influential parameters on wellbore stability are rock type, in-situ stress regime, mud pressure, chemical reactivity of the rock (mainly for shale formations), and pore fluid characteristics [23].

Rock type refers to the elemental composition, physical properties and mechanical features of hosting rocks in where the drilling operation is conducted. Properties such as density, porosity, elastic moduli, shear strength, Poisson's ratio, UCS, etc. are directly influential in the rock response to the different loading conditions [26,27].

In-situ stress regime is also a key factor in wellbore stability [28-31]. Adequate field tests must be conducted to measure and characterize the in-situ stress regime. The results of those tests will help the well designer to devise the wellbore trajectory with higher values of safety factor [32,33].

Mud pressure is also a highly influential parameter in wellbore stability. It stabilizes the wellbore wall while curtailing the pore fluid to enter the inner space of the wellbore. Mud type can be water-based or oil-based. In general, the type of the mud, mud pressure, and its rheological features have a great impact on the wellbore mechanical stability [24].

Chemical reactivity of hosting rocks is another important factor in wellbore stability. Some rocks, especially shale, exhibit a high tendency to react with the drilling mud. Such a high chemical reactivity expedites the rock degradation and failure at wellbore wall. Hence, the chemical reaction between shale and mud can eventually lead to enlargement of the wellbore diameter and wall instability [25].

Last but not least, pore pressure is a highly impactful parameter influencing wellbore stability. The poro-elastic parameters of subsurface formations are directly influenced by the magnitude of pore pressure [34]. Pore pressure leads to a decrease in the normal stresses while it does not have impact on shear stresses applied to the rock. The pore pressure impact on wellbore stability can be elucidated through the poroelasticity theory which will be described in Chapter 2.

1.3. Types of wellbore instability

In nature, rocks are under compression loading condition [12]. The mechanical equilibrium of subsurface rocks occurred during the redistribution of local stresses in the past geological eras. When a drill-bit penetrates the rock, the rock cuttings are removed and transmitted to the ground surface. The new vacant space leads to subsequent stress redistribution around the well [24]. Consequently, a damaged zone may be formed around the wellbore. The damaged zone undergoes induced deformations derived from the redistribution of new stresses. Such a stress redistribution process proceeds with time. Whenever the redistributed stresses in the damaged zone exceed the rocks' strength, wellbore instability issues may occur. This can cause many subsequent problems such as delays in the drilling process or the entire loss of the wellbore.

Wellbore instability issues occur due to either the mechanical stresses or physico-chemical interactions between the drilling mud and hosting rocks [25]. Bradley categorized the wellbore instability issues into two primary groups: tensile, and compressive failure [12]. Tensile failure is in the form of rock fracturing, leading to potential lost circulation issues. In contrast, compressive failure is in the form of wellbore diameter enlargement or reduction. Bradley also expressed that a petroleum engineer must have access to adequate geomechanical data for WSA [12]. The required data include the on-site stress regime, the drilling-induced stresses, mud pressure, rock strength characteristics, and mud impact on rock's strength. However, he did not consider the impact of pore fluid pressure change on the drilling-induced deformations around wellbore.

Regarding the in-situ stress, underground formations are subjected to either normal stress regimes or tectonically stress regimes. A normally stressed regime refers to the situation in which the overburden weight (vertical stress) is the greatest in-situ stress, while the least and maximum horizontal in-situ stresses are approximately equal. In contrast, tectonically stress regimes refer to situations which are not normally stressed once. Those regimes mainly deal with volcanic activities, fault movements, creeping salt domes, etc. [12].

Aadnøy and Chenevert expressed that the deeper the wellbore (the more intense stress regimes), the more potential for borehole instability [40]. Bradley stated that the pore pressure gradient for normally stressed regimes is almost consistent and equal to 10400 Pa/m. On the contrary, virgin pore pressure in tectonically stress regimes is approximately 20400 Pa/m [12].

Chapter 2: Poroelasticity Constitutive Equations and Fundamental Poro-elastic Parameters

2.1. Biot's Theory

Terzaghi had established his theory by performing one-dimensional (1D) laboratory tests [2,35]. Later, in 1941, Biot developed his comprehensive 3D theory when he was serving as a lecturer at Columbia University in the US. He published his work in a paper entitled "*General theory of three-dimensional consolidation*" [6]. He formulated the constitutive equations which are now considered as the building blocks of the poroelasticity theory. After that, Biot developed his works to formulate acoustic wave propagation in porous media such as rocks, soils, etc. [36-38].

Biot included a new parameter to quantify the volume of water which flows into or released from a soil sample under loading condition. That parameter was named as "the increment of water volume per unit volume of soil" [6]. The parameter was referred as $\boldsymbol{\zeta}$; however, in the field of hydrogeology, no distinct symbol has been utilized for it. This parameter was explained by Biot through the example of application of a slender tube used for withdrawing water from a soil specimen to explain the production mechanism in a water well.

After the 1950s, many researchers used Biot's constitutive equations to extract analytical solutions capable of explaining different engineering issues, e.g. 1D soil consolidation, ground subsidence, hydraulic fracturing, and aquifer compaction. Biot's linear constitutive equations were reformulated by Rice and Cleary in 1976 [39]. That reformulation found extensive utilization in addressing geomechanical issues. To describe the instant and lasting responses of porous rocks to applied stresses, they measured the poro-elastic properties in undrained and drained conditions, respectively.

When a material is subjected to external or internal stresses, the material undergoes strains (or deformations). In the theory of elasticity, there is need to at least two elastic parameters, like Bulk modulus and shear modulus, to formulate the deformations induced by the applied stresses. On the contrary, in poroelasticity theory, at least four poro-elastic parameters are required to establish those formulations [3].

2.2. Poroelasticity constitutive equations

There are two main poroelasticity constitutive equations which link the stresses applied on a porous rock to the resulting strains [3]. In what follows, those equations are elaborated through a simple example.

Assume a homogeneous porous rock which is exposed to an isotropic stress equal to σ (Figure 2.1). The pressure of pore fluid within the rock is p. Furthermore, the rock's initial bulk volume is V. Due to the applied stress, a volumetric strain, ϵ, occurs in the rock. Consequently, a percentage of the containing fluid exits from the rock. Thus, the fluid content in the rock changes; the fluid content increment is referred to by ζ.

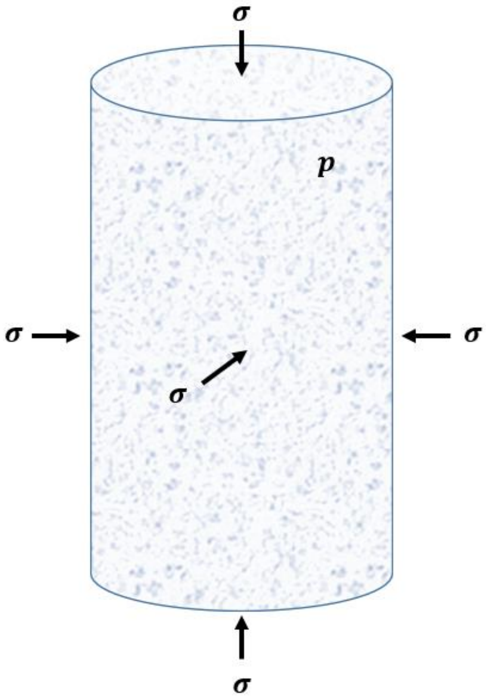

Figure 2.1. A homogenous porous rock under isotropic stress of σ.

The following assumptions are considered for sign convention: the applied stress, σ, is positive for compression state; on the contrary, the applied stress is negative for tension state. The value of p is positive if it is greater than atmospheric pressure (roughly 0.1 MPa), and vice versa. Furthermore, the volumetric strain, ϵ, is positive for expansion state while it is negative for compression state. The parameter of ζ is positive if fluid is added to the rock. On the other hand, it is negative if fluid is released from the rock.

Two main linear constitutive equations relate the dependent parameters of ϵ and ζ to the independent variables of σ and p, as shown below [3]:

$$\epsilon = a_{11}\sigma + a_{12}p \tag{2.1}$$

$$\zeta = a_{21}\sigma + a_{22}p \tag{2.2}$$

where ϵ is dimensionless volumetric strain; ζ indicates the dimensionless fluid content increment. Furthermore, a_{11}, a_{12}, a_{21}, and a_{22} are coefficients. These coefficients are obtained by dividing the variation of a dependent parameter to the variation of an independent parameter while other independent parameters are kept unchanged. The following relations define those coefficients [3]:

$$a_{11} = \frac{\delta\epsilon}{\delta\sigma}\bigg|_{\Delta p = 0} \equiv \frac{1}{K} \tag{2.3}$$

$$a_{12} = \frac{\delta\epsilon}{\delta p}\bigg|_{\Delta\sigma = 0} \equiv \frac{1}{H} \tag{2.4}$$

$$a_{21} = \frac{\delta\zeta}{\delta\sigma}\bigg|_{\Delta p = 0} \equiv \frac{1}{H} \tag{2.5}$$

$$a_{22} = \frac{\delta\zeta}{\delta p}\bigg|_{\Delta\sigma = 0} \equiv \frac{1}{R'} \tag{2.6}$$

where δ indicates the Kronecker delta. Furthermore, $\frac{1}{K}$ represents the drained compressibility of rock. Note that the drained compressibility is reciprocal of the rock's bulk modulus. Moreover, $\frac{1}{H}$ shows the poro-elastic expansion coefficient of rock, and $\frac{1}{R'}$ represents the unconstrained specific storage coefficient of rock. The conservation of energy necessitates that a_{12} is equivalent to a_{21} [3]. Furthermore, the subscriptions of $\Delta p = 0$ and $\Delta\sigma = 0$ indicate the loading conditions in which pore pressure and applied stress remain constant, respectively. The conditions of $\Delta p = 0$ is equivalent to the drained condition.

The parameter of $\frac{1}{K}$ is measured by dividing the change in the rock volumetric strain to the change in the applied stress under drained condition. The parameter of $\frac{1}{H}$ is measured by dividing the change in ϵ to the change in p when $\Delta\sigma = 0$. This parameter is not encountered in elasticity theory. Analogous to heat-induced expansion in thermoelasticity theory, the parameter of $\frac{1}{H}$ is referred to the poro-elastic expansion coefficient. Additionally, the coefficient of $\frac{1}{R'}$ is measured by dividing the variation of ζ to the variation of p when $\Delta\sigma = 0$.

The four abovementioned coefficients constitute the symmetric poro-elastic transformation matrix as follows [3]:

$$\begin{pmatrix} \frac{1}{K} & \frac{1}{H} \\ \frac{1}{H} & \frac{1}{R'} \end{pmatrix} \tag{2.7}$$

In this matrix, the diagonal components include $\frac{1}{K}$ and $\frac{1}{R'}$. In addition, the off-diagonal component is $\frac{1}{H}$. Substituting Eqs. (2.3-2.6) in Eqs. (2.1 and 2.2) gives [3]:

$$\epsilon = \frac{\delta V}{V} = \frac{1}{K}\sigma + \frac{1}{H}p \tag{2.8}$$

$$\zeta = \frac{1}{H}\sigma + \frac{1}{R'}p \tag{2.9}$$

Eqs. (2.8 and 2.9) are two main proroelasticity constitutive equations which relate the rock volumetric strain and fluid content increment to the pore pressure, applied stress, and poro-elastic parameters. In the subsequent sections, the formulas required to calculate poro-elastic parameters of rocks are described. For each parameter, the basic definition together with the pertinent mathematical formulations are provided.

2.3. Poro-elastic fundamental parameters

2.3.1. Bulk modulus

For any substance, bulk modulus shows the resistance of that substance against volumetric deformation [41]. Regarding rocks, bulk modulus is an indicator for rock resilience to compression. This parameter is commonly shown as *K*. However, it has different types depending on the loading conditions and fluid saturation. The value of *K* relies chiefly on the mineral composition, porosity, pore size distribution, and pore fluid type.

In poroelasticity, there is need to measure different types of bulk moduli. Those bulk moduli are:

- Undrained bulk modulus:

This parameter exhibits the rock resistance to compression under undrained conditions. Undrained condition is equivalent to $\zeta=0$. In other words, the parameter of ζ is zero during the undrained condition. The undrained bulk modulus is formulated as [42]:

$$K_u = -V\frac{\delta\sigma}{\delta V}\bigg|_{\zeta = 0} \tag{2.10}$$

In above equation, the rock's initial volume is shown as V.

- Drained bulk modulus:

This parameter represents the rock resistance to compression under drained condition. Drained condition is equivalent to $\Delta p = 0$. The drained bulk modulus is formulated as [42]:

$$K = -V\frac{\delta\sigma}{\delta V}\bigg|_{\Delta p = 0} \tag{2.11}$$

- Dry bulk modulus:

This parameter shows the dry rock resistance to compression under dry conditions. To dry the rock sample, it is commonly kept in oven for several hours depending on the internal temperature of the oven. Once the pore fluid is entirely evaporated, the dry sample is ready for test conduction. The following formula represents the dry bulk modulus, K_{dry} [42]:

$$K_{dry} = -V\frac{\delta\sigma}{\delta V}\bigg|_{m_f = 0} \tag{2.12}$$

where m_f is the fluid mass in the rock. The subscript $m_f = 0$ indicates that there must not be any fluid in the rock sample.

- Mineral bulk modulus:

This parameter shows the rock minerals' resistance to compression under constant temperature. In fact, K_s reflects the strength of rock matrix against the applied stresses. The following relation represents the mineral bulk modulus, K_s [42]:

$$K_s = -V_m(\frac{\delta\sigma}{\delta V_m})_T \tag{2.13}$$

where V_m is the initial volume of mineral, and δV_m shows the variation in the mineral volume. Furthermore, $\delta\sigma$ indicates the alteration in the external stress. Subscript T indicates that the test is conducted at a consistent temperature.

2.3.2. Skempton's coefficient

When a rock undergoes confining stress, the internal pore pressure increases within the pores. In poroelasticity theory, this phenomenon is formulated through the term of Skempton's coefficient. In laboratory setting, Skempton's coefficient is measured by increasing the confining stress incrementally. At each increment, the values of confining stress versus the pore pressure are recorded. The experiment must be conducted under undrained conditions. The following formula defines the Skempton's coefficient, B [21]:

$$B = \frac{\delta p}{\delta\sigma}|\zeta = 0 \tag{2.14}$$

where B indicates the dimensionless Skempton's coefficient. This parameter typically falls within the range of 0.5 to 1 for fluid-saturated rocks.

Skempton's coefficient is also stated based on the rock's bulk moduli [3]:

$$B = \frac{1-K/K_u}{1-K/K_s} \tag{2.15}$$

2.3.3. Biot's coefficient

When a rock sample undergoes external stresses, the fluid content changes, and the rock deforms. Biot's coefficient is defined as [3]:

$$\alpha = \frac{\delta V_f}{\delta V}|\Delta p = 0 \tag{2.16}$$

where, α is dimensionless Biot's coefficient. Furthermore, δV_f stands for the alteration in the pore fluid volume, and δV shows the variation in the rock bulk volume. This parameter lies in the range of $\varphi < \alpha \leq 1$, where φ stands for rock's porosity. For common soils, α is close to 1, which represents the remarkable role of pore pressure in bearing the applied stresses.

Parameter α is also expressed in terms of the rock's bulk moduli [3]:

$$\alpha = 1 - \frac{K_{dry}}{K_s} \tag{2.17}$$

Biot's coefficient is also stated in terms of Skempton's coefficient and rock's bulk moduli as [3]:

$$\alpha = \frac{1-\left(\frac{K}{K_u}\right)}{B} \tag{2.18}$$

2.3.4. Poisson's ratio

When a rock undergoes axial loading, lateral and longitudinal deformations occur in the rock. The relationship between lateral deformation and longitudinal deformation under axial loading is expressed through the Poisson's ratio term. This parameter is dimensionless, commonly shown as υ in the literature. Identical to the rock's bulk modulus, the parameter of υ can be measured under drained and undrained conditions.

Assume a cylindrical rock sample which is exposed to axial stress of σ_{11}. The subsequent paragraphs describe how Poisson's ratio can be determined under drained and undrained conditions:

- Drained Poisson's ratio:

This parameter is measured as [3]:

$$\upsilon = -\frac{\epsilon_{22}}{\epsilon_{11}}\bigg|_{\Delta p = 0;\ \sigma_{22} = 0} \tag{2.19}$$

In the above equation, υ indicates the drained Poisson's ratio. Moreover, ϵ_{22} along with ϵ_{11} represent the lateral and axial strain, respectively.

Note that subscript $\Delta p = 0$ refers to the drained loading condition. Furthermore, subscript $\sigma_{22} = 0$ indicates that no lateral stresses are applied on the sample.

The above relationship is accompanied with a negative sign because for common materials subjected to axial loading, their lateral strain is positive while the longitudinal strain is negative. Hence, the negative sign turns the ratio into a positive number.

- Undrained Poisson's ratio:

This parameter can be defined as [3]:

$$\upsilon_u = -\frac{\epsilon_{22}}{\epsilon_{11}}\bigg|_{\zeta = 0;\ \sigma_{22} = 0} \tag{2.20}$$

where υ_u indicates the undrained Poisson's ratio. Note that subscript $\zeta = 0$ refers to the undrained loading condition.

The following relationships link the parameters υ and υ_u [3]:

$$\upsilon_u = \frac{3\upsilon+\alpha B(1-2\upsilon)}{3-\alpha B(1-2\upsilon)} \tag{2.21}$$

$$\upsilon = \frac{3\upsilon_u-\alpha B(1+\upsilon_u)}{3-2\alpha B\ (1+\upsilon_u)} \tag{2.22}$$

Eq. (2.22) can be rearranged as [3]:

$$\frac{\upsilon_u-\upsilon}{1+\upsilon_u} = \frac{\alpha B(1-2\upsilon)}{3} \tag{2.23}$$

2.3.5. Shear modulus

Rocks are vulnerable to shear stress. Shear modulus is an indicator of rock's resistance against shear stress. It is commonly shown as G.

Assume a cylindrical porous rock which is subjected to shear stress, τ_{xy}, applied along with the rock's cross-sectional area. Consequently, a shear strain, ϵ_{xy}, occurs in the rock's cross-sectional area. The following formula relates τ_{xy} to ϵ_{xy} [43]:

$$G = \frac{\tau_{xy}}{\epsilon_{xy}} \tag{2.24}$$

The shear modulus of a specific rock can be measured in different loading conditions, i.e. drained or undrained conditions. Under drained condition, the following relation is used to relate G to K and υ [44]:

$$G = 3K\frac{1-2\upsilon}{2+2\upsilon} \tag{2.25}$$

For the undrained condition, the same equation can be utilized, as follows [3]:

$$G_u = 3K_u\frac{1-2\upsilon_u}{2+2\upsilon_u} \tag{2.26}$$

2.3.6. Young's modulus

This parameter manifests the stiffness of porous rocks against the tensile or compressive stresses. It is commonly shown as *E*. Moreover, it can be measured under drained and undrained conditions.

- Drained Young modulus

Assume a cylindrical porous rock sample which is subjected to axial stress of σ_{11}. Consequently, an axial strain, ϵ_{11}, occurs in the direction of rock's axis. The following relation connects σ_{11} to ϵ_{11} [42]:

$$E = \frac{\sigma_{11}}{\epsilon_{11}}\bigg|_{\Delta p = 0;\ \sigma_{22} = \sigma_{33} = 0} \tag{2.27}$$

where, *E* stands for drained Young's modulus. Furthermore, the subscript $\sigma_{22} = \sigma_{33} = 0$ indicates that no lateral stresses are acted on the sample.

The following formulas are used to relate *E* to *K*, *G* and v under drained condition [45]:

$$E = \frac{9KG}{3K+G} \tag{2.28}$$

$$E = 2G(1+v) \tag{2.29}$$

$$E = 3K(1-2v) \tag{2.30}$$

- Undrained Young's modulus:

Under undrained condition, Young's modulus is formulated as [42]:

$$E_u = \frac{\sigma_{11}}{\epsilon_{11}}\bigg|_{d_{m_f=0} = 0;\ \sigma_{22} = \sigma_{33} = 0} \tag{2.31}$$

where, E_u stands for the undrained Young's modulus. Like Eqs. (2.28-2.30), the following equations are established [45]:

$$E_u = \frac{9K_uG_u}{3K_u+G_u} \tag{2.32}$$

$$E_u = 2G_u(1+v_u) \tag{2.33}$$

$$E_u = 3K_u(1-2v_u) \tag{2.34}$$

2.3.7. Biot modulus

Biot modulus functions as an indication of the stiffness of porous rock. This parameter is commonly denoted as M and is calculated using the following equation [3]:

$$M = \frac{K_u - K}{\alpha^2} \tag{2.35}$$

where M is Biot modulus.

2.3.8. Unconstrained specific storage coefficient

Storage refers to the volume of fluid that needs to be introduced to or extracted from a porous rock to induce a change in pore pressure. This characteristic is represented by unconstrained specific storage coefficient, $\frac{1}{R}$ (see Eq. 2.6). It is commonly shown as S_σ in the literature. Furthermore, it is measured under conditions of constant applied stress. The formulation for S_σ is expressed as [3]:

$$S_\sigma = \frac{1}{R'} \equiv -\frac{\delta\zeta}{\delta p}\bigg|_{\Delta\sigma = 0} \tag{2.36}$$

Instead of the above equation, S_σ can be calculated through the following relation [3]:

$$S_\sigma = \frac{\alpha}{K\,B} \tag{2.37}$$

2.4. Pure compliance formulation

In the earlier subsections, four poro-elastic coefficients, a_{11}, a_{12}, a_{21}, and a_{22} were defined. It is now feasible to express these coefficients in terms of other poro-elastic parameters as follows [3]:

$$a_{11} = \frac{1}{K} \tag{2.38}$$

$$a_{12} = a_{21} = \frac{1}{H} = \frac{\alpha}{K} \tag{2.39}$$

$$a_{22} = \frac{1}{R'} = S_{\sigma} = \frac{\alpha}{KB} \tag{2.40}$$

Replacing the above equations in Eqs. (2.8 and 2.9) yields [3]:

$$\epsilon = \frac{1}{K}\sigma + \frac{\alpha}{K}p \tag{2.41}$$

$$\zeta = \frac{\alpha}{K}\sigma + \frac{\alpha}{KB}p \tag{2.42}$$

Based on the Eq. (2.41) and Eq. (2.42), it can be deduced that at least three main poro-elastic parameters including α, K, and B are required to formulate the ϵ and ζ as functions of σ and p for a specific porous rock.

This chapter gave a concise overview of the poroelasticity constitutive equations and the key poro-elastic parameters that govern the behavior of porous rocks under mechanical and hydraulic influences. By establishing the relationships between applied stress, strain, pore pressure, and fluid content, the chapter underscored the importance of those parameters in characterizing the hydro-mechanical responses of rocks.

Chapter 3: State-of-the-art

The early studies on wellbore stability started in the late 19th century. Kirsch pioneered the initial mathematical solution to calculate the drilling-induced stresses near a hole within an elastic plate [9]. Hubbert and Willis utilized Kirsch's solution to examine the stability of vertical wells subjected to non-uniform stresses [10]. They also included the effect of drilling mud pressure in Kirsch's solution. After that, Fairhurst extended Kirsch's solution to model the hydraulic fracturing operation in inclined wells [11]. It was concluded that in the absence of fluid infiltration into the formation, the pressure required for fracturing matches between the analytical and laboratory methods. However, in the case of fluid infiltration into the formation, which usually occurs, the fracturing pressure resulting from the analytical method is lower than the laboratory method.

Bradley carried out research to assess the borehole failure in salt domes [46].Then, in the subsequent years, he developed analytical solutions for wellbore stability analysis. In an outstanding work, Bradley developed a theoretical solution for WSA [12]. To formulate the stress concentration around wellbore, the elastic Kirsch's solution was utilized. Both Kirsch's solution and Bradley's solution will be described in the next chapter. In both solutions, the rock was assumed to be elastic. However, in Bradley's solution, the mud pressure from the drilling mud was applied to the wellbore. Furthermore, the wellbore wall was presumed impermeable (i.e. no mud infiltration was permitted). As a drawback, no pore pressure was included in the model. Bradley also described the potential wellbore failure mechanisms, including compressive failure and tensile failure. He assumed that the maximum stress state happens always at the wellbore wall. The next rigorous poro-elastic models such as Detournay and Cheng proved that this statement is not always true [13]. Nevertheless, Bradley's solution became the basis of numerous WSA studies [33,47,48].

Followed by Bradley, Aadnøy elaborated the mechanics of wellbore instability in oil/gas fields [49]. After that, Aadnøy and Chenevert investigated the instability mechanism in rocks under different loading circumstances [40]. However, they did not include the pore pressure impact on wellbore failure. The main reason was that they had applied the Mises failure criterion for prediction of rock instability. In such a criterion, the pore pressure does not affect the wellbore failure. Thus, the influence of porosity together with the stresses derived from the pore fluid flow in the pores had not been considered. Such neglect of pore pressure consequently led to an overestimation of the rock strength against the induced stresses during the drilling operations.

Parallel to the development of elastic solutions, several researchers strived to relate Biot's constitutive equations to porous rocks. Geertsma was the first person who linked Biot's constitutive equations to rock mechanics [22]. Afterwards, in the domain of wellbore stability analysis, Paslay and Cheatham [50], and Haimson and Fairhurst [51] investigated the role of pore pressure in stress concentration around wellbores [50, 51]. By using Biot's constitutive equations, those researchers showed that the rock-fluid interaction plays a significant function in wellbore stability.

Rice and Cleary reformed the Biot's constitutive formulas. This reformulation has been extensively used to address various geophysical challenges [39]. Those updated equations offered a more precise framework for analyzing the behavior of fluid-saturated rocks. Then, Detournay and Cheng investigated the effect of poro-elastic behavior of rocks during drilling operations of vertical wells [13]. They established a WSA mathematical approach using the Laplace transform. Furthermore, they incorporated their analytical solution into a numerical model. Through this, the impact of drilling-induced stresses and pore pressure on the wellbore stability was assessed. It was found that rock failure may occur in a distance behind the wellbore wall rather than the wall itself. This phenomenon has been confirmed by recent numerical studies [34].

After Detaurnay and Chenge, other researchers carried out WSA using poro-elastic approach [13]. Fun et al. studied the influence of rock strength on wellbore failure [52]. Furthermore, Yew and Liu developed an analytical solution to predict the safe mud weight in drilling operations [53]. Such a solution incorporated the pore pressure impact on wellbore failure. Furthermore, the Mohr-Coulomb as well as Drucker-Prager criterion were utilized to predict the failure occurrence around the well. From the findings, it was deduced that the pore pressure affects the rock failure around the wellbore. In fact, wellbore instability was reported as a problem highly sensitive to pore pressure.

Aoki et al. performed a WSA by considering shale strength anisotropy. They stated that at the commencement of drilling operation, the pore pressure around the well increases instantly which can be equivalent to the undrained loading condition. Nevertheless, the primary drawback of their investigation was neglecting the change in virgin pore pressure during mud infiltration into the surrounding rocks [54].

Cui et al. introduced an invaluable solution to formulate the drilling-induced stresses near a wellbore situated in an isotropic, homogeneous rock [14]. The problem was also numerically simulated by a finite element (FEM) model. The problem was decomposed into three distinct segments: poro-elastic plane strain loading, elastic uniaxial loading, and elastic anti-plane shear loading. Then, by applying superposition, those segments were integrated. Among available analytical poro-elastic solutions, the formulation developed by Cui et al. can be considered as the most comprehensive wellbore instability formulation as it accounts for the coupled fluid-rock interaction [14]. Due to its significance, this solution is thoroughly discussed in the next chapter.

Rahman et al. performed laboratory experiments and numerical modeling to assess the effects of mud and pore pressure on failure of wellbores drilled in shaly formations at the Australian Cooper basin [15]. To assess the influence of mud infiltration on the pore pressure change, some core samples were taken, and then, they were emplaced in a specific mud infiltration apparatus. The apparatus encompassed a core chamber, axial pressure cell, lateral pressure cell, pore pressure valves, different pressure ports, and a monitoring computer for recording the magnitudes of mud pressure and pore pressure.

To perform numerical modelling, the Mohr-Coulomb rock criterion was utilized. Furthermore, a safety factor was devised as follows[15]:

$$SF = \frac{\tau_u}{\tau} \tag{3.1}$$

where,

$$\tau_u = C + \left[\left(\frac{\sigma_1 + \sigma_3}{2} - \frac{\sigma_1 - \sigma_3}{2} Sin\phi - p \right) \right] tan\phi \tag{3.2}$$

$$\tau = \frac{\sigma_1 - \sigma_3}{2} cos\phi \tag{3.3}$$

where SF represents the factor of safety, τ_u indicates rock's shear strength, τ represents the shear stress applying on the rock, C indicates rock's cohesion, ϕ stands for the internal friction angle of rock, and p indicates pore pressure. Furthermore, σ_1 and σ_3 represent the highest and the least applied stresses on rock, respectively. If $\mathrm{SF} < 1$, rock failure occurs.

According to the numerical models, the possible wellbore failure modes were debated, and the appropriate safe mud window was determined. It was stated that the initial safe mud weight might get unsafe as the drilling process proceeds [15].

Awal et al. utilized Kirsch's solution through a poro-elastic approach to calculate the safe mud weight in two offshore wellbores in a shaly formation [16]. Several wellbore instability issues were already reported in the field. An indirect approach was introduced to enhance Kirsch's solution from classic linear isotropy into a transversely anisotropic scenario. The calculation methods of key factors, e.g. Biot's coefficient and in-situ stresses, were modified. Furthermore, the impact of anisotropy in Biot's coefficient included by considering three dissimilar values for Biot's coefficient. It was concluded that the tectonic state of the region has a great impact on the borehole stability. Furthermore, they expressed that a reliable poro-elastic analysis necessitates access to the data, specifically Biot's coefficient, rock elastic parameters, and on-site stress state.

Regel at al. used the poroelasticity theory to assess the stability of two vertical wellbores drilled in Danish Herjre field located in North Sea [18]. They computed the Biot's coefficient of subsurface formations by geophysical logs data. For chalk and shale rocks, it was calculated as 0.80, while for sandstone formations it was determined between 0.60 and 0.80. In addition, the lower limit of mud weight window was determined for both wellbores to prevent share failure occurrence.

Liu and Abousleiman investigated the mud cake impact on wellbore failure for a fractured formation [55]. The formation was assumed to have dual-porosity including the matrix porosity, and the fracture-derived porosity. Furthermore, the Drucker-Prager criterion was utilized to represent rock behavior under failure conditions. The analytical solution incorporated the impact of mudcake buildup on the borehole wall. It was deduced that mudcake buildup can effectively influence the resistance of borehole wall as it reduces the mud invasion into the rock fractures.

Zhang et al. developed an analytical- numerical solution for formulation of the stresses around an inclined wellbore drilled in an isotropic dual-porosity formation [17]. The hydro-mechanical interplay between rock and fluid was modeled via poroelasticity theory. This solution addressed the wellbore stability in two cases: with impermeable well wall, and permeable well wall. The impermeable well wall represented the condition in which mud cake prevented mud infiltration into the formation. On the contrary, the permeable wall represented the mud influx into the formation. An FEM-based model was generated to run numerical simulations. The wellbore stability analysis was conducted for several cases with dissimilar on-site stress magnitudes, and the relevant safe mud weight windows were identified.

In another study, Zhang et al. established a poro-elastic formulation to analytically evaluate the stability of a borehole drilled in shaley formations of the western Canadian overthrust belt [56]. The interplay between the pore fluid and drilling mud was also considered. The analytical solution was then integrated into a FEM-based numerical model. The rock was presumed to be an isotropic medium. Moreover, the following poro-elastic characteristics were specified to the generated model: $\alpha = 0.771$, $M = 15.8\ MPa$, $v = 0.189$, and $E = 20.6\ GPa$. The borehole diameter was 0.1 m. The results showed that shortly after drilling, the pore pressure in the surrounding rocks rapidly rises. This spike in pore pressure could cause potential failure around the wellbore. Over time, the pore pressure steadily dissipates into the surrounding rocks. Therefore, the tangential stresses around the borehole escalate. Zhang et al. also compared the results of their poro-elastic solution to the elastic solution proposed by Bradley [12,57]. They stated that Bradley's elastic solution overestimates the tangential stresses around the borehole, thereby leading to more conservative wellbore designation. They concluded that this overestimation stems from the assumption of constant pore pressure in Bradley's solution.

Liu et al. performed a fully coupled hydro-mechanical study to explore the influence of rock strength properties on wellbore instability [19]. The case study was a tight gas reservoir in China. The fluid-rock interaction was numerically modeled via an FEM-based program. Furthermore, Mohr-Coulomb criterion was specified to the rock. A safety factor akin to Eq. (3.1), was used to quantify the wellbore failure. The rock properties such as E, v, α, C, and ϕ were changed, and their impact on the rock failure was evaluated. They concluded that these rock properties have a great impact on wellbore stability when they change during the drilling process and rock-fluid interactions.

With the development of computers, wellbore stability analysis was vastly conducted via commercial programs such as ABAQUS, FLAC3D, UDEC, COMSOL, etc. There are many publications providing the results of numerical wellbore study analysis in literature [57-59]. The most of them are limited to a special case study, i.e. a certain oil/gas field.

A vast spectrum of numerical simulations was assigned to determine the secure mud weight [60, 61]. As an illustration, Darvishpour et al. used FLAC3D software to estimate the safe mud weight window in Iranian Asmari sandstone formation [60]. They determined the highest and least mud weight to prevent wellbore failure issues. Additionally, it was reported that the results closely aligned with the operational mud weight used in the actual field. On a negative note, in the numerical model, the value of Biot's coefficient was assigned equal to 1. This assumption was untrue as Biot's coefficient can be presumed as 1 just for ordinary soils, while the Asmari sandstone formation has a remarkable rock strength. For example, at shallow depth the UCS of the Asmari sandstone formation may exceed 60 MPa.

Hodge et al. established a hydro-mechanical model to evaluate wellbore stability under various loading conditions [62]. The conducted analysis highlighted the critical role of poro-elastic parameters in wellbore stability. They cited that when Biot's coefficient increased, the net shear stress around the wellbore escalated, posing a higher risk of wellbore failure. Additionally, it was stated that rocks with higher Young's modulus exhibit less sensitivity to pore pressure changes, resulting in a flatter shear stress profile after drilling commencement. Furthermore, stress regime was mentioned as a greatly contributing factor on the net shear stress around the well.

Salehi et al investigated wellbore stability in underbalanced drilling (UBD) conditions [57]. The case study was pertinent to two depleted Iranian fractured carbonate fields, referred to as field A and B. The study reported the occurrence of severe wellbore stability issues, e.g. lost circulation encountered during UBD in both fields. Using an elastoplastic model in FLAC^{3D} software, the authors conducted numerical simulations to estimate the optimum Equivalent Circulating Density (ECD) for both fields. The values for Poisson's ratio (0.33 for field A and 0.30 for field B) and Young's modulus (3.31×10^6 psi for field A and 0.66×10^6 psi for field B) were specified to the models. The researchers expressed that numerical modelling provided exact results validated by the field observations. However, the study also identified the need for further research and validation, particularly in field B, where uncertainties in rock mechanical properties might impact stability predictions.

Li and Gray examined the relation between Biot's coefficient and wellbore failure potential in reservoirs undergoing depletion. In their study, they considered Biot’s coefficient as 0.8 for an isotropic, homogeneous reservoir. The authors used the poro-elastic theory to develop an analytical model for determination of depletion-induced changes in far-field on-site stresses. The results highlighted that the wells aligned with the highest horizontal stress direction faced significant challenges, since fracture gradients could become extremely low, narrowing the mud weight window and reducing the margin for error. One drawback of the study was that Biot's coefficient and Poisson's ratio were presumed constant. Such an assumption might not hold true in all reservoir conditions, potentially affecting the accuracy of stability predictions [63].

In another study, Kanfar et al. implemented a numerical simulation to assess the influence of poro-elastic characteristics on wellbore stability, particularly in anisotropic formations. By employing a FEM-based formulation on generalized plane strain theory, the model effectively analyzed complex poro-elastic scenarios in anisotropic formations. The findings of the study suggested that anisotropic rocks show different values of poro-elastic constants like Biot’s coefficient and bulk modulus. Thus, particularly in complex anisotropic formations, the anisotropy of poro-elastic properties must be considered [64].

Li et al introduced a 3D poro-elasto-plastic numerical model to predict wellbore breakouts, focusing on the interactions between mechanical, hydraulic, and plastic behaviors around the wellbore. The model was grounded in the equations of poro-elasto-plasticity, which incorporate Biot’s coefficient to describe pore fluid pressure impact on effective stress. The study emphasized that mud infiltration into surrounding formation is influenced by the poro-elastic properties of the formation, and this phenomenon plays a critical role in wellbore stability [65].

Using Phase2 software, Akbarpour and Abdideh assessed wellbore stability in the Iranian Asmari reservoir. The focus was on the effects of various factors like on-site stress state, pore pressure, and drilling fluid pressure. Moreover, the impact of rock strength features such as Young’s modulus, rock’s cohesion, along with internal friction angle was evaluated. Furthermore, the impact of Biot's coefficient on wellbore stability was assessed. They stated that the choice of Biot’s coefficient influences the stress concentration around the wellbore. The authors also expressed that higher values of Biot’s coefficient imply an outstanding impact of pore fluid pressure on wellbore stability, affecting the predictions of safe mud weight windows for wellbore stability preservation [66].

Liu et al. studied the challenges associated with wellbore mechanical failure and lost circulation issues. Using poroelasticity theory, the authors derived some mathematical solutions for computation of stresses and pore pressures near the wellbore. Some of input rock properties were E=10.3 GPa, v_u =0.35, φ =0.14, and α=0.96. Asymptotic solutions were established for short-term ($t \to 0^+$) as well as long-term ($t \to \infty$) WSA. A significant discrepancy between the results was observed for two scenarios. It was also highlighted that conventional elastic models fail to properly predict wellbore instability issues, thus underscoring the importance of incorporating poro-elastic solutions for more accurate wellbore stability predictions [67].

As well as the poro-elastic response, some researchers evaluated the wellbore stability by including the temperature (thermal) effect [68-71]. Incorporating temperature in those models made them more complex than the pure poro-elastic models. In many of those models, the temperature was considered constant for a long profile of the rock which is not a true assumption. However, applying temperature-dependent properties of rocks requires time-consuming and expensive experiments.

Nguyen et al. examined the thermo-poro-elastic effects on borehole stability. They introduced a model which incorporated thermal effects, including heat transfer between the rock and mud. The research demonstrated that temperature variations alter the stress distribution around the borehole, affecting the required mud weight window for borehole instability prevention. The study also emphasized the role of Biot’s coefficient in wellbore stability, noting its significant influence, particularly at lower values, where higher rock compressibility exacerbates the impact on stress and stability predictions [72].

Wang et al. conducted quantitative risk assessment research to perform wellbore stability analysis. Historical drilling data were used to reduce uncertainties and enhance the accuracy of the research. Sensitivity analyses highlighted that rocks' cohesion, Biot's coefficient, internal friction angel, bulk modulus, and shear modulus had the greatest impacts on the safe mud pressure required to guarantee borehole stability. Except rock properties, the impacts of on-site stress regime and pore fluid pressure were also found to be highly noticeable. The study also developed a model for practical drilling designation and real-time monitoring. Such a model demonstrated high accuracy in identifying formations with potential wellbore instability occurrence [73]. However, it was noted that the effect of rock poro-elastic properties on wellbore stability might vary across different fields, necessitating specific simulations for each individual case.

Zhang et al. created a model for prediction of mechanical response of rock in deep-sea drilling (DSD) operations. The model integrated mud circulation within the borehole with rock strain. Poro-elastic parameters such as Biot's coefficient (0.80), shear modulus (15 GPa), and Poisson's ratios for drained (0.25) and undrained (0.34) conditions were specified to the numerical model. The study highlighted the significant impact of fluid circulation and poro-elastic parameters on wellbore stability [74].

Zhang et al. conducted a supplementary investigation to examine the impact of various parameters on wellbore stability during deep-sea drilling [75]. The analysis was built on the model developed in [74]. Hence, similar rock properties were given to the model. The research incorporated key poro-elastic relations to assess how fluid flow and mechanical deformation interact in the wellbore and surrounding reservoir. The results showed that changes in drilling depth (stress regime) and rock properties significantly impact the mechanical deformation around the wellbore.

As well as the thermal effect, the chemical effect on wellbore stability has been vastly also investigated. The most chemically wellbore failure issues have been reported in shale formations. Shales contain clay minerals which are highly reactive with mud. Interestingly, roughly 90% of the global wellbore failure issues have occurred in shaley rocks [25].It is noteworthy that shale formations encompass approximately 75% of oil/gas reservoirs [25]. The chemo-thermo-poroelastic analysis of wellbore stability is mainly conducted to choose the appropriate water-based drilling muds, the sensitivity of shale to washing, and determination of safe mud weight [76-79].

Furthermore, especially for shale formations, some researchers assessed the role of anisotropy of formation properties on wellbore stability [16,80-82]. Shale formations possess special features, including preferred fabric orientation and identifiable bedding planes. These features result in transversely isotropic characteristics like elasticity and strength. This inherent anisotropy in shale plays a pivotal role in inducing a unique stress redistribution pattern during drilling operations compared to the isotropic conditions typically encountered in conventional reservoirs. Consequently, the pattern of wellbore instability differs significantly from that observed in conventional reservoirs.

In recent decades, the use of artificial intelligence (AI) techniques in wellbore stability analysis has dramatically increased. Drilling operations are influenced by miscellaneous variables influencing the wellbore stability. The relation between those factors is commonly nonlinear and complex [83]. Machine learning is being considered for predicting wellbore stability in deep drilling due to its ability to handle complex relationships between drilling data and stability parameters [84]. For wellbore stability prediction, there are two types of machine learning approaches: non-full process, and full process. The first one predicts geological parameters and utilizes a mechanical model for wellbore stability prediction, while the second one directly predicts wellbore instability without any additional calculations. Despite its advantages, such as accuracy, applicability, and simplicity, the use of machine learning in wellbore stability scope is relatively new, and there's a need for more investigation in this area [85].

Some researchers suggested incorporating Quantitative Risk Analysis to assess wellbore failure risk derived from the random and uncertain nature of geological properties [86,87]. Quantitative Risk Analysis approach typically begins by identifying the distribution patterns of geological factors within the assessment models [88-90]. Subsequently, the Monte Carlo technique was employed for evaluating the borehole failure probability. Gao et al. developed novel evaluation models to examine the stability of vertical wells drilled within porous geological strata under varying stress conditions. Notably, the authors incorporated the uncertainty of geomechanical factors to perform a comprehensive wellbore instability risk assessment [91].

The incorporation of fluid-rock interaction has gone beyond the stability analysis of wellbores drilled for exploration of oil, gas, and water. For instance, the emerging horizontal directional drilling (HDD) is a straightforward example for this matter. The HDD technique is a modern trenchless construction method in which a shallow horizontal borehole is drilled to emplace the small-to-medium size pipelines [92]. Despite the deep oil/gas wellbores, the boreholes in HDD technique are mainly drilled in shallow loose soils. Wang and sterling performed an FEM-based analysis to assess the stability of shallow HDD wellbores. They determined the safe mud pressure during the HDD drilling operations [93].

In conclusion, the study of wellbore stability progressed significantly during the past decades, progressing from foundational analytical solutions to advanced numerical models that incorporate complex interactions between mechanical, hydraulic, and thermal effects. Early models provided critical insights into stress distribution around wellbores, while subsequent research expanded to include the influence of rock-fluid interactions, as well as anisotropy on wellbore stability. Modern approaches, particularly those utilizing poroelasticity and numerical simulations, have enhanced the accuracy of stability predictions, yet challenges remain, particularly in the need for field-specific simulations and the integration of diverse geomechanical factors. Continued advancements are essential for addressing the complexities of drilling in increasingly challenging environments.

Chapter 4: Stress Concentration around Wellbore

4.1. Elastic solutions

4.1.1. Kirsch's solution

In 1898, Ernst Gustav Kirsch developed the first mathematical solution for calculation of drilling-induced stresses [9]. Figure 4.1 illustrates a schematic view of Krisch's problem. A circular hole was drilled inside a semi-infinite, non-porous elastic plate, which was uniaxially loaded at points far from the hole. A uniaxial tensile stress equal to σ was also applied on the plate parallel to y axis direction. The plate was infinite in the lateral direction (x axis direction). In Figure 4.1, the radius of hole is illustrated as R. Furthermore, θ represents the polar angel measured from y axis towards x axis. The parameter of r represents the distance from the wellbore center. Note that no pore pressure and mud pressure are included in Kirsch's problem.

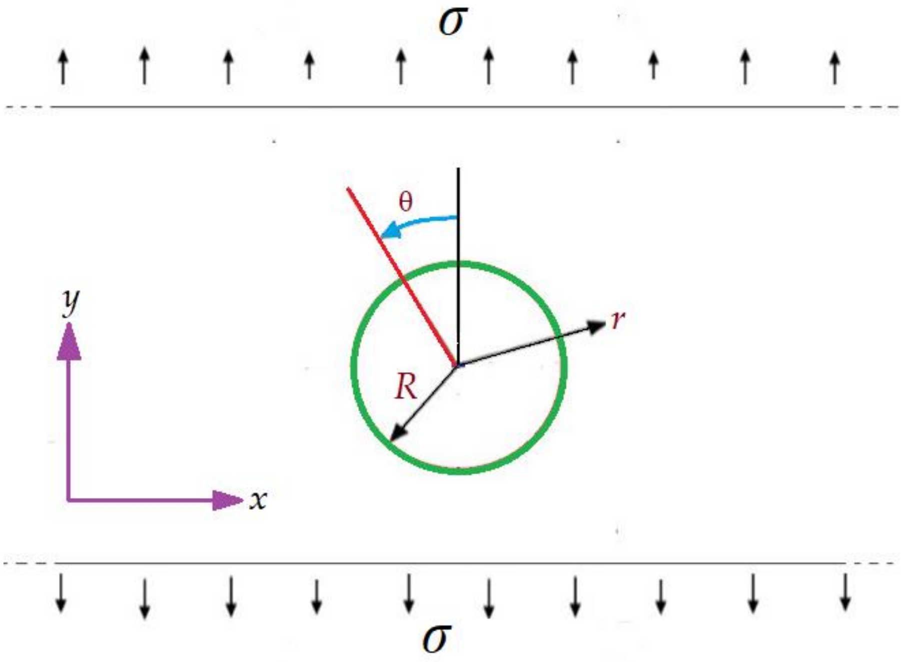

Figure 4.1: Kirsch's solution for a hole drilled within an uniaxially stressed plate.

To find a solution for stresses at any arbitrary point around the wellbore, the Airy stress function can be adopted. Airy developed a stress function of $\Psi(r,\theta)$ from which the stresses could be obtained through differentiation operation [94]. To extract Kirsch's solution, the Airy stress function is described here. Nevertheless, the entire elaboration of Airy stress function is out of this dissertation's scope, and it is presented just in a concise way.

In Figure 4.1, the normal stresses change as cos2θ. On the other side, the shear stresses change as sin2θ. Hence, the following Airy stress function can be defined for the Kirsch's circular hole problem [94]:

$$\Psi(r, \theta) = f(r) \cos 2\theta \tag{4.1}$$

where $\Psi(r, \theta)$ is stress function. Furthermore, $f(r)$ represents a function of r.

Using the Airy stress function, it can be shown that $f(r)$ has a general form as follows [93]:

$$f(r) = A_1 r^2 + A_2 r^4 + A_3 \frac{1}{r^2} + A_4 \tag{4.2}$$

here A_1, A_2, A_3, and A_4 are respectively the first, second, third, and fourth coefficient in Airy stress function for Kirsch's solution. By applying the boundary constraints at r=R, and r=∞, those coefficients are obtained as [94]:

$$A_1 = -\frac{\sigma}{4}, \; A_2 = 0, \; A_3 = -\frac{R^4\sigma}{4}, \text{ and } A_4 = -\frac{R^2\sigma}{2}$$

In a polar coordinate system, stresses are typically stated as radial (r), tangential (θ), and shear ($r\theta$) stresses. A radial stress is a type of normal stress acting perpendicular to a surface at a given radius. It represents stress in the direction of the radius, either compressive or tensile. The tangential stress, also known as hoop or circumferential stress, is the normal stress acting tangentially to a surface at a given radius. It represents the stress perpendicular to the radial direction. And finally, shear stress acts on a plane oriented radially and tangentially.

Consequently, the ultimate formulations for different stresses are obtained as follows [94]:

$$\sigma_r = \frac{\sigma}{2}(1 - \frac{R^2}{r^2}) + \frac{\sigma}{2}\left(1 - \frac{4R^2}{r^2} + \frac{3R^4}{r^4}\right) cos2\theta \tag{4.3}$$

$$\sigma_\theta = \frac{\sigma}{2}\left(1 + \frac{R^2}{r^2}\right) - \frac{\sigma}{2}(1 + \frac{3R^4}{r^4}) cos2\theta \tag{4.4}$$

$$\tau_{r\theta} = -\frac{\sigma}{2}\left(1 + \frac{2R^2}{r^2} + \frac{3R^4}{r^4}\right) cos2\theta \tag{4.5}$$

At r=R, the magnitude of the above stresses become [94]:

$$\sigma_r = 0 \tag{4.6}$$

$$\sigma_\theta = \sigma(1 - 2cos2\theta) \tag{4.7}$$

$$\tau_{r\theta} = -3\sigma cos2\theta \tag{4.8}$$

Based on the Eq. (4.7), the highest tangential stress on the hole wall gets 3σ at $\theta = \frac{\pi}{2}$. Furthermore, the highest shear stress acting on the wall gets 3σ at $\theta = \frac{\pi}{2}$.

Kirsch's solution was fundamental in understanding elastic stress concentration around a borehole, and it provided a basis for further developments in poro-elastic stress analyses. Hubbert and Wills and Fairhurst applied Kirsch's formulation for stress analysis around wellbores [10,11]. Later, the accuracy of Kirsch's equations was confirmed through photoelasticity theory and laboratory experiments [95]. These equations are still used in rock mechanics textbooks to represent stresses induced by drilling of a circular borehole [96]. Although Kirsch published his paper in 1898, the paper may not be an ideal reference to derive Kirsch's equations [9]. The reason is that it heavily references a contemporary German textbook [45].

4.1.2. Bradley's solution

Kirsch's solution had been fundamentally established for vertical holes. In 1979, Bradley combined Kirsch's and Fairhurst's solutions to formulate stress concentration around wellbores [12]. He assumed a circular inclined wellbore drilled within an infinite elastic plate (Figure 4.2). Pore pressure was not considered but mud pressure was incorporated in the solution. However, mud infiltration into the formation was not permitted. In fact, the wellbore wall was assumed to be impermeable. In Figure 4.2, p_m shows the mud pressure in the borehole.

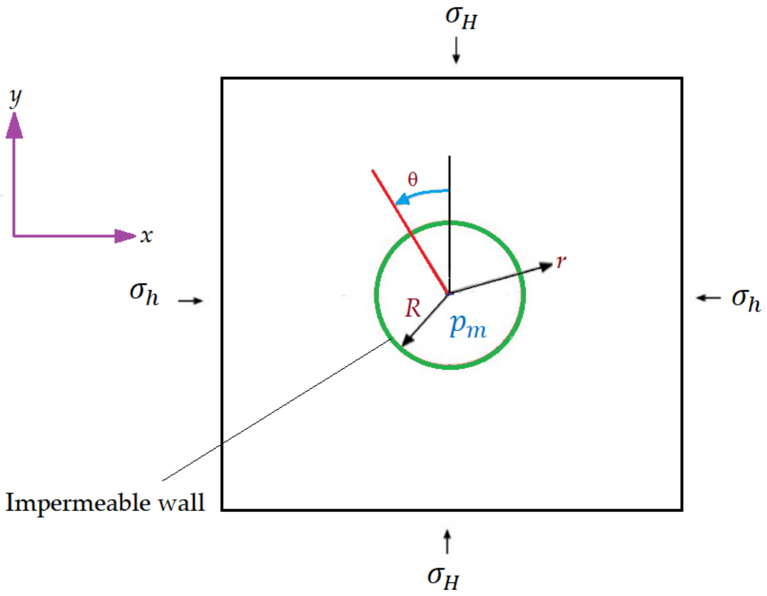

Figure 4.2: Bradley's configuration for a circular inclined borehole.

The following equations were developed to formulate the near-wellbore stresses as follows [12, 95]:

$$\sigma_r = \left(\frac{\sigma_x+\sigma_y}{2}\right)\left(1-\frac{R^2}{r^2}\right) + \left(\frac{\sigma_x-\sigma_y}{2}\right)\left(1+\frac{3R^4}{r^4}-\frac{4R^2}{r^2}\right)cos2\theta + \tau_{xy}\left(1+\frac{3R^4}{r^4}-\frac{4R^2}{r^2}\right)sin2\theta + p_m\frac{R^2}{r^2} \quad (4.9)$$

$$\sigma_\theta = \left(\frac{\sigma_x+\sigma_y}{2}\right)\left(1+\frac{R^2}{r^2}\right) - \left(\frac{\sigma_x-\sigma_y}{2}\right)\left(1+\frac{3R^4}{r^4}\right)cos2\theta - \tau_{xy}\left(1+\frac{3R^4}{r^4}\right)sin2\theta - p_m\frac{R^2}{r^2} \quad (4.10)$$

$$\sigma_z = \sigma_{zz} - v\left(2(\sigma_x-\sigma_y)\frac{R^2}{r^2}cos2\theta + 4\tau_{xy}\frac{R^2}{r^2}sin2\theta\right) \quad (4.11)$$

$$\tau_{r\theta} = \left(\frac{\sigma_x-\sigma_y}{2}\right)\left(1-\frac{3R^4}{r^4}+\frac{2R^2}{r^2}\right)sin2\theta + \tau_{xy}\left(1-\frac{3R^4}{r^4}+\frac{2R^2}{r^2}\right)cos2\theta \quad (4.12)$$

$$\tau_{\theta z} = (-\tau_{xz}sin\theta + \tau_{yz}cos\theta)(1+\frac{R^2}{r^2}) \quad (4.13)$$

$$\tau_{rz} = (\tau_{xz}cos\theta + \tau_{yz}sin\theta)(1-\frac{R^2}{r^2}) \quad (4.14)$$

In the above equations, σ_r, σ_θ, and σ_z respectively represent the radial, tangential, and vertical stress within polar coordinate system. Similarly, $\tau_{r\theta}$, $\tau_{\theta z}$, and τ_{rz} indicate the shear stress components. Moreover, σ_x, σ_y, and σ_{zz} represent on-site normal stresses rotated to the wellbore coordinate system. Similarly, τ_{xy}, τ_{xz}, and τ_{yz} stand for on-site shear stresses rotated to the wellbore coordinate system. *R* stands for the wellbore radius. The parameter of *r* stands for the distance from the wellbore center. The polar angle is represented as θ.

At *r*=*R*, Eqs. (4.9-4.14) are simplified as follows [56]:

$$\sigma_r = p_m \quad (4.15)$$

$$\sigma_\theta = (\sigma_x+\sigma_y-p_m) - 2(\sigma_x-\sigma_y)cos2\theta - 4\tau_{xy}sin2\theta \quad (4.16)$$

$$\sigma_z = \sigma_{zz} - v[2(\sigma_x-\sigma_y)cos2\theta + 4\tau_{xy}sin2\theta] \quad (4.17)$$

$$\tau_{\theta z} = 2(-\tau_{xz}sin\theta + \tau_{xy}cos\theta) \quad (4.18)$$

$$\tau_{r\theta} = 0 \quad (4.19)$$

$$\tau_{rz} = 0 \quad (4.20)$$

If the wellbore is vertical, Eqs. (4.9-4.14) can be rewritten as follows [56]:

$$\sigma_r = \left(\frac{\sigma_H+\sigma_h}{2}\right)\left(1-\frac{R^2}{r^2}\right) + \left(\frac{\sigma_H-\sigma_h}{2}\right)\left(1-\frac{4R^2}{r^2}+\frac{3R^2}{r^4}\right)cos2\theta + p_m\frac{R^2}{r^2} \quad (4.21)$$

$$\sigma_\theta = \left(\frac{\sigma_H+\sigma_h}{2}\right)\left(1+\frac{R^2}{r^2}\right) - \left(\frac{\sigma_H-\sigma_h}{2}\right)\left(1+\frac{3R^2}{r^4}\right)cos2\theta - p_m\frac{R^2}{r^2} \quad (4.22)$$

$$\sigma_z = \sigma_v - v\frac{2R^2}{r^2}(\sigma_H-\sigma_h)cos2\theta \quad (4.23)$$

$$\tau_{r\theta} = -\left(\frac{\sigma_H-\sigma_h}{2}\right)\left(1+\frac{2R^2}{r^2}-\frac{3R^4}{r^4}\right) sin2\theta \tag{4.24}$$

$$\tau_{rz} = 0 \tag{4.25}$$

$$\tau_{\theta z} = 0 \tag{4.26}$$

In the above equations, σ_H and σ_h represent the greatest and the least far-field on-site stresses, respectively. At *r*=*R*, the radial and tangential stresses can be readily determined as follows [56]:

$$\sigma_r = p_m \tag{4.27}$$

$$\sigma_\theta = (\sigma_H + \sigma_h) - 2(\sigma_H - \sigma_h)cos2\theta - p_m \tag{4.28}$$

At *r*=*R*, the highest and the least values of tangential stress are obtained as follows [56]:

$$\sigma_{\theta_{max}} = 3\sigma_H - \sigma_h - p_m \qquad \text{, at} \quad \theta = 90^\circ \tag{4.29}$$

$$\sigma_{\theta_{min}} = 3\sigma_h - \sigma_H - p_m \qquad \text{, at} \quad \theta = 0^\circ \tag{4.30}$$

In comparison to Kirsch's solution, Bradley's solution is a 3D formulation. Moreover, it considers the mud pressure although no mud influx into the formation is permitted. Note that the formation pore pressure is not considered in Bradley's solution. Despite the mentioned drawbacks, Bradley's equations have been widely used in petroleum engineering for WSA.

4.1.3. Bradley's solution with pore pressure consideration

The main drawback of Bradley's solution was that it did not consider the pore fluid pressure within the formation. As is widely recognized, rocks often are porous media containing pore fluids. The effect of pore pressure on the hydro-mechanical behavior of rock-fluid medium is described by the effective stress concept as follows [56]:

$$\sigma'_{ij} = \sigma_{ij} - \alpha\delta_{ij}p \tag{4.31}$$

where σ'_{ij} indicates the effective stress. Furthermore, σ_{ij} stands for the total stress. The indices of i and j can be specified as 1, 2, and 3. α stands for Biot's coefficient. p is pore pressure. Also, the sign of δ stands for the Kronecker delta.

To include pore pressure parameter in Bradley's solution, let's assume a circular vertical borehole drilled in an isotropic elastic medium (Figure 4.3). The greatest and the least horizontal stresses are shown as σ_H and σ_h, respectively. Pore pressure is constant, and α is assumed as 1. Also, no mud flow out and pore fluid influx into the wellbore are permitted (impermeable wellbore wall).

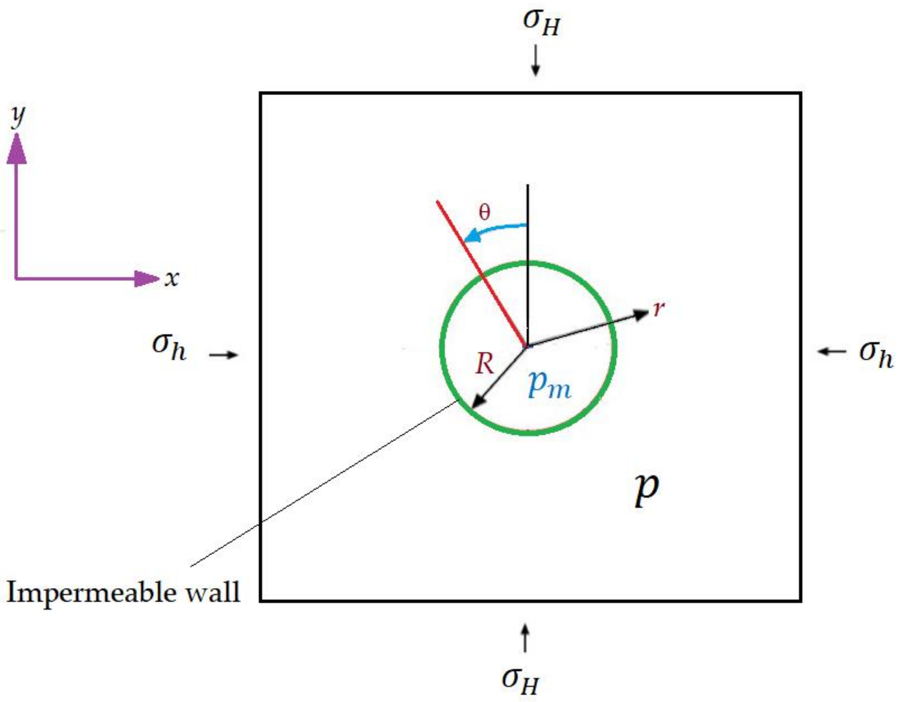

Figure 4.3: Modified Bradley's solution with pore pressure consideration.

As is well-known, the pore pressure only affects normal stress. It has no influence on shear stress. Therefore, Eqs. (4.21-4.23) change, while Eqs. (4.24-4.26) remain unchanged, as follows [56]:

$$\sigma'_r = \left(\frac{\sigma_H+\sigma_h-2p}{2}\right)\left(1-\frac{R^2}{r^2}\right)+\left(\frac{\sigma_H-\sigma_h}{2}\right)\left(1-\frac{4R^2}{r^2}+\frac{3R^2}{r^4}\right)cos2\theta+(p_m-p)\frac{R^2}{r^2} \tag{4.32}$$

$$\sigma'_\theta = \left(\frac{\sigma_H+\sigma_{h-2p}}{2}\right)\left(1+\frac{R^2}{r^2}\right)-\left(\frac{\sigma_H-\sigma_h}{2}\right)\left(1+\frac{3R^2}{r^4}\right)cos2\theta-(p_m-p)\frac{R^2}{r^2} \tag{4.33}$$

$$\sigma'_z = \sigma_v - p - v\frac{2R^2}{r^2}(\sigma_H-\sigma_h)cos2\theta \tag{4.34}$$

$$\tau_{r\theta} = -\left(\frac{\sigma_H-\sigma_h}{2}\right)\left(1+\frac{2R^2}{r^2}-\frac{3R^4}{r^4}\right)sin2\theta \tag{4.35}$$

$$\tau_{rz} = 0 \tag{4.36}$$

$$\tau_{\theta z} = 0 \tag{4.37}$$

where, σ_v stands for the vertical principal stress.

Subsequently, at the borehole wall, the effective normal stresses are determined as follows [56]:

$$\sigma'_r = p_m - p \tag{4.38}$$

$$\sigma'_\theta = \sigma_H + \sigma_h - p - p_m - 2(\sigma_H - \sigma_h)cos2\theta \tag{4.39}$$

$$\sigma'_z = \sigma_v - p - v[2(\sigma_H - \sigma_h)cos2\theta] \tag{4.40}$$

Then, the least and the highest values of effective tangential stresses at *r*=*R* are obtained as follows [56]:

$$\sigma'_{\theta_{max}} = 3\sigma_H - \sigma_h - p - p_m \qquad \text{, at} \quad \theta = 90^{\circ} \tag{4.41}$$

$$\sigma'_{\theta_{min}} = 3\sigma_h - \sigma_H - p - p_m \qquad \text{, at} \quad \theta = 0^{\circ} \tag{4.42}$$

Note that angles of $\theta = 90^{\circ}$ and $\theta = 0^{\circ}$ represent the direction of σ_h and σ_H, respectively.

In this described solution, the pore fluid pressure was assumed as an unchanged parameter, and α was presumed as 1. Nevertheless, the change in the pore pressure, and hydro-mechanical interaction (poro-elastic effect) between fluid and rock were not considered. These are the main disadvantages of the above elastic solution.

4.2. Poro-elastic solutions

Considering the significant impact of fluid-rock interaction on wellbore stability, different analytical solutions were developed using the poroelasticity theory. The analytical elastic solutions presented before did not account for fluid infiltration from/into the porous rock.

Some researchers developed analytical or numerical-analytical formulations to consider the fluid-rock interaction in WSA [13,14,17,97]. In what follows, the solution established by Cui et al. will be presented [14]. This solution is an inclusive formulation for poro-elastic wellbore stability analysis.

4.2.1. Cui et al.'s solution

Cui et al. established a mathematical formulation to formulate the drilling-induced stresses around a wellbore embedded in an isotropic, homogeneous porous rock [14]. Let's consider an inclined wellbore drilled in an isotropic porous medium (Figure 4.4a). The $x'y'z'$ Cartesian coordinate system indicates the far-field in-situ coordinate system. Furthermore, the far-field on-site stresses within the region are represented by $S_{x'}, S_{y'}$ and $S_{z'}$. The native pore pressure is p_0.

To facilitate the wellbore simulation, there is need to define a local wellbore coordinate system. For the given wellbore, let's assign a local wellbore coordinate system, i.e. xyz (Figure 4.4b). This coordinate system is created by rotation the $x'y'z'$ coordinate system. The z axis is aligned with the longitudinal axis of the wellbore. Moreover, φ_z stands for the angle between z' and z axes. It is noteworthy that φ_z is also known as the wellbore deviation angle. In addition, φ_x indicates the angle between x' and x axes. Stresses in $x'y'z'$ are then transformed to xyz system (Figure 4.4c).

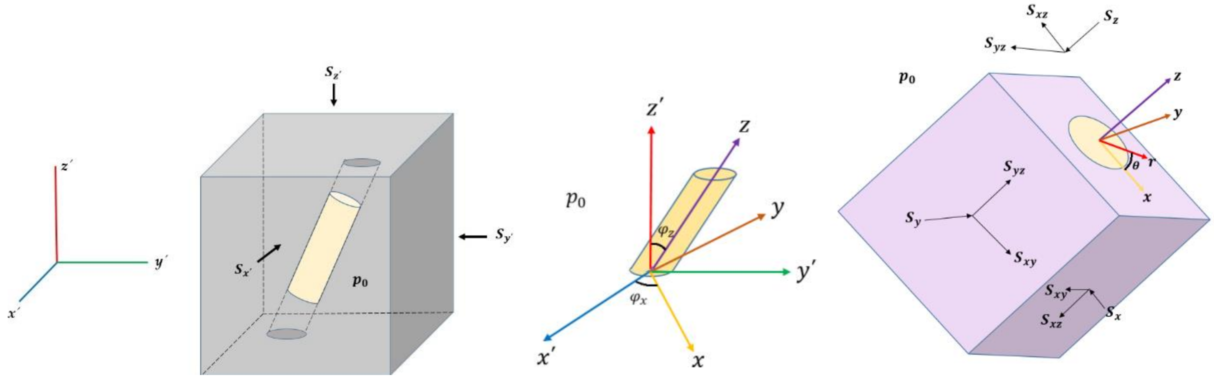

(a) (b) (c)

Figure 4.4: (a) Far-field in-situ coordinate system; (b) the spatial illustration of far-field and local wellbore coordinate systems; (c) different components of stresses in wellbore coordinate system.

The following matrix can be utilized to transform the far-field in-situ stresses to the local wellbore coordinate system [14,17]:

$$\begin{Bmatrix} S_x \\ S_y \\ S_z \\ S_{xy} \\ S_{yz} \\ S_{xz} \end{Bmatrix} = \begin{bmatrix} l_{xx'}^2 & l_{xy'}^2 & l_{xz'}^2 \\ l_{yx'}^2 & l_{yy'}^2 & l_{yz'}^2 \\ l_{zx'}^2 & l_{zy'}^2 & l_{zz'}^2 \\ l_{xx'}l_{yx'} & l_{xy'}l_{yy'} & l_{xz'}l_{yz'} \\ l_{yx'}l_{zx'} & l_{zy'}l_{yy'} & l_{zz'}l_{yz'} \\ l_{zx'}l_{xx'} & l_{zy'}l_{xy'} & l_{zz'}l_{xz'} \end{bmatrix} \times \begin{Bmatrix} S_{x'} \\ S_{y'} \\ S_{z'} \end{Bmatrix} \tag{4.43}$$

where

$$\begin{Bmatrix} l_{xx'} & l_{xy'} & l_{xz'} \\ l_{yx'} & l_{yy'} & l_{yz'} \\ l_{zx'} & l_{zy'} & l_{zz'} \end{Bmatrix} = \begin{bmatrix} cos\varphi_x cos\varphi_z & sin\varphi_x cos\varphi_x & -sin\varphi_z \\ -sin\varphi_x & cos\varphi_x & 0 \\ cos\varphi_x sin\varphi_z & sin\varphi_x sin\varphi_z & cos\varphi_z \end{bmatrix} \tag{4.44}$$

In the above equation, S_x, S_y, S_z indicate the normal stresses in xyz system. On the other side, S_{xy}, S_{yz}, and S_{zx} represent the shear stresses in the same coordinate system. Furthermore, $l_{xx'}$, $l_{xy'}$, $l_{xz'}$, $l_{yx'}$, $l_{yy'}$, $l_{yz'}$, $l_{zx'}$, $l_{zy'}$, and $l_{zz'}$ are trigonometric parameters.

Now, the problem illustrated in Figure 4.4c can be decomposed to three separate segments as follows (Figure 4.5):

I. The poro-elastic plane strain loading condition

II. The elastic uni-axial loading condition

III. The elastic anti-plane shear loading condition

Note that the vertical stress, S_z, is divided into two components within segments *I* and *II*, as follows [14]:

$$S_z = S_z^1 + S_z^2 \tag{4.45}$$

where S_z represents the vertical stress, S_z^1 stands for the vertical stress component within the segment *I*, and S_z^2 indicates the vertical stress component within the segment *II*.

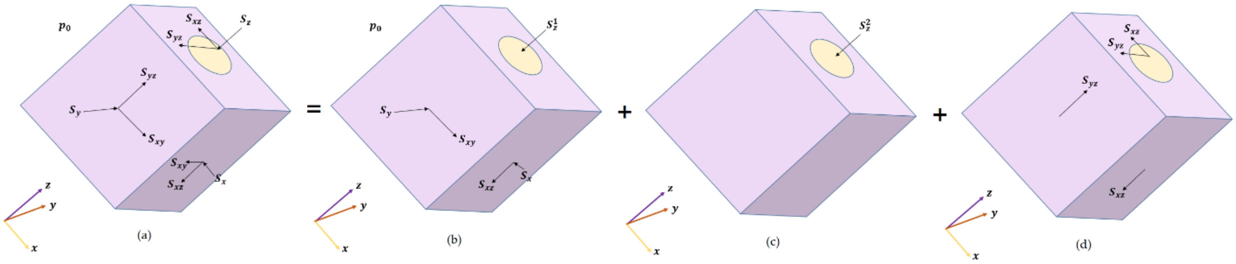

Figure 4.5: (a) the spatial illustration of stresses in local wellbore coordinate system; (b) segment *I*; (c) segment *II*; (d) segment *III*.

Using the above decomposition, the problem can be solved by superposition [14]. The solution for each individual segment is presented in Sections 4.3.1.1., 4.3.1.2., and 4.3.1.3, respectively. After that, the superposition of those individual solutions is provided in Section 4.3.1.4.

4.2.1.1. Solution for segment *I*

To achieve this solution, firstly, it is essential to transform the xyz coordinate system to a new coordinate system, $x''y''z''$. This new coordinate system is chosen so that x'' axis and y'' axis are parallel to the direction of σ_h and σ_H, respectively. Therefore, the xyz coordinate system is rotated about z axis till x'' axis and y'' axis coincide with directions of σ_h and σ_H, respectively (Figure 4.6). The $x''y''z''$ coordinate system can be named the "Principal stress coordinate system". This name reflects the fact that the coordinate axes are parallel to the principal stresses (σ_h and σ_H) directions.

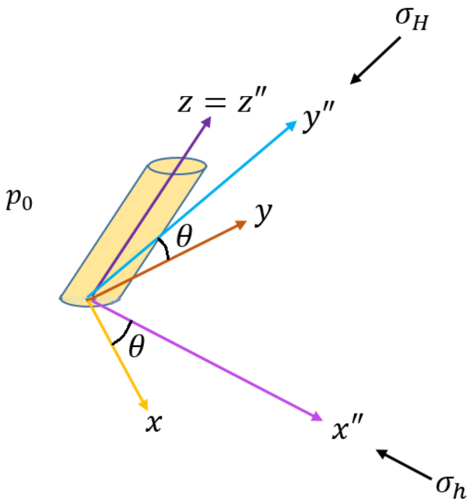

Figure 4.6: The principal stress coordinate system ($x''y''z''$).

The rotation angle between x and x'' axes is obtained as follows [14]:

$$\theta_r = \frac{1}{2} tan^{-1} \frac{2S_{xy}}{S_x - S_y} \tag{4.46}$$

In the $x''y''z''$ system, the following relation can be expressed as [14]:

$$\theta'' = \theta - \theta_r \tag{4.47}$$

where θ'' is the polar angle in $x''y''z''$ coordinate system, and θ is the polar angle in xyz coordinate system.

In the $x''y''z''$ coordinate system, the far-field stresses at $r \rightarrow \infty$ are given by [14]:

$$\sigma_{x''x''} = -(P_0 - S_0) \tag{4.48}$$

$$\sigma_{y''y''} = -(P_0 + S_0) \tag{4.49}$$

$$\sigma_{x''y''} = 0 \tag{4.50}$$

$$p = p_0 \tag{4.51}$$

In the above equations, P_0 and S_0 represent the far-field mean compressive stress and the far-field deviatoric stress, respectively. These parameters are defined as follows [14]:

$$P_0 = \frac{S_x + S_y}{2} \tag{4.52}$$

$$S_0 = \sqrt{\frac{S_x + S_y}{2} + S_{xy}^2} \tag{4.53}$$

Baded on the above far-field stress conditions, the solution for segment *I* is achieved as follows [14]:

$$\sigma_{rr}^{(I)} = -P_0 + S_0 cos2(\theta - \theta_r) + \sigma_{rr}^{(1)} + \sigma_{rr}^{(2)} + \sigma_{rr}^{(3)} \tag{4.54}$$

$$\sigma_{\theta\theta}^{(I)} = -P_0 - S_0 cos2(\theta - \theta_r) + \sigma_{\theta\theta}^{(1)} + \sigma_{\theta\theta}^{(2)} + \sigma_{\theta\theta}^{(3)} \tag{4.55}$$

$$\sigma_{zz}^{(I)} = v\left[\sigma_{rr}^{(1)} + \sigma_{\theta\theta}^{(1)}\right] - \alpha(1 - 2v)p^{(I)} \tag{4.56}$$

$$\tau_{r\theta}^{(I)} = -S_0\, sin2(\theta - \theta_r) + \tau_{r\theta}^{(3)} \tag{4.57}$$

$$\tau_{rz}^{(I)} = \tau_{\theta z}^{(I)} = 0 \tag{4.58}$$

$$p^{(I)} = p_0 + p^{(2)} + p^{(3)} \tag{4.59}$$

In the above equations, the subscript (*I*) means that the corresponding parameter belongs to segment *I* (or poro-elastic plane stress problem). Furthermore, the subscripts $^{(1),\,(2)}$ and $^{(3)}$ illustrate the poro-elastic plane stress problem in three different states: Lame, diffusion, and poro-elastic deviatoric stress loading, respectively [13]. The mathematical relations for calculation of parameters pertinent to those three cases are explained below.

1. Lame state

In Eqs. (4.54-4.59), two stresses including $\sigma_{rr}^{(1)}$ and $\sigma_{\theta\theta}^{(1)}$ belong to the Lame state. Those two parameters can be computed as follows [14]:

$$\sigma_{rr}^{(1)} = H(t)P_0\frac{R^2}{r^2} \tag{4.60}$$

$$\sigma_{\theta\theta}^{(1)} = -H(t)P_0\frac{R^2}{r^2} \tag{4.61}$$

where the Heaviside step function of *H(t)* is expressed as follows:

$$H(t) = \begin{cases} 1 & t > 0 \\ 0 & t \leq 0 \end{cases} \tag{4.62}$$

where *t* indicates the time after the drilling commencement.

2. Diffusion state

In Eqs. (4.54-4.59), two stress components including $\sigma_{rr}^{(2)}$ and $\sigma_{\theta\theta}^{(2)}$ as well as pore pressure $p^{(2)}$ are related to diffusion state. One approach to determine those three parameters is the Laplace transformation [13]. If the Laplace transformation is utilized, the three variables are obtained as follows [14]:

$$\tilde{\sigma}_{rr}^{(2)} = -\frac{2\eta p_0}{s}\left[\frac{R}{r}\frac{k_1(\xi)}{\beta k_0(\beta)} - \frac{R^2}{r^2}\frac{k_1(\beta)}{\beta k_0(\beta)}\right] \tag{4.63}$$

$$\tilde{\sigma}_{\theta\theta}^{(2)} = -\frac{2\eta p_0}{s}\left[\frac{R}{r}\frac{k_1(\xi)}{\beta k_0(\beta)} - \frac{R^2}{r^2}\frac{k_1(\beta)}{\beta k_0(\beta)} + \frac{k_0(\xi)}{k_0(\beta)}\right] \tag{4.64}$$

$$\tilde{p}^{(2)} = -\frac{p_0}{s}\frac{k_0(\xi)}{k_0(\beta)} \tag{4.65}$$

where, the ~ sign refers to the Laplace transform. Moreover, *s* represents the transform parameter, and η represents the poro-elastic stress coefficient which is calculated as follows [14]:

$$\eta = \frac{3(v_u - v)}{2B(1-v)(1+v_u)} = \alpha\frac{1-2v}{2(1-v)} \tag{4.66}$$

Moreover, k_n represents the modified Bessel function pertinent to the second kind of order *n*. It should be noted that k_n is a function of ξ and β as follows [14]:

$$\xi = r\sqrt{\frac{s}{c}} \tag{4.67}$$

$$\beta = R\sqrt{\frac{s}{c}} \tag{4.68}$$

In the above equations, ξ and β are dependent parameters. Furthermore, c refers to the generalized consolidation coefficient calculated as follows [13]:

$$c = \frac{2\kappa B^2 G(1-v)(1+v_u)^2}{9(1-v_u)(v_u-v)}\nabla^2 p \tag{4.69}$$

where κ represents the permeability coefficient, and other parameters have been already defined in Chapter 2.

3. Poro-elastic deviatoric stress loading state

In Eqs. (4.54-4.59), three stress components including $\sigma_{rr}^{(3)}$, $\sigma_{\theta\theta}^{(3)}$, and $\tau_{r\theta}^{(3)}$ as well as pore pressure $p^{(3)}$ are related to this state which is an entirely poro-elastic problem. If the Laplace transform is used, the corresponding parameters are computed as follows [14]:

$$\tilde{\sigma}_{rr}^{(3)} = \frac{S_0}{s}\Bigl\{\frac{B(1+v_u)}{3(1-v_u)}C_1\Bigl[\frac{1}{\xi}K_1(\xi)+\frac{6}{\xi^2}K_2(\xi)\Bigr]-\frac{1}{1-v_u}C_2\frac{R^2}{r^2}-3C_3\frac{R^4}{r^4}\Bigr\}cos2(\theta-\theta_r) \qquad (4.70)$$

$$\tilde{\sigma}_{\theta\theta}^{(3)} = \frac{S_0}{s}\Bigl\{-\frac{B(1+v_u)}{3(1-v_u)}C_1\Bigl[\frac{1}{\xi}K_1(\xi)+(1\frac{6}{\xi^2})K_2(\xi)\Bigr]+3C_3\frac{R^4}{r^4}\Bigr\}cos2(\theta-\theta_r) \qquad (4.71)$$

$$\tilde{\tau}_{r\theta}^{(3)} = \frac{S_0}{s}\Bigl\{\frac{2B(1+v_u)}{3(1-v_u)}C_1\Bigl[\frac{1}{\xi}K_1(\xi)+\frac{3}{\xi^2}K_2(\xi)-\frac{1}{2(1-v_u)}C_2\frac{R^2}{r^2}-3C_3\frac{R^4}{r^4}\Bigr\}\Bigr]sin2(\theta-\theta_r) \qquad (4.72)$$

$$\tilde{p}^3 = \frac{S_0}{s}\Bigl[\frac{B^2(1-v)(1+v_u)^2}{9(1-v_u)(v_u-v)}C_1K_2(\xi)+\frac{B(1+v_u)}{3(1-v_u)}C_2\frac{R^2}{r^2}\Bigr]cos2(\theta-\theta_r) \qquad (4.73)$$

In the above equations, C_1, C_2, and C_3 represent the first, second, and third coefficients in Laplace transform of poro-elastic deviatoric stress loading state. These coefficients can be obtained as follows [14]:

$$C_1 = \frac{12\beta(1-v_u)(v_u-v)}{B(1+v_u)(D_2-D_1)} \qquad (4.74)$$

$$C_2 = \frac{4(1-v_u)D_2}{(D_2-D_1)} \qquad (4.75)$$

$$C_3 = -\frac{\beta(D_2+D_1)+8(v_u-v)K_2(\beta)}{\beta(D_2-D_1)} \qquad (4.76)$$

in which

$$D_1 = 2(v_u-v)K_1(\beta) \qquad (4.77)$$

$$D_2 = \beta(1-v)K_2(\beta) \qquad (4.78)$$

where D_1 and D_2 respectively indicate the factor related to modified Bessel function of the second kind of order 1 and order 2.

4.2.1.2. Solution for segment *II*

As Figure 4.5c illustrates, under elastic uni-axial loading condition, only a consistent uni-axial stress, S_z^2, is applied to the rock. Moreover, there is no virgin pore pressure in this case. Therefore, the following relations can be derived as [14]:

$$\sigma_{zz}^{(II)} = -S_z + [v(S_x + S_y) + \alpha(1 - 2v)p_0] \tag{4.79}$$

$$\sigma_{rr}^{(II)} = \sigma_{\theta\theta}^{(II)} = \tau_{r\theta}^{(II)} = \tau_{rz}^{(II)} = \tau_{\theta z}^{(II)} = p^{(II)} = 0 \tag{4.80}$$

4.2.1.3. Solution for segment *III*

As shown in Figure 4.5d, in this case, only shear stresses are acting on the rock. This problem was previously addressed in work published by Bradley [12]. The corresponding solution is given by [14]:

$$\tau_{rz}^{(III)} = -(S_{xz}\cos\theta + S_{yz}\sin\theta)[1 - H(t)\frac{R^2}{r^2}] \tag{4.81}$$

$$\tau_{\theta z}^{(III)} = (S_{xz}\sin\theta - S_{yz}\cos\theta)[1 + H(t)\frac{R^2}{r^2}] \tag{4.82}$$

$$\sigma_{rr}^{(III)} = \sigma_{\theta\theta}^{(III)} = \sigma_{zz}^{(III)} = \tau_{r\theta}^{(III)} = p^{(III)} = 0 \tag{4.83}$$

4.2.1.4. Superposition of solutions *I*, *II*, and *III*.

Lastly, by superposition of the solutions obtained for segments *I*, *II*, and *III*, the ultimate poro-elastic solution is expressed as follows [14]:

$$\sigma_{rr} = \sigma_{rr}^{(I)} \tag{4.84}$$

$$\sigma_{\theta\theta} = \sigma_{\theta\theta}^{(I)} \tag{4.85}$$

$$\sigma_{zz} = \sigma_{zz}^{(I)} + \sigma_{zz}^{(II)} \tag{4.86}$$

$$\tau_{r\theta} = \tau_{r\theta}^{(I)} \tag{4.87}$$

$$\tau_{rz} = \tau_{rz}^{(III)} \tag{4.88}$$

$$\tau_{\theta z} = \tau_{\theta z}^{(III)} \tag{4.89}$$

$$p = p^{(I)} \tag{4.90}$$

Chapter 5: Methodology

5.1. Laboratory part

The methodology of the present research consisted of two complementary parts: The first part involved conducting physical experiments in the laboratory to obtain experimental data. Through these experiments, not only the physical, mechanical, and poro-elastic characteristics of the sandstone samples were obtained, but rocks' behavior under various loading conditions, including drained and undrained conditions, was also analyzed. In the field, two methods are utilized to measure the geomechanical properties of rocks: direct laboratory tests and indirect acoustic log data. The first method is liable, while it is considerably costly, moreover, it is very difficult to have adequate samples from all depths of the field. On the contrary, the indirect acoustic data is more widespread, and it characterizes the rock along the different depth profiles. Nevertheless, this data must be appropriately calibrated using the laboratory tests in which the exact correlations between the shear/compressional wave velocity and rock strength properties are extracted [98].

Determining the different characteristics of a rock requires the use of various laboratory instruments. The laboratory of Drilling and Geo-Engineering Department at AGH University of Kraków is equipped with a wide range of laboratory equipment that allows researchers to measure different characteristics of rock samples. For the present research, the following laboratory instruments were used:

1. Cutting machine

This machine was used for the initial cutting of large slab of rocks. Figure 5.1 shows this machine. The operating procedure involves placing a rock slab in front of the machine's circular blade. Upon activating the motor, the circular blade cuts the rock slab into smaller pieces. During the cutting process, water is sprayed onto the blade through a nozzle to reduce wear and tear on the blade.

Figure 5.1: Cutting machine.

2. Drilling machine

In the next step, the smaller rock pieces obtained from the cutting machine are placed under the drill bit of the drilling machine to extract cylindrical cores. Figure 5.2 shows this drilling machine. The machine can deliver cylindrical rock cores of several centimeters in length. In the present research, a 38 mm diameter steel coring bit was used. Water was utilized to cool the drill bit during the drilling process as well as reducing the wear and tear on the bit.

Figure 5.2: Drilling machine.

3. Smoothing machine

In the subsequent step, the circular cross-sections of the rock cores were smoothed and flattened using a smoothing machine to ensure that they were free of any roughness or asymmetry. This machine is shown in Figure 5.3. Additionally, using this machine, the cores were cut to the desired length along their longitudinal axis.

Figure 5.3: Smoothing machine.

4. Oven

After preparing the rock samples to the desired dimensions, the samples were placed in an oven to completely dry out any moisture. Figure 5.4 shows the oven used for this purpose. For 24 hours, the samples were kept in the oven at 90°C.

Figure 5.4: Oven.

5. Balance

After drying the rock samples in the oven, a balance was used to measure their weights. Figure 5.5 shows the balance used.

Figure 5.5: Balance.

After this stage, the samples were grouped into two categories: the first one, consisting of 15 samples, was used for measuring the UCS, cohesion, and internal friction angle of Tumlin sandstone. The second group, including 30 samples, was used to measure the poro-elastic parameters of the Tumlin sandstone. In what follows, three applied laboratory apparatuses used for those purposes are described.

6. Triaxial compression testing machine

A triaxial compression testing machine was used for measuring the mechanical properties of the first group of rock samples. This machine is shown in Figure 5.6. Using this device, the rock's strength properties, including cohesion, UCS, and internal friction angle, were determined.

Figure 5.6: Triaxial compression testing machine.

The average UCS of Tumlin sandstone was found to be 42.3 MPa. Additionally, the linear Mohr-Coulomb failure criterion was extracted for the rock. The common form of this criterion is expressed as follows [1]:

$$\tau = C + \mu\sigma_n \tag{5.1}$$

where, τ stands for the shear stress, and C represents the rock's cohesion. Furthermore, σ_n indicates the normal stress. Moreover, μ illustrates the internal friction angle coefficient, which is defined as [1]:

$$\mu = \tan\phi \tag{5.2}$$

Where ϕ indicates the internal friction angle of rock. It is also possible to state Eq. (5.1) based on the highest and lowest applied stresses at the failure moment, as follows [1]:

$$\sigma_1 = C_0 + q\sigma_3 \tag{5.3}$$

where σ_1 represents the axial stress at the failure moment, C_0 represents the rock's UCS, σ_3 indicates the lateral stress at the failure moment, and q is the flow factor which depends on ϕ. The following relations are used to calculate q and C_0 as follows [1]:

$$q = \frac{1+\sin\phi}{1-\sin\phi} \tag{5.4}$$

$$C_0 = 2C\,\frac{\cos\phi}{1-\sin\phi} \tag{5.5}$$

In this research, to obtain the values of q and C_0 in the laboratory setting, the triaxial experiments were executed on five Tumlin sandstone specimens. The magnitudes of σ_3 and σ_1 at the failure moment were recorded. Then, for all samples, the σ_1-σ_3 graph was drawn, and the values of q and C_0 were computed.

In the subsequent step, the internal friction angle can be calculated by rearranging Eq. (5.4) as follows [1]:

$$\phi = \mathrm{Sin}^{-1}\frac{(q-1)}{(q+1)} \tag{5.6}$$

After calculating ϕ from the above equation, the rock's cohesion was obtained as [1]:

$$C = C_0\,\frac{(1-sin\phi)}{2\cos\phi} \tag{5.7}$$

Furthermore, the rock's tensile strength can be determined using the following relation:

$$\sigma_t = 2C \frac{\cos\phi}{1+\sin\phi} \tag{5.8}$$

7. Saturation apparatus

The second group, consisting of 30 samples, was adopted to determine the poro-elastic characteristics of the sandstone. After weighing the dry mass of these 30 samples using the balance (Figure 5.5), they were all saturated with water. Figure 5.7 shows the saturation device used. The saturation process involved placing the samples inside the device's chamber. Then, a vacuum pump was utilized to evacuate the air from the chamber. Following this, the water inlet valve was opened, allowing the chamber to fill with water. Subsequently, the water pressure inside the chamber was increased using a manual lever to ensure complete saturation of the samples. The samples were kept in the chamber for 24 hours to achieve full saturation.

Figure 5.7: Saturation apparatus.

8. AVS apparatus

After saturation, all 30 samples were weighed again, and their porosity and density were measured. Each sample was then placed in the AVS apparatus to measure V_s and V_p under varying lateral and axial pressures. Figure 5.8 shows this device.

Figure 5.8: AVS apparatus.

It is worth mentioning that two types of S-wave were propagated in the specimens: S1-wave, and S2-wave. When the rock specimen was isotropic, therefore the velocity of S1-wave and S2-wave were roughly equal. If those velocities were unequal, it showed that there is anisotropy in the specimen structure. Based on the conducted experiments, the values of S1-wave and S2-wave were always equal.

Lateral and axial pressures were applied in intervals of 3.5 MPa, up to a maximum of 42 MPa. Those experiments were executed under both drained and undrained circumstances. Finally, for different lateral and axial pressures, the poro-elastic parameters for each sample (and on average for Tumlin sandstone) were measured as follows [1]:

$$\nu = \frac{\frac{1}{2}-\left(V_s/V_p\right)^2}{1-\left(V_s/V_p\right)^2} \tag{5.9}$$

$$E = \rho\frac{V_p^2(1+\nu)(1-2\nu)}{(1-\nu)} \tag{5.10}$$

$$K = \rho({V_p}^2 - \frac{4}{3}{V_s}^2) \tag{5.11}$$

$$G = \rho V_s^2 \tag{5.12}$$

The above equations were used for calculation of those four poro-elastic parameters under both drained and undrained loading circumstances.

As mentioned earlier, by AVS laboratory tests, the dynamic poro-elastic properties of Tumlin sandstone were measured for different confining pressures. Incorporating the confining pressure effects on the rock strength characteristics provides more accurate results than elastic models and poro-elastic models in which the rock strength characteristics are presumed consistent and independent of confining pressure [20, 24]. Santarelli et al. stated that the rocks’ elastic moduli change with confining pressure [20]. It is an accepted general rule that the ultimate failure of rock directly depends on the effective confining stress. In better words, the plastic deformation of the rock is prevented due to the presence of hydrostatic compression.

5.2. Numerical part

The second part of the methodology involved performing numerical simulations to analyze the impact of the rock's dynamic poro-elastic properties on wellbore stability. The FLAC3D software was used to conduct the numerical simulations. The software was licensed for one year through the Itasca Educational Partnership (IEP) Research Program, provided by the manufacturing company, Itasca Consulting Group.

In this step, an appropriate geometric mesh was first constructed in FLAC3D. The mesh was cubic in shape, encompassing a wellbore with a radius of 0.1 m located precisely in the middle of the model. After constructing the preliminary mesh, the loading conditions applied during the laboratory tests were simulated through numerical models. For this purpose, various numerical models were created with loading boundary conditions corresponding to the hydrostatic stresses previously applied to the samples. Each of these loading conditions represented the placement of the rock at different depths. In each of these models, the mechanical, physical, and dynamic poro-elastic properties of the samples were input as functions of the applied lateral and axial pressures.

Finally, after drilling the wellbore in the models, the instability of the rock around the wellbore was examined. The impact of rock's dynamic poro-elastic properties on wellbore stability was considered in two scenarios: (1) at the precise moment of drilling initiation, when the rock around the wellbore is under undrained behavior, which can also represent a scenario where no fluid penetration into the rock occurs, and (2) during the transition from undrained to drained behavior, when fluid begins to penetrate the rock surrounding the wellbore.

Ultimately, the wellbore instability in both scenarios (1 and 2) was assessed using the safety factor mentioned in Eq. (3.1). Additionally, a parametric study was executed to assess and analyze the impact of each poro-elastic property on wellbore stability.

Chapter 6: Laboratory Research

6.1. Compression tests

When a poro-elastic object is suddenly subjected to an external stress, at $t = 0^+$ (instant of loading), the loading condition is undrained, and the behavior of the object is elastic. Similarly, at the start of drilling ($t = 0^+$), the rock has an elastic behavior [99]. After $t = 0^+$, the rock behavior transforms from elastic to poro-elastic state.

As mentioned in the previous chapter, 45 Tumlin sandstone specimens were prepared to conduct laboratory tests. The first group of samples consisted of 15 specimens which were utilized for measurement of rock’s mechanical characteristics. The mechanical characteristics of those specimens were measured by the triaxial compression testing machine. The machine was a product of MATEST, an Italian company situated in Arcore, Italy. This apparatus was equipped with the Servo-Plus Evolution load measuring system. The device was deployed to measure the rock's strength features, such as UCS, cohesion, as well as internal friction angle. Following this, the linear failure criterion for Tumlin sandstone was extracted. The measurements achieved by triaxial compression testing machine are elaborated below.

Of the 15 samples selected to measure the rock’s mechanical characteristics, 10 were used for measuring the rock’s UCS, and 5 were deployed to determine the rock’s cohesion along with internal friction angle. Figure 6.1 illustrates those samples. The diameter of all samples was 38 millimeters with the ratio of length to diameter equal to 2.

Figure 6.1: left) ten samples for measurement of rock’s UCS; right) five samples for measurement of cohesion an internal friction angel of rock.

After conducting uniaxial tests on the first 10 samples, the average UCS of the rock was found to be 42.3 MPa. Table 6.1 summarizes the relevant data from these tests.

Table 6.1. Data of UCS measurement tests.

Sample Code	Dry Mass (g)	Diameter (mm)	UCS (MPa)
R1	102.95	38	42.3
R2	101.25	38	43.3
R3	100.41	38	44.5
R4	100.65	38	43.1
R5	100.88	38	42.1
R6	94.56	38	40.1
R7	99.64	38	44.0
R8	104.22	38	42.5
R9	105.68	38	40.8
R10	93.48	38	40.2

Then, triaxial experiments were performed on the remaining 5 specimens. For this purpose, each sample was placed inside a loading cell, and both axial (σ_1) and lateral (σ_3) pressures were increased to a specified level. The lateral pressure was then held unchanged while the axial pressure was raised till the sandstone specimen was broken. Table 6.2 presents the characteristics of the corresponding samples along with the values of the lateral and axial stresses at the failure moment.

Table 6.2. Triaxial tests data.

Sample Code	Diameter (mm)	σ_3 (MPa)	σ_1 (MPa)
R11	38	1	46
R12	38	2	56
R13	38	3	65
R14	38	4	64
R15	38	5	78

The Mohr-Coulomb failure criterion relationship obtained for the rock samples is illustrated in Figure 6.2 and is expressed as follows:

$$\sigma_1 = 40.2 + 7.2\,\sigma_3 \tag{6.1}$$

The coefficient of determination of Eq. (6.1) is 0.92, indicating that the derived relationship has a high level of accuracy.

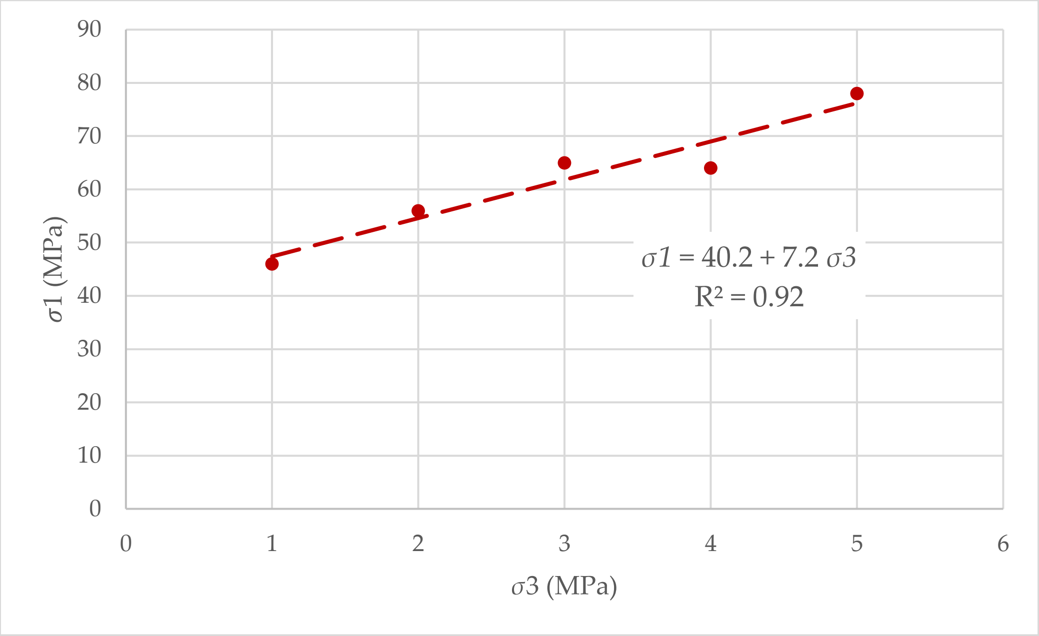

Figure 6.2: Mohr-Coulomb failure graph for sandstone samples.

By comparing Eq. (6.1) with Eq. (5.3), it can be deduced that $C_0 = 40.2$, and $q = 7.2$. It is noteworthy that the value of C_0 is close to the average UCS measured through uni-axial UCS tests.

Then, using Eq. (5.6) and Eq. (5.7), the values of ϕ and C are calculated as 49.11°, and 7.49 MPa, respectively.

Additionally, using Eq. (5.8), the rock's tensile strength is calculated as 5.59 MPa.

6.2. AVS tests

The second group, consisting of 30 samples, was used for measurement of poro-elastic parameters of Tumlin sandstone specimens. The corresponding samples are illustrated in Figure 6.3. Those samples, firstly, were fully saturated with water. Afterward, the physical characteristics of them were determined in the laboratory. Table 6.3 presents the summary of the measured physical properties. The average density and porosity of the specimens was determined as 2530 kg/m^3 and 15.70%, respectively.

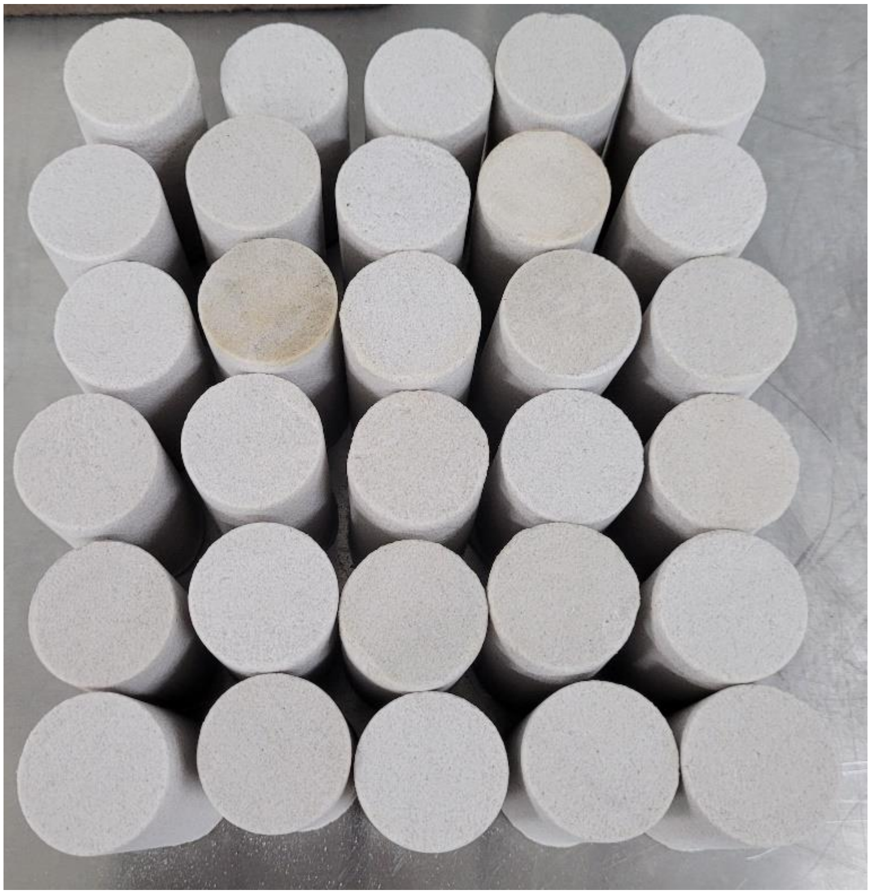

Figure 6.3: thirty samples utilized for measurement of poro-elastic parameters of rock.

Table 6.3. Physical properties of 30 sandstone samples used for AVS tests.

Sample Code	Dry Mass (g)	Diameter (mm)	Density (kg/m³)	Porosity (%)
S1	97.58	38	2.49	15.54
S2	99.94	38	2.48	16.50
S3	97.00	38	2.54	15.68
S4	99.24	38	2.53	16.71
S5	99.90	38	2.48	16.40
S6	100.38	38	2.59	15.51
S7	97.45	38	2.54	15.35
S8	98.20	38	2.47	15.52
S9	97.30	38	2.47	15.19
S10	99.05	38	2.52	15.38
S11	97.55	38	2.55	15.55
S12	101.00	38	2.56	15.06
S13	91.27	38	2.52	15.86
S14	99.12	38	2.54	15.05
S15	104.77	38	2.53	15.98
S16	104.84	38	2.53	15.00
S17	108.44	38	2.53	15.15
S18	112.14	38	2.54	15.21
S19	104.76	38	2.53	14.89
S20	100.21	38	2.57	16.98
S21	102.31	38	2.51	16.27
S22	101.98	38	2.48	14.57
S23	98.47	38	2.56	17.28
S24	100.37	38	2.56	15.62
S25	99.24	38	2.63	16.67
S26	104.94	38	2.54	15.12
S27	103.50	38	2.57	16.40
S28	103.18	38	2.58	16.01
S29	98.38	38	2.51	15.54
S30	99.97	38	2.47	15.02

Then, the conduction of AVS experiments started. The AVS tests were executed under two loading circumstances: undrained and drained. In other words, the poro-elastic properties of each saturated rock sample were measured under both conditions. The objective was to calculate poro-elastic parameters consisting of shear modulus, Poisson's ratio, bulk modulus, and Young's modulus under both conditions. Those parameters were necessary for determining other poro-elastic properties including Biot’s coefficient, Skempton’s coefficient, Biot modulus, as well as the unconstrained specific storage coefficient.

The procedure of conducting AVS tests under both undrained and drained loading conditions is explained below. The obtained results also are provided. It should be noted 1. Since the magnitudes of axial and radial pressures were equal, the term ‘hydrostatic stress’ is used hereafter. All experiments adhered to a hydrostatic stress level up to 42 MPa (the rock’s UCS value). Preserving the hydrostatic stress below the UCS value guaranteed that failure does not occur in the samples during the loading condition.

6.2.1. Undrained conditions

The primary principle for undrained loading condition is that the change in the pore fluid mass during the test must be zero. In other words, no fluid flows out or enters the sandstone specimen. In all tests, the pore fluid was water. The procedure of undrained tests for all samples was as follows:

1. Placing the rock sample into the coreholder while the valves controlling the water were fully closed for keeping undrained conditions.
2. Propagating acoustic waves through the rock sample.
3. Incrementally increasing the hydrostatic stress using a hand pump at consistent intervals nearly equal to 3.50 MPa. Twelve loading intervals were used for each sample. The applied loading hydrostatic stress in those intervals was 3.52, 6.99, 10.61, 13.84, 17.47, 20.82, 24.17, 27.70, 31.20, 34.67, 38.14, and 41.59 MPa.
4. Recording the flight time and velocity of the propagated acoustic waves in each loading interval. Furthermore, the corresponding hydrostatic stress and pore fluid pressure were measured.
5. Lastly, four undrained poro-elastic parameters including K_u, G_u, v_u, and E_u were calculated using Eqs. (5.9-5.12).

Appendix 1 summarizes the results of undrained tests for all 30 samples. Table 6.4 shows the average calculated results for those samples in different loading intervals.

Table 6.4. The average measured parameters for 30 samples in different hydrostatic stress levels (undrained condition).

Interval number	Hydrostatic stress (MPa)	Pore pressure (MPa)	Time of flight (μs)			Wave speed (m/s)			v_u	E_u (GPa)	K_u (GPa)	G_u (GPa)
			P-wave	S1-wave	S2 -Wave	P-wave	S1-wave	S2-wave				
1	3.5	3.4	32.4	66.1	66.1	3751	1438	1438	0.414	14.79	28.63	5.23
2	7.0	6.9	32.4	65.9	65.9	3820	1448	1447	0.416	15.02	29.86	5.30
3	10.5	10.3	32.4	65.7	65.7	3887	1457	1457	0.418	15.23	31.08	5.37
4	13.9	13.6	32.4	65.5	65.5	3961	1468	1468	0.420	15.48	32.44	5.45
5	17.5	17.0	32.4	65.4	65.4	4025	1475	1475	0.422	15.66	33.68	5.51
6	20.8	20.2	32.4	65.1	65.1	4112	1488	1488	0.424	15.96	35.37	5.60
7	24.2	23.4	32.4	65.1	65.1	4112	1488	1488	0.424	15.96	35.37	5.60
8	27.7	26.8	32.4	65.1	65.1	4112	1488	1488	0.424	15.96	35.37	5.60
9	31.2	30.1	32.4	65.1	65.1	4112	1488	1488	0.424	15.96	35.37	5.60
10	34.6	33.3	32.4	65.1	65.1	4112	1488	1488	0.424	15.96	35.37	5.60
11	38.1	36.5	32.4	65.1	65.1	4112	1488	1488	0.424	15.96	35.37	5.60
12	41.6	39.7	32.3	65.1	65.1	4112	1488	1488	0.424	15.96	35.37	5.60

Based on Table 6.4, it can be observed that as hydrostatic stress increases, the values of four measured undrained poro-elastic parameters change. Figure 6.4 illustrates the trend of changes in those parameters with hydrostatic stress for Tumlin sandstone. The following empirical correlations were extracted between those poro-elastic parameters and hydrostatic stress:

$$K_u = 3.1787\, ln(Pc) + 24.35 \tag{6.2}$$

$$E_u = 0.5484\, ln(Pc) + 14.06 \tag{6.3}$$

$$v_u = 0.0048\, ln(Pc) + 0.40 \tag{6.4}$$

$$G_u = 0.1749\, ln(Pc) + 4.99 \tag{6.5}$$

In all above equations, Pc (MPa) denotes the applied hydrostatic stress. Additionally, the correlation coefficient for all above equations is equal to or higher than 0.92, which demonstrates a strong fit between the undrained poro-elastic parameters and hydrostatic stress.

Figure 6.4 exhibits that among the poro-elastic parameters, Poisson's ratio (dashed line) exhibits the least variation with increasing hydrostatic stress. In contrast, the undrained bulk modulus shows the highest changes with increasing hydrostatic stress. Additionally, the figure indicates that for hydrostatic stresses below 21 MPa, the increase in undrained poro-elastic parameters is progressive. However, when the hydrostatic stress exceeds 21 MPa, those poro-elastic parameters do not change significantly. Therefore, when hydrostatic stress is below half of rock's UCS, the four undrained poro-elastic parameters have a direct relationship with hydrostatic stress. Conversely, if hydrostatic stress exceeds 21 MPa, a further increase in hydrostatic stress does not have a remarkable impact on those poro-elastic parameters. Hence, from this important point, it can be deduced that hydrostatic stress influences those four undrained poro-elastic properties only up to a certain threshold.

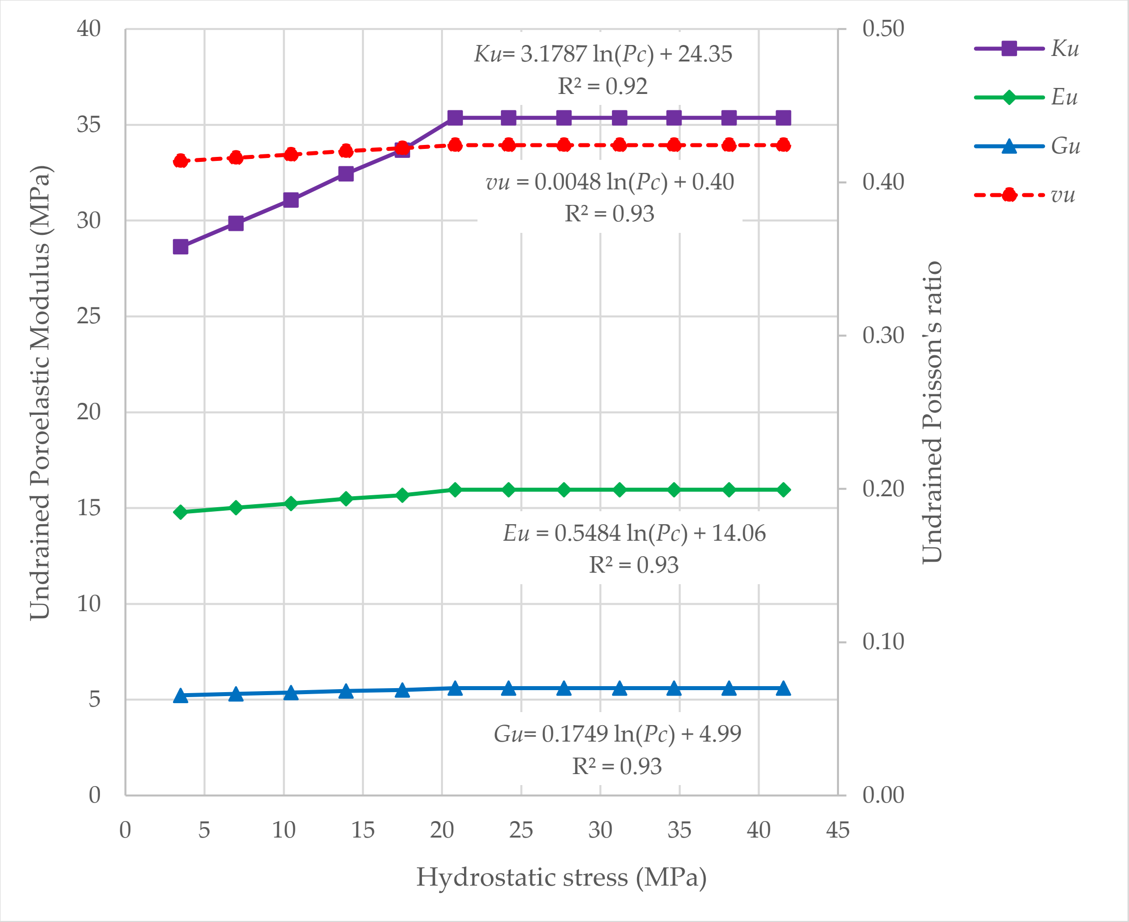

Figure 6.4: The empirical correlations formulating K_u, G_u, v_u, and E_u as a function of hydrostatic stress for Tumlin sandstone samples.

Another key point, that can be inferred from Table 6.4, is that as hydrostatic stress increases, the pore pressure also increases correspondingly. However, it can be observed that as hydrostatic stress continues to rise, the discrepancy between the magnitude of hydrostatic stress and pore pressure becomes larger. This phenomenon is illustrated through Figure 6.5; the bar chart demonstrates the discrepancy between the hydrostatic stress and pore fluid pressure, i.e. $P_C - p$, for different loading intervals. For Interval 12, the differential pressure nearly amounts to 2 MPa, meaning that the pore pressure bears a less percentage of the confining pressure.

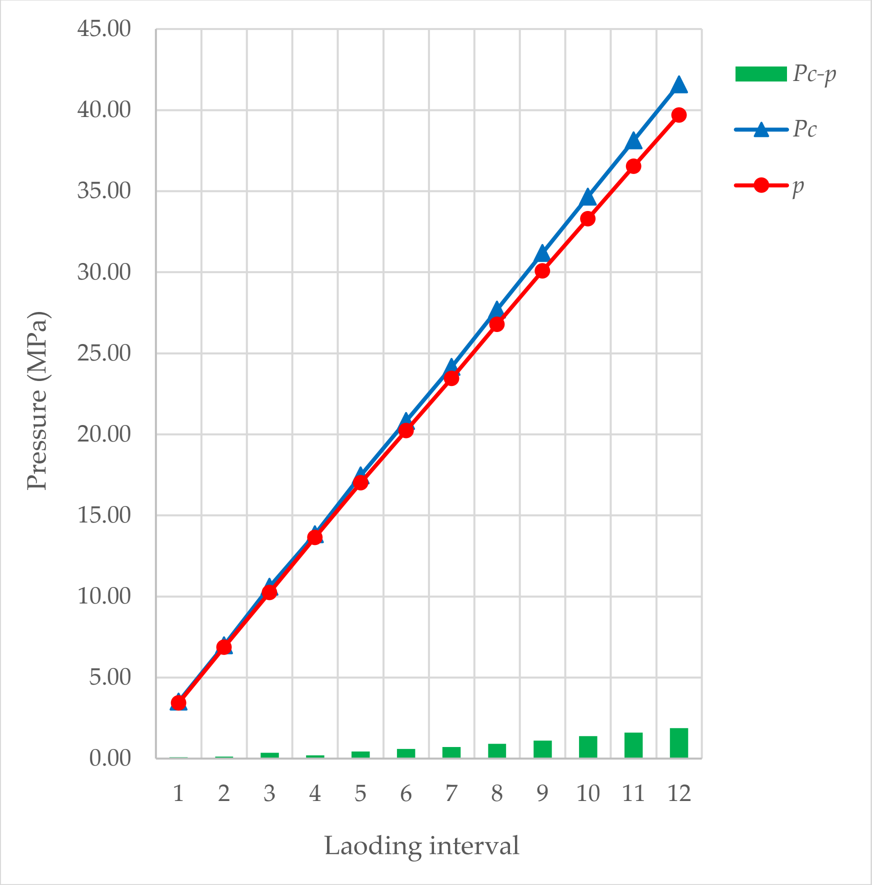

Figure 6.5: The discrepancy between the hydrostatic stress and the measured pore pressure under different loading intervals.

The above-mentioned discrepancy may be also illustrated using the parameter of Skempton's coefficient. Figure 6.6 illustrates the variation of Skempton's coefficient with hydrostatic stress. The underlying empirical correlation relates the Skempton's coefficient to hydrostatic stress as follows:

$$B = -0.0016\, ln(Pc) + 0.99 \tag{6.6}$$

The correlation coefficient for the above correlation is 0.98, demonstrating the close agreement between the variables. The Skempton's coefficient values shown in Figure 6.6 were used for numerical modeling, which will be explained in the next chapter.

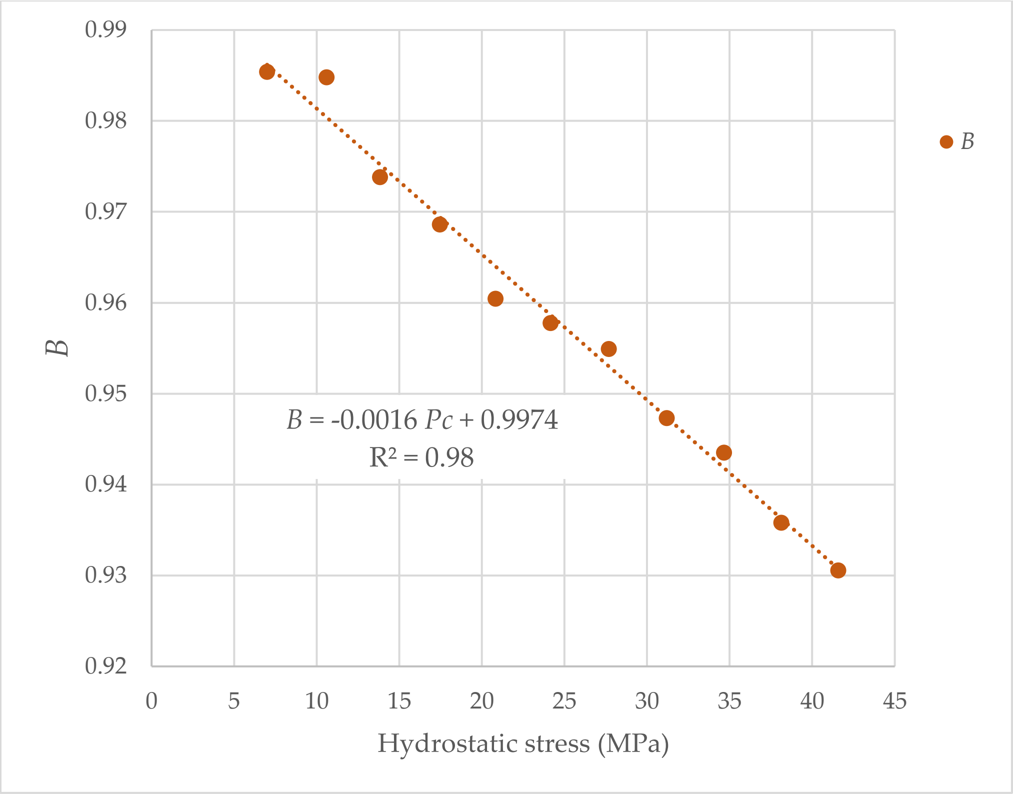

Figure 6.6: The variation of Skempton's coefficient with hydrostatic stress.

6.2.2. Drained Conditions

To satisfy drained loading conditions, it is only necessary to keep the inlet and outlet valves of the loading chamber open while applying hydrostatic stress, allowing the water within the rock sample to easily exit. Therefore, in the next phase, drained experiments were performed for all 30 previous sandstone specimens, and thus, those drained poro-elastic parameters were measured. The procedure for the drained tests was the same as for the undrained loading tests; however, the only difference was that the pore water was allowed to escape from the rock samples during applying the hydrostatic stress.

The drained tests were also performed in 12 loading intervals. Finally, four drained poro-elastic parameters were determined for each rock specimen using Eqs. (5.9-5.12).

Appendix 2 illustrates the entire drained measurements for all 30 samples. Table 6.5 also shows the average calculated results for those samples in different loading intervals.

Table 6.5. The average measured parameters for 30 samples in different hydrostatic stress levels (drained condition).

Interval number	Hydrostatic stress (MPa)	Pore pressure (MPa)	Time of flight (µs)			Wave speed (m/s)			*V*	*E* (GPa)	*K* (GPa)	*G* (GPa)
			P-wave	S1-wave	S2 -Wave	P-wave	S1-wave	S2-wave				
1	3.5	0.1	36.2	63.5	63.5	2793	1577	1577	0.266	15.93	11.35	6.29
2	7.0	0.1	35.7	63.3	63.3	2887	1591	1591	0.282	16.42	12.55	6.41
3	10.6	0.1	35.3	63.0	63.0	2979	1612	1612	0.293	17.01	13.69	6.58
4	13.8	0.1	35.0	62.8	62.8	3054	1625	1624	0.302	17.40	14.70	6.68
5	17.5	0.1	34.7	62.7	62.7	3121	1632	1631	0.312	17.67	15.68	6.74
6	20.8	0.1	34.4	62.5	62.5	3196	1641	1641	0.320	18.00	16.78	6.82
7	24.2	0.1	34.3	62.5	62.5	3210	1644	1644	0.321	18.08	16.97	6.84
8	27.7	0.1	34.2	62.4	62.4	3227	1647	1647	0.323	18.16	17.22	6.86
9	31.2	0.1	34.2	62.4	62.4	3242	1648	1648	0.325	18.22	17.44	6.88
10	34.7	0.1	34.1	62.3	62.3	3263	1652	1652	0.327	18.33	17.76	6.91
11	38.1	0.1	34.0	62.3	62.3	3279	1656	1656	0.328	18.43	17.99	6.94
12	41.6	0.1	34.0	62.3	62.3	3293	1658	1658	0.330	18.50	18.20	6.96

According to Table 6.5, it can be observed that during the drained loading tests, the pore pressure was kept constant (around ambient pressure). Furthermore, as hydrostatic stress increases, the drained poro-elastic parameters including K, G, v, and E change. Figure 6.7 depicts the trend of corresponding changes in drained poro-elastic parameters with hydrostatic stress for sandstone samples. The underlying empirical correlations were established between those drained poro-elastic parameters and hydrostatic stress:

$$K = 3.0126\, ln(Pc) + 7.08 \tag{6.7}$$

$$E = 1.1011\, ln(Pc) + 14.47 \tag{6.8}$$

$$v = 0.0274\, ln(Pc) + 0.23 \tag{6.9}$$

$$G = 0.2827\, ln(Pc) + 5.91 \tag{6.10}$$

where, Pc (MPa) represents the applied hydrostatic stress. In addition, the correlation coefficient for all above correlations is equal or larger than 0.98 which illustrates the close agreement between the drained poro-elastic parameters and hydrostatic stress.

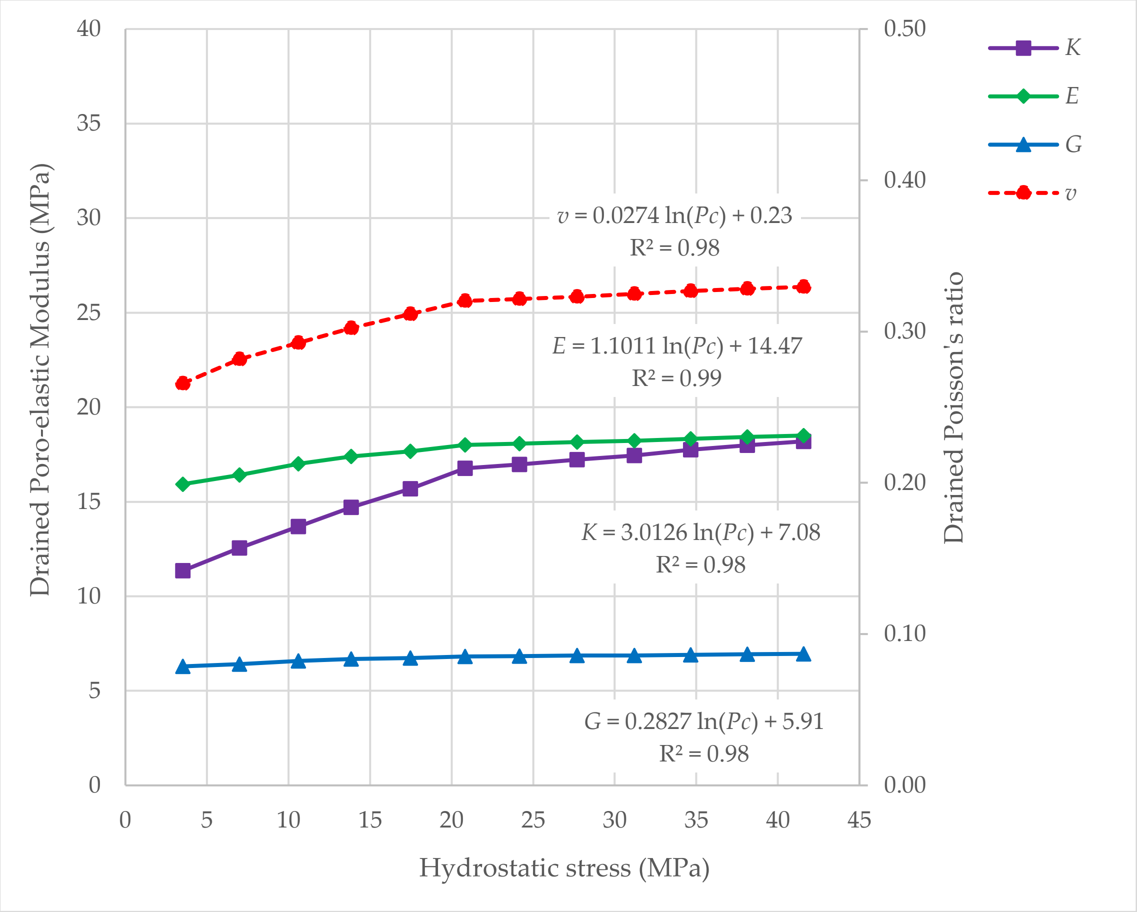

Figure 6.7: The empirical correlations formulating K, G, v, and E as a function of hydrostatic stress for Tumlin sandstone samples.

Among those four drained parameters, the drained shear modulus shows the least variation with hydrostatic stress, while the drained bulk modulus exhibits the most significant changes.

Figure 6.7 also shows that for hydrostatic stresses below 21 MPa, the increase in four drained poro-elastic parameters is progressive. However, when hydrostatic stress exceeds 21 MPa, the values of the poro-elastic parameters remain relatively consistent. Therefore, like undrained condition, when hydrostatic stress is below half of UCS, the four drained poro-elastic parameters have a direct relationship with hydrostatic stress. On the other hand, if hydrostatic stress surpasses 21 MPa, further increases in stress do not lead to a significant increase in those poro-elastic parameters. Thus, it can be inferred that, under drained conditions, the hydrostatic stress impacts on those four drained poro-elastic properties only up to a certain threshold.

So far, for both loading circumstances, the measurement procedure of four aforesaid poro-elastic parameters has been described. Additionally, Skempton's coefficient was correlated with hydrostatic stress.

Next, other poro-elastic parameters consisting of α, M, and S_σ can be calculated. To achieve this, those parameters were calculated for 12 intervals of hydrostatic stress using Eq. (2.18), Eq. (2.35), and Eq. (2.37) from Chapter 2. Table 6.6 presents the calculated values of those parameters.

Table 6.6. Calculated values for Biot's coefficient, Biot's modulus, and unconstrained specific storage coefficient for different hydrostatic stress levels.

Interval number	Hydrostatic stress (MPa)	α	M (GPa)	S_σ ((GPa)$^{-1}$)
1	3.5	0.61	46.44	0.0404
2	7.0	0.59	49.73	0.0366
3	10.6	0.57	53.51	0.0332
4	13.8	0.56	56.58	0.0310
5	17.5	0.56	57.41	0.0301
6	20.8	0.55	61.45	0.0280
7	24.2	0.54	63.07	0.0270
8	27.7	0.54	62.23	0.0271
9	31.2	0.54	61.46	0.0272
10	34.7	0.53	62.69	0.0264
11	38.1	0.53	61.86	0.0265
12	41.6	0.53	61.12	0.0266

Based on Table 6.6, the empirical correlation between each of poro-elastic parameters including α, M, and S_σ, and hydrostatic stress was determined.

Figure 6.8 illustrates the variation of Biot's coefficient with hydrostatic stress. It reveals that α declines logarithmically as hydrostatic stress increases. The mathematical form of this relationship is:

$$\alpha = -0.034\, ln(Pc) + 0.65 \tag{6.11}$$

Here, α represents the Biot's coefficient, while Pc (MPa) denotes the applied hydrostatic stress. Additionally, correlation coefficient for this relation is 0.98, which is an indicator of a strong fit between the variables. Furthermore, Biot's coefficient ranged between 0.53 and 0.61. Figure 6.8 also illustrates the reduction of α as the hydrostatic stress increases.

The values of α shown in Figure 6.8 were used for various hydrostatic stress levels in the numerical simulation presented in the next chapter.

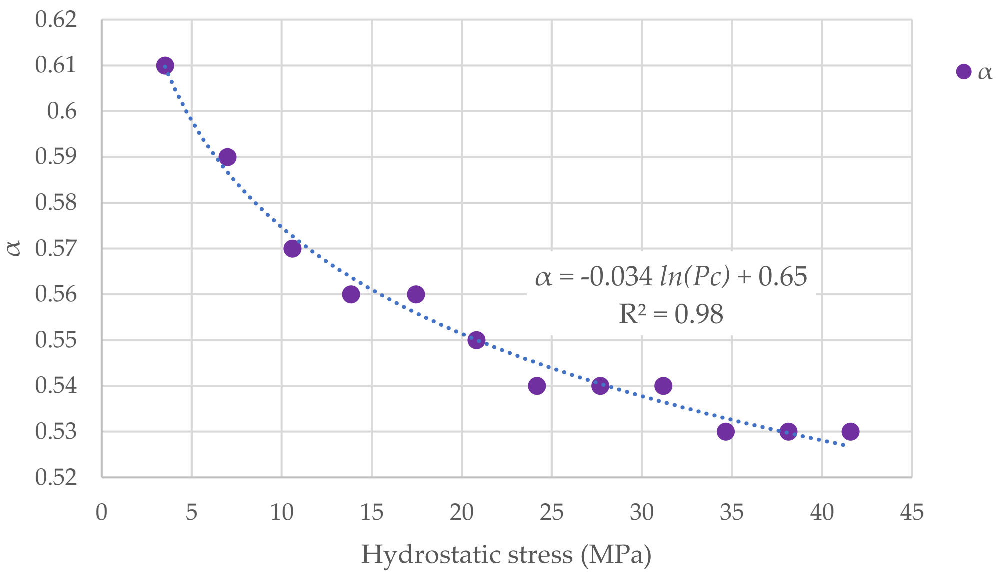

Figure 6.8: Empirical correlation between Biot's coefficient and hydrostatic stress.

The variation of Biot modulus with hydrostatic stress has been depicted in Figure 6.9. It demonstrates that Biot modulus increases logarithmically as hydrostatic stress rises. The corresponding empirical relationship is:

$$M = 7.061\, ln(Pc) + 37.56 \tag{6.12}$$

where M denotes the Biot modulus. The coefficient of determination for this relationship is 0.91 which exhibits a strong correlation between the variables. The values of Biot modulus presented in Figure 6.9 were applied to different hydrostatic stress levels in the numerical simulation discussed in the next chapter.

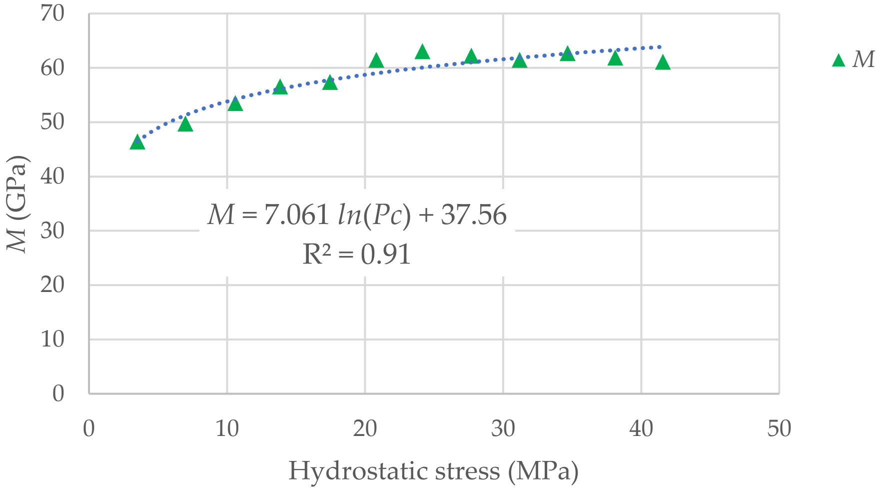

Figure 6.9: Empirical correlation between Biot modulus and hydrostatic stress.

Figure 6.10 depicts the relation between the unconstrained specific storage coefficient and hydrostatic stress. It shows a logarithmic decrease in the unconstrained specific storage coefficient as hydrostatic stress rises. The corresponding empirical correlation is:

$$S_\sigma = -0.011\, ln(Pc) + 0.06 \tag{6.13}$$

where S_σ represents the unconstrained specific storage coefficient. The coefficient of determination for this relationship is 0.97 which indicates a strong correlation between the unconstrained specific storage coefficient and hydrostatic stress.

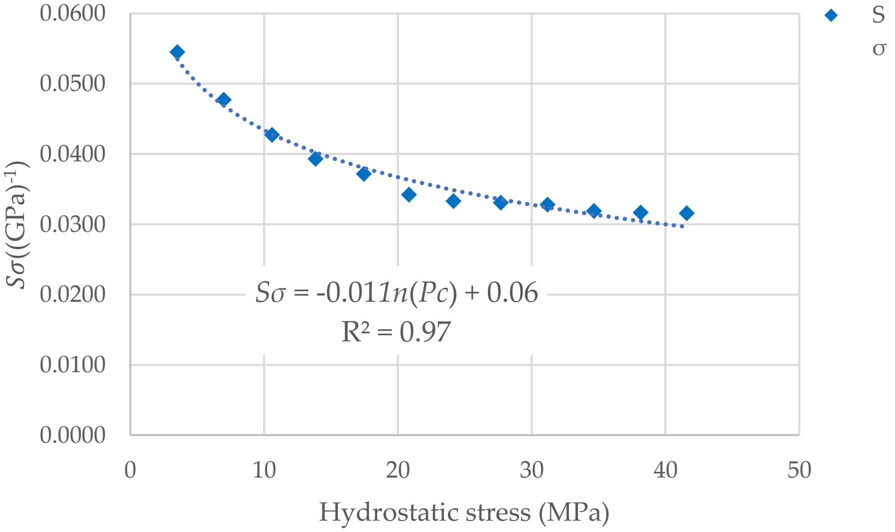

Figure 6.10: Empirical correlation between unconstrained specific storage coefficient and hydrostatic stress.

6.2.3 Discussion on the laboratory results

The AVS tests demonstrated that the values of four poro-elastic characteristics of Poisson’s ratio, Young’s modulus, bulk modulus, as well as shear modulus depend on the level of hydrostatic stress, the rock’s UCS, and the loading conditions (drained or undrained). Figure 6.11 shows this phenomenon.

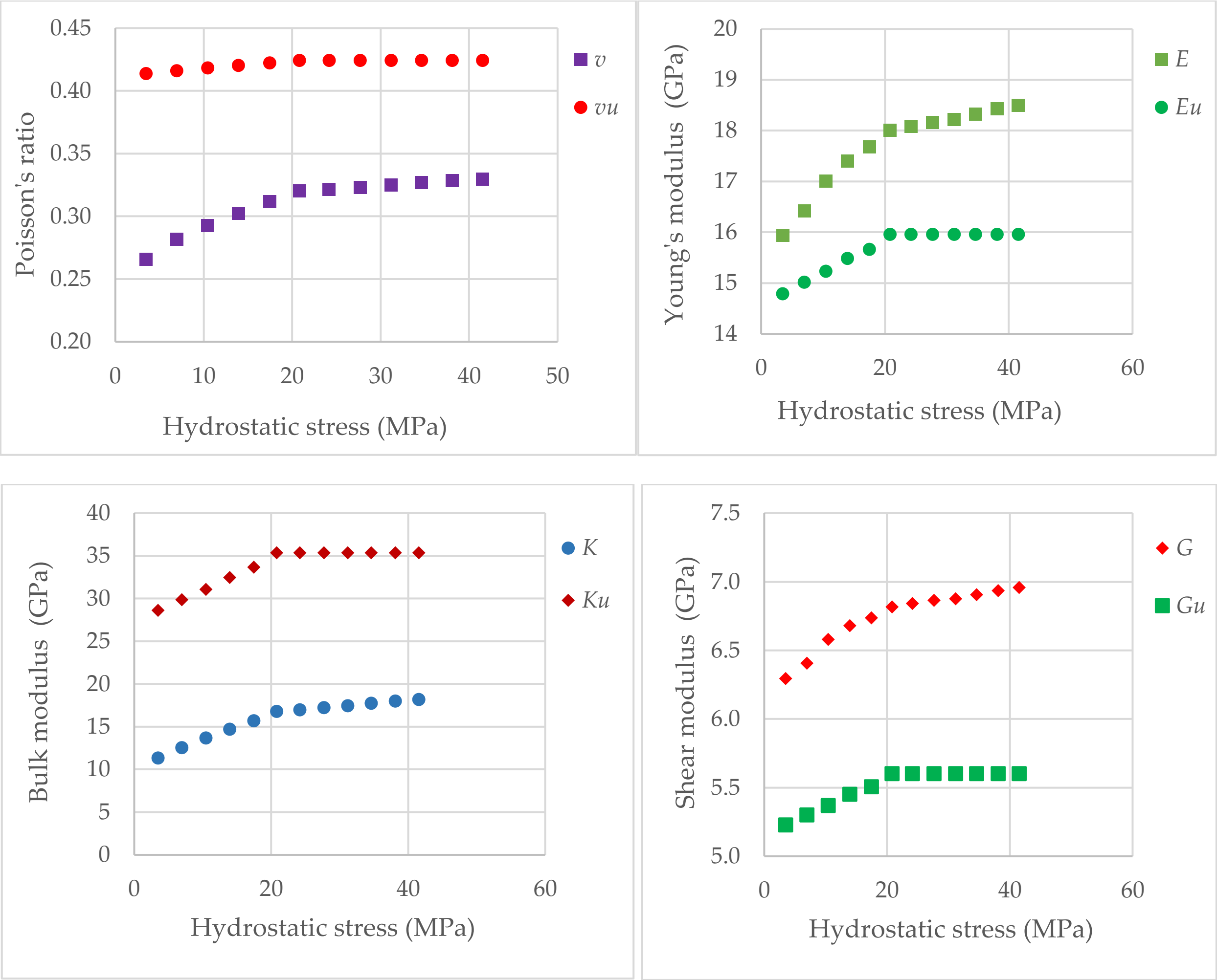

Figure 6.11. The variation of Young's modulus, Poisson's ratio, bulk modulus, and shear modulus with hydrostatic stress under drained to an undrained condition.

Regarding the hydrostatic stress, when it is below half of rock’s UCS, the poro-elastic parameters change linearly. However, when the hydrostatic stress exceeds this threshold, the poro-elastic parameters remain nearly constant. Therefore, the underlying conclusions are induced about the effects of hydrostatic stress and rock’s UCS on poro-elastic parameters:

1. For hydrostatic stresses less than half of rock’s UCS, the differences between the poro-elastic parameters in drained and undrained conditions tend to increase in a linear and progressive manner. This highlights that as hydrostatic stress increases up to this threshold, the rock's behavior changes more predictably, with steady variations in mechanical properties. This can be important for drilling operations, as it allows for better planning and anticipation of how the rock will behave under various stresses.
2. Furthermore, under lower hydrostatic stress, the rock exhibits more elastic behavior, which means that the poro-elastic parameters change more uniformly between drained and undrained states. The differences in these parameters are more significant, indicating that the transition to undrained conditions has a more substantial effect when the stress is relatively low.
3. When hydrostatic stress exceeds half of rock’s UCS, the differences between the poro-elastic parameters in drained and undrained conditions become less significant. This non-linear behavior indicates that the rock's response to stress is less sensitive to changes in hydrostatic pressure once it crosses the 21 MPa threshold.
4. In high-stress environments, the reduced differences in mechanical properties between drained and undrained conditions imply that the rock's behavior becomes more uniform. This could mean that in deeper drilling depths, the rock might be less prone to unexpected changes in deformation characteristics, which could be beneficial for maintaining wellbore stability.
5. The 21 MPa hydrostatic stress level acts as a critical threshold where the rock’s behavior changes from being more elastic and responsive to stress (below 21 MPa) to being more stable and less sensitive to further stress increases (above 21 MPa). This threshold likely corresponds to a transition in the rock's internal structure or pore pressure distribution, impacting how it handles additional stress.

Furthermore, comparison of poro-elastic coefficients in drained and undrained conditions can serve as a valuable benchmark for assessing the rock's response during the initiation of drilling operations, where the rock's behavior shifts from a drained state to an undrained state. Table 6.7 illustrates the differences in four poro-elastic parameters, including shear modulus, Young's modulus, Poisson's ratio, and bulk modulus, as the loading conditions shifts to undrained state. To provide a clearer understanding, this data is also presented as a box plot in Figure 6.12. The given box plot exhibits the distribution and variability of each poro-elastic parameter without the influence of hydrostatic stress.

Table 6.7. The difference in shear modulus, Young's modulus, Poisson's ratio, and bulk modulus, as the rock goes under undrained condition.

Interval number	Hydrostatic stress (MPa)	$v_u - v$	$E_u - E$ (GPa)	$K_u - K$ (GPa)	$G_u - G$ (GPa)
1	3.5	0.148	-1.145	17.280	-1.065
2	7.0	0.134	-1.406	17.310	-1.105
3	10.6	0.126	-1.775	17.385	-1.208
4	13.8	0.118	-1.913	17.744	-1.229
5	17.5	0.111	-2.010	18.003	-1.231
6	20.8	0.104	-2.042	18.589	-1.214
7	24.2	0.103	-2.121	18.392	-1.238
8	27.7	0.101	-2.205	18.146	-1.261
9	31.2	0.099	-2.261	17.921	-1.273
10	34.7	0.097	-2.370	17.610	-1.304
11	38.1	0.096	-2.467	17.378	-1.333
12	41.6	0.095	-2.542	17.170	-1.355

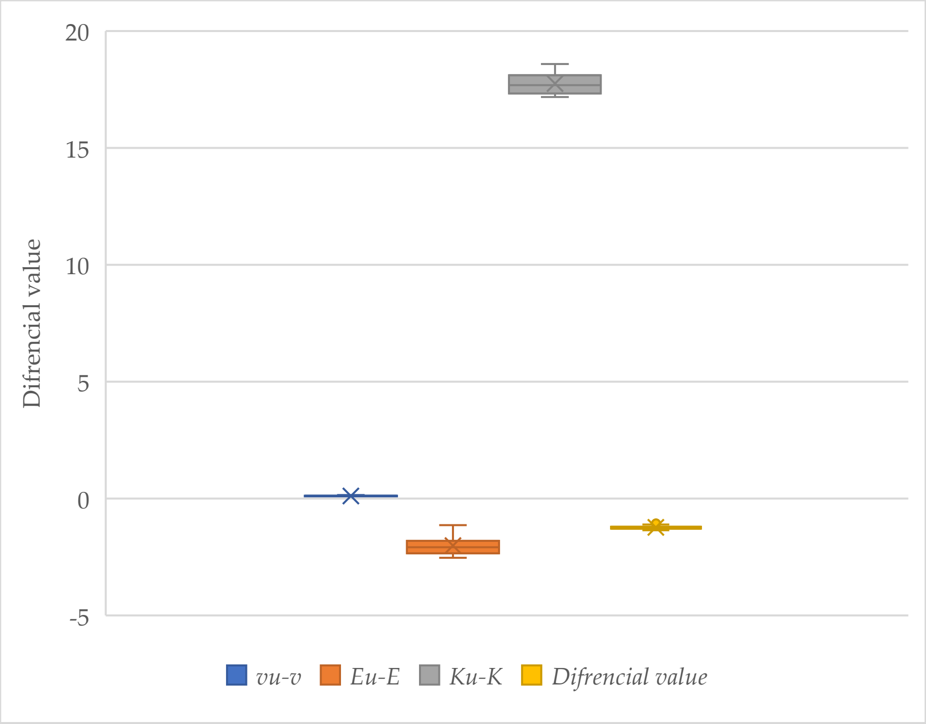

Figure 6.12. The distribution of the poro-elastic parameters differences in drained and undrained conditions.

According to the Table 6.7 and Figure 6.12, the following results can be deduced:

1) As the loading shifts to undrained conditions, Poisson's ratio increases. This suggests that the rock becomes more incompressible in the undrained state, leading to a higher lateral strain relative to axial strain. This behavior could indicate that the rock may exhibit more lateral expansion during drilling, potentially increasing the risk of borehole instability or wellbore enlargement.
2) The decrease in Young's modulus under undrained conditions means the rock becomes less stiff when it undergoes the undrained loading conditions. This reduction in stiffness implies that the rock will deform more under the same applied stress, which can lead to increased drilling-induced damage, such as fractures or wellbore collapse, especially if the rock is unable to support the loads imposed by the drilling equipment.
3) The differences in bulk modulus are much larger than those for other properties, with a median value around 17.5 GPa. The bulk modulus shows the greatest sensitivity and variability, indicating that it undergoes the most significant changes relative to other poro-elastic parameters when the loading conditions shifts to undrained conditions.
4) The shear modulus decreases under undrained conditions, indicating a reduction in the rock's resistance to shear deformation. This could mean that the rock is more prone to shear failure or deformation during drilling, leading to problems such as wellbore instability.

The experimental results also indicate significant variations in Biot's coefficient, Biot modulus, and unconstrained specific storage coefficient under different hydrostatic stress levels. As hydrostatic stress increases, Biot's coefficient decreases logarithmically, suggesting a reduced pore fluid pressure impact on the effective stress. Conversely, Biot modulus increases, implying that the rock becomes less compressible as stress levels rise. Additionally, the unconstrained specific storage coefficient decreases, indicating a lower capacity for fluid storage under higher stress.

On the other side, the experimental results highlight distinct behaviors in these three properties under hydrostatic stress levels below and above 21 MPa. Based on these results the following results can be stated:

1) When hydrostatic stress is less than 21 MPa, Biot's coefficient is relatively higher, ranging between 0.56 and 0.61, and decreases as stress increases. This trend indicates

that the sandstone formation is more responsive to pore pressure alterations, potentially leading to greater wellbore instability issues if not carefully managed. Additionally, the unconstrained specific storage coefficient is higher, suggesting a greater fluid storage capacity, which could contribute to pore pressure buildup and potential wellbore failure if drilling pressures are not adequately controlled.

2) At hydrostatic stress levels exceeding 21 MPa, the Biot's coefficient stabilizes around 0.53-0.54, and the Biot modulus increases significantly, indicating that the rock becomes stiffer and less susceptible to pore pressure fluctuations. The reduced unconstrained specific storage coefficient suggests lower fluid storage capacity, potentially reducing the risk of pore pressure-induced wellbore collapse. However, the increased stiffness could lead to a more brittle rock response, raising concerns about the risk of fracturing during drilling.

Overall, according to the observed trends of different poro-elastic parameters during the laboratory tests, it can be expressed that at the start of the drilling phase (transition to undrained conditions) the Tumlin sandstone rock will behave more plastically and exhibit less stiffness and greater deformation. This can complicate drilling operations by increasing the likelihood of wellbore instability, requiring careful management of drilling pressures and mud properties to prevent mechanical failures. The increase in Poisson's ratio, as well as the reduction in Young's and shear moduli, highlights the need for appropriate drilling strategies, such as controlled drilling rates and mud pressures, to mitigate the risks associated with undrained conditions.

Furthermore, wellbore stability in the Tumlin sandstone formation requires careful consideration of hydrostatic stress levels. Below 21 MPa, managing pore pressure is critical to prevent wellbore instability, while above 21 MPa, attention should be given to controlling drilling pressures to avoid fracturing in a stiffer, less responsive rock.

Chapter 7: Numerical simulation

7.1. Problem statement

In this research, the numerical simulations were performed via FLAC3D software, which is widely used in geomechanics, rock mechanics, and soil mechanics.

The software has the capability to simulate fluid-rock interaction problems. In fact, it simply entitles the users to perform a fully hydro-mechanical coupled analysis computing rock deformations and fluid flow in rocks. In FLAC3D, a fully hydro-mechanical coupling occurs in two ways: pore pressure change causes volumetric strains, and reversely, the resulting strains change the pore pressure.

In this research, a one-year license FLAC3D software was utilized. The software developer company, known as Itasca Consulting Group, provided this license under the Itasca Education Partnership (IEP) program.

In the relevant literature, previous investigations have shown that the rocks' strength properties depend on the confining pressure [20]. In the current research, the AVS tests conducted confirm those statements. In fact, the AVS tests exhibited that poro-elastic parameters of Tumlin sandstone specimens were directly dependent on the level of hydrostatic stress.

During the AVS tests, when the hydrostatic stress was below half of the UCS, the poro-elastic parameters of the rock increased remarkably. However, after proceeding the hydrostatic stress more than this threshold, the changes in poro-elastic parameters were noticeably reduced. The corresponding diagrams were illustrated in the previous chapter.

To create accurate numerical models the problem conditions must be simulated properly. Thus, it was attempted to create numerical models exactly compatible with the conducted AVS experiments. During the AVS tests, the loading conditions were changed by altering the hydrostatic stress which was subjected to the rock samples in both axial and radial directions. Hence, in this research, those loading conditions were simulated in numerical models.

In the laboratory setting, the AVS experiments were executed in both undrained and drained conditions. During those tests, the hydrostatic stress increased incrementally from 0 to 42 MPa. The increment was 3.5 MPa.

To numerically simulate the above-mentioned loading conditions, the following scheme was devised. Consider the Tumlin sandstone layer stretching from the surface down to the depth of 1700 meters (Figure 7.1). A vertical well is drilled from the top to the base of the layer.

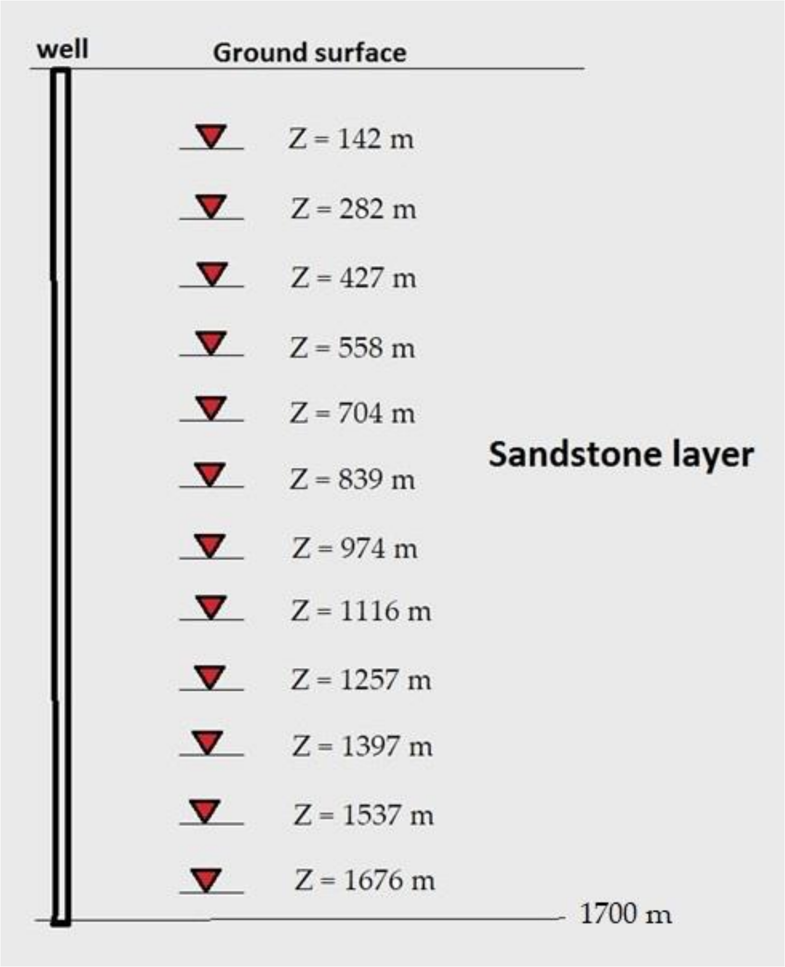

Figure 7.1. The Tumlin sandstone layer modeled in FLAC3D.

For any arbitrary rock element in the sandstone layer, the vertical stress is equivalent to the overburden weight which can be calculated using the underlying equation:

$$\sigma_z = \rho . g . z \tag{7.1}$$

where, σ_z represents the vertical stress (overburden weight), ρ represents the sandstone density, and g is gravitational acceleration. Furthermore, z stands for depth. For the sandstone layer, ρ was experimentally measured as 2530 kg/m^3. Moreover, g is assumed as 9.81 m/s^2. As the depth escalates, the vertical stress heightens too. The vertical stress acting on the sandstone layer can be considered as the axial pressure applied on the sandstone specimens during the AVS laboratory experiments. To find the depths equivalent to the applied axial pressures on the sandstone specimens, Eq. (7.1) was solved for z, as:

$$z = (\rho . g)/\sigma_z \tag{7.2}$$

The above equation was utilized to find the equivalent depths by specifying the laboratory axial pressure values to σ_z . Table 7.1 shows the corresponding equivalent depths.

Table 7.1: The depths equivalent to the applied axial pressures in laboratory.

Depth	Equivalent depth (m)	Laboratory axial Pressure (MPa)
Z1	142	3.5
Z2	282	7.0
Z3	427	10.6
Z4	558	13.8
Z5	704	17.5
Z6	839	20.8
Z7	974	24.2
Z8	1116	27.7
Z9	1257	31.2
Z10	1397	34.7
Z11	1537	38.1
Z12	1676	41.6

Since, during applying the hydrostatic stress, the axial pressure along with confining pressure were always identical, the horizontal stresses applied to the numerical models were specified as same as the vertical stresses.

The sketch of sandstone layer shown in Figure 7.1 entitles us to accurately simulate the laboratory loading conditions. Based on Table 7.1, 12 numerical models representing the sandstone rock in different depths, i.e. *Z1, Z2, Z3, …., Z12*, were generated. The in-situ stresses applying on each case were equal to the hydrostatic stress.

7.2. Model set up

Figure 7.2 illustrates the different stages performed in FLAC3D software for numerical simulation. The first step is to set up an appropriate model for the problem.

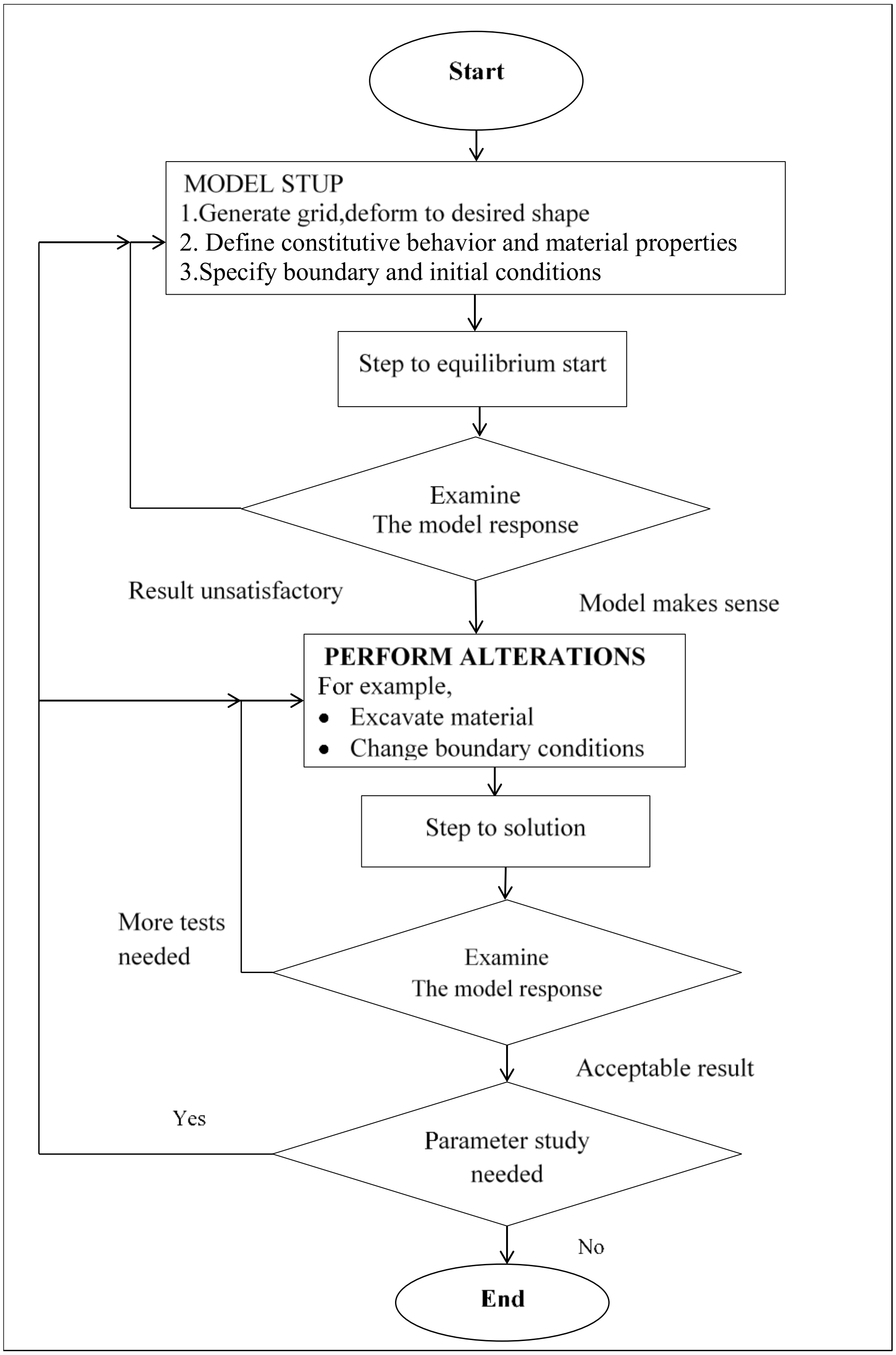

Figure 7.2. Different stages of numerical simulation in FLAC3D.

The model set up task was initiated by generating a cubic-shape mesh. Figure 7.3 demonstrates the corresponding mesh. The length, height, and width of the mesh were equal to 10 meters. Moreover, in the center of the mesh, a fine-mesh cylinder with radius of 10 cm was generated to represent the wellbore. The generated mesh was utilized for all twelve numerical models.

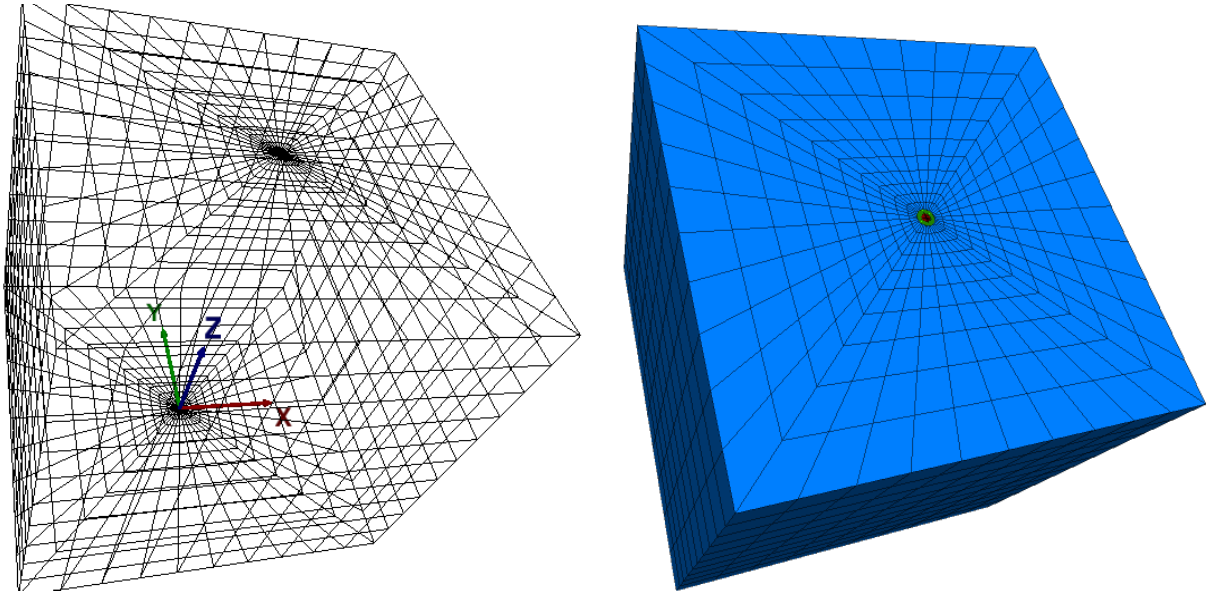

Figure 7.3. Mesh geometry for numerical modeling.

In FLAC3D software, the user can specify any name to a group of specific elements; hence, the central cylindrical mesh was named as "well" group. The "well" group was 10 cm in radius and 5 m in height. Figure 7.4 depicts the geometry of "well" group in the model.

Moreover, for precise prediction of displacements around the wellbore, the surrounding elements were defined with a small size. Those elements were specified to a distinct group named "wall". In fact, the "wall" group was an annuals space surrounding the "well" group. The thickness and length of the annual space was 10 cm and 5 cm, respectively. In Figure 7.4, the "wall" group can be seen. The "wall" group represents the rock elements directly around the wellbore. The well and wall groups were fine-mesh. Modelling the well and wall with fine elements increases the running time of the numerical simulation. Having said this, it contributes to calculate the deformations and stresses more precisely.

After performing the numerical simulations, the drilling-induced deformations and stresses in the “wall” elements were analyzed. Through this, the stability of the wellbore wall was assessed.

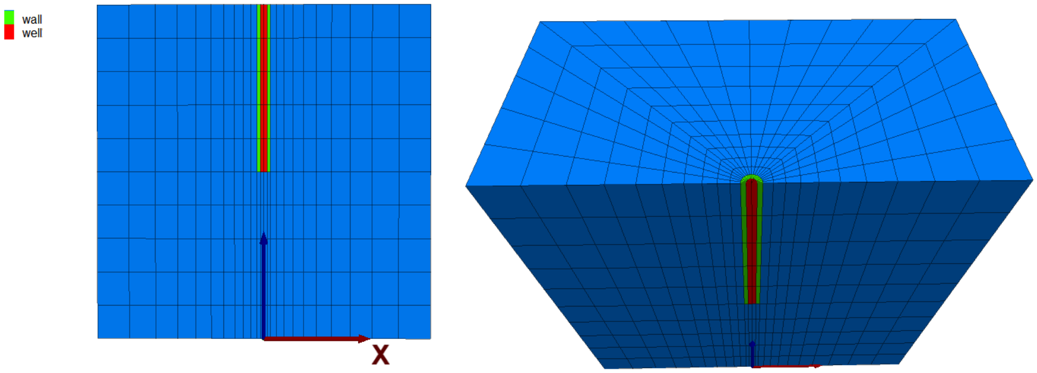

Figure 7.4. The geometry of “well” and “wall” groups in the initial generated model.

The second step of model set up was to define a constitutive behavior for the Tumlin sandstone rock. The constitutive behavior of sandstone was specified as the relation mentioned in Eq. 6.1.

After specifying the failure criterion, the different characteristics of Tumlin sandstone were assigned to the model. Since twelve models were created for different depths, and the rock characteristics were dependent to the drilling depth (hydrostatic stress), the applied rock properties will be presented in subsequent sections in where the numerical simulation of each model is elaborated.

After assigning the rock properties to each model, the boundary and initial constraints were defined. Thus, the model’s boundaries were fixed. The initial conditions including the nodes’ velocities and displacements were defined as zero, and the gravitational acceleration was assumed as 9.81 m/s^2.

7.3. Running the numerical models

Twelve numerical models representing different depths of Z1, Z2, Z3, …, and Z12 were created. The models' elements included the Tumlin sandstone rock and water (as pore fluid). In all models, the mesh geometry along with boundary conditions were identical. However, the rock characteristics were different based on the conducted laboratory tests.

As previously mentioned, when the drill bit starts to drill the rock, the loading state changes to undrained condition. Thus, in the real field, when drilling of the wellbore starts, the pore fluid prevents the mud from infiltrating into the surrounding formation. Such interaction between mud and pore fluid is highly complex which relies on a diverse range of parameters. As the mud continues to circulate in the wellbore, it gradually infiltrates into the formation. In other words, mud infiltration induces additional pressure in the adjacent formations. Hence, after mud infiltration into the formation, the loading conditions change from undrained to drained state. This issue affects the numerical results. Therefore, in the wellbore stability analysis, both undrained and drained loading conditions must be considered in numerical modeling.

In this study, the numerical models were conducted in two scenarios: rock-mud interaction under undrained condition (no mud infiltration to the formation), and rock-mud interaction under drained condition (mud infiltration to the formation). From the time perspective, the first case is equivalent to the drilling time at t = 0+, at which the rock is drilled while the pore pressure instantly heightens as a response to the drilling operation. As the drilling process proceeds, the second scenario occurs, and the mud infiltrates into the adjacent rocks. An identical procedure was already undertaken by some researchers to exclude the impact of mud interaction with native pore pressure in coupled poro-elastic wellbore stability analysis [56].

In the first scenario, the drilling process was simulated for twelve models without the infiltration of mud into the wellbore wall. In this case, the wellbore wall acted as an impermeable boundary. This assumption excludes the effect of mud infiltration during the undrained loading condition. The mud pressure was kept between the formation pore pressure and maximum fracture gradient calculated using the following equation:

$$FG_{max} = \frac{2v}{1-v}(\sigma_v - p) + p \tag{7.3}$$

where FG_{max} indicates the maximum fracture gradient. Equation (7.3) was used to compute the maximum fracture gradient [100,101]

In the second scenario, the drilling process was executed for those twelve models while the mud infiltration into the formation was permitted. In this case, the wellbore wall acted as a permeable boundary permitting the mud and pore fluid exchange. In what follows, those two scenarios together with the obtained results are described.

7.3.1. Undrained condition

- ***Model 1***

Model 1 represented sandstone rock at depth of 142 m. This model is equivalent to the AVS tests performed under the hydrostatic stress equal to 3.52 MPa. Table 7.2 summarizes the different characteristics specified to model 1. The main poro-elastic parameters whose impact on wellbore stability were assessed are highlighted in the table.

Table 7.2. Data used in numerical simulation of Model 1.

Object	Property	Unit	Value
Sandstone rock	Depth from the ground surface	m	142
	Dry density	kg/m^3	2530
	Cohesion	MPa	5.09
	Friction angle	degree	57.80
	Tensile strength	MPa	2.94
	Porosity	%	15.7
	Biot's coefficient	-	0.61
	Biot Modulus	GPa	46.44
	unconstrained specific storage coefficient	GPa^{-1}	0.04
	Skempton's coefficient	-	0.99
	Bulk modulus	GPa	11.4
	Shear modulus	GPa	6.29
	Poisson's ratio	-	0.27
Wellbore	radius	cm	10
In-situ stresses	σ_v	MPa	3.52
	σ_{Hmax}	MPa	3.52
	σ_{hmin}	MPa	3.52
Pore fluid	Pore pressure	MPa	3.44
	Pore fluid density	kg/m^3	1000
	Saturation degree	-	1

After specifying the corresponding characteristics to rock and pore fluid (water), the model was run. It successfully reached the static equilibrium state, thereby indicating that the rock characteristics along with the initial and boundary constrains were properly assigned.

After reaching the static equilibrium, the wellbore was drilled. To do this, the mesh elements of "well" group were removed. Then, the model was run to evaluate the drilling-derived deformations. After running the model, it reached the equilibrium state. No failure was observed at the wellbore wall. The highest radial displacement at wall was 2.59×10^{-5} m which was negligible. Figure 7.5 shows the calculated displacements around the wellbore. Moreover, Figure 7.6 shows that no plasticity state occurred around the wellbore.

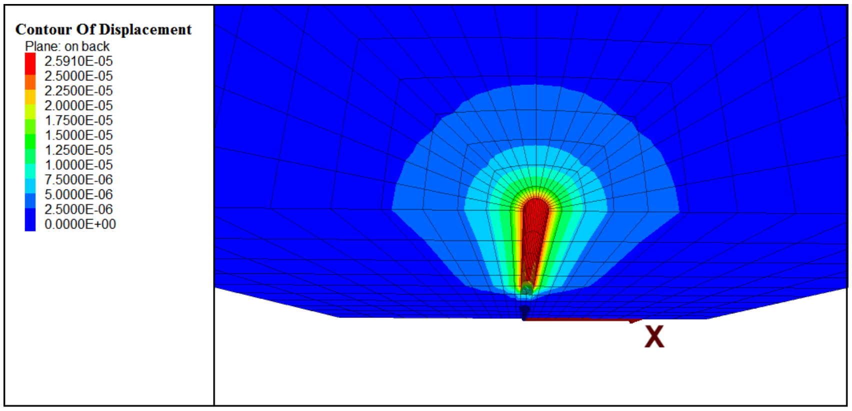

Figure 7.5: The contour of radial displacements around the wellbore for Model 1.

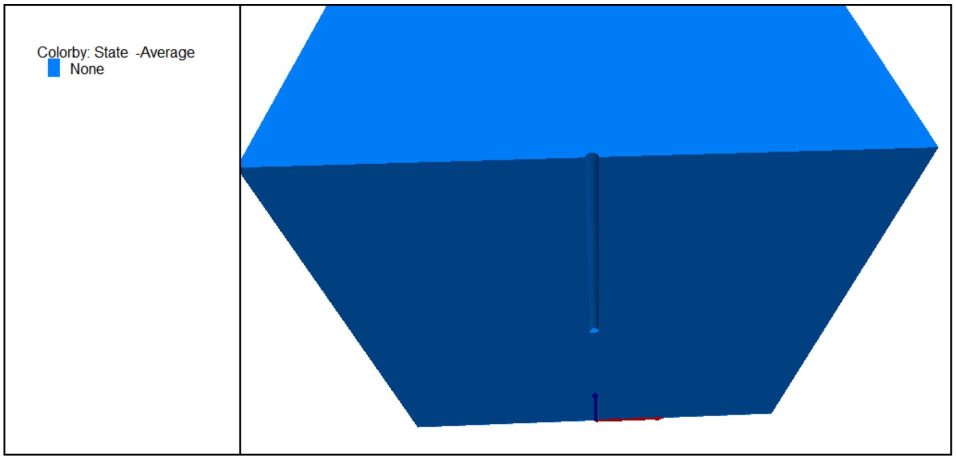

Figure 7.6: The non-presence of plasticity state of rock around wellbore for Model 1.

- ***Model 2***

Model 2 represented the sandstone rock at depth of 282 m. This model is equivalent to the AVS tests performed under the hydrostatic stress equal to 7 MPa. Table 7.3 summarizes the physical, mechanical, and poro-elastic properties specified to model 2. The main poro-elastic parameters whose impact on the wellbore stability was evaluated are highlighted in the table.

Table 7.3. Data used in numerical simulation of Model 2.

Object	Property	Unit	Value
Sandstone rock	Depth from the ground surface	m	282
	Dry density	kg/m^3	2530
	Cohesion	MPa	5.66
	Friction angle	degree	55.40
	Tensile strength	MPa	3.53
	Porosity	%	15.7
	Biot's coefficient	-	0.59
	Biot Modulus	GPa	49.73
	unconstrained specific storage coefficient	GPa^{-1}	0.036
	Skempton's coefficient	-	0.98
	Bulk modulus	GPa	12.6
	Shear modulus	GPa	6.41
	Poisson's ratio	-	0.28
Wellbore	radius	cm	10
In-situ stresses	σ_v	MPa	7.00
	σ_{Hmax}	MPa	7.00
	σ_{hmin}	MPa	7.00
Pore fluid	Pore pressure	MPa	6.87
	Pore fluid density	kg/m^3	1000
	Saturation degree	-	1

After defining the rock and pore fluid (water) characteristics, the numerical model was executed. The model successfully achieved a state of static equilibrium, confirming that the rock features, along with the initial and boundary constrains, were correctly applied. After reaching the static equilibrium state, the wellbore was drilled, and the model was run again. The model reached a static equilibrium, and no failure was observed at the wellbore wall. The highest radial displacement at wall was 1.68×10^{-4} m which is negligible.

Figure 7.7 illustrates the calculated displacements around the wellbore. Moreover, similar to model 1, no failure was observed around the wellbore.

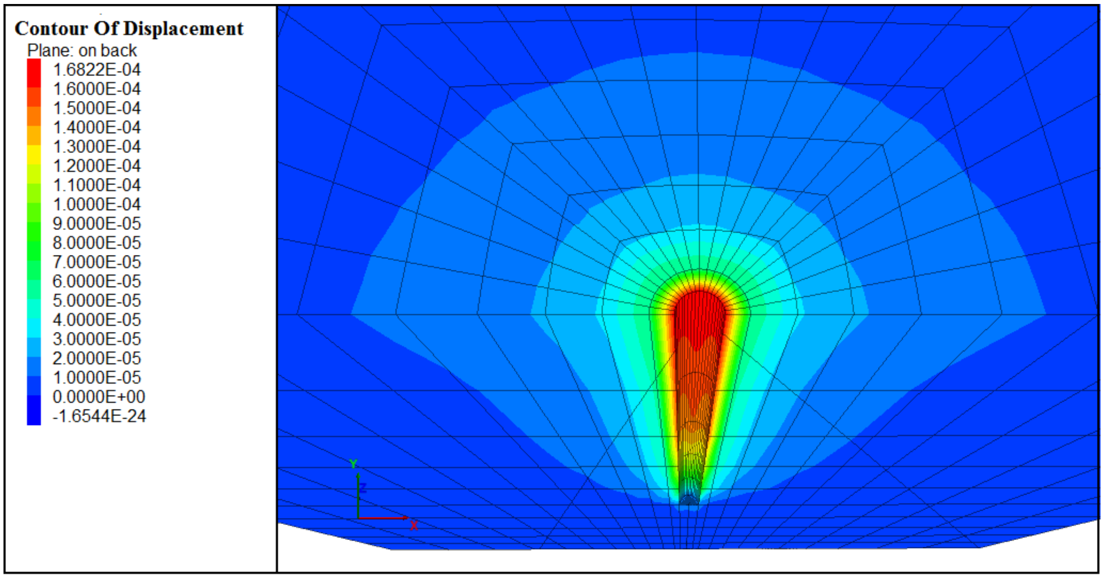

Figure 7.7: Contour of radial displacements around the wellbore for Model 2.

- ***Model 3***

Model 3 represented the sandstone rock at depth of 427 m. This model is equivalent to the AVS tests performed under the hydrostatic stress equal to 10.6 MPa. Table 7.4 summarizes the physical, mechanical, and poro-elastic properties specified to model 3.

Table 7.4. Data used in numerical simulation of Model 3.

Object	Property	Unit	Value
Sandstone rock	Depth from the ground surface	m	427
	Dry density	kg/m^3	2530
	Cohesion	MPa	6.15
	Friction angle	degree	53.80
	Tensile strength	MPa	4.02
	Porosity	%	15.7
	Biot's coefficient	-	0.57
	Biot Modulus	GPa	53.51
	unconstrained specific storage coefficient	GPa^{-1}	0.033
	Skempton's coefficient	-	0.97
	Bulk modulus	GPa	13.7
	Shear modulus	GPa	6.58
	Poisson's ratio	-	0.29
Wellbore	Radius	cm	10
In-situ stresses	σ_v	MPa	10.6
	σ_{Hmax}	MPa	10.6
	σ_{hmin}	MPa	10.6
Pore fluid	Pore pressure	MPa	10.26
	Pore fluid density	kg/m^3	1000
	Saturation degree	-	1

After setting the rock and pore fluid (water) characteristics, the numerical model was executed. The model reached static equilibrium, indicating that the rock properties together with the initial and boundary constrains were accurately assigned. After reaching the static equilibrium state, the wellbore was drilled, and the model was run. The model reached a static equilibrium, and no failure was observed at the wellbore wall. The highest radial displacement at wall was 5.22×10^{-4} m which is slightly more than Model 1 and Model 2. Figure 7.8 illustrates the calculated displacements around the wellbore. Moreover, like model 1 and Model 2, no remarkable rock failure was observed around the wellbore.

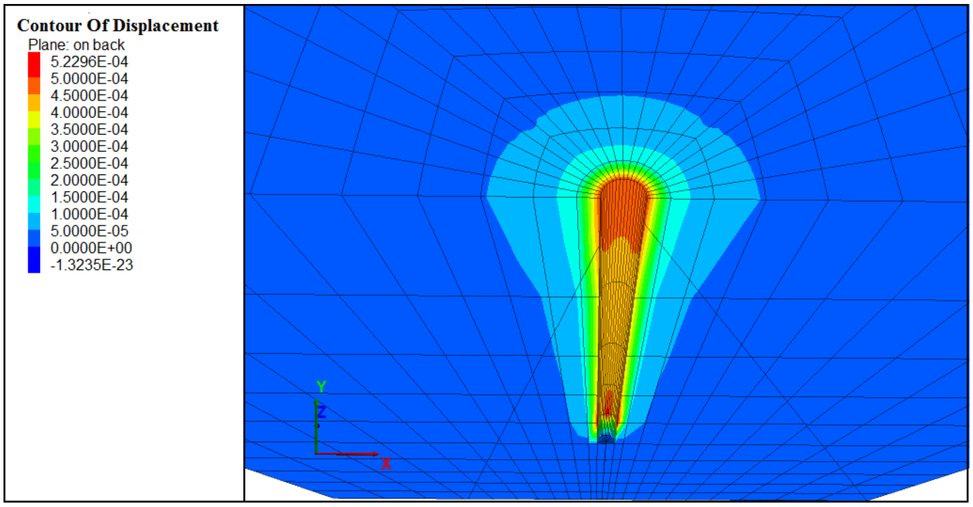

Figure 7.8: The contour of radial displacements around the wellbore for Model 3.

- ***Model 4***

Model 4 represented the sandstone rock at depth of 558 m. This model is equivalent to the AVS tests performed under the hydrostatic stress equal to 13.85 MPa. Table 7.5 summarizes the physical, mechanical, and poro-elastic properties specified to model 4.

Table 7.5. Data used in numerical simulation of Model 4.

Object	Property	Unit	Value
Sandstone rock	Depth from the ground surface	m	558
	Dry density	kg/m^3	2530
	Cohesion	MPa	6.63
	Friction angle	degree	52.20
	Tensile strength	MPa	4.54
	Porosity	%	15.7
	Biot's coefficient	-	0.56
	Biot Modulus	GPa	56.58
	unconstrained specific storage coefficient	GPa^{-1}	0.031
	Skempton's coefficient	-	0.97
	Bulk modulus	GPa	14.7
	Shear modulus	GPa	6.68
	Poisson's ratio	-	0.30
Wellbore	radius	cm	10
In-situ stresses	σ_v	MPa	13.85
	σ_{Hmax}	MPa	13.85
	σ_{hmin}	MPa	13.85
Pore fluid	Pore pressure	MPa	13.63
	Pore fluid density	kg/m^3	1000
	Saturation degree	-	1

After specifying the corresponding characteristics to the rock and pore fluid (water), the model was solved. It successfully reached the static equilibrium state, thereby indicating that the rock properties, and initial and boundary conditions were properly assigned to the model. Then, the wellbore was drilled, and the model was run again. The model achieved static equilibrium, with no signs of failure detected at the wellbore wall. The highest radial displacement at the wall was 8.97×10^{-4} m which is slightly more than the previous models. Figure 7.9 illustrates the calculated displacements around the wellbore. No remarkable failure was observed around the wellbore.

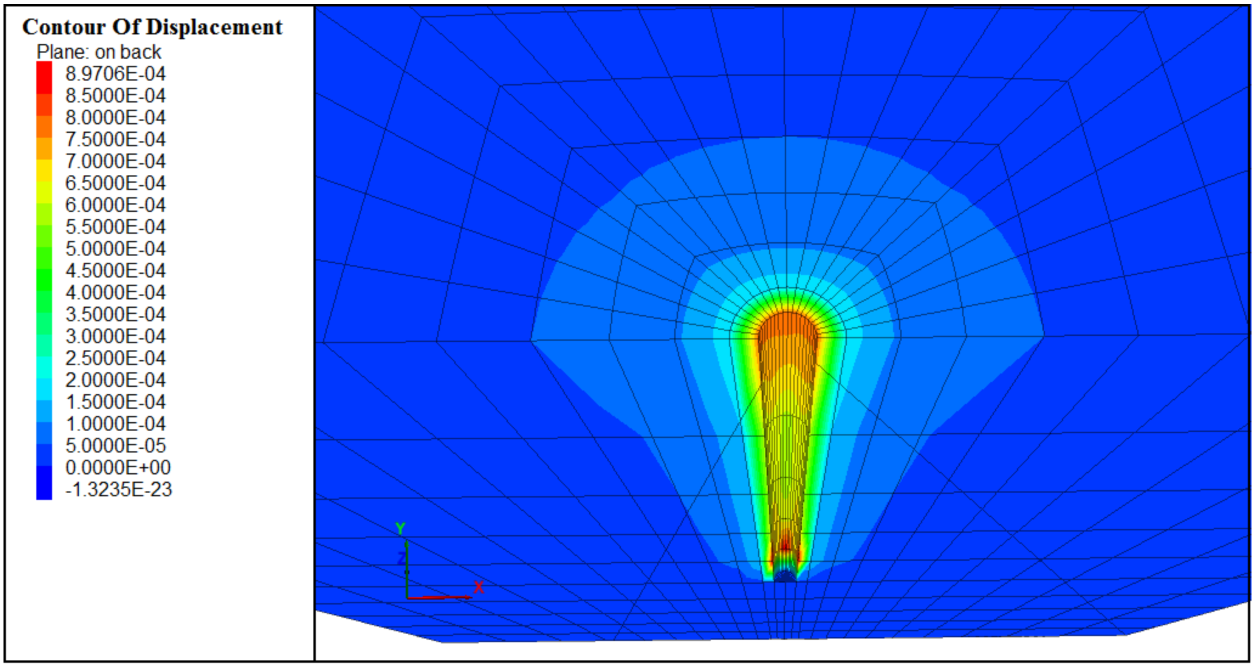

Figure 7.9: The contour of radial displacements around the wellbore for Model 4.

- ***Model 5***

Model 5 represented the sandstone rock at depth of 704 m. This model is equivalent to the AVS tests performed under the hydrostatic stress equal to 17.47 MPa. Table 7.6 summarizes the physical, mechanical, and poro-elastic properties specified to model 5.

Table 7.6. Data used in numerical simulation of Model 5.

Object	Property	Unit	Value
Sandstone rock	Depth from the ground surface	m	704
	Dry density	kg/m³	2530
	Cohesion	MPa	7.00
	Friction angle	degree	50.70
	Tensile strength	MPa	5.00
	Porosity	%	15.7
	Biot's coefficient	-	0.56
	Biot Modulus	GPa	57.41
	unconstrained specific storage coefficient	GPa^{-1}	0.03
	Skempton's coefficient	-	0.96
	Bulk modulus	GPa	15.7
	Shear modulus	GPa	6.74
	Poisson's ratio	-	0.31
Wellbore	radius	cm	10
In-situ stresses	σ_v	MPa	17.47
	σ_{Hmax}	MPa	17.47
	σ_{hmin}	MPa	17.47
Pore fluid	Pore pressure	MPa	17.03
	Pore fluid density	kg/m³	1000
	Saturation degree	-	1

After assigning the relevant characteristics to the rock and water, the numerical model was executed. The model successfully achieved a state of static equilibrium, confirming that the rock properties, along with the initial and boundary constraints, were correctly assigned. Afterwards, the wellbore was drilled, and the model was run again. The model reached a static equilibrium. The maximum displacement around the wellbore was 1.30 mm (Figure 7.10).

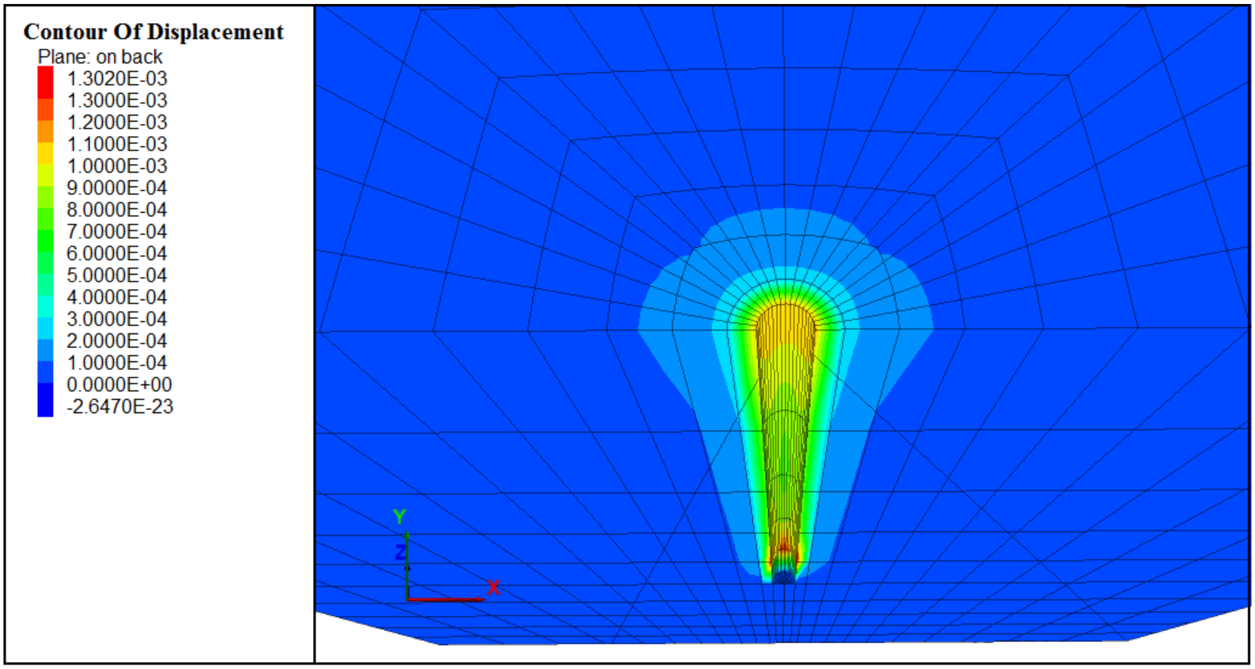

Figure 7.10: The contour of radial displacements around the wellbore for Model 5.

- ***Model 6***

Model 6 represented the sandstone rock at depth of 839 m. This model is equivalent to the AVS tests performed under the hydrostatic stress equal to 20.82 MPa. Table 7.7 summarizes the physical, mechanical, and poro-elastic properties specified to model 6.

Table 7.7. Data used in numerical simulation of Model 6.

Object	Property	Unit	Value
Sandstone rock	Depth from the ground surface	m	839
	Dry density	kg/m^3	2530
	Cohesion	MPa	7.49
	Friction angle	degree	49.11
	Tensile strength	MPa	5.59
	Porosity	%	15.7
	Biot’s coefficient	-	0.55
	Biot Modulus	GPa	61.45
	unconstrained specific storage coefficient	GPa^{-1}	0.028
	Skempton’s coefficient	-	0.96
	Bulk modulus	GPa	16.8
	Shear modulus	GPa	6.82
	Poisson’s ratio	-	0.32
Wellbore	radius	cm	10
In-situ stresses	σ_v	MPa	20.82
	σ_{Hmax}	MPa	20.82
	σ_{hmin}	MPa	20.82
Pore fluid	Pore pressure	MPa	20.23
	Pore fluid density	kg/m^3	1000
	Saturation degree	-	1

After assigning the rock characteristics to both the rock and water, the numerical model was executed. The model successfully reached static equilibrium, indicating that the rock features, along with the initial and boundary constraints, were correctly applied. The model achieved static equilibrium, with no failure detected at the wellbore wall. After reaching the static equilibrium state, the wellbore was drilled, and the model was run again. Like the previous models, the model reached a static equilibrium. Figure 7.11 illustrates the radial displacements in the model. The maximum radial displacement near the wellbore was 1.61 mm.

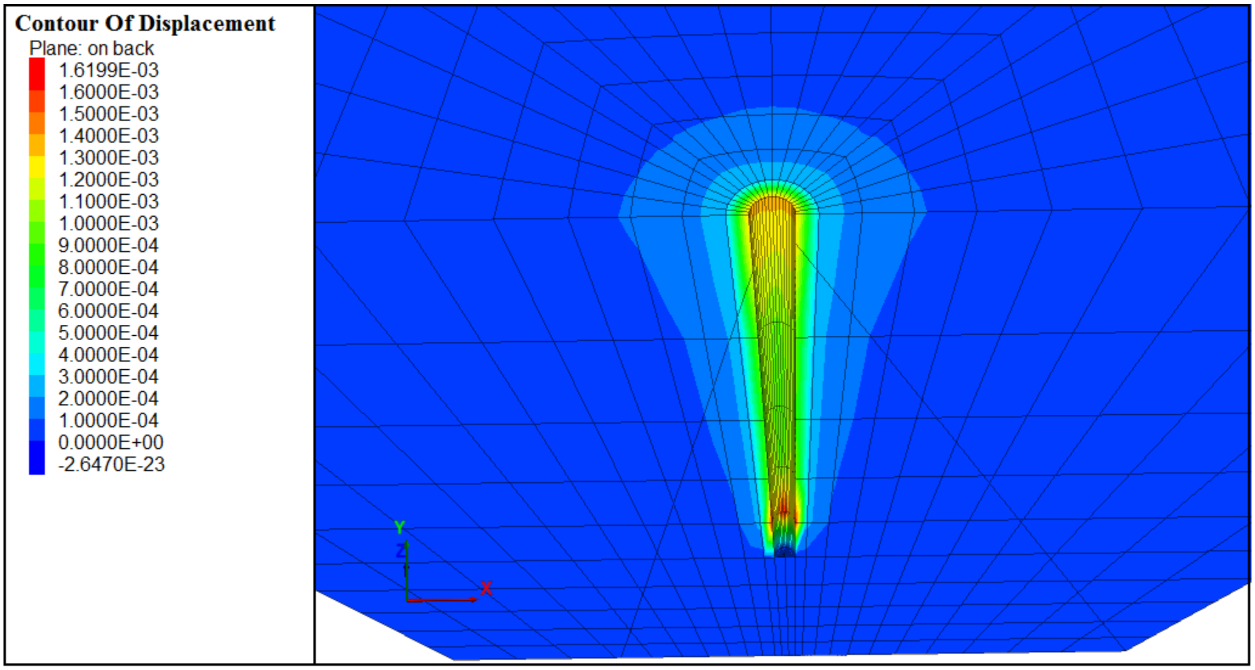

Figure 7.11: The contour of radial displacements around the wellbore for Model 6.

- ***Model 7***

The Model 7 represented the sandstone rock in depth of 974 m. This model is equivalent to the AVS tests performed under the hydrostatic stress equal to 24.17 MPa. Table 7.8 summarizes the physical, mechanical, and poro-elastic properties specified to model 7.

Table 7.8. Data used in numerical simulation of Model 7.

Object	Property	Unit	Value
Sandstone rock	Depth from the ground surface	m	974
	Dry density	kg/m^3	2530
	Cohesion	MPa	7.49
	Friction angle	degree	49.11
	Tensile strength	MPa	5.59
	Porosity	%	15.7
	Biot's coefficient	-	0.54
	Biot Modulus	GPa	63.07
	unconstrained specific storage coefficient	GPa^{-1}	0.027
	Skempton's coefficient	-	0.95
	Bulk modulus	GPa	17.0
	Shear modulus	GPa	6.84
	Poisson's ratio	-	0.32
Wellbore	radius	cm	10
In-situ stresses	σ_v	MPa	24.17
	σ_{Hmax}	MPa	24.17
	σ_{hmin}	MPa	24.17
Pore fluid	Pore pressure	MPa	23.45
	Pore fluid density	kg/m^3	1000
	Saturation degree	-	1

After assigning the relevant characteristics to the rock and water, the numerical model was executed. It successfully attained a state of static equilibrium, confirming that the rock properties together with the initial and boundary variables were correctly applied. After reaching the static equilibrium state, the wellbore was drilled, and the model was run again. Like the previous models, the model reached a static equilibrium. The maximum displacement around the wellbore was 2.18 mm (Figure 7.12).

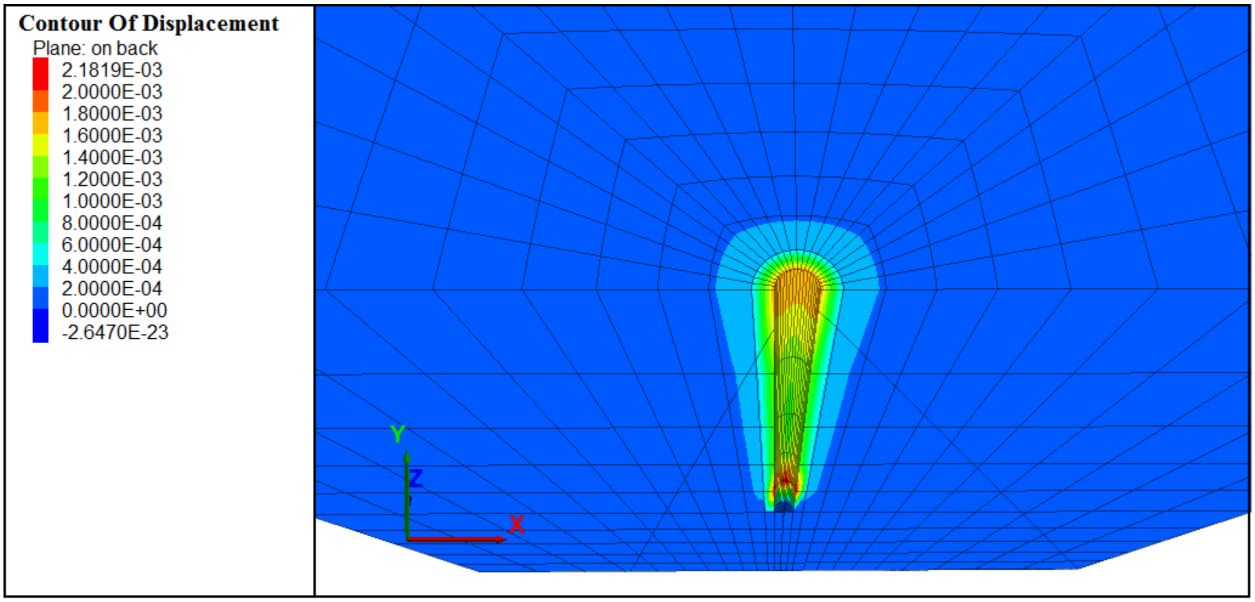

Figure 7.12: The contour of radial displacements around the wellbore for Model 7.

- ***Model 8***

Model 8 represented the sandstone rock in depth of 1116 m. This model is equivalent to the AVS tests performed under the hydrostatic stress equal to 27.70 MPa. Table 7.9 summarizes the physical, mechanical, and poro-elastic properties specified to model 8.

Table 7.9. Data used in numerical simulation of Model 8.

Object	Property	Unit	Value
	Depth from the ground surface	m	1116
	Dry density	kg/m^3	2530
	Cohesion	MPa	7.49
	Friction angle	degree	49.11
	Tensile strength	MPa	5.59
	Porosity	%	15.7
	Biot's coefficient	-	0.54
	Biot Modulus	GPa	62.23
	unconstrained specific storage coefficient	GPa^{-1}	0.027
	Skempton's coefficient	-	0.95
	Bulk modulus	GPa	17.2
	Shear modulus	GPa	6.86
	Poisson's ratio	-	0.32
Wellbore	radius	cm	10
In-situ stresses	σ_v	MPa	27.70
	σ_{Hmax}	MPa	27.70
	σ_{hmin}	MPa	27.70
Pore fluid	Pore pressure	MPa	26.78
	Pore fluid density	kg/m^3	1000
	Saturation degree	-	1

After assigning the relevant characteristics to the rock and water, the numerical model was executed. It successfully reached the static equilibrium, confirming that the rock properties, along with other variables were correctly specified to the model. Afterwards, the wellbore was drilled, and the model was run again. Like the previous models, the model reached a static equilibrium. The maximum displacement around the wellbore was 2.87 mm (Figure 7.13).

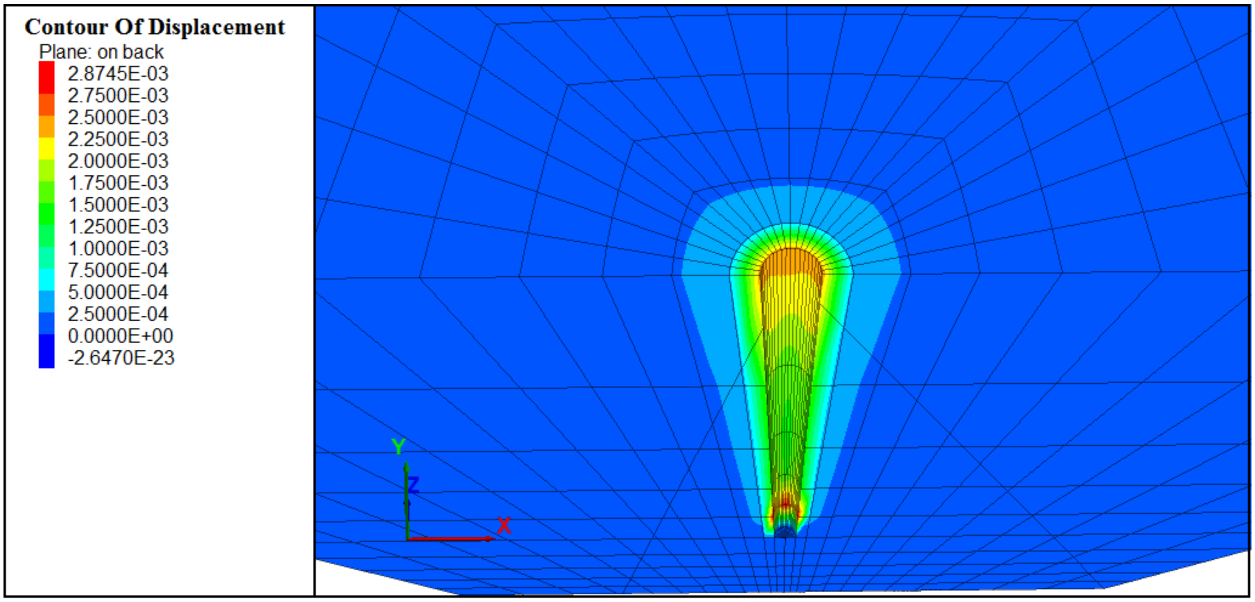

Figure 7.13: The contour of radial displacements around the wellbore for Model 8.

- ***Model 9***

Model 9 represented the sandstone rock in depth of 1257 m. This model is equivalent to the AVS tests performed under the hydrostatic stress equal to 31.20 MPa. Table 7.10 summarizes the physical, mechanical, and poro-elastic properties specified to model 9.

Table 7.10. Data used in numerical simulation of Model 9.

Object	Property	Unit	Value
Sandstone rock	Depth from the ground surface	m	1257
	Dry density	kg/m^3	2530
	Cohesion	MPa	7.49
	Friction angle	degree	49.11
	Tensile strength	MPa	5.59
	Porosity	%	15.7
	Biot's coefficient	-	0.54
	Biot Modulus	GPa	61.46
	unconstrained specific storage coefficient	Pa^{-1}	0.027
	Skempton's coefficient	-	0.94
	Bulk modulus	GPa	17.4
	Shear modulus	GPa	6.88
	Poisson's ratio	-	0.32
Wellbore	radius	cm	10
In-situ stresses	σ_v	MPa	31.20
	σ_{Hmax}	MPa	31.20
	σ_{hmin}	MPa	31.20
Pore fluid	Pore pressure	MPa	30.80
	Pore fluid density	kg/m^3	1000
	Saturation degree	-	1

After setting the appropriate characteristics for the rock and water, the numerical model was run. It successfully achieved static equilibrium, demonstrating that the rock characteristics, along with the initial and boundary constraints, were accurately assigned. After reaching the static equilibrium state, the wellbore was drilled, and the model was run again. Like the previous models, the model reached a static equilibrium. The maximum displacement around the wellbore was 3.85 mm (Figure 7.14).

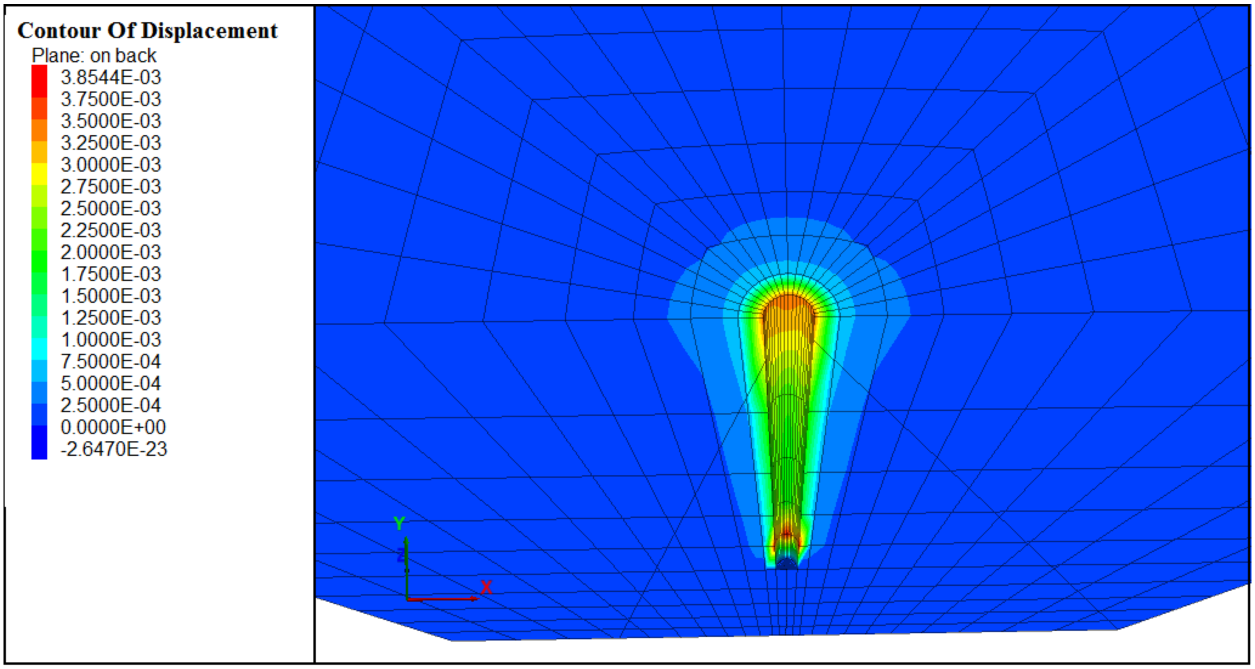

Figure 7.14: The contour of radial displacements around the wellbore for Model 9.

- ***Model 10***

Model 10 represented the sandstone rock in depth of 1397 m. This model is equivalent to the AVS tests performed under the hydrostatic stress equal to 34.67 MPa. Table 7.11 summarizes the physical, mechanical, and poro-elastic properties specified to model 10.

Table 7.11. Data used in numerical simulation of Model 10.

Object	Property	Unit	Value
Sandstone rock	Depth from the ground surface	m	1397
	Dry density	kg/m^3	2530
	Cohesion	MPa	7.49
	Friction angle	degree	49.11
	Tensile strength	MPa	5.59
	Porosity	%	15.7
	Biot's coefficient	-	0.53
	Biot Modulus	GPa	62.69
	unconstrained specific storage coefficient	GPa^{-1}	0.026
	Skempton's coefficient	-	0.94
	Bulk modulus	GPa	17.8
	Shear modulus	GPa	6.91
	Poisson's ratio	-	0.33
Wellbore	radius	cm	10
In-situ stresses	σ_v	MPa	34.67
	σ_{Hmax}	MPa	34.67
	σ_{hmin}	MPa	34.67
Pore fluid	Pore pressure	MPa	33.29
	Pore fluid density	kg/m^3	1000
	Saturation degree	-	1

After importing the rock and water characteristics, the numerical model was executed. It achieved static equilibrium, which indicated that the rock features, along with the initial and boundary limits, were correctly configured. After reaching the static equilibrium state, the wellbore was drilled, and the model was run again. The model reached a static equilibrium; however, a remarkable closure (reduction in wellbore diameter) was observed. Figure 7.15 illustrates the displacements around the wellbore. The highest radial displacement at the wall was 4.64 mm. Moreover, Figure 7.16 shows that significant shear and tension plasticity states have been initiated around the wellbore.

Model 10 is a critical state in stability of the drilled wellbore. In better words, it implies that after depth of 1397 m, the potential of wellbore failure increases markedly. The diagonal wellbore closure was 9.28 mm. Hence, it can be expressed that the wellbore radius declines from 10 cm to nearly 9 cm.

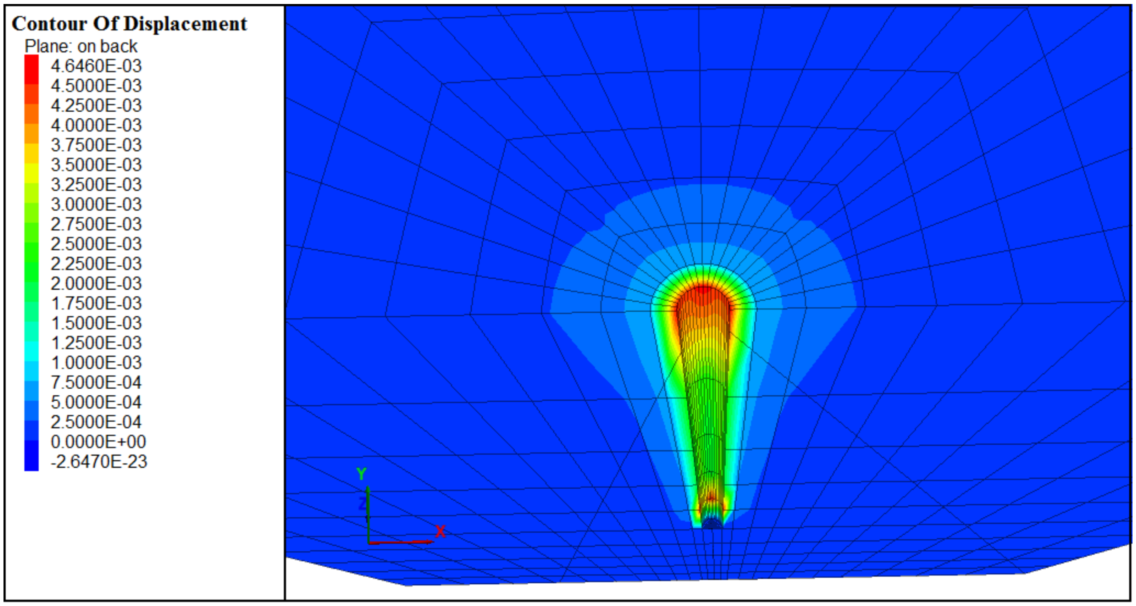

Figure 7.15: The contour of radial displacements around the wellbore for Model 10.

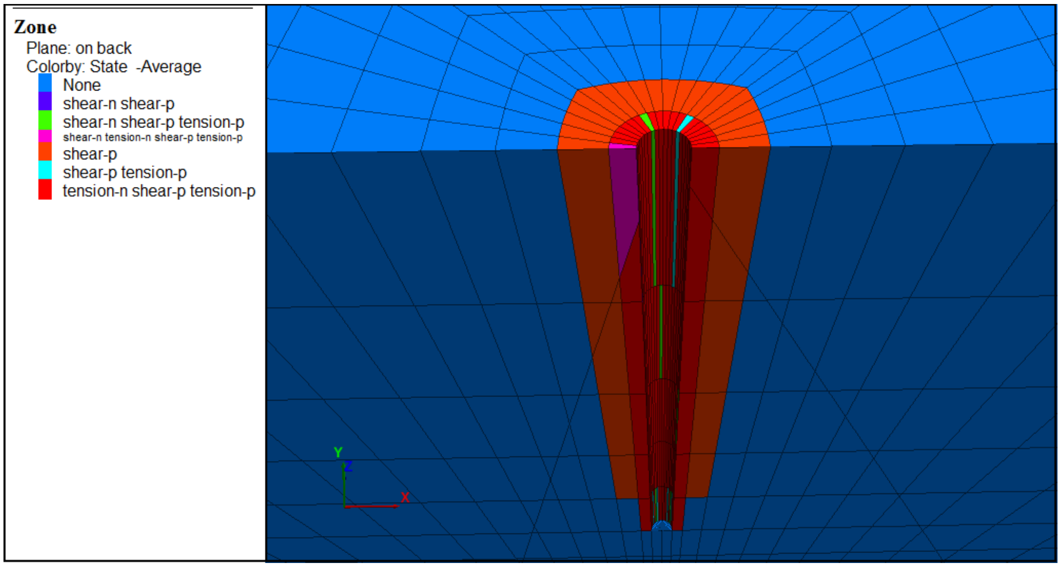

Figure 7.16: The plasticity states of rock zones around wellbore for Model 10.

- ***Model 11***

Model 11 represented the sandstone rock in depth of 1537 m. This model is equivalent to the AVS tests performed under the hydrostatic stress equal to 38.14 MPa. Table 7.12 summarizes the physical, mechanical, and poro-elastic properties specified to model 11.

Table 7.12. Data used in numerical simulation of Model 11.

Object	Property	Unit	Value
Sandstone rock	Depth from the ground surface	m	1537
	Dry density	kg/m^3	2530
	Cohesion	MPa	7.49
	Friction angle	degree	49.11
	Tensile strength	MPa	5.59
	Porosity	%	15.7
	Biot's coefficient	-	0.53
	Biot Modulus	GPa	61.86
	unconstrained specific storage coefficient	GPa^{-1}	0.026
	Skempton's coefficient	-	0.93
	Bulk modulus	GPa	18.0
	Shear modulus	GPa	6.94
	Poisson's ratio	-	0.33
Wellbore	radius	cm	10
In-situ stresses	σ_v	MPa	38.15
	σ_{Hmax}	MPa	38.15
	σ_{hmin}	MPa	38.15
Pore fluid	Pore pressure	MPa	36.54
	Pore fluid density	kg/m^3	1000
	Saturation degree	-	1

After reaching the static equilibrium state, the wellbore was drilled, and the model was run again. Like the previous models, the model reached a static equilibrium. However, the maximum radial displacement around the wellbore was 8.12 mm (Figure 7.17). Hence, compared to Model 10, the displacements at the wellbore wall were approximately two times more. Thus, the wellbore radios declined from 10 cm to approximately 8.4 cm.

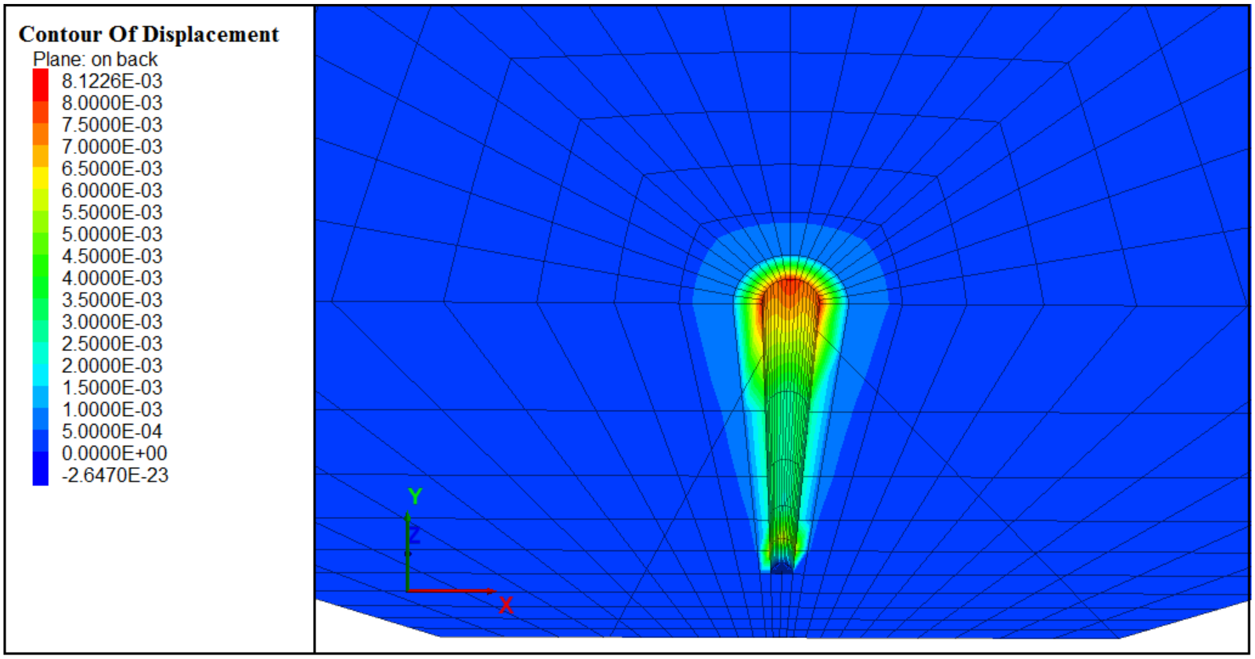

Figure 7.17: The contour of radial displacements around the wellbore for Model 11.

- ***Model 12***

Model 12 represented the sandstone rock in depth of 1676 m. This model is equivalent to the AVS tests performed under the hydrostatic stress equal to 41.59 MPa. Table 7.13 summarizes the physical, mechanical, and poro-elastic properties specified to model 12.

Table 7.13. Data used in numerical simulation of Model 12.

Object	Property	Unit	Value
Sandstone rock	Depth from the ground surface	m	1676
	Dry density	kg/m^3	2530
	Cohesion	MPa	7.49
	Friction angle	degree	49.11
	Tensile strength	MPa	5.59
	Porosity	%	15.7
	Biot's coefficient	-	0.53
	Biot Modulus	GPa	61.12
	Storage coefficient	GPa^{-1}	0.026
	Skempton's coefficient	-	0.92
	Bulk modulus	GPa	18.2
	Shear modulus	GPa	6.96
	Poisson's ratio	-	0.33
Wellbore	radius	cm	10
In-situ stresses	σ_v	MPa	40.60
	σ_{Hmax}	MPa	40.60
	σ_{hmin}	MPa	40.60
Pore fluid	Pore pressure	MPa	39.70
	Pore fluid density	kg/m^3	1000
	Saturation degree	-	1

After specifying the characteristics of the rock and water, the numerical model was run. It reached static equilibrium, confirming that the rock properties, initial conditions, and boundary conditions were accurately set. After drilling the wellbore, the radial displacements did not reach a static equilibrium, and the wall completely collapsed. Figure 7.18 illustrates the radial displacements around the wellbore. As it can be seen, the displacements at wellbore wall exceeded 1.79 cm towards the wellbore center. Moreover, Figure 7.19 shows that the shear and tension plasticity states have been stretched behind the wall, indicating that the wall totally underwent failure.

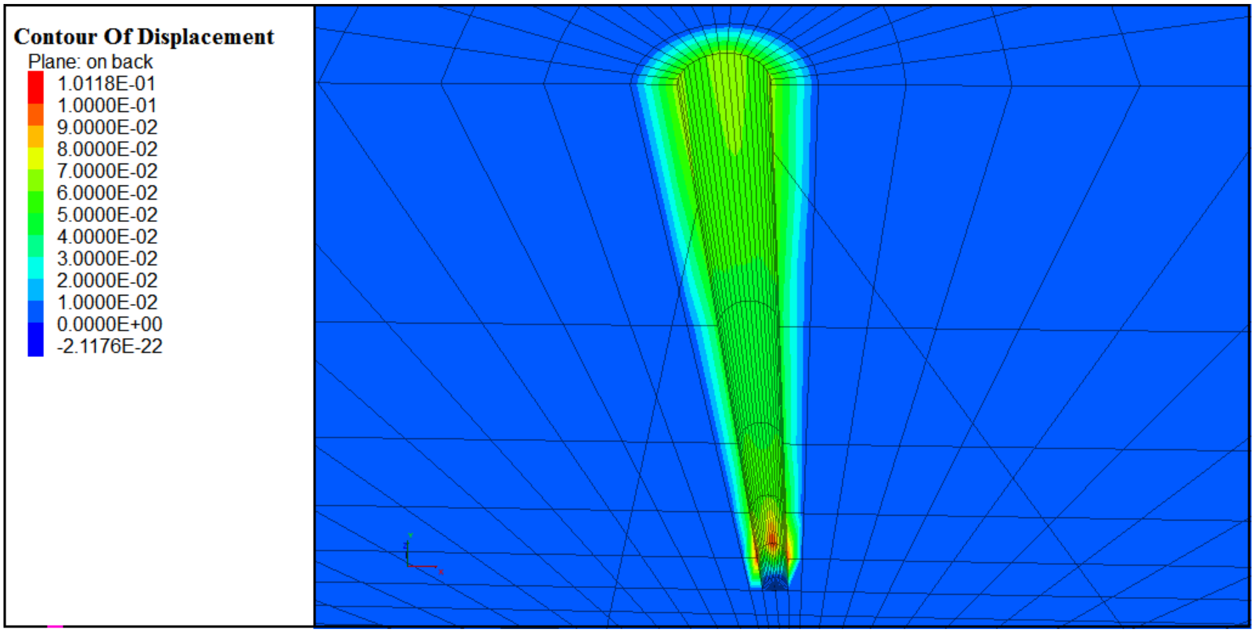

Figure 7.18: The contour of radial displacements around the wellbore for Model 12.

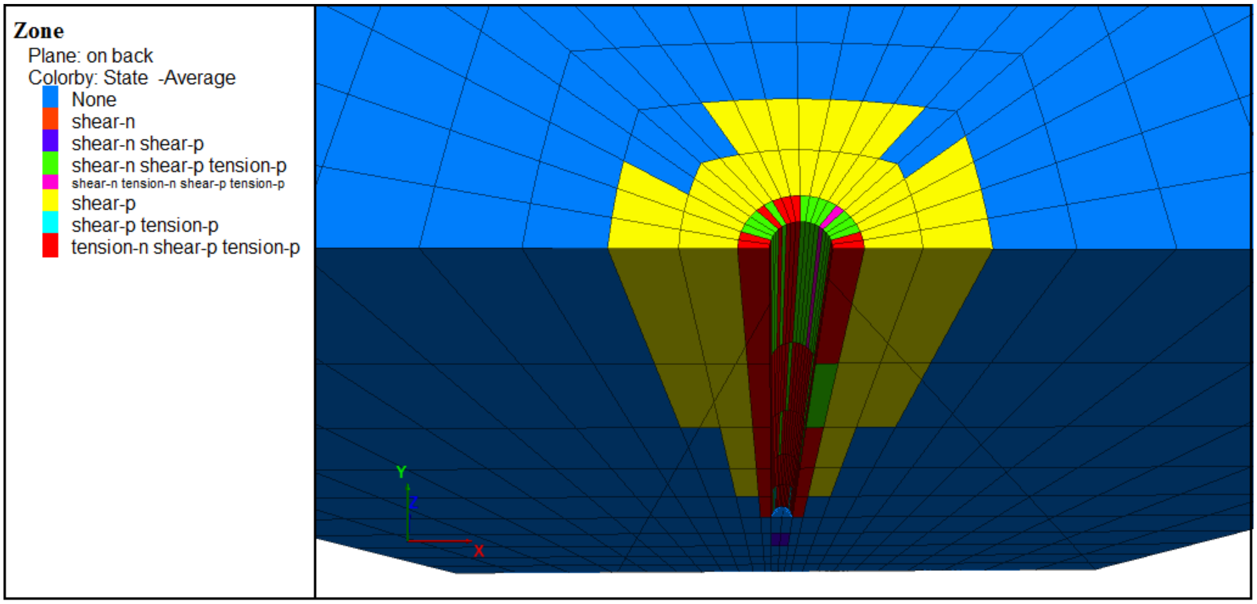

Figure 7.19: The plasticity states of rock zones around the wellbore for Model 12.

In the first scenario, the drilling process was simulated for twelve models while drilling mud pressure was acted on the wellbore wall. The wall was set as impermeable boundary. This entitled us to exclude the impact of mud infiltration on the calculations. Figure 7.20 depicts the maximum radial displacements and calculated safety factor for different drilling depths. Initially, as depth increases, there is a gentle increase in displacement from approximately 0 mm to a 4 mm at depth 1400 m. Concurrently, as depth increases to 1400 m, the safety factor shows a significant decrease, suggesting that the surrounding formation is becoming less stable.

Beyond the depth of 1400 m, further increase in depth leads to a dramatic rise in radial displacement and a sharp decline in the safety factor. This suggests that the system has surpassed its optimal stability threshold, resulting in significant deformation and reduced safety. After a depth of 1400 m, the sharp change indicates a potential failure point, where the rock may no longer withstand the conditions imposed by the increasing depth. Therefore, it can be deduced that for depth more than 1400 meters, the wellbore drilled in the Tumlin sandstone undergoes rock failure as reduction in diameter (wellbore closure).

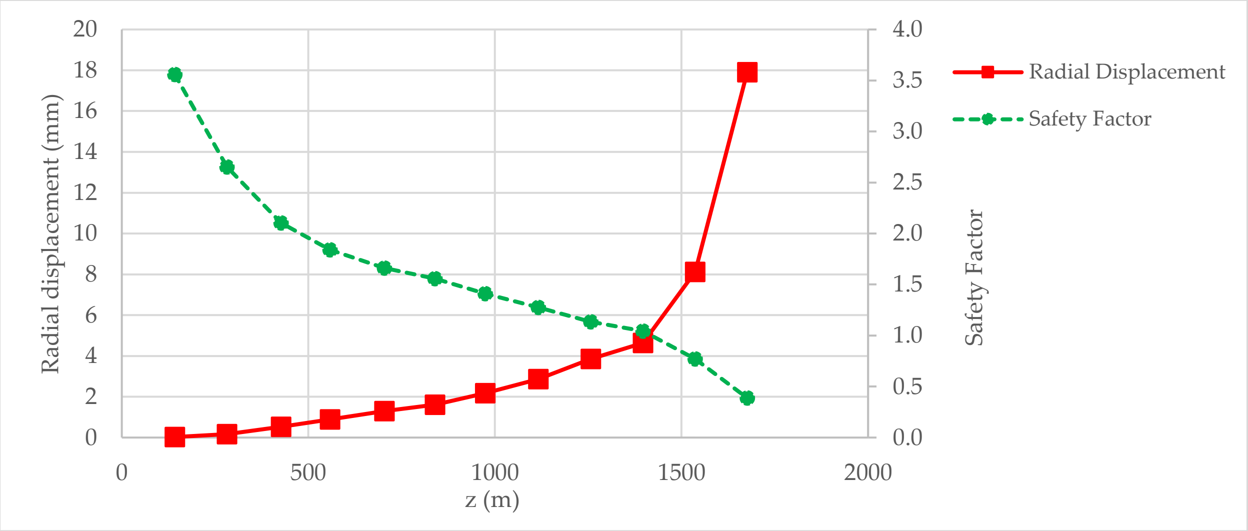

Figure 7.20: Maximum of radial displacements and the equivalent safety factor values for 12 numerical models (undrained condition).

7.3.2. Drained condition

In the second scenario, the drilling process was executed for those twelve numerical models while the mud was allowed to infiltrate into the formation. Therefore, the rock was loaded under drained condition. In this section, the effect of mud interaction with formation on wellbore stability is elaborated.

Figure 7.21 depicts the maximum radial displacements and calculated safety factor for different drilling depths in drained condition. As can be seen for all drilling depths the highest radial displacement of the wall is less than 0.01 mm which is very neglectable. Furthermore, the safety factor for all drilling depths is higher than 4. Thus, it can be deduced that if an appropriate mud pressure between the pore pressure and fracture gradient is selected, the wellbore is highly stable during the loading transition from undrained to drained condition. As a supplementary part, a casing with steel properties (*v*=0.2, and *E*=200 GPa) was also installed in the wellbore. For this case, the displacements were also very minor for all drilling depths.

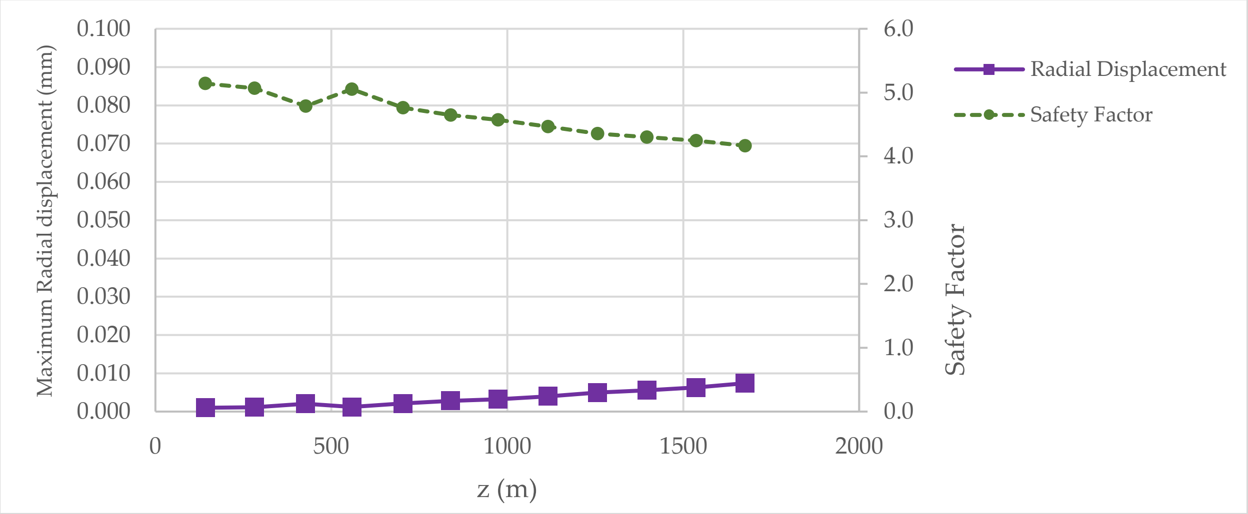

Figure 7.21: Maximum of radial displacements and the equivalent safety factor values for 12 numerical models (drained condition).

7.3.3. Comparing wellbore failure in drained and undrained conditions

To provide a comparison, the results presented in Figures 7.20 and 7.21 are depicted in Figure 7.22.

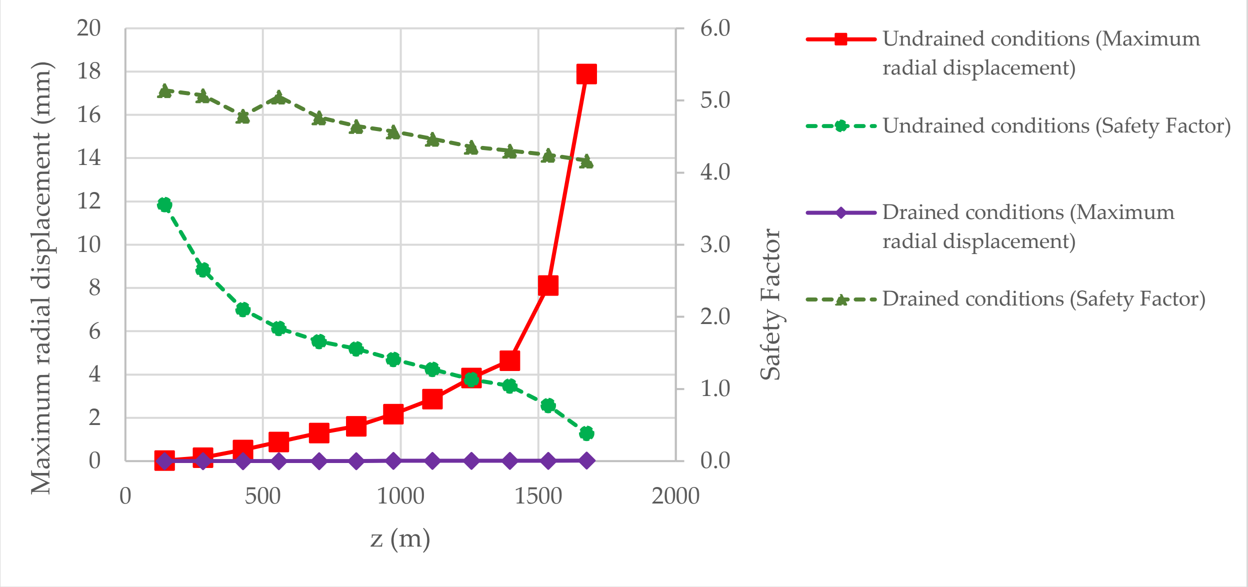

Figure 7.22: Maximum of radial displacements and the equivalent safety factor values for 12 numerical models for both undrained and drained conditions.

As indicated by Figure 7.22, it is turned out that the safety factor for well stability at any arbitrary drilling depth is larger under the drained condition in comparison with the undrained circumstances. Another key point is that the discrepancy between the safety factor of drained and undrained conditions has a direct relationship with depth. Specifically, when the drilling depth surpasses 1400 m, this discrepancy is heightened. For depths less than 1400 m, both undrained and drained safety factors are higher than 1, thereby indicating the stable wellbore. On the other hand, for depths more than 1400 m the safety factor of undrained conditions falls below 1, indicating the wellbore failure potential in the form of wellbore closure.

Regarding the maximum radial displacement, it is concluded that the rock around the wellbore undergoes higher radial strains for undrained condition compared with drained condition. Such a radial strains become more severe when the drilling depths exceeds 1400 m.

Chapter 8: Parametric study

8.1. Procedure of parametric study

In the performed numerical models, the hydrostatic stress and pore pressure changed with depth. As the depth increased, the wellbore wall was more prone to failure, specifically during the very early stages of drilling operation when the rock was under undrained condition. In the previous chapter, since the drilling depth changed in the models, the sole impact of each individual poro-elastic parameter on wellbore stability was unclear. In this chapter, it is attempted to understand how different values of poro-elastic parameters affect wellbore failure. To achieve this, a parametric study is conducted.

In general, parametric study is used in various fields, including engineering, to understand how changes in parameters affect the outcomes of a model or system. A parametric study involves systematically varying one, two, or more parameters while keeping other variables constant to understand the impact of subsequent changes on the outputs. It is often used to examine the behavior of a system across a range of parameter values and to identify trends or patterns in the output as the parameters change.

In the current chapter, a parametric study is conducted for three important models including Model 9, Model 10, and Model 11. As was observed in the previous chapter, these three models underwent significant wall radial displacements. Model 12 was not considered since it was mechanically unstable, and the influence of poro-elastic parameters on wellbore instability was not reflected properly.

The parametric study was conducted based on the following procedure:

1. Firstly, a specific depth or model, e.g. Model 9, was selected. Since the parameters of hydrostatic stress, pore pressure, and Skempton's coefficient rely directly on loading conditions, they were considered constant during the parametric study analysis. Table 8.1 shows the constant parameters for parametric study for Model 9.

Table 8.1: Constant parameters for parametric study for Model 9.

Model	Depth (m)	Pc (MPa)	p (MPa)	B
9	1257	31.20	30.08	0.94

2. For Model 9, 30 measurements had been already taken under undrained condition (Every measurement belonged to conducting an undrained test on one specific rock

sample. Note that there were 30 rock specimens). Those 30 measurements were sorted into nine separate groups based on the value of K_u. Hence, nine groups of undrained measurements were established. Table 8.2 summarizes those groups for Model 9.

Table 8.2: Nine groups of undrained measurements established based on the K_u for Model 9.

Group	*Ku* (MPa)		
	Minimum	Maximum	Average
Group 1	27	29	27.6
Group 2	29	31	30.0
Group 3	31	33	31.4
Group 4	33	35	33.9
Group 5	35	37	35.8
Group 6	37	39	37.8
Group 7	39	40	39.4
Group 8	40	42	40.7
Group 9	42	44	43.6

4. For Model 9, 30 measurements also had been already taken under drained condition (Every measurement belonged to conducting a drained test on one specific rock sample). Those 30 measurements were also sorted to nine separate groups based on the K value. Therefore, nine groups of drained measurements were created. Table 8.3 presents those drained groups for Model 9 based on K.

Table 8.3: Nine groups of drained measurements established based on the K for Model 9.

Group	*K* (MPa)		
	Minimum	Maximum	Average
Group 1	13	14	13.8
Group 2	14	15	14.5
Group 3	15	16	15.6
Group 4	16	17	16.4
Group 5	17	18	17.4
Group 6	18	19	18.7
Group 7	19	20	19.5
Group 8	20	21	20.6
Group 9	21	22	21.1

4. After sorting the undrained and drained measurements to nine distinct groups, the values of K_u and K were utilized to calculate the average Biot's coefficient, average Biot modulus, and average unconstrained specific storage coefficient for each group.

Moreover, the average of other parameters such as G, E, and v were also calculated for those nine groups. Table 8.4 shows the nine groups created for Model 9. These nine groups were utilized in parametric study.

Table 8.4: Nine groups created for Model 9, utilized in parametric study.

Group	K (GPa)	K_u (GPa)	α	M (GPa)	G (GPa)	ν	E (GPa)	S_σ ((GPa)$^{-1}$)
1	13.8	27.6	0.53	48.98	6.48	0.30	16.8	0.0330
2	14.5	30.0	0.55	51.59	6.54	0.30	17.1	0.0323
3	15.6	31.4	0.53	55.73	6.76	0.31	17.7	0.0294
4	16.4	33.9	0.55	58.39	6.72	0.32	17.7	0.0029
5	17.4	35.4	0.54	61.46	6.88	0.32	18.22	0.00272
6	18.7	37.8	0.54	66.56	6.88	0.34	18.4	0.0253
7	19.5	39.4	0.53	69.59	7.18	0.34	19.2	0.0242
8	20.6	40.7	0.52	73.54	7.48	0.34	20.0	0.0225
9	21.1	43.6	0.55	75.11	8.52	0.32	22.5	0.0226

5. Using Table 8.4, nine numerical models for Model 9 were created. In other words, while the loading condition parameters were kept constant, the data presented in Table 8.4 were imported to numerical models. Then, those nine numerical models were run. Those results will be presented in the subsequent subsection.

After conducting the parametric study for Model 9, the above procedure was repeated for Model 10 and Model 11. The following tables summarize the sorted groups for Model 10 and Model 11.

Table 8.5: Constant parameters for parametric study for Model 10.

Model	Depth (m)	Pc (MPa)	p (MPa)	B
10	1397	34.67	33.29	0.94

Table 8.6: Nine groups of undrained measurements established based on the K_u for Model 10.

Group	*Ku* (MPa)		
	Minimum	Maximum	Average
Group 1	27	29	27.6
Group 2	29	31	30.0
Group 3	31	33	31.4
Group 4	33	35	33.9
Group 5	35	37	35.8
Group 6	37	39	37.8
Group 7	39	40	39.4
Group 8	40	42	40.7
Group 9	42	44	43.6

Table 8.7: Nine groups of drained measurements established based on the K for Model 10.

Group	K (MPa)		
	Minimum	Maximum	Average
Group 1	13	14	13.9
Group 2	14	15	14.7
Group 3	15	16	15.9
Group 4	16	17	16.3
Group 5	17	18	17.6
Group 6	18	19	18.6
Group 7	19	20	19.6
Group 8	20	21	20.2
Group 9	21	22	21.7

Table 8.8: Nine groups created for Model 10, utilized in parametric study.

Group	K (GPa)	K_u (GPa)	α	M (GPa)	G (GPa)	ν	E (GPa)	S_σ ((GPa)$^{-1}$)
1	13.9	27.6	0.53	48.7	6.5	0.30	16.82	0.0330
2	14.7	30.0	0.54	51.6	6.6	0.31	17.20	0.0320
3	15.9	31.4	0.53	55.8	6.7	0.32	17.68	0.0291
4	16.3	33.9	0.55	57.2	6.7	0.32	17.79	0.0296
5	17.8	35.4	0.53	62.2	6.91	0.33	18.33	0.0266
6	18.6	37.8	0.54	65.0	6.88	0.33	18.36	0.261
7	19.6	39.4	0.54	68.5	7.44	0.33	19.80	0.244
8	20.2	40.7	0.54	70.8	7.13	0.34	19.14	0.239
9	21.7	43.6	0.54	76.1	8.50	0.33	22.55	0.0219

Table 8.9: Constant parameters for parametric study for Model 11.

Model	Depth (m)	*Pc* (MPa)	*p* (MPa)	*B*
11	1537	38.14	36.54	0.93

Table 8.10: Nine groups of undrained measurements established based on the K_u for Model 11.

Group	*Ku* (MPa)		
	Minimum	Maximum	Average
Group 1	27	29	27.6
Group 2	29	31	30.0
Group 3	31	33	31.4
Group 4	33	35	33.9
Group 5	35	37	35.8
Group 6	37	39	37.8
Group 7	39	40	39.4
Group 8	40	42	40.7
Group 9	42	44	43.6

Table 8.11: Nine groups of drained measurements established based on the *K* for Model 11.

Group	*K* (MPa)		
	Minimum	Maximum	Average
Group 1	13	14	13.91
Group 2	14	15	14.52
Group 3	15	16	15.48
Group 4	16	17	16.44
Group 5	17	18	17.31
Group 6	18	19	18.0
Group 7	19	20	19.52
Group 8	20	21	20.56
Group 9	21	22	21.89

Table 8.12: Nine groups created for Model 11, utilized in parametric study.

Group	K (GPa)	K_u (GPa)	α	M (GPa)	G (GPa)	ν	E (GPa)	S_σ ((GPa)$^{-1}$)
1	13.91	27.6	0.53	48.19	6.47	0.30	16.8	0.0333
2	14.52	30.0	0.55	50.34	6.70	0.30	17.4	0.0330
3	15.48	31.4	0.55	53.62	6.48	0.32	17.1	0.0310
4	16.44	33.9	0.55	57.01	6.68	0.32	17.6	0.0296
5	17.31	35.8	0.56	60.03	6.87	0.32	18.2	0.0283
6	18.0	35.4	0.53	61.86	6.94	0.33	18.43	0.0265
7	19.52	39.4	0.54	67.61	7.18	0.34	19.2	0.0249
8	20.56	40.7	0.53	71.24	7.27	0.34	19.5	0.0234
9	21.89	43.6	0.54	75.83	8.52	0.33	22.6	0.0218

8.2. Results of parametric study

After creating nine separate groups for Model 9, Mode1 10, and Model 11, the relevant numerical simulations were performed, and the numerical results were interpreted.

Figures 8.1, 8.2, and 8.3 show the impact of five poro-elastic parameters including *K*, *Ku*, *E*, *G*, and *M* on the highest radial displacement at wall for those three models. According to those figures, as those poro-elastic parameters increase, the highest radial displacement at the wall decreases.

According to Figure 8.1, the radial displacement is more sensitive to the change in *G*, *E*, and *K*. Hence, a slight increase in these three parameters may lead to dramatic reduction in wall displacement. Furthermore, wall displacement has the least sensitivity to changes in Biot modulus. In other words, altering Biot modulus has the smallest impact on the displacement of the wall compared to changes in other parameters. After Biot modulus, the undrained bulk modulus has the next least sensitivity to wall displacement among the parameters being considered.

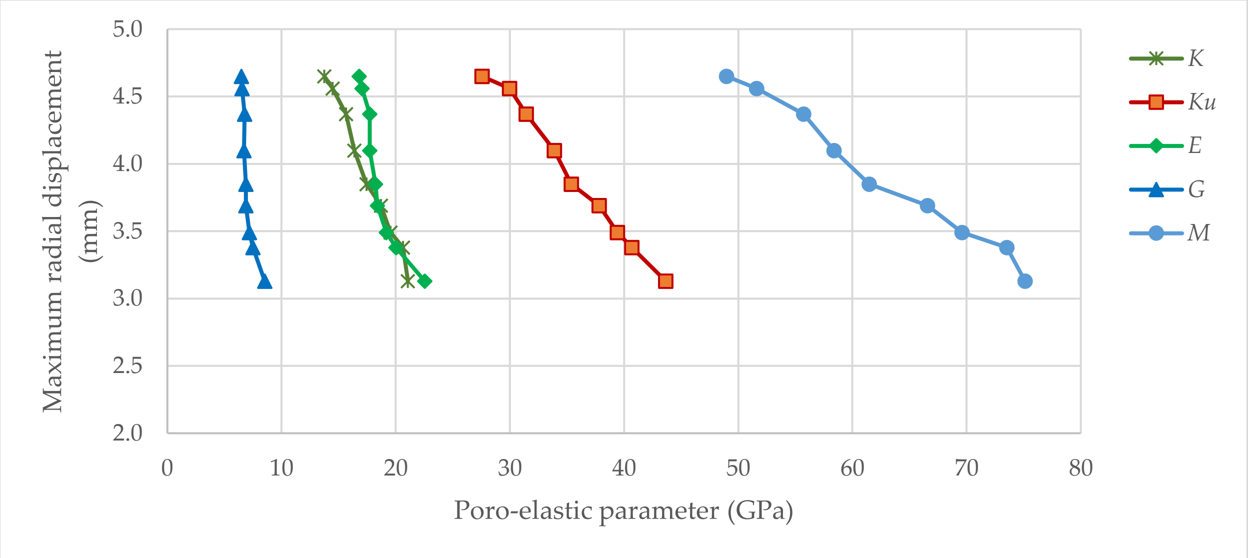

Figure 8.1: Influence of poro-elastic parameters of *K*, *Ku*, *E*, *G*, and *M* on the maximum radial displacement at wellbore wall for Model 9.

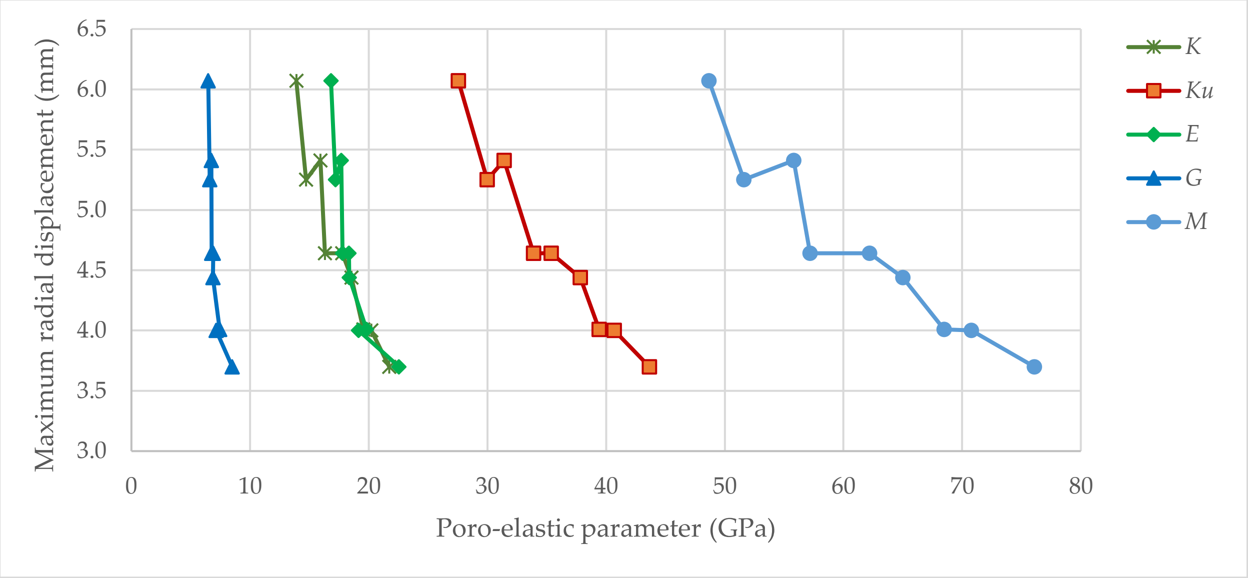

Figure 8.2: Influence of poro-elastic parameters of *K*, *Ku*, *E*, *G*, and *M* on the maximum radial displacement at wellbore wall for Model 10.

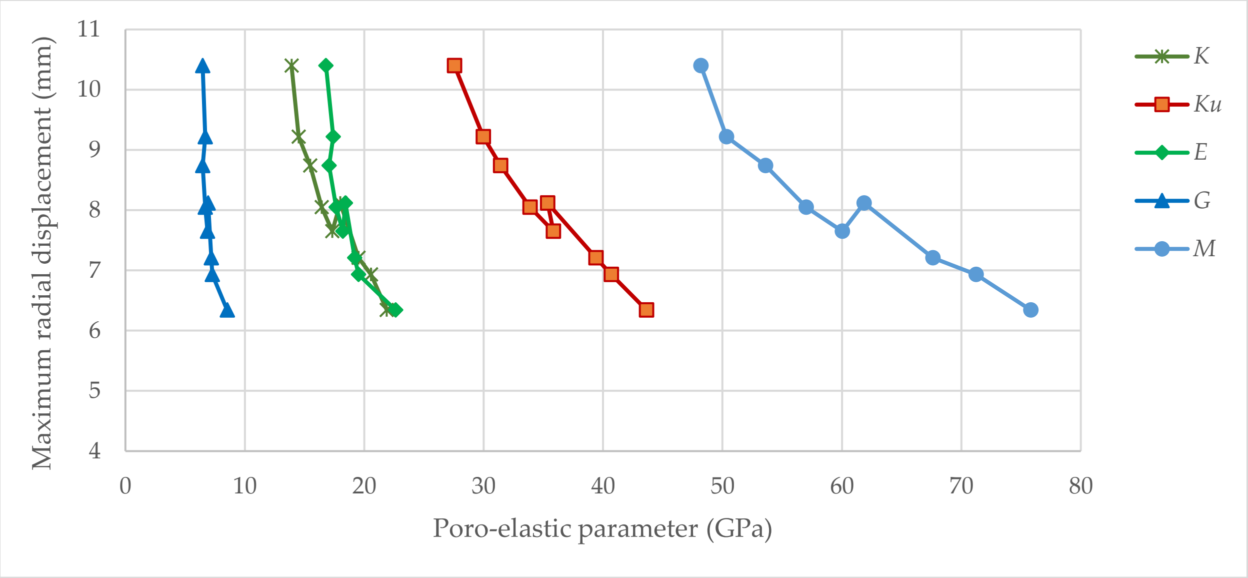

Figure 8.3: Influence of poro-elastic parameters of *K*, *Ku*, *E*, *G*, and *M* on the maximum radial displacement at wellbore wall for Model 11.

The impact of the above-mentioned poro-elastic parameters on the wall displacement has also been shown in Figures 8.4-8.8. In these figures, the impact of each parameter on maximum radial displacement at wellbore wall has been shown for those three models. Apparently, the higher values of *K*, *Ku*, *E*, *G*, and *M*, the less displacement at wellbore wall.

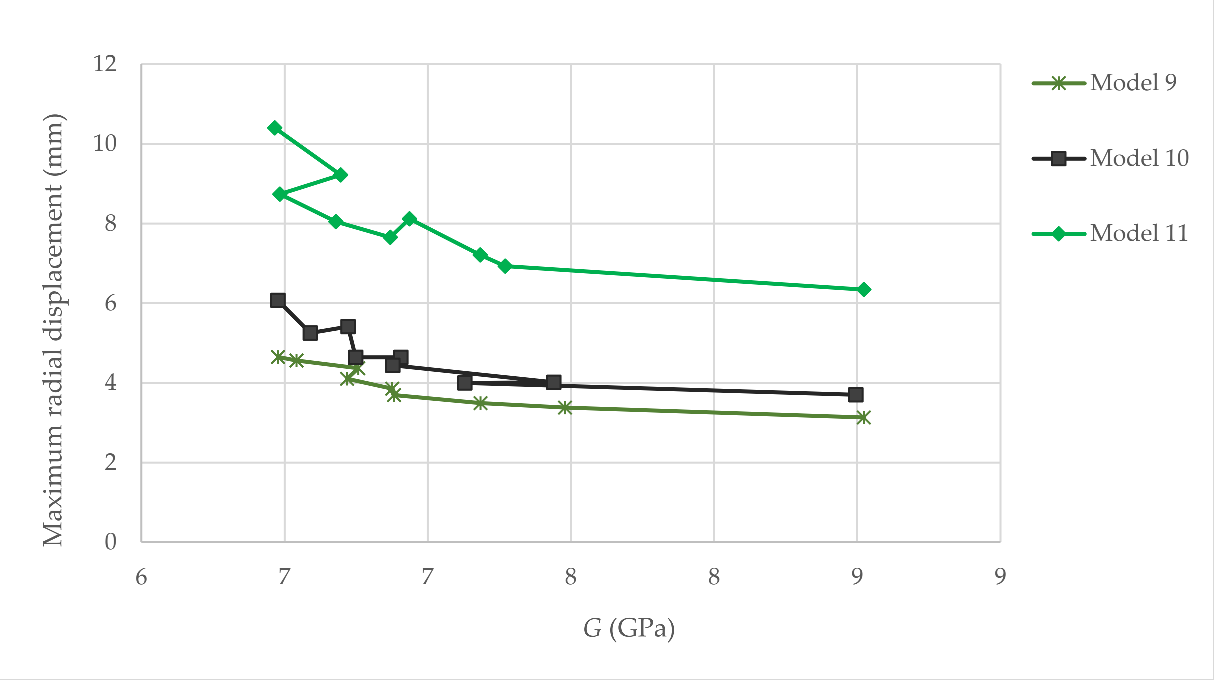

Figure 8.4: The variation of maximum radial displacement at wellbore wall with shear modulus for Model 9, Model 10, and Model 11.

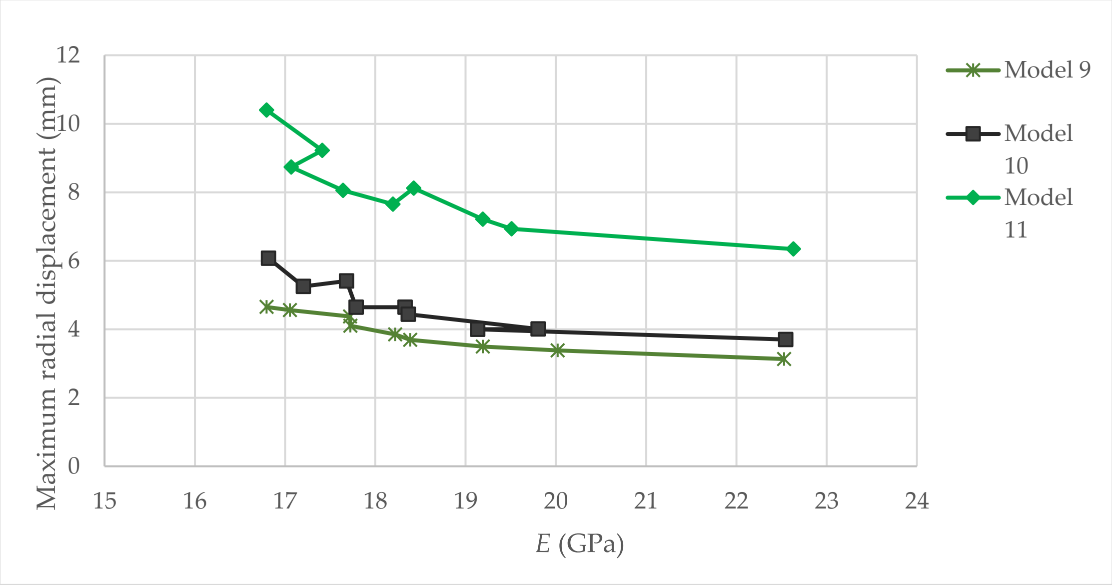

Figure 8.5: The variation of maximum radial displacement at wellbore wall with Young's modulus for Model 9, Model 10, and Model 11.

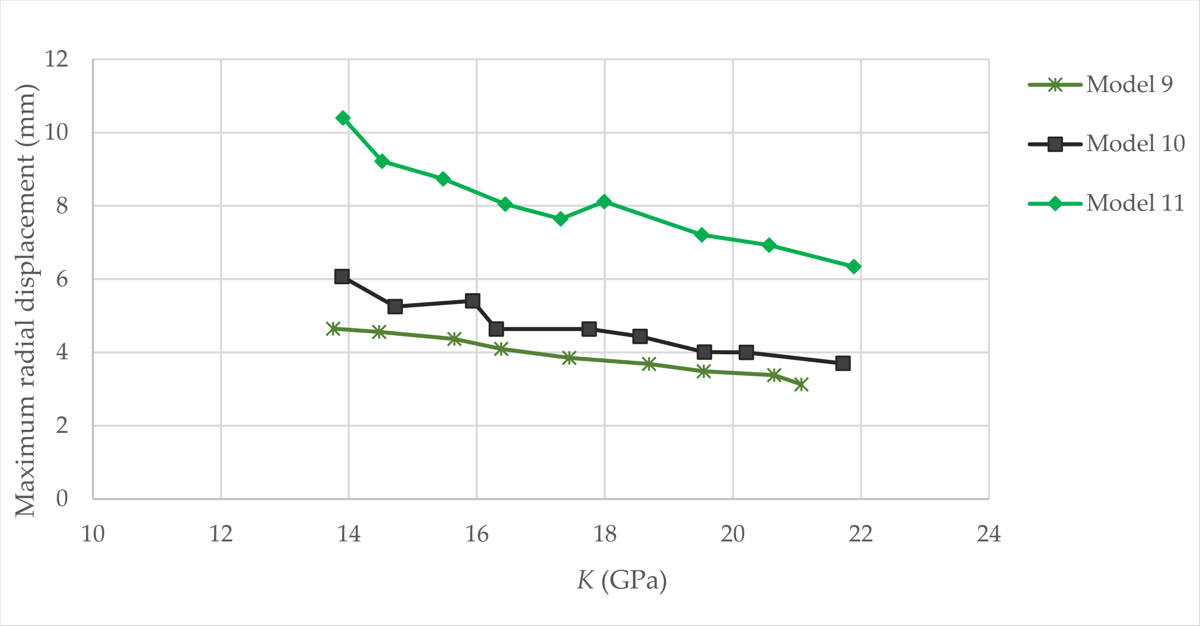

Figure 8.6: The variation of maximum radial displacement at wellbore wall with drained bulk modulus for Model 9, Model 10, and Model 11.

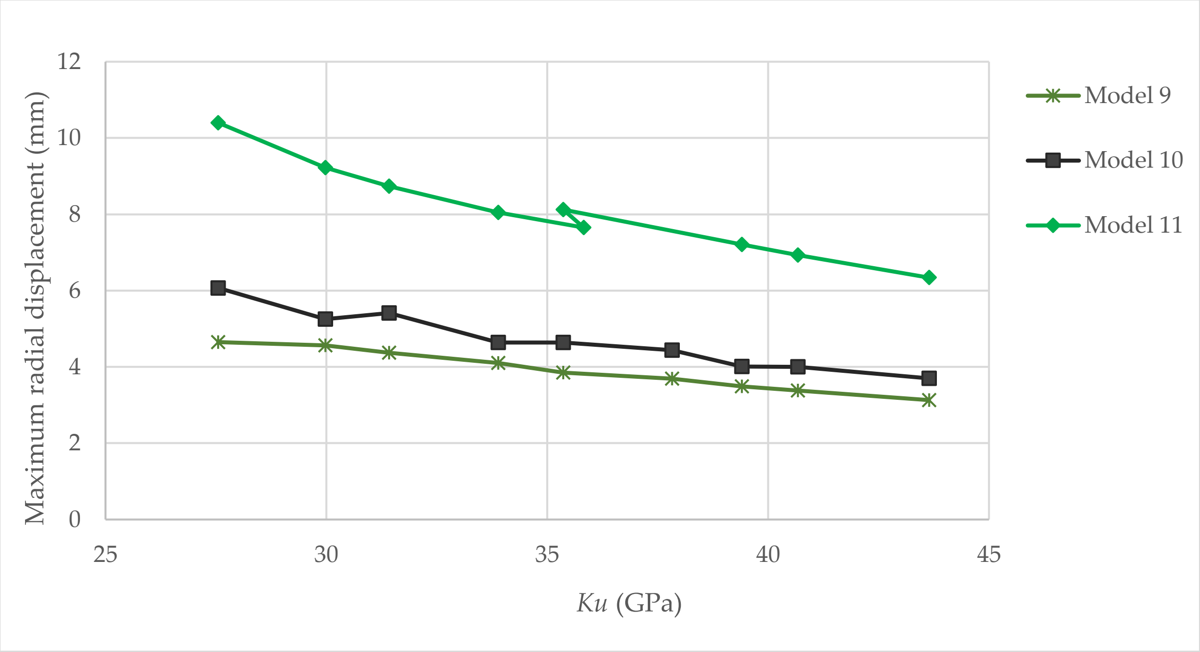

Figure 8.7: The variation of maximum radial displacement at wellbore wall with undrained bulk modulus for Model 9, Model 10, and Model 11.

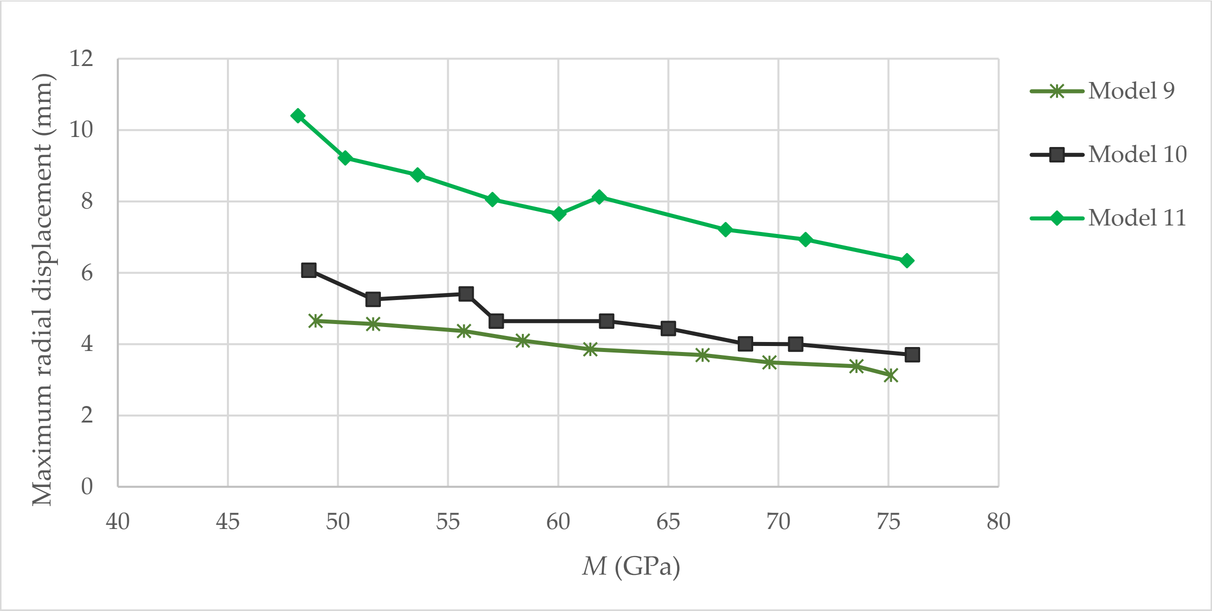

Figure 8.8: The variation of maximum radial displacement at wellbore wall with Biot modulus for Model 9, Model 10, and Model 11.

As well as the poro-elastic parameters of *K*, *Ku*, *E*, *G*, and *M*, the impacts of other poro-elastic parameters, i.e. v, α, and S_σ on the highest radial displacement at wall were also considered. Figure 8.9 depicts the correlation between v and highest radial displacement at wall for those three models. Apparently, as v increases, the maximum radial displacement at wellbore wall decreases.

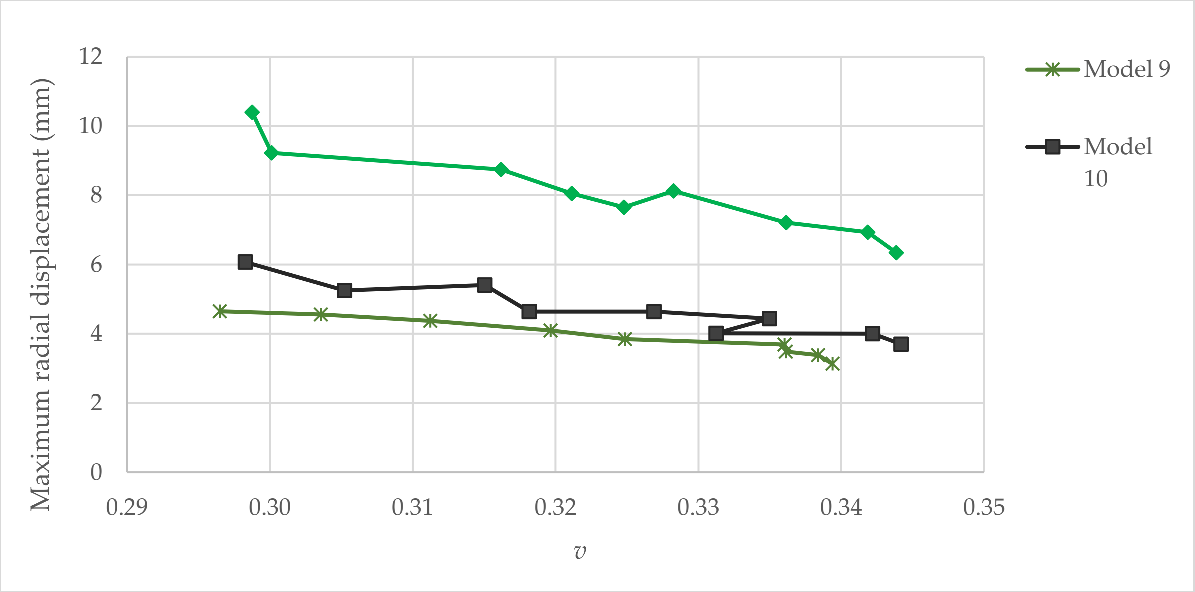

Figure 8.9: Relation between v and highest radial displacement at wall for Model 9, Model 10, and Model 11.

Figure 8.10 depicts the relation between α and highest radial displacement at wall for those three models., As α increases, the highest radial displacement at wall decreases.

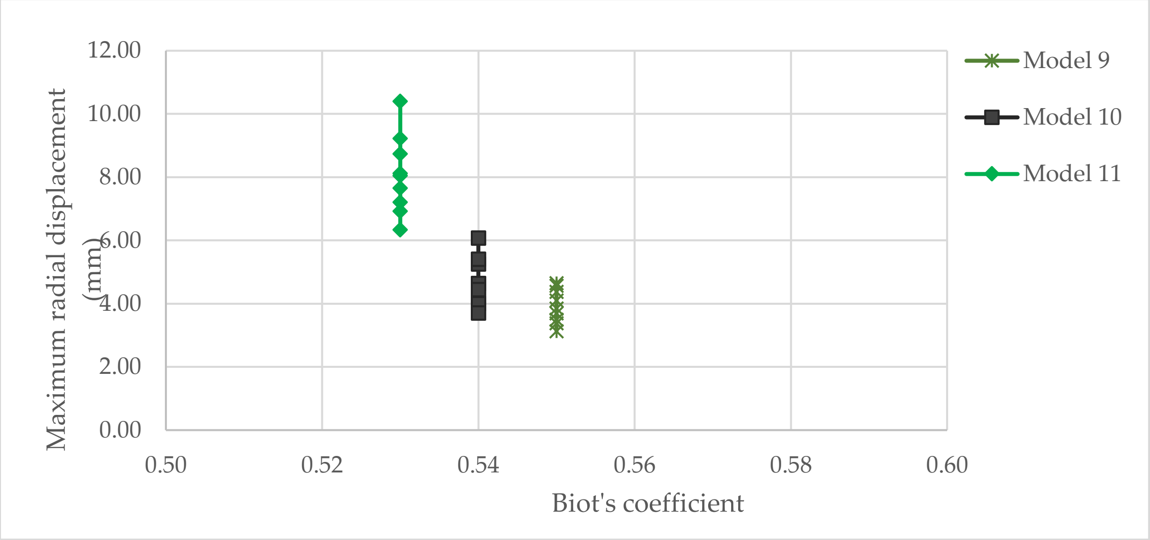

Figure 8.10: Relation between α and highest radial displacement at wall for Model 9, Model 10, and Model 11.

The impact of unconstrained specific storage coefficient on the highest radial displacement at the wall is shown in Figure 8.11. Apparently, when the unconstrained specific storage coefficient increases, the maximum radial displacement at wellbore wall rises.

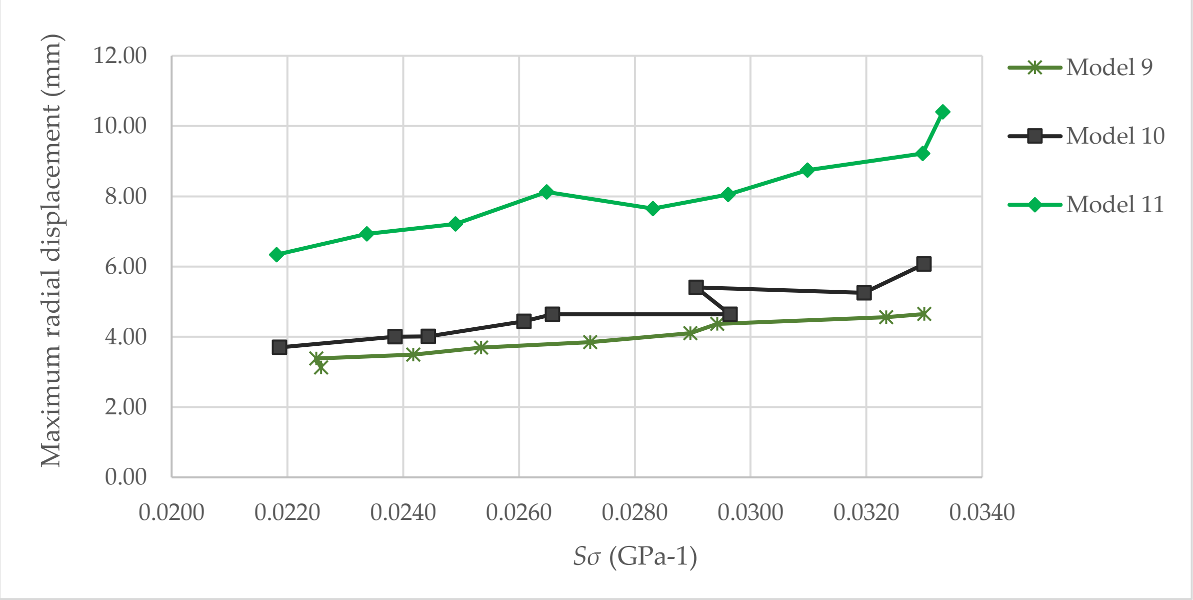

Figure 8.11: Relationship between unconstrained specific storage coefficient and maximum radial displacement at wellbore wall for Model 9, Model 10, and Model 11.

From the aforesaid results, it can be turned out that in constant loading conditions (constant depth), the poro-elastic parameters do not exhibit identical impact on the wellbore stability. The poro-elastic parameters including K, K_u, G, K, M, v, and α have a direct relationship with wellbore stability. On the other hand, unconstrained specific storage coefficient shows an indirect relationship with wellbore stability. This means that as the unconstrained specific storage coefficient gets higher, the potential of wall failure becomes larger.

Chapter 9: Conclusions

Based on laboratory measurements and numerical simulations, the following conclusions were drawn concerning the influence of dynamic poro-elastic parameters on wellbore stability in Tumlin sandstone:

1. The AVS tests revealed that the rock's dynamic poro-elastic parameters remarkably rely on the magnitude of applied hydrostatic stress. Hence, for numerical wellbore stability analysis, it is better to use such a stress-dependent parameters rather than constant values. Consequently, the predictions of wellbore stability analysis will be more accurate.
2. The dynamic poro-elastic parameters of Tumlin sandstone including Skempton's coefficient, bulk modulus, Young's modulus, shear modulus, Poisson's ratio, Biot's coefficient, Biot modulus, and unconstrained specific storage coefficient exhibited different trends with hydrostatic stress.
3. Dynamic Skempton's coefficient, Biot's coefficient, and unconstrained specific storage coefficient exhibit a decreasing trend with increasing hydrostatic stress. However, while the Skempton's coefficient decreases linearly, the Biot's coefficient and the unconstrained specific storage coefficient follow a logarithmic decline
4. On the contrary, other dynamic poro-elastic parameters, including bulk modulus, Young's modulus, shear modulus, Poisson's ratio, and Biot modulus increase with hydrostatic stress. This behavior is independent of the loading condition, whether undrained or drained.
5. At the start of drilling ($t = 0^+$), the Tumlin sandstone undergoes an undrained loading condition. Shortly after $t = 0^+$, the rock undergoes from undrained to drained loading conditions. These transitions in loading conditions were considered in the numerical simulations. It was revealed that the loading conditions have a great impact on the results obtained from coupled fluid-rock wellbore stability analysis, as it influences the poro-elastic parameters of the rock. Tumlin sandstone is more prone to failure when it is under undrained loading condition.
6. At the start of drilling ($t = 0^+$), Young's modulus and shear modulus of Tumlin sandstone decrease while Poisson's ratio and bulk modulus increase.
7. The reduction in Young's modulus under undrained conditions illustrates that the rock becomes less stiff. This decrease in stiffness means the rock will deform more during the early stages of drilling. This leads to greater drilling-induced damage, such as fractures or wellbore collapse, particularly if the rock cannot support the drilling-induced stresses.

8. At the start of drilling ($t = 0^+$), the shear modulus also decreases under undrained conditions, indicating a reduction in the rock's resistance to shear deformation. This reduction implies that the rock is more susceptible to shear failure or deformation during early stages of drilling, which could result in issues such as wellbore instability.
9. At the start of drilling ($t = 0^+$), the increase in Poisson’s ratio indicates that Tumlin sandstone becomes less compressible under undrained conditions. This results in greater lateral strain compared to axial strain, highlighting that the rock may experience more lateral expansion during drill-bit penetration. This behavior heightens the wellbore instability risk in the form of wellbore diameter enlargement.
10. At the start of drilling ($t = 0^+$), the bulk modulus exhibits the most remarkable changes compared to other poro-elastic properties. This phenomenon demonstrates that Tumlin sandstone tends to compensate deformations derived from the reduction in Young’s modulus and shear modulus and increase in Poisson’s ratio.
11. Shortly after $t = 0^+$, when loading condition changes from undrained to drained, the pore pressure in the surrounding Tumlin sandstone reduces. Consequently, the effective stress acting on the rock increases. Furthermore, the poro-elastic parameters including Young’s modulus, shear modulus, and Poisson’s ratio escalate. Such an increase in effective stress and poro-elastic parameters lead to mechanical stabilization of the wellbore wall.
12. At any arbitrary drilling depth, the safety factor for wellbore stability is lower under undrained conditions compared to drained conditions. Thus, the maximum radial displacements around the wellbore were larger for undrained conditions in comparison with the drained conditions.
13. The difference in safety factors between undrained and drained conditions is directly dependent on the drilling depth. Specifically, when the drilling depth exceeds 1400 m, this difference becomes more intense.
14. As the depth increases, the discrepancy between the rock’s poro-elastic parameters under drained and undrained conditions is smaller compared with the shallower depths. This finding implies that the mechanical behavior of Tumlin sandstone becomes more consistent for the deeper depths. This could mean that in deeper, high-stress levels, the rock is less likely to experience unexpected changes in deformation characteristics, which can be advantageous for maintaining wellbore stability.

References

1. Zhang JJ. *Applied petroleum geomechanics*. Gulf Professional Publishing: Houston, Texas, United States: 2019. ISBN: 978-0-12-814814-3, https://doi.org/10.1016/C2017-0-01969-9
2. Terzaghi, K. Die berechnung der durchlauigkeitmfiffer des tones aus dem verlauf der hydrndynamischen spannuagserscheinungen. *Sber. Akad. Wiss. Wien. Math. Naturwiss. KI., Abt. lla* **1923**, *132*, 105–124.
3. Wang, H.F. *Theory of linear poroelasticity with applications to geomechanics and hydrogeology*; Princeton University Press: Oxford, UK, 2000.
4. King, F.H. *Observations and experiments on the fluctuations in the level and rate of movement of ground-water on the Wisconsin agricultural experiment station farm and at Whitewater, Wisconsin*; Weather Bureau: Washington, DC, USA, 1892; No. 5.
5. Meinzer, O.E. Compressibility and elasticity of artesian aquifers. *Econ. Geol.* **1928**, *23*, 263–291, doi:10.2113/gsecongeo.23.3.263.
6. Biot, M.A. General Theory of three-dimensional consolidation. *J. Appl. Phys.* **1941**, *12*, 155–164, doi:10.1063/1.1712886.
7. Pawlica, W. Ilaste rudy żelazne Starachowic. Spraw. Państw. Inst. Geol. 1920, 1(1), 1–52. Warszawa, Poland.
8. Gradziński, R.; Gągol, J.; Ślączka, A. The Tumlin sandstone (Holy Cross Mts, central Poland): Lower Triassic deposits of aeolian dunes and interdune areas. *Acta Geol. Pol.* **1979**, *29*, 151-176.
9. Kirsch, E.G. Die Theorie der elastizität und die bedürfnisse der festigkeitslehre. *Zeitschrift des Vereines deutscher Ingenieure* **1898**, *42*, 797–807.
10. Hubbert, M.K.; Willis, D.G. Mechanics of hydraulic fracturing. *Trans. AIME* **1957**, *210*(01), 153–168. https://doi.org/10.2118/686-G
11. Fairhurst, C. Methods of determining in-situ rock stresses at great depths. Minnesota: University of Minnesota, USA, 1967.
12. Bradley, W.B. Failure of inclined boreholes. *Journal of Energy Resources Technology* **1979**, *101*(4), 232. https://doi.org/10.1115/1.3446925
13. Detournay, E.; Cheng, A.-D. Poroelastic response of a borehole in a non-hydrostatic stress field. *Int. J. Rock Mech. Min. Sci. Geomech. Abstr.* **1988**, *25*(3), 171–182. https://doi.org/10.1016/0148-9062(88)92299-1
14. Cui, L.; Cheng, A.H.-D.; Abousleiman, Y. Poroelastic solution for an inclined borehole. *J. Appl. Mech.* **1997**, *64(1)*, 32–38. https://doi.org/10.1115/1.2787291
15. Rahman, M.K.; Naseby, D.; Rahman, S.S. Borehole collapse analysis incorporating time-dependent pore pressure due to mud penetration in shales. *J. Pet. Sci. Eng.* **2000**, *28*(1–2), 13–31. https://doi.org/10.1016/S0920-4105(00)00064-4
16. Awal, M.R.; Khan, M.S.; Mohiuddin, M.A.; Abdulraheem, A.; Azeemuddin, M. A new approach to borehole trajectory optimisation for increased hole stability. In Proceedings of the SPE Middle East Oil and Gas Show and Conference, Bahrain, 17 March 2001; Paper No. SPE-68092-MS. https://doi.org/10.2118/68092-MS
17. Zhang, J.; Bai, M.; Roegiers, J.C. Dual-porosity poroelastic analyses of wellbore stability. *Int. J. Rock Mech. Min. Sci.* **2003**, *40*(4), 473–483. https://doi.org/10.1016/S1365-1609(03)00019-4

18. Regel, J.B.; Orozova-Bekkevold, I.; Andreassen, K.A.; van Gilse, N.H.; Fabricius, I.L. Effective stresses and shear failure pressure from in situ Biot's coefficient, Hejre Field, North Sea. *Geophys. Prospect.* **2017**, *65*(3), 808–822. https://doi.org/10.1111/1365-2478.12442
19. Liu, J.; Ma, T.; Fu, J.; Peng, N.; Qiu, Y.; Liu, Y.; Gao, J. Fully coupled two-phase hydro-mechanical model for wellbore stability analysis in tight gas formations considering the variation of rock mechanical parameters. *J. Nat. Gas Sci. Eng.* **2023**, *115*, 205023. https://doi.org/10.1016/j.jgsce.2023.205023
20. Santarelli, F.J.; Brown, E.T.; Maury, V. Analysis of borehole stresses using pressure-dependent, linear elasticity. *Int. J. Rock Mech. Min. Sci.* **1986**, *23*(6), 445–449. https://doi.org/10.1016/0148-9062(86)92310-7
21. Zamani, M.A.M.; Knez, D. Experimental investigation on the relationship between Biot’s coefficient and hydrostatic stress for enhanced oil recovery projects. *Energies* **2023**, *16*, 4999. https://doi.org/10.3390/en16134999.
22. Geertsma, J. Problems of rock mechanics in petroleum production engineering. In Proceedings of the 1st ISRM Congress; Lisbon, Portugal, 25 September 1966; Paper No. ISRM-1CONGRESS.
23. Kang, Y.; Yu, M.; Miska, S.Z.; Takach, N.E. Wellbore stability: a critical review and introduction to DEM. In Proceedings of the SPE Annual Technical Conference and Exhibition, New Orleans, LA, USA, 4–7 October 2009; Paper No. SPE-124669-MS. DOI: 10.2118/124669-MS.
24. Zeynali, M.E. Mechanical and physico-chemical aspects of wellbore stability during drilling operations. *J. Petrol. Sci. Eng.* **2012**, *82*, 120–124. https://doi.org/10.1016/j.petrol.2012.01.006
25. Ibrahim, A. A review of mathematical modelling approaches to tackling wellbore instability in shale formations. *J. Nat. Gas Sci. Eng.* **2021**, *89*, 103870. https://doi.org/10.1016/j.jngse.2021.103870
26. Labenski, F.; Reid, P.; Santos, H. Drilling fluids approaches for control of wellbore instability in fractured formations. In Proceedings of the SPE/IADC Middle East Drilling Technology Conference and Exhibition, Abu Dhabi, United Arab Emirates, 20–22 October 2003; Paper No. SPE-85304-MS. DOI: 10.2118/85304-MS.
27. Huang, L.; Yu, M.; Miska, S.; Takach, N.; Bloys, J.B. Parametric sensitivity study of chemo-poro-elastic wellbore stability considering transversely isotropic effects in shale formations. In Proceedings of the SPE Canadian Unconventional Resources Conference, Calgary, Alberta, Canada, 30 October 2012; Paper No. SPE-162751-MS. DOI: 10.2118/162751-MS.
28. Timoshenko, S.P.; Goodier, J.N.; Abramson, H. N. *Theory of elasticity*, 3rd ed. ASME. J. Appl. Mech. September 1970; 37(3): 888. https://doi.org/10.1115/1.3408648
29. Morita, N. Well Orientation effect on borehole stability. In Proceedings of the SPE Annual Technical Conference and Exhibition, Houston, Texas, USA, 26 September 2004; Paper No. SPE-89896-MS. DOI: 10.2118/89896-MS.
30. Jaeger, J.C.; Cook, N.G.W.; Zimmerman, C. *Fundamentals of rock mechanics*, 4th ed.; Wiley-Blackwell: Malden, MA, USA, 2007; pp. 488. ISBN: 978-0-632-05759-7, http://dx.doi.org/10.1017/CBO9780511735349
31. Al-Ajmi, A.M.; Zimmerman, R.W. A new well path optimization model for increased mechanical borehole stability. *Journal of Petroleum Science and Engineering* **2009**, *69*(1–2), 53–62. DOI: 10.1016/j.petrol.2009.05.018.

32. Russell, K.A.; Ayan, C.; Hart, N.J.; Rodriguez, J.M.; Scholey, H.; Sugden, C.; Davidson, J.K. Predicting and preventing wellbore instability using the latest drilling and logging technologies: Tullich field development, North Sea. In Proceedings of the SPE Annual Technical Conference and Exhibition, Denver, Colorado, USA, 5 October 2003; Paper No. SPE-84269-MS. DOI: 10.2118/84269-MS.
33. Kaarstad, E.; Aadnoy, B.S. Optimization of borehole stability using 3-d stress optimization. In Proceedings of the SPE Annual Technical Conference and Exhibition, Dallas, Texas, USA, 9 October 2005; Paper No.SPE-97149-MS. https://doi.org/10.2118/97149-MS
34. Knez, D.; Zamani, M.A.M. Empirical Formula for Dynamic Biot Coefficient of Sandstone Samples from South-West of Poland. *Energies* **2021**, *14*, 5514. https://doi.org/10.3390/en14175514.
35. Terzaghi, K.; Peck, R.B.; Mesri, G. *Soil mechanics in engineering practice*, 3rd ed.; John Wiley & Sons: Hoboken, NY, USA, 1996.
36. Biot, M.A. Theory of elasticity and consolidation for a porous anisotropic solid. *J. Appl. Phys.* **1955**, *26*(2), 182–185. https://doi.org/10.1063/1.1721956
37. Biot, M.A. General solutions of the equations of elasticity and consolidation for a porous material. *J. Appl. Mech.*, Trans. Am. Soc. Mech. Engrs **1956**, 23(1), 91–96. https://doi.org/10.1115/1.4011213
38. Biot, M.A. Mechanics of deformation and acoustic propagation in porous media. *Journal of Applied Physics* **1962**, *33,* 1482–1498. https://doi.org/10.1063/1.1728759
39. Rice, J.R.; Cleary, M.P. Some basic stress diffusion solutions for fluid-saturated elastic porous media with compressible constituents. *Reviews of Geophysics and Space Physics* **1976**, *14(2)*, 227–241. https://doi.org/10.1029/RG014i002p00227
40. Aadnøy, B.S.; Chenevert, M.E. Stability of highly inclined boreholes. *SPE Drilling Engineering* **1987**, *2*(04), 364–374. https://doi.org/10.2118/16052-PA
41. Knez, D.; Khalilidermani, M.; Zamani, M.A.M. Water influence on the determination of the rock matrix bulk modulus in reservoir engineering and rock-fluid coupling projects. *Energies* **2023**, *16*, 1769. https://doi.org/10.3390/en16041769.
42. Hart, D.J.; Wang, H.F. Laboratory measurements of a complete set of poroelastic moduli for Berea Sandstone and Indiana Limestone. *J. Geophys. Res.* **1995**, *100*, 17741–17751. https://doi.org/10.1029/95JB01242
43. Wikipedia. Shear modulus. Available online: https://en.wikipedia.org/wiki/Shear_modulus (accessed on 20 August 2024).
44. Rice, J.R. Elasticity of fluid-infiltrated porous solids (poroelasticity). *Stress* **1998**, *2*(2).
45. Fjaer, E.; Holt, R.M.; Horsrud, P.; Raaen, A.M.; Risnes, R. *Petroleum related rock mechanics*, 2nd ed.; Elsevier: Amsterdam, Netherlands, 2008. ISBN: 978-0-444-50260-5, ISSN: 0376-7361
46. Bradley, W.B. Borehole failure near salt domes. In Proceedings of the *SPE Annual Technical Conference and Exhibition*, Houston, Texas, 1 October 1978. Paper No. SPE-7503. https://doi.org/10.2118/7503-MS
47. McLean, M.R.; Addis, M.A. Wellbore stability analysis: a review of current methods of analysis and their field application. In Proceedings of the Society of Petroleum Engineers, Houston, Texas, 27 February 1990. Paper No. SPE-19941-MS, https://doi.org/10.2118/19941-MS

48. Franquet, J.A.; Verma, N.K.; Azeemuddin, M.; Al Shamali, A.A.; Al-Morakhi, R.; Reji, E.C. Openhole stability analysis of horizontal wellbores under production scenarios in Jurassic carbonate reservoirs of west Kuwait. In Proceedings of the Society of Petroleum Engineers, Manama, Bahrain, 11 March 2007. Paper No. SPE-105332-MS, https://doi.org/10.2118/105332-MS
49. Aadnøy, B.S. A complete elastic model for fluid-induced and in-situ generated stresses with the presence of a borehole. *Energy Sources* **1987**, *9*(4), 239–259. https://doi.org/10.1080/00908318708908700
50. Paslay, P.R.; Cheatham, J.B. Rock stresses induced by flow of fluids into boreholes. *SPE J.* **1963**, *3*(01), 85–94. https://doi.org/10.2118/482-PA
51. Haimson, B.; Fairhurst, C. Initiation and extension of hydraulic fractures in rocks. *SPE J.* **1967**, *7*(03), 310–318. https://doi.org/10.2118/1710-PA
52. Fun, G.F.; Whitfill, D.L.; Schuh, P.R. Use of borehole stability analysis for successful drilling of high-angle hole. In Proceedings of the SPE/IADC Drilling Conference and Exhibition, Dallas, Texas, USA. 28 February 1988; Paper No. SPE-17235-MS. https://doi.org/10.2118/17235-MS
53. Yew, C.H.; Liu, G. Pore fluid and wellbore stabilities. In Proceedings of the SPE International Oil and Gas Conference and Exhibition, Beijing, China, 24 March 1992; Paper No. SPE-22381-MS. https://doi.org/10.2118/22381-MS
54. Aoki, T.; Tan, C.P.; Bamford, W.E. Effects of deformation and strength anisotropy on borehole failures in saturated shales. *Int. J. Rock Mech. Min. Sci. Geomech. Abstr.* **1993**, *30*(7), 1031–1034. https://doi.org/10.1016/0148-9062(93)90067-N.
55. Liu, C.; Abousleiman, Y.N. Multiporosity/Multipermeability inclined-wellbore solutions with mudcake effects. *SPE J.* **2018**, *23*(5), 1723–1747. https://doi.org/10.2118/191135-PA
56. Zhang, J.; Keaney, G.; Standifird, W. Wellbore stability with consideration of pore pressure and drilling fluid interactions. In Proceedings of the Golden Rocks 2006, The 41st U.S. Symposium on Rock Mechanics (USRMS), Golden, Colorado, USA, 17 June 2006; Paper No. ARMA-06-922
57. Salehi, S.; Hareland, G.; Nygaard, R. Numerical simulations of wellbore stability in under-balanced-drilling wells. *J. Pet. Sci. Eng.* **2010**, *72*(3–4), 229–235. https://doi.org/10.1016/j.petrol.2010.03.022
58. Lee, M.; Eckert, A.; Nygaard, R. Mesh optimization for finite element models of wellbore stress analysis. In Proceedings of the 45th US Rock Mechanics/Geomechanics Symposium, San Francisco, California, USA, 26 June 2011; Paper No. ARMA-11- 365.
59. Yousefian, H.; Soltanian, H.; Marji, M.F.; Moazen, M. Numerical simulation of a wellbore stability in an Iranian oilfield utilizing core data. *J. Pet. Sci. Eng.* **2018**, *168*, 577–592. https://doi.org/10.1016/j.petrol.2018.04.051
60. Darvishpour, A.; Seifabad, M.C.; Wood, D.A.; Ghorbani, H. Wellbore stability analysis to determine the safe mud weight window for sandstone layers. *Pet. Explor. Dev.* **2019**, *46*(5), 1031–1038. https://doi.org/10.1016/S1876-3804(19)60260-0
61. Deangeli, C.; Marchelli, M. Combined effect of pore water overpressure, far-field stresses, and strength parameters in wellbore stability. *Front. Earth Sci.* **2022**, *10*, 860818. https://doi.org/10.3389/feart.2022.860818

62. Hodge, M.; Valencia, K.L.; Chen, Z.; Rahman, S.S. Analysis of time-dependent wellbore stability of underbalanced wells using a fully coupled poroelastic model. In Proceedings of the SPE Annual Technical Conference and Exhibition, San Antonio, TX, USA, 24 September 2006; Paper No. SPE-102873-MS, https://doi.org/10.2118/102873-MS
63. Li, X.; Gray, K.E. Wellbore stability of deviated wells in depleted reservoir. In Proceedings of the SPE Annual Technical Conference and Exhibition, Houston, TX, USA. 28 September 2015; https://doi.org/10.2118/174860-MS
64. Kanfar, M.F.; Chen, Z.; Rahman, S.S. Effect of material anisotropy on time-dependent wellbore stability. *Int. J. Rock Mech. Min. Sci.* **2015**, *78*, 36–45. https://doi.org/10.1016/j.ijrmms.2015.04.024
65. Li, X.; El Mohtar, C.S.; Gray, K.E. 3D poro-elasto-plastic modeling of breakouts in deviated wells. *J. Pet. Sci. Eng.* **2019**, *174*, 913–920. https://doi.org/10.1016/j.petrol.2018.11.086
66. Akbarpour, M.; Abdideh, M. Wellbore stability analysis based on geomechanical modeling using finite element method. *Model. Earth Syst. Environ.* **2020**, *6*, 617–626. https://doi.org/10.1007/s40808-020-00716-x
67. Liu, C.; Han, Y.; Phan, D.T.; Abousleiman, Y.N. Stress solutions for short-and long-term wellbore stability analysis. *J. Nat. Gas Sci. Eng.* **2022**, *105*, 104693. https://doi.org/10.1016/j.jngse.2022.104693
68. Ghassemi, A.; Diek, A. Porothermoelasticity for swelling shales. *J. Pet. Sci. Eng.* **2002**, *34*(1–4), 123–135. https://doi.org/10.1016/S0920-4105(02)00159-6
69. Ekbote, S.; Abousleiman, Y. Porochemoelastic solution for an inclined borehole in a transversely isotropic formation. *J. Eng. Mech.* **2006**, *132*(7), 754–763. https://doi.org/10.1061/(ASCE)0733-9399(2006)132:7(754)
70. Gomar, M.; Goodarznia, I.; Shadizadeh, S.R. A transient fully coupled thermo-poroelastic finite element analysis of wellbore stability. *Arab. J. Geosci.* **2015,** *8*, 3855–3865. https://doi.org/10.1007/s12517-014-1461-4
71. Gao, J.; Deng, J.; Lan, K.; Tang, S.; Liu, Y.; Zhao, X. Porothermoelastic effect on wellbore stability in transversely isotropic medium subjected to local thermal non-equilibrium. *Int. J. Rock Mech. Min. Sci.* **2017**, *96*, 66–84. https://doi.org/10.1016/j.ijrmms.2016.12.007
72. Nguyen, D.; Miska, S.; Yu, M.; Saasen, A. Modeling thermal effects on wellbore stability. In Proceedings of the SPE Trinidad and Tobago Section Energy Resources Conference, Port of Spain, Trinidad, 27 June 2010; Paper No. SPE-133428-MS, https://doi.org/10.2118/133428-MS
73. Wang, Y.; Duan, L.; Zhang, F.; Lian, M.; Li, B. Dynamic wellbore stability analysis based on thermo-poro-elastic model and quantitative risk assessment method. *Geoenergy Sci. Eng.* **2023**, *229*, 212063. https://doi.org/10.1016/j.geoen.2023.212063
74. Zhang, L.; Zhang, Z.; Wu, B.; Zhang, X.; Nie, Y.; Wang, G.; Yang, L. A fully coupled thermo-poro-elastic model predicting the stability of wellbore in deep-sea drilling. Part A: Analytic solutions. *Geoenergy Sci. Eng.* **2023a**, *228*, 211950. https://doi.org/10.1016/j.geoen.2023.211950
75. Zhang, L.; Zhang, Z.; Wu, B.; Zhang, X.; Nie, Y.; Zhang, H.; Wang, G.; Yang, L. A fully coupled thermo-poro-elastic model predicting the stability of wellbore in deep-sea drilling. Part B: Sensitivity analysis. *Geoenergy Sci. Eng.* **2023b**, *228*, 211973. https://doi.org/10.1016/j.geoen.2023.211973

76. Roshan, H.; Rahman, S.S. A fully coupled chemo-poroelastic analysis of pore pressure and stress distribution around a wellbore in water active rocks. *Rock Mech. Rock Eng.* **2011**, *44*, 199–210. https://doi.org/10.1007/s00603-010-0104-7
77. Zhou, X.; Gassemi, A. Finite element analysis of coupled chemo-poro-thermo-mechanical effects around a wellbore in swelling shale. *Int. J. Rock Mech. Min. Sci.* **2009**, *46*(4), 769–778. https://doi.org/10.1016/j.ijrmms.2008.11.009
78. Rafieepour, S.; Jalayeri, H.; Ghotbi, C.; Pishvaie, M.R. Simulation of wellbore stability with thermo-hydro-chemo-mechanical coupling in troublesome formations: an example from Ahwaz oil field, SW Iran. *Arab. J. Geosci.* **2015**, *8*, 379–396. https://doi.org/10.1007/s12517-013-1116-x
79. Rafieepour, S.; Zamiran, S.; Ostadhassan, M. A cost-effective chemo-thermo-poroelastic wellbore stability model for mud weight design during drilling through shale formations. *J. Rock Mech. Geotech. Eng.* **2020**, *12*(4), 768–779. https://doi.org/10.1016/j.jrmge.2019.12.008
80. Økland, D.; Cook, J.M. Bedding-related borehole instability in high-angle wells. In Proceedings of the SPE/ISRM Rock Mechanics in Petroleum Engineering, Trondheim, Norway, 8 July 1998. https://doi.org/10.2118/47285-MS
81. Zhang, J. Borehole stability analysis accounting for anisotropies in drilling to weak bedding planes. *Int. J. Rock Mech. Min. Sci.* **2013**, *60*, 160–170. https://doi.org/10.1016/j.ijrmms.2012.12.025 Zhang JJ. *Applied petroleum geomechanics*. Gulf Professional Publishing: Houston, Texas, United States: 2019. ISBN: 978-0-12-814814-3, https://doi.org/10.1016/C2017-0-01969-9
82. Singh, A.; Rao, K.S.; Ayothiraman, R. An analytical solution to wellbore stability using Mogi-Coulomb failure criterion. *J. Rock Mech. Geotech. Eng.* **2019**, *11*(6), 1211–1230. https://doi.org/10.1016/j.jrmge.2019.03.004
83. Ma, T.; Zhang, Y.; Qiu, Y.; Liu, Y. Effect of parameter correlation on risk analysis of wellbore instability in deep igneous formations. *J. Pet. Sci. Eng.* **2022**, *208,* 109521. https://doi.org/10.1016/j.petrol.2021.109521
84. Xu, J.; Tian, Y.; Ma, P.; Rus, D.; Sueda, S.; Matusik, W. Prediction-guided multiobjective reinforcement learning for continuous robot control. In Proceedings of the International Conference on Machine Learning, Vienna, Austria, 13–18 July 2020.
85. Xu, K.; Liu, Z.; Chen, Q.; Zhang, Q.; Ling, X.; Cai, X.; He, Q.; Yang, M. Application of machine learning in wellbore stability prediction: A review. *Geoenergy Sci. Eng.* **2023**, 232, 212409. https://doi.org/10.1016/j.geoen.2023.212409
86. Ottesen, R.H.; Zheng, R.H.; McCann, R.C. Borehole stability assessment using quantitative risk analysis. In Proceedings of SPE/IADC Drilling Conference, Amsterdam, Netherland, 9 March 1999; Paper No. SPE- 52864-MS. https://doi.org/10.2118/52864-MS
87. Moos, D.; Peska, P.; Finkbeiner, T.; Zoback, M. Comprehensive wellbore stability analysis utilizing Quantitative Risk Assessment. *J. Pet. Sci. Eng.* **2003**, *38*(3–4), 97–109. https://doi.org/10.1016/S0920-4105(03)00024-X
88. Mostafavi, V.; Aadnoy, B.S.; Hareland, G. Model – based uncertainty assessment of wellbore stability analyses and downhole pressure estimations. In Proceedings of the 45th US Rock Mechanics/Geomechanics Symposium, San Francisco, California, USA, 26 June 2011; Paper No. ARMA-11-127.

89. Ostadhassan, M.; Jabbari, H.; Zamiran, S.; Osouli, A.; Bubach, B.; Oster, B. Probabilistic time-dependent thermo-chemo-poroelastic borehole stability analysis in shale formations. In Proceedings of the 49th US Rock Mechanics/Geomechanics Symposium, San Francisco, California, USA, 28 June 2015. Paper No. ARMA-2015-310
90. Gholami, R.; Rabiei, M.; Rasouli, V.; Aadnoy, B.; Fakhari, N. Application of quantitative risk assessment in wellbore stability analysis. *J. Pet. Sci. Eng.* **2015**, *135*, 185–200. https://doi.org/10.1016/j.petrol.2015.09.013
91. Gao, J.; Chen, F.; Zhao, Y.; Meng, M.; Peng, H.; Bian, G.; Huang, L. Quantitative risk analysis and parameter sensitivity evaluation of wellbore instability in poroelastic media considering uncertainty of geomechanical parameters. *Comput. Geotech.* **2024**, *170*, 106234. https://doi.org/10.1016/j.compgeo.2024.106234
92. Marshall, A.; Knight, M.; Duyvestyn, G. Laboratory investigation into surface movement due to near surface horizontal pressurized bores. In Proceedings of North American Society for Trenchless Technology No-Dig Conference, Nashville, Tennessee, USA, 25-28 March 2001.
93. Wang, X.; Sterling, R.L. Stability analysis of a borehole wall during horizontal directional drilling. *Tunn. Undergr. Space Technol.* **2007**, *22*(5-6), 620–632. https://doi.org/10.1016/j.tust.2007.01.002
94. Roylance, D. General stress analysis: closed-form solutions; Available online: https://web.mit.edu/course/3/3.11/www/modules/airy.pdf (accessed on 21 February 2001).
95. Yamamoto, K.; Shioya, Y.; Matsunaga, T.; Kikuchi, S.; Tantawi, I. A mechanical model of shale instability problems offshore Abu Dhabi. In Proceedings of Abu Dhabi International Petroleum Exhibition and Conference, Abu Dhabi, UAE, 13 October 2002. https://doi.org/10.2118/78494-MS
96. Lea, J.F.; Nickens, H.V. Solving gas-well liquid-loading problems. *J Pet Technol* **2004**, *56 (04)*, 30–36. https://doi.org/10.2118/72092-JPT
97. Bratli, R.K.; Horsrud, P.; Risnes, R. Rock mechanics applied to the region near a wellbore. In Proceedings of the Fifth International Congress on Rock Mechanics, Melbourne, Australia, 10 April 1983.
98. Al-Bazali, T.; Zhang, J.; Chenevert, M.E.; Sharma, M.M. Factors controlling the compressive strength and acoustic properties of shales when interacting with water-based fluids. *Int. J. Rock Mech. Min. Sci.* **2008**, *45*(5), 729–738. https://doi.org/10.1016/j.ijrmms.2007.08.012
99. Cheng, A. *Poroelasticity*; Springer: 2016; ISBN 978-3-319-25200-1, doi: 10.1007/978-3-319-25202-5.
100. Zhang, J.; Standifird, W.B.; Lenamond, C. Casing ultradeep, ultralong salt sections in deep water: a case study for failure diagnosis and risk mitigation in record-depth well. In Proceedings of the SPE Annual Technical Conference and Exhibition, Denver, Colorado, USA, September 2008. Doi: https://doi.org/10.2118/114273-MS
101. Zhang, J. Pore pressure prediction from well logs: methods, modifications, and new approaches. *Earth Science Reviews* **2011**, 108, 50–63. https://doi.org/10.1016/j.earscirev.2011.06.001

Nomenclature

Symbol	Description	Unit
A_1	First coefficient in Airy stress function for Kirsch's solution	-
A_2	Second coefficient in Airy stress function for Kirsch's solution	-
A_3	Third coefficient in Airy stress function for Kirsch's solution	-
A_4	Fourth coefficient in Airy stress function for Kirsch's solution	-
B	Skempton's coefficient	-
C	Rock's cohesion	Pa
C_0	Uniaxial compressive strength in Mohr-coulomb failure criterion	Pa
C_1	First coefficient in Laplace transform of poro-elastic deviatoric stress loading state	-
C_2	Second coefficient in Laplace transform of poro-elastic deviatoric stress loading state	-
C_3	Third coefficient in Laplace transform of poro-elastic deviatoric stress loading state	-
D_1	Factor related to modified Bessel function of the second kind of order 1	-
D_2	Factor related to modified Bessel function of the second kind of order 2	-
E	Drained Young's modulus of rock	Pa
E_u	Undrained Young's modulus of rock	Pa
FG_{max}	Maximum fracture gradient	Pa
G	Drained shear modulus	Pa
G_u	Undrained shear modulus	Pa
$H(t)$	Heaviside step function	-
K	Drained bulk modulus	Pa
K_{dry}	Dry bulk modulus	Pa
K_s	Mineral bulk modulus	Pa
K_u	Undrained bulk modulus	Pa
M	Biot modulus	Pa
P_0	Far-field mean compressive stress	Pa

P_c	Hydrostatic stress	Pa
R	Wellbore radius	m
S_0	Far-field deviatoric stress	Pa
S_x	Far-field normal in-situ stress in x direction	Pa
S_{xy}	Far-field shear in-situ stress in xy plane	Pa
S_{xz}	Far-field shear in-situ stress in xz plane	Pa
S_y	Far-field normal in-situ stress in y direction	Pa
S_{yz}	Far-field shear in-situ stress in yz plane	Pa
S_z	Far-field normal in-situ stress in z direction	Pa
S_z^1	Vertical stress component in segment I	Pa
S_z^2	Vertical stress component in segment II	Pa
$S_{x'}$	Far-field normal in-situ stress in x' direction	Pa
$S_{y'}$	Far-field normal in-situ stress in y' direction	Pa
$S_{z'}$	Far-field normal in-situ stress in z' direction	Pa
S_σ	Unconstrained specific storage coefficient of rock	Pa^{-1}
SF	Safety factor	-
T	Temperature	°C
V	Bulk volume of the rock	Pa
V_f	Volume of pore fluid	M^3
V_m	Initial volume of mineral(s) of the rock	M^3
V_p	Compressional wave velocity	m/s
V_s	Shear wave velocity	m/s
a_{11}	Coefficient relating the stress to volumetric strain in linear poro-elastic constitutive equation	Pa^{-1}
a_{12}	Coefficient relating the pore pressure to volumetric strain in linear poro-elastic constitutive equation	Pa^{-1}

a_{21}	Coefficient relating the stress to fluid content increment in linear poro-elastic constitutive equation	Pa^{-1}
a_{22}	Coefficient relating the pore pressure to fluid content increment in linear poro-elastic constitutive equation	Pa^{-1}
c	Generalized consolidation coefficient	-
$f(r)$	Function of r in Airy stress function	-
g	Gravitational acceleration	N/kg
i	Index	-
J	Index	-
k_0	Modified Bessel function pertinent to the second kind of order 0	-
k_1	Modified Bessel function pertinent to the second kind of order 1	-
k_2	Modified Bessel function pertinent to the second kind of order 2	-
k_n	Modified Bessel function pertinent to the second kind of order n	-
$l_{xx'}$	Trigonometric Parameter for stress transformation from $x'y'z'$ to xyz coordinate system	-
$l_{xy'}$	Trigonometric Parameter for stress transformation from $x'y'z'$ to xyz coordinate system	-
$l_{xz'}$	Trigonometric Parameter for stress transformation from $x'y'z'$ to xyz coordinate system	-
$l_{yx'}$	Trigonometric Parameter for stress transformation from $x'y'z'$ to xyz coordinate system	-
$l_{yy'}$	Trigonometric Parameter for stress transformation from $x'y'z'$ to xyz coordinate system	-
$l_{yz'}$	Trigonometric Parameter for stress transformation from $x'y'z'$ to xyz coordinate system	-
$l_{zx'}$	Trigonometric Parameter for stress transformation from $x'y'z'$ to xyz coordinate system	-
$l_{zy'}$	Trigonometric Parameter for stress transformation from $x'y'z'$ to xyz coordinate system	-
$l_{zz'}$	Trigonometric Parameter for stress transformation from $x'y'z'$ to xyz coordinate system	-
m_f	Mass of pore fluid	kg
p	Pore pressure	Pa
$p^{(I)}$	Pore pressure in segment I	Pa
$p^{(II)}$	Pore pressure in segment II	Pa
$p^{(III)}$	Pore pressure in segment III	Pa

$p^{(2)}$	Pore pressure in diffusion state	Pa
$p^{(3)}$	Pore pressure in poro-elastic deviatoric stress loading state	Pa
p_0	Pore pressure at reference state	Pa
$\tilde{p}^{(2)}$	Pore pressure in diffusion state obtained by Laplace transform	Pa
$\tilde{p}^3$	Pore pressure in poro-elastic deviatoric stress loading state obtained by Laplace transform	Pa
p_m	Mud pressure	Pa
q	Flow factor in Mohr-coulomb failure criterion	-
r	Distance from the wellbore center	Pa
s	Transform parameter in Laplace transform	-
t	Time after drilling commencement	s
xyz	Local wellbore coordinate system	-
$x'y'z'$	Cartesian far-field coordinate system	-
$x''y''z''$	Principal stress coordinate system	-
α	Biot's coefficient	-
β	Dependent parameter in Laplace transform	-
δ	Kronecker delta	-
δ_{ij}	Kronecker delta in ij direction	-
ζ	Increment of fluid content	-
η	Poro-elastic stress coefficient	Pa
θ	Polar angel	degree
θ_r	Rotation angle	degree
θ''	Polar angle in $x''y''z''$ coordinate system	degree
μ	Internal friction angle coefficient	-
ξ	Dependent parameter in Laplace transform	-
ρ	Rock's density	Kg/m^3
σ	Stress	Pa

σ_1	Maximum applied stress on the rock during triaxial compression test	Pa
σ_3	Minimum applied stress on the rock during triaxial compression test	Pa
σ_{11}	Axial stress applied on rock sample	Pa
σ_{22}	Lateral stress applied on rock sample	Pa
σ_{33}	Lateral stress applied on rock sample	Pa
σ_H	The highest horizontal in-situ stress	Pa
σ_h	The least horizontal in-situ stress	Pa
σ_{ij}	Total stress in *ij* direction	Pa
σ_n	Normal stress in Mohr-coulomb failure criterion	Pa
σ_r	Radial stress (Normal stress in radial direction)	Pa
σ_{rr}	Radial stress	Pa
$\sigma_{rr}^{(1)}$	Radial stress in Lame state	Pa
$\sigma_{rr}^{(2)}$	Radial stress in diffusion state	Pa
$\sigma_{rr}^{(3)}$	Radial stress in poro-elastic deviatoric stress loading state	Pa
$\sigma_{rr}^{(I)}$	Radial stress in segment *I*	Pa
$\sigma_{rr}^{(II)}$	Radial stress in segment *II*	Pa
$\sigma_{rr}^{(III)}$	Radial stress in segment *III*	Pa
σ_t	Tensile strength in Mohr-coulomb failure criterion	Pa
σ_θ	Tangential stress (Normal stress in circumferential direction)	Pa
$\sigma_{\theta\theta}$	Tangential stress	Pa
$\sigma_{\theta\theta}^{(1)}$	Tangential stress in Lame state	Pa
$\sigma_{\theta\theta}^{(2)}$	Tangential stress in diffusion state	Pa
$\sigma_{\theta\theta}^{(3)}$	Tangential stress in poro-elastic deviatoric stress loading state	Pa
$\sigma_{\theta\theta}^{(I)}$	Tangential stress in segment *I*	Pa
$\sigma_{\theta\theta}^{(II)}$	Tangential stress in segment *II*	Pa
$\sigma_{\theta\theta}^{(III)}$	Tangential stress in segment I*II*	Pa

σ_x	In-situ normal stress component rotated to the wellbore coordinate system	Pa
σ_y	In-situ normal stress component rotated to the wellbore coordinate system	Pa
σ_z	Vertical stress in polar coordinate system	Pa
σ_{zz}	In-situ normal stress component rotated to the wellbore coordinate system	Pa
$\sigma_{zz}^{(I)}$	Vertical stress in segment *I*	Pa
$\sigma_{zz}^{(II)}$	Vertical stress in segment *II*	Pa
$\sigma_{zz}^{(III)}$	Vertical stress in segment *III*	Pa
σ_v	Vertical principal stress	Pa
σ'_{ij}	Effective stress in ij direction	Pa
σ'_r	Effective radial stress (Normal stress in radial direction)	Pa
σ'_θ	Effective tangential stress (Normal stress in tangential direction)	Pa
σ'_z	Effective vertical stress in polar coordinate system	Pa
$\acute{\sigma}$	Effective stress	Pa
$\sigma_{\theta_{max}}$	Maximum tangential stress at wellbore wall	Pa
$\sigma_{\theta_{min}}$	Minimum tangential stress at wellbore wall	Pa
$\sigma'_{\theta_{max}}$	Maximum tangential effective stress at wellbore wall	Pa
$\sigma'_{\theta_{min}}$	Minimum tangential effective stress at wellbore wall	Pa
$\tilde{\sigma}_{rr}^{(2)}$	Radial stress in diffusion state obtained by Laplace transform	Pa
$\tilde{\sigma}_{rr}^{(3)}$	Radial stress in poro-elastic deviatoric stress loading state obtained by Laplace transform	Pa
$\tilde{\sigma}_{\theta\theta}^{(2)}$	Tangential stress in diffusion state obtained by Laplace transform	Pa
$\tilde{\sigma}_{\theta\theta}^{(3)}$	Tangential stress in poro-elastic deviatoric stress loading state obtained by Laplace transform	Pa
$\sigma_{x''x''}$	Far-field normal stress at $r\to\infty$ in x''direction	Pa
$\sigma_{x''y''}$	Far-field shear stress at $r\to\infty$ in $x''y''$plane	Pa
$\sigma_{y''y''}$	Far-field normal stress at $r\to\infty$ in y''direction	Pa
κ	Permeability coefficient	-
ρ_f	Pore fluid density	Kg/m^3

ρ_{f_0}	Pore fluid density in the reference state	Kg/m³
φ	Rock's porosity	-
φ_x	The angle between x' axis and x axis	degree
φ_z	The angle between z' axis and z axis	degree
ϕ	Internal friction angle of rock	degree
ϵ	Volumetric strain	-
ϵ_{11}	Axial strain	-
ϵ_{22}	Lateral strain	-
ϵ_{xy}	Shear strain in the direction of rock cross-sectional area	Pa
τ	Shear stress acting on the rock	Pa
τ_u	Rock's shear strength	Pa
$\tau_{r\theta}$	Shear stress in $r\theta$ plane	Pa
$\tau_{r\theta}^{(I)}$	Shear stress in $r\theta$ plane related to segment *I*	Pa
$\tau_{r\theta}^{(II)}$	Shear stress in $r\theta$ plane related to segment *II*	Pa
$\tau_{r\theta}^{(III)}$	Shear stress in $r\theta$ plane related to segment *III*	Pa
$\tau_{r\theta}^{(3)}$	Shear stress in poro-elastic deviatoric stress loading state	Pa
τ_{rz}	Shear stress in rz plane	Pa
$\tau_{rz}^{(I)}$	Shear stress in rz plane related to segment *I*	Pa
$\tau_{rz}^{(II)}$	Shear stress in rz plane related to segment *II*	Pa
$\tau_{rz}^{(III)}$	Shear stress in rz plane related to segment *III*	Pa
τ_{xy}	Shear stress in xy plane (in wellbore coordinate system)	Pa
τ_{xz}	Shear stress in xz plane (in wellbore coordinate system)	Pa
τ_{yz}	Shear stress in yz plane (in wellbore coordinate system)	Pa
$\tau_{\theta z}$	Shear stress in θz plane	Pa
$\tau_{\theta z}^{(I)}$	Shear stress in θz plane related to segment *I*	Pa
$\tau_{\theta z}^{(II)}$	Shear stress in θz plane related to segment *II*	Pa

$\tau_{\theta z}^{(III)}$	Shear stress in θz plane related to segment III	Pa
$\tilde{\tau}_{r\theta}^{(3)}$	Shear stress in poro-elastic deviatoric stress loading state obtained by Laplace transform	Pa
$\Psi(r,\theta)$	Stress function	-
υ	Drained Poisson's ratio	-
υ_u	Undrained Poisson's ratio	-
$\frac{1}{K}$	Drained compressibility of rock	Pa^{-1}
$\frac{1}{H}$	Poro-elastic expansion coefficient of rock	Pa^{-1}
$\frac{1}{R'}$	Unconstrained specific storage coefficient	Pa^{-1}

Appendix 1 and 2

Appendix 1: AVS tests under undrained loading condition.

Sample 1

Interval number	Hydrostatic stress (MPa)	Pore pressure (MPa)	Time of flight (μs)			Wave speed (m/s)			v_u	E_u (GPa)	K_u (GPa)	G_u (GPa)
			P-wave	S1-wave	S2 -Wave	P-wave	S1-wave	S2-wave				
1	3.5	3.5	32.4	66.0	66.0	3694	1419	1419	0.413	14.15	27.22	5.00
2	7.0	7.0	32.2	65.8	65.8	3761	1429	1429	0.416	14.37	28.38	5.07
3	10.6	10.5	32.0	65.6	65.6	3832	1439	1439	0.418	14.59	29.61	5.15
4	14.1	14.0	31.8	65.4	65.4	3905	1449	1449	0.420	14.82	30.92	5.22
5	17.8	17.5	31.6	65.4	65.4	3981	1449	1449	0.424	14.86	32.40	5.22
6	20.9	20.5	31.4	65.2	65.2	4059	1460	1460	0.426	15.09	33.88	5.29
7	24.1	23.6	31.4	65.2	65.2	4059	1460	1460	0.426	15.09	33.88	5.29
8	27.7	26.9	31.4	65.2	65.2	4059	1460	1460	0.426	15.09	33.88	5.29
9	31.1	30.1	31.4	65.2	65.2	4059	1460	1460	0.426	15.09	33.88	5.29
10	34.6	33.5	31.4	65.2	65.2	4059	1460	1460	0.426	15.09	33.88	5.29
11	38.0	36.6	31.4	65.2	65.2	4059	1460	1460	0.426	15.09	33.88	5.29
12	41.5	39.9	31.4	65.2	65.2	4059	1460	1460	0.426	15.09	33.88	5.29

Sample 2

Interval number	Hydrostatic stress (MPa)	Pore pressure (MPa)	Time of flight (μs)			Wave speed (m/s)			v_u	E_u (GPa)	K_u (GPa)	G_u (GPa)
			P-wave	S1-wave	S2 -Wave	P-wave	S1-wave	S2-wave				
1	3.5	3.2	32.4	66.0	66.0	3829	1471	1471	0.413	15.19	29.23	5.37
2	6.9	6.4	32.4	65.8	65.8	3829	1482	1482	0.412	15.39	29.13	5.45
3	10.4	9.7	32.2	65.8	65.8	3899	1482	1482	0.416	15.43	30.48	5.45
4	13.9	12.9	32.0	65.6	65.6	3972	1492	1492	0.418	15.67	31.80	5.53
5	17.7	16.4	32.0	65.4	65.4	3972	1502	1502	0.417	15.88	31.70	5.61
6	20.7	19.1	32.0	65.0	65.0	3972	1524	1524	0.414	16.31	31.48	5.77
7	24.1	22.2	32.0	65.0	65.0	3972	1524	1524	0.414	16.31	31.48	5.77
8	27.7	25.3	32.0	65.0	65.0	3972	1524	1524	0.414	16.31	31.48	5.77
9	31.1	28.4	32.0	65.0	65.0	3972	1524	1524	0.414	16.31	31.48	5.77
10	34.7	31.5	32.0	65.0	65.0	3972	1524	1524	0.414	16.31	31.48	5.77
11	38.3	34.7	32.0	65.0	65.0	3972	1524	1524	0.414	16.31	31.48	5.77
12	41.7	37.5	32.0	65.0	65.0	3972	1524	1524	0.414	16.31	31.48	5.77

Appendix 1: AVS tests under undrained loading condition.

Sample3

Interval number	Hydrostatic stress (MPa)	Pore pressure (MPa)	Time of flight (μs)			Wave speed (m/s)			v_u	E_u (GPa)	K_u (GPa)	G_u (GPa)
			P-wave	S1-wave	S2 -Wave	P-wave	S1-wave	S2-wave				
1	3.5	3.4	32.6	66.4	66.4	3540	1366	1366	0.413	13.36	25.47	4.73
2	6.9	6.9	32.4	66.0	66.0	3604	1385	1385	0.413	13.74	26.45	4.86
3	10.3	10.1	32.0	65.8	65.8	3738	1394	1394	0.419	13.99	28.86	4.93
4	13.8	13.5	31.8	65.6	65.6	3810	1404	1404	0.421	14.21	30.13	5.00
5	17.2	16.9	31.4	65.4	65.4	3960	1414	1414	0.427	14.47	33.01	5.07
6	20.8	20.4	31.2	65.2	65.2	4040	1424	1424	0.429	14.70	34.54	5.14
7	24.2	23.7	31.2	65.2	65.2	4040	1424	1424	0.429	14.70	34.54	5.14
8	27.7	27.1	31.2	65.2	65.2	4040	1424	1424	0.429	14.70	34.54	5.14
9	31.2	30.5	31.2	65.2	65.2	4040	1424	1424	0.429	14.70	34.54	5.14
10	34.6	33.7	31.2	65.2	65.2	4040	1424	1424	0.429	14.70	34.54	5.14
11	38.2	37.1	31.2	65.2	65.2	4040	1424	1424	0.429	14.70	34.54	5.14
12	41.5	40.2	31.2	65.2	65.2	4040	1424	1424	0.429	14.70	34.54	5.14

Sample 4

Interval number	Hydrostatic stress (MPa)	Pore pressure (MPa)	Time of flight (μs)			Wave speed (m/s)			v_u	E_u (GPa)	K_u (GPa)	G_u (GPa)
			P-wave	S1-wave	S2 -Wave	P-wave	S1-wave	S2-wave				
1	3.5	3.5	32.2	66.2	66.2	3807	1427	1427	0.418	14.62	29.82	5.15
2	7.0	7.0	32.0	66.0	66.0	3879	1437	1437	0.420	14.84	31.11	5.22
3	10.6	10.5	31.8	65.8	65.8	3952	1447	1447	0.423	15.07	32.48	5.30
4	14.1	14.0	31.6	65.4	65.4	4029	1467	1467	0.424	15.51	33.83	5.45
5	17.8	17.5	31.4	65.4	65.4	4109	1467	1467	0.427	15.55	35.47	5.45
6	20.9	20.5	31.2	65.2	65.2	4192	1478	1478	0.429	15.79	37.11	5.53
7	24.2	23.6	31.2	65.2	65.2	4192	1478	1478	0.429	15.79	37.11	5.53
8	27.8	27.0	31.2	65.2	65.2	4192	1478	1478	0.429	15.79	37.11	5.53
9	31.2	30.2	31.2	65.2	65.2	4192	1478	1478	0.429	15.79	37.11	5.53
10	34.6	33.4	31.2	65.2	65.2	4192	1478	1478	0.429	15.79	37.11	5.53
11	38.3	36.9	31.2	65.2	65.2	4192	1478	1478	0.429	15.79	37.11	5.53
12	41.5	39.9	31.2	65.2	65.2	4192	1478	1478	0.429	15.79	37.11	5.53

Appendix 1: AVS tests under undrained loading condition.

Sample 5

Interval number	Hydrostatic stress (MPa)	Pore pressure (MPa)	Time of flight (µs)			Wave speed (m/s)			v_u	E_u (GPa)	K_u (GPa)	G_u (GPa)
			P-wave	S1-wave	S2 -Wave	P-wave	S1-wave	S2-wave				
1	3.4	3.4	32.6	66.2	66.2	3761	1461	1461	0.411	14.94	28.01	5.29
2	6.9	6.8	32.4	66.0	66.0	3829	1471	1471	0.413	15.17	29.19	5.37
3	10.4	10.2	32.2	65.8	65.8	3899	1482	1482	0.416	15.40	30.43	5.44
4	13.9	13.6	32.0	65.6	65.6	3972	1492	1492	0.418	15.65	31.75	5.52
5	17.7	17.3	32.0	65.4	65.4	3972	1502	1502	0.417	15.85	31.65	5.60
6	20.8	20.3	31.8	65.2	65.2	4048	1513	1513	0.419	16.11	33.04	5.68
7	24.3	23.8	31.8	65.2	65.2	4048	1513	1513	0.419	16.11	33.04	5.68
8	27.6	27.1	31.8	65.2	65.2	4048	1513	1513	0.419	16.11	33.04	5.68
9	31.2	30.5	31.8	65.2	65.2	4048	1513	1513	0.419	16.11	33.04	5.68
10	34.6	33.8	31.8	65.2	65.2	4048	1513	1513	0.419	16.11	33.04	5.68
11	38.2	37.2	31.8	65.2	65.2	4048	1513	1513	0.419	16.11	33.04	5.68
12	41.9	40.7	31.8	65.2	65.2	4048	1513	1513	0.419	16.11	33.04	5.68

Sample 6

Interval number	Hydrostatic stress (MPa)	Pore pressure (MPa)	Time of flight (µs)			Wave speed (m/s)			v_u	E_u (GPa)	K_u (GPa)	G_u (GPa)
			P-wave	S1-wave	S2 -Wave	P-wave	S1-wave	S2-wave				
1	3.5	3.2	32.4	66.2	66.2	3649	1392	1392	0.415	14.19	27.75	5.01
2	6.9	6.4	32.0	66.0	66.0	3785	1402	1402	0.420	14.44	30.27	5.08
3	10.4	9.7	31.8	65.8	65.8	3857	1412	1412	0.423	14.67	31.61	5.15
4	13.9	12.9	31.6	65.6	65.6	3932	1422	1422	0.425	14.90	33.02	5.23
5	17.7	16.4	31.4	65.4	65.4	4010	1432	1432	0.427	15.13	34.52	5.30
6	20.7	19.1	31.0	65.2	65.2	4175	1442	1442	0.432	15.40	37.92	5.38
7	24.1	22.2	31.0	65.2	65.2	4175	1442	1442	0.432	15.40	37.92	5.38
8	27.7	25.4	31.0	65.2	65.2	4175	1442	1442	0.432	15.40	37.92	5.38
9	31.3	28.6	31.0	65.2	65.2	4175	1442	1442	0.432	15.40	37.92	5.38
10	34.6	31.6	31.0	65.2	65.2	4175	1442	1442	0.432	15.40	37.92	5.38
11	38.2	34.8	31.0	65.2	65.2	4175	1442	1442	0.432	15.40	37.92	5.38
12	41.5	37.6	31.0	65.2	65.2	4175	1442	1442	0.432	15.40	37.92	5.38

Appendix 1: AVS tests under undrained loading condition.

Sample 7

Interval number	Hydrostatic stress (MPa)	Pore pressure (MPa)	Time of flight (µs)			Wave speed (m/s)			v_u	E_u (GPa)	K_u (GPa)	G_u (GPa)
			P-wave	S1-wave	S2 -Wave	P-wave	S1-wave	S2-wave				
1	3.6	3.6	32.6	66.4	66.4	3540	1366	1366	0.413	13.37	25.48	4.73
2	7.1	7.0	32.4	66.0	66.0	3604	1385	1385	0.413	13.75	26.46	4.87
3	10.4	10.3	32.4	66.0	66.0	3604	1385	1385	0.413	13.75	26.46	4.87
4	14.0	13.8	32.2	65.8	65.8	3670	1394	1394	0.416	13.97	27.59	4.93
5	17.2	16.9	32.0	65.6	65.6	3738	1404	1404	0.418	14.19	28.79	5.00
6	20.8	20.3	31.6	65.2	65.2	3883	1424	1424	0.422	14.64	31.41	5.15
7	24.2	23.6	31.6	65.2	65.2	3883	1424	1424	0.422	14.64	31.41	5.15
8	27.7	26.9	31.6	65.2	65.2	3883	1424	1424	0.422	14.64	31.41	5.15
9	31.4	30.4	31.6	65.2	65.2	3883	1424	1424	0.422	14.64	31.41	5.15
10	34.6	33.4	31.6	65.2	65.2	3883	1424	1424	0.422	14.64	31.41	5.15
11	38.1	36.6	31.6	65.2	65.2	3883	1424	1424	0.422	14.64	31.41	5.15
12	41.6	39.9	31.6	65.2	65.2	3883	1424	1424	0.422	14.64	31.41	5.15

Sample 8

Interval number	Hydrostatic stress (MPa)	Pore pressure (MPa)	Time of flight (µs)			Wave speed (m/s)			v_u	E_u (GPa)	K_u (GPa)	G_u (GPa)
			P-wave	S1-wave	S2 -Wave	P-wave	S1-wave	S2-wave				
1	3.5	3.4	32.4	66.2	66.2	3739	1427	1427	0.415	14.22	27.82	5.03
2	7.0	6.9	32.4	66.0	66.0	3739	1437	1437	0.413	14.41	27.72	5.10
3	10.5	10.4	32.2	65.8	65.8	3807	1447	1447	0.416	14.63	28.91	5.17
4	14.1	13.9	32.0	65.6	65.6	3879	1457	1457	0.418	14.86	30.16	5.24
5	17.7	17.4	31.8	65.6	65.6	3952	1457	1457	0.421	14.90	31.59	5.24
6	20.8	20.4	31.8	65.4	65.4	3952	1467	1467	0.420	15.10	31.49	5.32
7	24.2	23.6	31.8	65.4	65.4	3952	1467	1467	0.420	15.10	31.49	5.32
8	27.7	26.9	31.8	65.4	65.4	3952	1467	1467	0.420	15.10	31.49	5.32
9	31.1	30.2	31.8	65.4	65.4	3952	1467	1467	0.420	15.10	31.49	5.32
10	34.7	33.6	31.8	65.4	65.4	3952	1467	1467	0.420	15.10	31.49	5.32
11	38.3	37.0	31.8	65.4	65.4	3952	1467	1467	0.420	15.10	31.49	5.32
12	41.5	39.9	31.8	65.4	65.4	3952	1467	1467	0.420	15.10	31.49	5.32

Appendix 1: AVS tests under undrained loading condition.

Sample 9

Interval number	Hydrostatic stress (MPa)	Pore pressure (MPa)	Time of flight (µs)			Wave speed (m/s)			v_u	E_u (GPa)	K_u (GPa)	G_u (GPa)
			P-wave	S1-wave	S2 -Wave	P-wave	S1-wave	S2-wave				
1	3.4	3.1	32.4	66.0	66.0	3694	1419	1419	0.413	14.05	27.03	4.97
2	6.9	6.4	32.4	65.8	65.8	3694	1429	1429	0.412	14.23	26.94	5.04
3	10.4	9.7	32.2	65.8	65.8	3761	1429	1429	0.416	14.27	28.19	5.04
4	13.9	12.9	32.0	65.6	65.6	3832	1439	1439	0.418	14.49	29.41	5.11
5	17.7	16.3	32.0	65.4	65.4	3832	1449	1449	0.417	14.68	29.31	5.18
6	20.8	19.1	32.0	65.0	65.0	3832	1470	1470	0.414	15.08	29.11	5.33
7	24.1	22.1	32.0	65.0	65.0	3832	1470	1470	0.414	15.08	29.11	5.33
8	27.7	25.3	32.0	65.0	65.0	3832	1470	1470	0.414	15.08	29.11	5.33
9	31.1	28.4	32.0	65.0	65.0	3832	1470	1470	0.414	15.08	29.11	5.33
10	34.7	31.5	32.0	65.0	65.0	3832	1470	1470	0.414	15.08	29.11	5.33
11	38.1	34.5	32.0	65.0	65.0	3832	1470	1470	0.414	15.08	29.11	5.33
12	41.5	37.4	32.0	65.0	65.0	3832	1470	1470	0.414	15.08	29.11	5.33

Sample 10

Interval number	Hydrostatic stress (MPa)	Pore pressure (MPa)	Time of flight (µs)			Wave speed (m/s)			v_u	E_u (GPa)	K_u (GPa)	G_u (GPa)
			P-wave	S1-wave	S2 -Wave	P-wave	S1-wave	S2-wave				
1	3.5	3.5	32.2	66.0	66.0	3761	1419	1419	0.417	14.37	28.85	5.07
2	7.0	7.0	32.0	65.8	65.8	3832	1429	1429	0.419	14.59	30.10	5.14
3	10.6	10.5	31.8	65.6	65.6	3905	1439	1439	0.421	14.82	31.43	5.21
4	14.1	14.0	31.6	65.4	65.4	3981	1449	1449	0.424	15.06	32.83	5.29
5	17.8	17.4	31.4	65.4	65.4	4059	1449	1449	0.427	15.09	34.43	5.29
6	20.9	20.5	31.2	65.2	65.2	4141	1460	1460	0.429	15.33	36.02	5.36
7	24.1	23.7	31.2	65.2	65.2	4141	1460	1460	0.429	15.33	36.02	5.36
8	27.7	27.1	31.2	65.2	65.2	4141	1460	1460	0.429	15.33	36.02	5.36
9	31.2	30.5	31.2	65.2	65.2	4141	1460	1460	0.429	15.33	36.02	5.36
10	34.5	33.6	31.2	65.2	65.2	4141	1460	1460	0.429	15.33	36.02	5.36
11	37.9	36.8	31.2	65.2	65.2	4141	1460	1460	0.429	15.33	36.02	5.36
12	41.5	40.2	31.2	65.2	65.2	4141	1460	1460	0.429	15.33	36.02	5.36

Appendix 1: AVS tests under undrained loading condition.

Sample 11

Interval number	Hydrostatic stress (MPa)	Pore pressure (MPa)	Time of flight (µs)			Wave speed (m/s)			v_u	E_u (GPa)	K_u (GPa)	G_u (GPa)
			P-wave	S1-wave	S2 -Wave	P-wave	S1-wave	S2-wave				
1	3.5	3.5	32.2	66.0	66.0	3670	1385	1385	0.417	13.83	27.78	4.88
2	7.0	7.0	32.0	65.8	65.8	3738	1394	1394	0.419	14.05	28.98	4.95
3	10.5	10.5	31.8	65.6	65.6	3810	1404	1404	0.421	14.27	30.26	5.02
4	14.1	14.0	31.6	65.4	65.4	3883	1414	1414	0.424	14.50	31.61	5.09
5	17.7	17.4	31.4	65.4	65.4	3960	1414	1414	0.427	14.53	33.15	5.09
6	20.8	20.5	31.2	65.2	65.2	4040	1424	1424	0.429	14.76	34.68	5.16
7	24.1	23.6	31.2	65.2	65.2	4040	1424	1424	0.429	14.76	34.68	5.16
8	27.7	27.1	31.2	65.2	65.2	4040	1424	1424	0.429	14.76	34.68	5.16
9	31.1	30.4	31.2	65.2	65.2	4040	1424	1424	0.429	14.76	34.68	5.16
10	34.6	33.7	31.2	65.2	65.2	4040	1424	1424	0.429	14.76	34.68	5.16
11	38.2	37.1	31.2	65.2	65.2	4040	1424	1424	0.429	14.76	34.68	5.16
12	41.5	40.2	31.2	65.2	65.2	4040	1424	1424	0.429	14.76	34.68	5.16

Sample 12

Interval number	Hydrostatic stress (MPa)	Pore pressure (MPa)	Time of flight (µs)			Wave speed (m/s)			v_u	E_u (GPa)	K_u (GPa)	G_u (GPa)
			P-wave	S1-wave	S2 -Wave	P-wave	S1-wave	S2-wave				
1	3.5	3.4	32.6	66.4	66.2	3628	1400	1410	0.412	14.25	26.93	5.05
2	7.0	6.9	32.4	66.0	66.0	3694	1419	1419	0.413	14.56	28.02	5.15
3	10.5	10.3	32.2	65.8	65.8	3761	1429	1429	0.416	14.79	29.21	5.22
4	13.9	13.7	32.0	65.6	65.6	3832	1439	1439	0.418	15.02	30.48	5.30
5	17.5	17.2	31.8	65.6	65.6	3905	1439	1439	0.421	15.06	31.93	5.30
6	20.8	20.4	31.6	65.2	65.4	3981	1460	1449	0.423	15.40	33.30	5.41
7	24.2	23.7	31.6	65.2	65.4	3981	1460	1449	0.423	15.40	33.30	5.41
8	27.7	27.1	31.6	65.2	65.4	3981	1460	1449	0.423	15.40	33.30	5.41
9	31.3	30.6	31.6	65.2	65.4	3981	1460	1449	0.423	15.40	33.30	5.41
10	34.6	33.8	31.6	65.2	65.4	3981	1460	1449	0.423	15.40	33.30	5.41
11	38.0	37.0	31.6	65.2	65.4	3981	1460	1449	0.423	15.40	33.30	5.41
12	41.6	40.4	31.6	65.2	65.4	3981	1460	1449	0.423	15.40	33.30	5.41

Appendix 1: AVS tests under undrained loading condition.

Sample 13

Interval number	Hydrostatic stress (MPa)	Pore pressure (MPa)	Time of flight (µs)			Wave speed (m/s)			v_u	E_u (GPa)	K_u (GPa)	G_u (GPa)
			P-wave	S1-wave	S2 -Wave	P-wave	S1-wave	S2-wave				
1	3.5	3.4	32.0	65.0	65.0	3551	1363	1363	0.414	13.21	25.51	4.67
2	7.0	6.8	32.0	64.8	64.8	3551	1372	1372	0.412	13.39	25.42	4.74
3	10.5	10.3	31.8	64.8	64.8	3619	1372	1372	0.416	13.43	26.64	4.74
4	14.1	13.8	31.6	64.6	64.6	3689	1382	1382	0.418	13.64	27.84	4.81
5	17.3	17.0	31.6	64.4	64.4	3689	1393	1393	0.417	13.83	27.75	4.88
6	21.0	20.5	31.6	64.0	64.0	3689	1413	1413	0.414	14.22	27.55	5.03
7	24.2	23.5	31.6	64.0	64.0	3689	1413	1413	0.414	14.22	27.55	5.03
8	27.6	26.7	31.6	64.0	64.0	3689	1413	1413	0.414	14.22	27.55	5.03
9	31.0	29.9	31.6	64.0	64.0	3689	1413	1413	0.414	14.22	27.55	5.03
10	34.6	33.2	31.6	64.0	64.0	3689	1413	1413	0.414	14.22	27.55	5.03
11	38.1	36.4	31.6	64.0	64.0	3689	1413	1413	0.414	14.22	27.55	5.03
12	41.4	39.5	31.6	64.0	64.0	3689	1413	1413	0.414	14.22	27.55	5.03

Sample 14

Interval number	Hydrostatic stress (MPa)	Pore pressure (MPa)	Time of flight (µs)			Wave speed (m/s)			v_u	E_u (GPa)	K_u (GPa)	G_u (GPa)
			P-wave	S1-wave	S2 -Wave	P-wave	S1-wave	S2-wave				
1	3.5	3.5	32.6	66.2	66.2	3584	1392	1392	0.411	13.90	26.06	4.92
2	6.9	6.9	32.4	66.0	66.0	3649	1402	1402	0.413	14.11	27.16	4.99
3	10.4	10.1	32.2	65.8	65.8	3716	1412	1412	0.416	14.33	28.32	5.06
4	13.8	13.5	31.8	65.6	65.6	3857	1422	1422	0.421	14.60	30.95	5.13
5	17.3	16.9	31.4	65.4	65.4	4010	1432	1432	0.427	14.86	33.90	5.21
6	20.8	20.4	31.2	65.0	65.0	4091	1452	1452	0.428	15.30	35.37	5.36
7	24.1	23.6	31.2	65.0	65.0	4091	1452	1452	0.428	15.30	35.37	5.36
8	27.7	27.1	31.2	65.0	65.0	4091	1452	1452	0.428	15.30	35.37	5.36
9	31.3	30.5	31.2	65.0	65.0	4091	1452	1452	0.428	15.30	35.37	5.36
10	34.5	33.6	31.2	65.0	65.0	4091	1452	1452	0.428	15.30	35.37	5.36
11	37.9	36.8	31.2	65.0	65.0	4091	1452	1452	0.428	15.30	35.37	5.36
12	41.6	40.2	31.2	65.0	65.0	4091	1452	1452	0.428	15.30	35.37	5.36

Appendix 1: AVS tests under undrained loading condition.

Sample 15

Interval number	Hydrostatic stress (MPa)	Pore pressure (MPa)	Time of flight (µs)			Wave speed (m/s)			v_u	E_u (GPa)	K_u (GPa)	G_u (GPa)
			P-wave	S1-wave	S2 -Wave	P-wave	S1-wave	S2-wave				
1	3.5	3.5	32.8	66.4	66.4	3783	1485	1485	0.409	15.71	28.73	5.58
2	7.0	6.9	32.6	66.2	66.2	3850	1496	1496	0.411	15.95	29.92	5.65
3	10.5	10.3	32.6	66.2	66.2	3850	1496	1496	0.411	15.95	29.92	5.65
4	13.9	13.6	32.4	66.0	66.0	3919	1506	1506	0.413	16.20	31.17	5.73
5	16.9	16.5	32.4	65.8	65.8	3919	1516	1516	0.412	16.41	31.07	5.81
6	20.8	20.2	32.4	65.4	65.4	3919	1538	1538	0.409	16.84	30.85	5.98
7	24.3	23.5	32.4	65.4	65.4	3919	1538	1538	0.409	16.84	30.85	5.98
8	27.8	26.8	32.4	65.4	65.4	3919	1538	1538	0.409	16.84	30.85	5.98
9	31.0	29.9	32.4	65.4	65.4	3919	1538	1538	0.409	16.84	30.85	5.98
10	34.8	33.4	32.4	65.4	65.4	3919	1538	1538	0.409	16.84	30.85	5.98
11	37.9	36.4	32.4	65.4	65.4	3919	1538	1538	0.409	16.84	30.85	5.98
12	41.4	39.6	32.4	65.4	65.4	3919	1538	1538	0.409	16.84	30.85	5.98

Sample 16

Interval number	Hydrostatic stress (MPa)	Pore pressure (MPa)	Time of flight (µs)			Wave speed (m/s)			v_u	E_u (GPa)	K_u (GPa)	G_u (GPa)
			P-wave	S1-wave	S2 -Wave	P-wave	S1-wave	S2-wave				
1	3.5	3.4	32.8	66.4	66.4	3739	1468	1468	0.409	15.36	28.09	5.45
2	7.0	6.9	32.4	66.2	66.2	3874	1478	1478	0.415	15.64	30.58	5.53
3	10.5	10.3	32.2	66.0	66.0	3945	1489	1489	0.417	15.88	31.88	5.60
4	13.9	13.6	32.0	65.6	65.6	4019	1509	1509	0.418	16.34	33.16	5.76
5	17.7	17.4	31.8	65.4	65.4	4095	1520	1520	0.420	16.60	34.62	5.84
6	20.8	20.4	31.6	65.2	65.2	4175	1531	1531	0.422	16.86	36.17	5.93
7	24.2	23.6	31.6	65.2	65.2	4175	1531	1531	0.422	16.86	36.17	5.93
8	27.7	27.0	31.6	65.2	65.2	4175	1531	1531	0.422	16.86	36.17	5.93
9	31.1	30.3	31.6	65.2	65.2	4175	1531	1531	0.422	16.86	36.17	5.93
10	34.7	33.7	31.6	65.2	65.2	4175	1531	1531	0.422	16.86	36.17	5.93
11	38.0	36.9	31.6	65.2	65.2	4175	1531	1531	0.422	16.86	36.17	5.93
12	41.6	40.2	31.6	65.2	65.2	4175	1531	1531	0.422	16.86	36.17	5.93

Appendix 1: AVS tests under undrained loading condition.

Sample 17

Interval number	Hydrostatic stress (MPa)	Pore pressure (MPa)	Time of flight (µs)			Wave speed (m/s)			v_u	E_u (GPa)	K_u (GPa)	G_u (GPa)
			P-wave	S1-wave	S2 -Wave	P-wave	S1-wave	S2-wave				
1	3.5	3.5	32.6	66.2	66.2	3938	1530	1530	0.411	16.73	31.36	5.93
2	6.9	6.9	32.4	66.2	66.2	4009	1530	1530	0.415	16.77	32.79	5.93
3	10.4	10.2	32.2	65.8	65.8	4083	1551	1551	0.416	17.25	34.08	6.09
4	13.8	13.5	32.0	65.6	65.6	4159	1562	1562	0.418	17.52	35.56	6.18
5	17.3	16.9	31.8	65.4	65.4	4238	1573	1573	0.420	17.80	37.12	6.27
6	20.8	20.4	31.4	65.2	65.2	4406	1584	1584	0.426	18.12	40.68	6.36
7	24.1	23.7	31.4	65.2	65.2	4406	1584	1584	0.426	18.12	40.68	6.36
8	27.7	27.1	31.4	65.2	65.2	4406	1584	1584	0.426	18.12	40.68	6.36
9	31.1	30.4	31.4	65.2	65.2	4406	1584	1584	0.426	18.12	40.68	6.36
10	34.6	33.7	31.4	65.2	65.2	4406	1584	1584	0.426	18.12	40.68	6.36
11	38.1	37.1	31.4	65.2	65.2	4406	1584	1584	0.426	18.12	40.68	6.36
12	41.5	40.2	31.4	65.2	65.2	4406	1584	1584	0.426	18.12	40.68	6.36

Sample 18

Interval number	Hydrostatic stress (MPa)	Pore pressure (MPa)	Time of flight (µs)			Wave speed (m/s)			v_u	E_u (GPa)	K_u (GPa)	G_u (GPa)
			P-wave	S1-wave	S2 -Wave	P-wave	S1-wave	S2-wave				
1	3.5	3.4	32.6	66.6	66.6	4071	1560	1560	0.414	17.44	33.78	6.17
2	6.9	6.8	32.4	66.4	66.4	4144	1571	1571	0.416	17.71	35.20	6.25
3	10.3	10.2	32.2	66.0	66.0	4220	1592	1592	0.417	18.22	36.58	6.43
4	13.9	13.6	31.8	65.8	65.8	4381	1604	1604	0.423	18.55	39.96	6.52
5	17.3	16.9	31.8	65.6	65.6	4381	1615	1615	0.421	18.79	39.84	6.61
6	20.8	20.3	31.4	65.4	65.4	4554	1626	1626	0.427	19.13	43.64	6.70
7	24.1	23.4	31.4	65.4	65.4	4554	1626	1626	0.427	19.13	43.64	6.70
8	27.7	26.8	31.4	65.4	65.4	4554	1626	1626	0.427	19.13	43.64	6.70
9	31.1	29.9	31.4	65.4	65.4	4554	1626	1626	0.427	19.13	43.64	6.70
10	34.6	33.2	31.4	65.4	65.4	4554	1626	1626	0.427	19.13	43.64	6.70
11	38.2	36.6	31.4	65.4	65.4	4554	1626	1626	0.427	19.13	43.64	6.70
12	41.6	39.7	31.4	65.4	65.4	4554	1626	1626	0.427	19.13	43.64	6.70

Appendix 1: AVS tests under undrained loading condition.

Sample 19

Interval number	Hydrostatic stress (MPa)	Pore pressure (MPa)	Time of flight (μs)			Wave speed (m/s)			v_u	E_u (GPa)	K_u (GPa)	G_u (GPa)
			P-wave	S1-wave	S2 -Wave	P-wave	S1-wave	S2-wave				
1	3.5	3.4	32.6	66.6	66.6	3805	1458	1458	0.414	15.18	29.39	5.37
2	7.0	6.9	32.4	66.4	66.4	3874	1468	1468	0.416	15.41	30.62	5.44
3	10.5	10.3	32.2	66.2	66.2	3945	1478	1478	0.418	15.65	31.92	5.52
4	13.9	13.6	32.2	65.8	65.8	3945	1499	1499	0.416	16.06	31.72	5.67
5	17.7	17.2	31.8	65.4	65.4	4095	1520	1520	0.420	16.56	34.55	5.83
6	20.8	20.2	31.4	65.2	65.2	4257	1531	1531	0.426	16.87	37.86	5.92
7	24.1	23.3	31.4	65.2	65.2	4257	1531	1531	0.426	16.87	37.86	5.92
8	27.6	26.6	31.4	65.2	65.2	4257	1531	1531	0.426	16.87	37.86	5.92
9	31.2	29.9	31.4	65.2	65.2	4257	1531	1531	0.426	16.87	37.86	5.92
10	34.5	33.0	31.4	65.2	65.2	4257	1531	1531	0.426	16.87	37.86	5.92
11	38.0	36.2	31.4	65.2	65.2	4257	1531	1531	0.426	16.87	37.86	5.92
12	41.6	39.6	31.4	65.2	65.2	4257	1531	1531	0.426	16.87	37.86	5.92

Sample 20

Interval number	Hydrostatic stress (MPa)	Pore pressure (MPa)	Time of flight (μs)			Wave speed (m/s)			v_u	E_u (GPa)	K_u (GPa)	G_u (GPa)
			P-wave	S1-wave	S2 -Wave	P-wave	S1-wave	S2-wave				
1	3.5	3.5	32.2	66.0	66.0	3807	1437	1437	0.417	15.00	30.12	5.29
2	7.0	7.0	32.0	65.8	65.8	3879	1447	1447	0.419	15.23	31.42	5.37
3	10.5	10.3	31.8	65.6	65.6	3952	1457	1457	0.421	15.47	32.80	5.44
4	13.9	13.7	31.6	65.4	65.4	4029	1467	1467	0.424	15.72	34.27	5.52
5	17.3	16.9	31.4	65.4	65.4	4109	1467	1467	0.427	15.75	35.94	5.52
6	20.8	20.2	31.2	65.2	65.2	4192	1478	1478	0.429	16.00	37.60	5.60
7	24.1	23.3	31.2	65.2	65.2	4192	1478	1478	0.429	16.00	37.60	5.60
8	27.7	26.7	31.2	65.2	65.2	4192	1478	1478	0.429	16.00	37.60	5.60
9	31.2	29.9	31.2	65.2	65.2	4192	1478	1478	0.429	16.00	37.60	5.60
10	34.7	33.2	31.2	65.2	65.2	4192	1478	1478	0.429	16.00	37.60	5.60
11	38.0	36.3	31.2	65.2	65.2	4192	1478	1478	0.429	16.00	37.60	5.60
12	41.7	39.6	31.2	65.2	65.2	4192	1478	1478	0.429	16.00	37.60	5.60

Appendix 1: AVS tests under undrained loading condition.

Sample 21

Interval number	Hydrostatic stress (MPa)	Pore pressure (MPa)	Time of flight (µs)			Wave speed (m/s)			v_u	E_u (GPa)	K_u (GPa)	G_u (GPa)
			P-wave	S1-wave	S2 -Wave	P-wave	S1-wave	S2-wave				
1	3.6	3.6	32.2	66.0	66.0	3945	1489	1489	0.417	15.73	31.59	5.55
2	7.1	7.0	32.0	65.8	65.8	4019	1499	1499	0.419	15.98	32.96	5.63
3	10.4	10.3	31.8	65.6	65.6	4095	1509	1509	0.421	16.23	34.41	5.71
4	14.0	13.8	31.6	65.4	65.4	4175	1520	1520	0.424	16.48	35.95	5.79
5	17.2	16.9	31.4	65.4	65.4	4257	1520	1520	0.427	16.52	37.69	5.79
6	20.8	20.3	31.2	65.2	65.2	4343	1531	1531	0.429	16.78	39.43	5.87
7	24.1	23.5	31.2	65.2	65.2	4343	1531	1531	0.429	16.78	39.43	5.87
8	27.7	26.8	31.2	65.2	65.2	4343	1531	1531	0.429	16.78	39.43	5.87
9	31.1	30.0	31.2	65.2	65.2	4343	1531	1531	0.429	16.78	39.43	5.87
10	34.6	33.3	31.2	65.2	65.2	4343	1531	1531	0.429	16.78	39.43	5.87
11	38.1	36.6	31.2	65.2	65.2	4343	1531	1531	0.429	16.78	39.43	5.87
12	41.6	39.8	31.2	65.2	65.2	4343	1531	1531	0.429	16.78	39.43	5.87

Sample 22

Interval number	Hydrostatic stress (MPa)	Pore pressure (MPa)	Time of flight (µs)			Wave speed (m/s)			v_u	E_u (GPa)	K_u (GPa)	G_u (GPa)
			P-wave	S1-wave	S2 -Wave	P-wave	S1-wave	S2-wave				
1	3.5	3.4	32.2	66.2	66.2	3899	1461	1461	0.418	15.00	30.60	5.29
2	7.0	6.9	32.0	66.0	66.0	3972	1471	1471	0.420	15.23	31.92	5.36
3	10.5	10.4	31.8	65.8	65.8	4048	1482	1482	0.423	15.47	33.32	5.44
4	13.9	13.7	31.6	65.6	65.6	4126	1492	1492	0.425	15.71	34.81	5.51
5	17.5	17.2	31.4	65.4	65.4	4208	1502	1502	0.427	15.95	36.40	5.59
6	20.8	20.3	31.2	65.2	65.2	4293	1513	1513	0.429	16.21	38.08	5.67
7	24.2	23.5	31.2	65.2	65.2	4293	1513	1513	0.429	16.21	38.08	5.67
8	27.8	27.0	31.2	65.2	65.2	4293	1513	1513	0.429	16.21	38.08	5.67
9	31.2	30.2	31.2	65.2	65.2	4293	1513	1513	0.429	16.21	38.08	5.67
10	34.6	33.3	31.2	65.2	65.2	4293	1513	1513	0.429	16.21	38.08	5.67
11	38.1	36.6	31.2	65.2	65.2	4293	1513	1513	0.429	16.21	38.08	5.67
12	41.5	39.7	31.2	65.2	65.2	4293	1513	1513	0.429	16.21	38.08	5.67

Appendix 1: AVS tests under undrained loading condition.

Sample 23

Interval number	Hydrostatic stress (MPa)	Pore pressure (MPa)	Time of flight (μs)			Wave speed (m/s)			v_u	E_u (GPa)	K_u (GPa)	G_u (GPa)
			P-wave	S1-wave	S2 -Wave	P-wave	S1-wave	S2-wave				
1	3.5	3.4	32.4	66.0	66.0	3694	1419	1419	0.413	14.58	28.05	5.16
2	6.9	6.9	32.0	65.8	65.8	3832	1429	1429	0.419	14.84	30.61	5.23
3	10.3	10.2	31.8	65.6	65.6	3905	1439	1439	0.421	15.07	31.96	5.30
4	13.8	13.6	31.6	65.4	65.4	3981	1449	1449	0.424	15.31	33.39	5.38
5	17.2	16.9	31.4	65.2	65.2	4059	1460	1460	0.426	15.55	34.91	5.45
6	20.8	20.3	31.0	65.2	65.2	4227	1460	1460	0.432	15.62	38.46	5.45
7	24.2	23.5	31.0	65.2	65.2	4227	1460	1460	0.432	15.62	38.46	5.45
8	27.9	27.1	31.0	65.2	65.2	4227	1460	1460	0.432	15.62	38.46	5.45
9	31.4	30.4	31.0	65.2	65.2	4227	1460	1460	0.432	15.62	38.46	5.45
10	34.6	33.4	31.0	65.2	65.2	4227	1460	1460	0.432	15.62	38.46	5.45
11	38.2	36.7	31.0	65.2	65.2	4227	1460	1460	0.432	15.62	38.46	5.45
12	41.6	39.9	31.0	65.2	65.2	4227	1460	1460	0.432	15.62	38.46	5.45

Sample 24

Interval number	Hydrostatic stress (MPa)	Pore pressure (MPa)	Time of flight (μs)			Wave speed (m/s)			v_u	E_u (GPa)	K_u (GPa)	G_u (GPa)
			P-wave	S1-wave	S2 -Wave	P-wave	S1-wave	S2-wave				
1	3.6	3.5	32.4	65.4	65.4	3694	1449	1449	0.409	15.14	27.73	5.37
2	7.0	6.9	32.2	65.2	65.2	3761	1460	1460	0.411	15.39	28.92	5.45
3	10.4	10.3	32.0	65.0	65.0	3832	1470	1470	0.414	15.63	30.18	5.53
4	13.8	13.6	32.0	65.0	65.0	3832	1470	1470	0.414	15.63	30.18	5.53
5	17.3	17.0	32.0	65.0	65.0	3832	1470	1470	0.414	15.63	30.18	5.53
6	20.8	20.3	31.8	64.4	64.4	3905	1503	1503	0.413	16.32	31.30	5.77
7	24.2	23.5	31.8	64.4	64.4	3905	1503	1503	0.413	16.32	31.30	5.77
8	27.7	26.8	31.8	64.4	64.4	3905	1503	1503	0.413	16.32	31.30	5.77
9	31.3	30.1	31.8	64.4	64.4	3905	1503	1503	0.413	16.32	31.30	5.77
10	34.7	33.4	31.8	64.4	64.4	3905	1503	1503	0.413	16.32	31.30	5.77
11	38.2	36.6	31.8	64.4	64.4	3905	1503	1503	0.413	16.32	31.30	5.77
12	41.5	39.6	31.8	64.4	64.4	3905	1503	1503	0.413	16.32	31.30	5.77

Appendix 1: AVS tests under undrained loading condition.

Sample 25

Interval number	Hydrostatic stress (MPa)	Pore pressure (MPa)	Time of flight (μs)			Wave speed (m/s)			v_u	E_u (GPa)	K_u (GPa)	G_u (GPa)
			P-wave	S1-wave	S2 -Wave	P-wave	S1-wave	S2-wave				
1	3.5	3.5	32.2	66.0	66.2	3670	1385	1375	0.418	14.17	28.69	5.00
2	7.0	7.0	32.0	65.8	66.0	3738	1394	1385	0.420	14.39	29.93	5.07
3	10.6	10.5	31.8	65.6	65.8	3810	1404	1394	0.422	14.62	31.24	5.14
4	14.1	14.0	31.6	65.4	65.6	3883	1414	1404	0.424	14.85	32.64	5.21
5	17.8	17.5	31.4	65.4	65.4	3960	1414	1414	0.427	14.98	34.17	5.25
6	20.9	20.5	31.2	65.2	65.2	4040	1424	1424	0.429	15.22	35.76	5.32
7	24.2	23.7	31.2	65.2	65.2	4040	1424	1424	0.429	15.22	35.76	5.32
8	27.7	27.1	31.2	65.2	65.2	4040	1424	1424	0.429	15.22	35.76	5.32
9	31.1	30.3	31.2	65.2	65.2	4040	1424	1424	0.429	15.22	35.76	5.32
10	34.7	33.7	31.2	65.2	65.2	4040	1424	1424	0.429	15.22	35.76	5.32
11	38.2	36.9	31.2	65.2	65.2	4040	1424	1424	0.429	15.22	35.76	5.32
12	41.4	39.9	31.2	65.2	65.2	4040	1424	1424	0.429	15.22	35.76	5.32

Sample 26

Interval number	Hydrostatic stress (MPa)	Pore pressure (MPa)	Time of flight (μs)			Wave speed (m/s)			v_u	E_u (GPa)	K_u (GPa)	G_u (GPa)
			P-wave	S1-wave	S2 -Wave	P-wave	S1-wave	S2-wave				
1	3.5	3.5	32.8	66.0	66.0	3739	1489	1489	0.406	15.79	27.95	5.62
2	7.0	7.0	32.6	65.8	65.8	3805	1499	1499	0.408	16.04	29.11	5.70
3	10.5	10.3	32.6	65.8	65.8	3805	1499	1499	0.408	16.04	29.11	5.70
4	13.9	13.7	32.4	65.6	65.6	3874	1509	1509	0.410	16.29	30.34	5.78
5	17.3	16.9	32.4	65.4	65.4	3874	1520	1520	0.409	16.51	30.23	5.86
6	20.8	20.2	32.2	65.0	65.0	3945	1542	1542	0.410	16.99	31.41	6.03
7	24.2	23.5	32.2	65.0	65.0	3945	1542	1542	0.410	16.99	31.41	6.03
8	27.6	26.6	32.2	65.0	65.0	3945	1542	1542	0.410	16.99	31.41	6.03
9	31.2	30.0	32.2	65.0	65.0	3945	1542	1542	0.410	16.99	31.41	6.03
10	34.8	33.3	32.2	65.0	65.0	3945	1542	1542	0.410	16.99	31.41	6.03
11	38.0	36.3	32.2	65.0	65.0	3945	1542	1542	0.410	16.99	31.41	6.03
12	41.4	39.4	32.2	65.0	65.0	3945	1542	1542	0.410	16.99	31.41	6.03

Appendix 1: AVS tests under undrained loading condition.

Sample 27

Interval number	Hydrostatic stress (MPa)	Pore pressure (MPa)	Time of flight (µs)			Wave speed (m/s)			v_u	E_u (GPa)	K_u (GPa)	G_u (GPa)
			P-wave	S1-wave	S2 -Wave	P-wave	S1-wave	S2-wave				
1	3.5	3.4	32.2	66.0	66.0	3899	1471	1471	0.417	15.75	31.63	5.56
2	7.0	6.9	32.0	66.0	66.0	3972	1471	1471	0.420	15.79	33.11	5.56
3	10.5	10.3	31.8	65.6	65.6	4048	1492	1492	0.421	16.25	34.45	5.72
4	14.1	13.9	31.6	65.4	65.4	4126	1502	1502	0.424	16.51	36.00	5.80
5	17.3	17.0	31.4	65.2	65.2	4208	1513	1513	0.426	16.77	37.63	5.88
6	21.0	20.6	31.2	65.0	65.0	4293	1524	1524	0.428	17.03	39.38	5.97
7	24.2	23.6	31.2	65.0	65.0	4293	1524	1524	0.428	17.03	39.38	5.97
8	27.8	27.0	31.2	65.0	65.0	4293	1524	1524	0.428	17.03	39.38	5.97
9	31.4	30.5	31.2	65.0	65.0	4293	1524	1524	0.428	17.03	39.38	5.97
10	34.5	33.4	31.2	65.0	65.0	4293	1524	1524	0.428	17.03	39.38	5.97
11	38.2	36.8	31.2	65.0	65.0	4293	1524	1524	0.428	17.03	39.38	5.97
12	41.9	40.2	31.2	65.0	65.0	4293	1524	1524	0.428	17.03	39.38	5.97

Sample 28

Interval number	Hydrostatic stress (MPa)	Pore pressure (MPa)	Time of flight (µs)			Wave speed (m/s)			v_u	E_u (GPa)	K_u (GPa)	G_u (GPa)
			P-wave	S1-wave	S2 -Wave	P-wave	S1-wave	S2-wave				
1	3.5	3.4	32.2	66.0	66.0	3853	1454	1454	0.417	15.45	31.02	5.45
2	7.0	6.9	32.0	65.8	65.8	3925	1464	1464	0.419	15.69	32.36	5.53
3	10.5	10.3	31.8	65.6	65.6	4000	1474	1474	0.421	15.93	33.78	5.61
4	13.9	13.7	31.6	65.4	65.4	4078	1485	1485	0.424	16.19	35.30	5.68
5	17.7	17.4	31.4	65.2	65.2	4158	1495	1495	0.426	16.44	36.90	5.77
6	20.8	20.3	31.2	65.2	65.2	4242	1495	1495	0.429	16.48	38.72	5.77
7	24.3	23.7	31.2	65.2	65.2	4242	1495	1495	0.429	16.48	38.72	5.77
8	27.7	26.9	31.2	65.2	65.2	4242	1495	1495	0.429	16.48	38.72	5.77
9	31.3	30.4	31.2	65.2	65.2	4242	1495	1495	0.429	16.48	38.72	5.77
10	34.6	33.4	31.2	65.2	65.2	4242	1495	1495	0.429	16.48	38.72	5.77
11	38.1	36.7	31.2	65.2	65.2	4242	1495	1495	0.429	16.48	38.72	5.77
12	41.5	39.8	31.2	65.2	65.2	4242	1495	1495	0.429	16.48	38.72	5.77

Appendix 1: AVS tests under undrained loading condition.

Sample 29

Interval number	Hydrostatic stress (MPa)	Pore pressure (MPa)	Time of flight (µs)			Wave speed (m/s)			v_u	E_u (GPa)	K_u (GPa)	G_u (GPa)
			P-wave	S1-wave	S2 -Wave	P-wave	S1-wave	S2-wave				
1	3.5	3.4	32.4	66.2	66.2	3694	1410	1410	0.415	14.08	27.54	4.98
2	6.9	6.8	32.0	66.0	66.0	3832	1419	1419	0.420	14.33	30.05	5.05
3	10.4	10.2	31.8	65.8	65.8	3905	1429	1429	0.423	14.56	31.37	5.12
4	13.8	13.6	31.6	65.6	65.6	3981	1439	1439	0.425	14.78	32.77	5.19
5	17.3	17.0	31.4	65.4	65.4	4059	1449	1449	0.427	15.02	34.26	5.26
6	20.8	20.3	31.0	65.2	65.2	4227	1460	1460	0.432	15.29	37.63	5.34
7	24.4	23.8	31.0	65.2	65.2	4227	1460	1460	0.432	15.29	37.63	5.34
8	27.8	26.9	31.0	65.2	65.2	4227	1460	1460	0.432	15.29	37.63	5.34
9	31.5	30.4	31.0	65.2	65.2	4227	1460	1460	0.432	15.29	37.63	5.34
10	35.0	33.7	31.0	65.2	65.2	4227	1460	1460	0.432	15.29	37.63	5.34
11	38.3	36.8	31.0	65.2	65.2	4227	1460	1460	0.432	15.29	37.63	5.34
12	41.9	40.0	31.0	65.2	65.2	4227	1460	1460	0.432	15.29	37.63	5.34

Sample 30

Interval number	Hydrostatic stress (MPa)	Pore pressure (MPa)	Time of flight (µs)			Wave speed (m/s)			v_u	E_u (GPa)	K_u (GPa)	G_u (GPa)
			P-wave	S1-wave	S2 -Wave	P-wave	S1-wave	S2-wave				
1	3.5	3.4	32.2	66.0	66.0	3853	1454	1454	0.417	14.79	29.70	5.22
2	6.9	6.9	32.0	65.8	65.8	3925	1464	1464	0.419	15.02	30.99	5.29
3	10.3	10.2	31.8	65.6	65.6	4000	1474	1474	0.421	15.26	32.35	5.37
4	13.9	13.6	31.6	65.4	65.4	4078	1485	1485	0.424	15.50	33.80	5.44
5	17.3	16.9	31.4	65.2	65.2	4158	1495	1495	0.426	15.75	35.34	5.52
6	20.8	20.4	31.2	65.2	65.2	4242	1495	1495	0.429	15.78	37.08	5.52
7	24.1	23.7	31.2	65.2	65.2	4242	1495	1495	0.429	15.78	37.08	5.52
8	27.6	27.0	31.2	65.2	65.2	4242	1495	1495	0.429	15.78	37.08	5.52
9	31.0	30.3	31.2	65.2	65.2	4242	1495	1495	0.429	15.78	37.08	5.52
10	34.5	33.6	31.2	65.2	65.2	4242	1495	1495	0.429	15.78	37.08	5.52
11	37.9	36.9	31.2	65.2	65.2	4242	1495	1495	0.429	15.78	37.08	5.52
12	41.4	40.1	31.2	65.2	65.2	4242	1495	1495	0.429	15.78	37.08	5.52

Appendix 2: AVS tests under drained loading condition.

Sample 1

Interval number	Hydrostatic stress (MPa)	Pore pressure (MPa)	Time of flight (μs)			Wave speed (m/s)			*v*	*E* (GPa)	*K* (GPa)	*G* (GPa)
			P-wave	S1-wave	S2 -Wave	P-wave	S1-wave	S2-wave				
1	3.4	0.1	36.0	63.4	63.4	2789	1560	1560	0.272	15.38	11.27	6.04
2	6.9	0.1	35.6	63.2	63.2	2867	1572	1572	0.285	15.77	12.24	6.14
3	10.4	0.1	35.2	62.8	62.8	2950	1596	1596	0.293	16.37	13.18	6.33
4	13.9	0.1	34.8	62.6	62.6	3037	1609	1609	0.305	16.78	14.34	6.43
5	17.3	0.1	34.4	62.6	62.6	3130	1609	1609	0.320	16.98	15.76	6.43
6	20.9	0.1	34.2	62.6	62.6	3178	1609	1609	0.328	17.07	16.52	6.43
7	24.3	0.1	34.2	62.6	62.6	3178	1609	1609	0.328	17.07	16.52	6.43
8	28.0	0.1	34.2	62.6	62.6	3178	1609	1609	0.328	17.07	16.52	6.43
9	31.0	0.1	34.0	62.4	62.4	3228	1621	1621	0.331	17.39	17.18	6.53
10	34.5	0.1	34.0	62.4	62.4	3228	1621	1621	0.331	17.39	17.18	6.53
11	38.2	0.1	34.0	62.4	62.4	3228	1621	1621	0.331	17.39	17.18	6.53
12	41.4	0.1	34.0	62.4	62.4	3228	1621	1621	0.331	17.39	17.18	6.53

Sample 2

Interval number	Hydrostatic stress (MPa)	Pore pressure (MPa)	Time of flight (μs)			Wave speed (m/s)			*v*	*E* (GPa)	*K* (GPa)	*G* (GPa)
			P-wave	S1-wave	S2 -Wave	P-wave	S1-wave	S2-wave				
1	3.4	0.1	36.0	63.4	63.4	2891	1617	1617	0.272	16.52	12.10	6.49
2	7.1	0.1	35.8	63.4	63.4	2931	1617	1617	0.281	16.63	12.68	6.49
3	10.8	0.1	35.4	63.2	63.2	3014	1629	1629	0.294	17.05	13.77	6.59
4	13.9	0.1	35.0	63.2	63.2	3102	1629	1629	0.310	17.26	15.11	6.59
5	17.7	0.1	34.8	63.2	63.2	3148	1629	1629	0.317	17.36	15.82	6.59
6	20.9	0.1	34.8	63.2	63.2	3148	1629	1629	0.317	17.36	15.82	6.59
7	24.1	0.1	34.8	63.2	63.2	3148	1629	1629	0.317	17.36	15.82	6.59
8	27.7	0.1	34.8	63.2	63.2	3148	1629	1629	0.317	17.36	15.82	6.59
9	31.2	0.1	34.6	63.2	63.2	3195	1629	1629	0.324	17.46	16.57	6.59
10	34.6	0.1	34.6	63.2	63.2	3195	1629	1629	0.324	17.46	16.57	6.59
11	38.2	0.1	34.6	63.2	63.2	3195	1629	1629	0.324	17.46	16.57	6.59
12	41.5	0.1	34.6	63.2	63.2	3195	1629	1629	0.324	17.46	16.57	6.59

Appendix 2: AVS tests under drained loading condition.

Sample 3

Interval number	Hydrostatic stress (MPa)	Pore pressure (MPa)	Time of flight (μs)			Wave speed (m/s)			*v*	*E* (GPa)	*K* (GPa)	*G* (GPa)
			P-wave	S1-wave	S2 -Wave	P-wave	S1-wave	S2-wave				
1	3.4	0.1	36.4	63.4	63.4	2649	1522	1522	0.254	14.72	9.96	5.87
2	7.0	0.1	36.0	63.0	63.0	2721	1545	1545	0.262	15.28	10.70	6.05
3	10.5	0.1	35.2	63.0	62.8	2878	1545	1557	0.295	15.80	12.86	6.10
4	13.8	0.1	35.0	62.4	62.4	2920	1582	1582	0.292	16.40	13.16	6.34
5	17.3	0.1	34.6	62.4	62.4	3008	1582	1582	0.309	16.61	14.48	6.34
6	20.8	0.1	34.4	62.4	62.4	3053	1582	1582	0.317	16.71	15.18	6.34
7	24.3	0.1	34.2	62.2	62.2	3101	1594	1594	0.320	17.02	15.78	6.45
8	27.7	0.1	34.2	62.2	62.2	3101	1594	1594	0.320	17.02	15.78	6.45
9	31.2	0.1	34.0	62.2	62.2	3150	1594	1594	0.328	17.12	16.56	6.45
10	34.7	0.1	34.0	62.2	62.2	3150	1594	1594	0.328	17.12	16.56	6.45
11	38.2	0.1	34.0	62.2	62.2	3150	1594	1594	0.328	17.12	16.56	6.45
12	41.7	0.1	34.0	62.2	62.2	3150	1594	1594	0.328	17.12	16.56	6.45

Sample 4

Interval number	Hydrostatic stress (MPa)	Pore pressure (MPa)	Time of flight (μs)			Wave speed (m/s)			*v*	*E* (GPa)	*K* (GPa)	*G* (GPa)
			P-wave	S1-wave	S2 -Wave	P-wave	S1-wave	S2-wave				
1	3.5	0.1	36.0	63.4	63.4	2823	1579	1579	0.272	16.06	11.76	6.31
2	7.0	0.1	35.4	62.8	62.8	2943	1616	1616	0.284	16.97	13.12	6.61
3	10.5	0.1	35.0	62.2	62.2	3029	1654	1654	0.288	17.84	13.99	6.93
4	13.9	0.1	34.8	62.4	62.4	3074	1641	1641	0.301	17.74	14.83	6.82
5	17.7	0.1	34.4	62.2	62.2	3168	1654	1654	0.313	18.18	16.17	6.93
6	20.7	0.1	34.0	62.2	62.2	3268	1654	1654	0.328	18.39	17.79	6.93
7	24.1	0.1	34.0	62.2	62.2	3268	1654	1654	0.328	18.39	17.79	6.93
8	27.6	0.1	33.8	62.0	62.0	3320	1668	1668	0.331	18.74	18.52	7.04
9	31.1	0.1	33.8	62.0	62.0	3320	1668	1668	0.331	18.74	18.52	7.04
10	34.6	0.1	33.6	62.0	62.0	3374	1668	1668	0.338	18.84	19.43	7.04
11	38.1	0.1	33.6	62.0	62.0	3374	1668	1668	0.338	18.84	19.43	7.04
12	42.0	0.1	33.6	62.0	62.0	3374	1668	1668	0.338	18.84	19.43	7.04

Appendix 2: AVS tests under drained loading condition.

Sample 5

Interval number	Hydrostatic stress (MPa)	Pore pressure (MPa)	Time of flight (µs)			Wave speed (m/s)			*v*	*E* (GPa)	*K* (GPa)	*G* (GPa)
			P-wave	S1-wave	S2 -Wave	P-wave	S1-wave	S2-wave				
1	3.5	0.1	36.2	63.4	63.4	2852	1617	1617	0.263	16.37	11.53	6.48
2	7.1	0.1	35.8	63.4	63.4	2931	1617	1617	0.281	16.61	12.66	6.48
3	10.9	0.1	35.2	63.2	63.2	3058	1629	1629	0.302	17.13	14.40	6.58
4	13.9	0.1	35.0	63.0	63.0	3102	1642	1642	0.305	17.45	14.95	6.68
5	17.7	0.1	35.0	63.0	63.0	3102	1642	1642	0.305	17.45	14.95	6.68
6	21.0	0.1	34.8	63.0	63.0	3148	1642	1642	0.313	17.55	15.66	6.68
7	24.2	0.1	34.6	62.6	62.6	3195	1668	1668	0.313	18.10	16.12	6.89
8	27.7	0.1	34.4	62.0	62.0	3244	1708	1708	0.308	18.92	16.45	7.23
9	31.1	0.1	34.4	62.0	62.0	3244	1708	1708	0.308	18.92	16.45	7.23
10	34.8	0.1	34.4	62.0	62.0	3244	1708	1708	0.308	18.92	16.45	7.23
11	38.4	0.1	34.2	61.8	61.8	3295	1722	1722	0.312	19.28	17.11	7.35
12	41.7	0.1	34.2	61.8	61.8	3295	1722	1722	0.312	19.28	17.11	7.35

Sample 6

Interval number	Hydrostatic stress (MPa)	Pore pressure (MPa)	Time of flight (µs)			Wave speed (m/s)			*v*	*E* (GPa)	*K* (GPa)	*G* (GPa)
			P-wave	S1-wave	S2 -Wave	P-wave	S1-wave	S2-wave				
1	3.5	0.1	36.0	63.8	63.8	2755	1518	1518	0.282	15.28	11.69	5.96
2	7.1	0.1	35.4	63.6	63.6	2872	1529	1529	0.302	15.75	13.28	6.05
3	10.8	0.1	34.8	62.6	62.6	3000	1589	1589	0.305	17.05	14.57	6.53
4	13.9	0.1	34.4	62.4	62.4	3092	1602	1602	0.317	17.47	15.87	6.63
5	17.3	0.1	34.0	62.4	62.4	3179	1602	1602	0.330	17.65	17.29	6.63
6	20.8	0.1	33.6	62.4	62.4	3293	1602	1602	0.345	17.85	19.19	6.63
7	24.2	0.1	33.6	62.4	62.4	3293	1602	1602	0.345	17.85	19.19	6.63
8	27.7	0.1	33.6	62.4	62.4	3303	1602	1602	0.346	17.86	19.38	6.63
9	31.1	0.1	33.4	62.4	62.4	3336	1602	1602	0.350	17.92	19.94	6.63
10	34.9	0.1	33.4	62.4	62.4	3347	1602	1602	0.352	17.93	20.13	6.63
11	38.1	0.1	33.2	61.8	61.8	3403	1641	1641	0.349	18.78	20.68	6.96
12	41.5	0.1	33.2	62.0	62.0	3403	1627	1627	0.352	18.52	20.82	6.85

Appendix 2: AVS tests under drained loading condition.

Sample 7

Interval number	Hydrostatic stress (MPa)	Pore pressure (MPa)	Time of flight (µs)			Wave speed (m/s)			*v*	*E* (GPa)	*K* (GPa)	*G* (GPa)
			P-wave	S1-wave	S2 -Wave	P-wave	S1-wave	S2-wave				
1	3.6	0.1	36.4	63.8	63.8	2649	1499	1499	0.265	14.42	10.21	5.70
2	6.9	0.1	35.8	63.6	63.6	2759	1510	1510	0.286	14.88	11.59	5.79
3	10.8	0.1	35.4	62.8	62.8	2829	1557	1557	0.283	15.78	12.10	6.15
4	13.8	0.1	35.2	62.6	62.6	2878	1569	1569	0.288	16.10	12.68	6.25
5	17.5	0.1	34.8	62.4	62.4	2963	1582	1582	0.301	16.52	13.81	6.35
6	20.8	0.1	34.4	62.6	62.6	3053	1569	1569	0.320	16.51	15.32	6.25
7	24.1	0.1	34.4	62.6	62.6	3053	1569	1569	0.320	16.51	15.32	6.25
8	27.8	0.1	34.2	62.6	62.6	3101	1569	1569	0.328	16.60	16.06	6.25
9	31.1	0.1	34.2	62.6	62.6	3101	1569	1569	0.328	16.60	16.06	6.25
10	34.5	0.1	34.2	62.6	62.6	3101	1567	1567	0.329	16.55	16.09	6.23
11	38.2	0.1	34.0	62.6	62.6	3140	1569	1569	0.333	16.67	16.68	6.25
12	3.6	0.1	36.4	63.8	63.8	2649	1499	1499	0.265	14.42	10.21	5.70

Sample 8

Interval number	Hydrostatic stress (MPa)	Pore pressure (MPa)	Time of flight (µs)			Wave speed (m/s)			*v*	*E* (GPa)	*K* (GPa)	*G* (GPa)
			P-wave	S1-wave	S2 -Wave	P-wave	S1-wave	S2-wave				
1	41.5	0.1	34.0	62.6	62.6	3150	1569	1569	0.335	16.69	16.84	6.25
2	3.6	0.1	36.2	63.6	63.6	2789	1567	1567	0.269	15.39	11.13	6.06
3	6.9	0.1	35.8	63.4	63.4	2856	1579	1579	0.280	15.76	11.94	6.15
4	10.8	0.1	35.4	62.8	62.8	2943	1616	1616	0.284	16.56	12.80	6.45
5	13.8	0.1	35.0	62.6	62.6	3029	1628	1628	0.297	16.98	13.93	6.55
6	17.5	0.1	34.6	62.4	62.4	3120	1641	1641	0.309	17.41	15.17	6.65
7	20.8	0.1	34.6	62.4	62.4	3120	1641	1641	0.309	17.41	15.17	6.65
8	24.1	0.1	34.6	62.4	62.4	3130	1641	1641	0.310	17.43	15.32	6.65
9	27.6	0.1	34.4	62.4	62.4	3168	1641	1641	0.317	17.51	15.91	6.65
10	31.0	0.1	34.4	62.4	62.4	3168	1641	1641	0.317	17.51	15.91	6.65
11	34.7	0.1	34.4	62.4	62.4	3178	1641	1641	0.318	17.53	16.07	6.65
12	38.0	0.1	34.2	62.4	62.4	3207	1641	1641	0.323	17.59	16.53	6.65

Appendix 2: AVS tests under drained loading condition.

Sample 9

Interval number	Hydrostatic stress (MPa)	Pore pressure (MPa)	Time of flight (μs)			Wave speed (m/s)			*v*	*E* (GPa)	*K* (GPa)	*G* (GPa)
			P-wave	S1-wave	S2 -Wave	P-wave	S1-wave	S2-wave				
1	3.6	0.1	36.2	63.6	63.6	2752	1548	1548	0.269	15.00	10.80	5.91
2	6.9	0.1	36.2	63.6	63.6	2744	1548	1548	0.267	14.98	10.70	5.91
3	10.8	0.1	35.6	63.0	63.0	2867	1584	1584	0.280	15.85	12.03	6.19
4	13.8	0.1	35.2	63.0	63.0	2950	1584	1584	0.297	16.06	13.21	6.19
5	17.5	0.1	35.0	62.6	62.6	2993	1609	1609	0.297	16.56	13.58	6.38
6	20.8	0.1	34.8	62.0	62.0	3037	1647	1647	0.292	17.30	13.83	6.70
7	24.2	0.1	34.8	62.0	62.0	3037	1647	1647	0.292	17.30	13.83	6.70
8	27.7	0.1	34.8	62.0	62.0	3037	1647	1647	0.292	17.30	13.83	6.70
9	31.2	0.1	34.6	62.0	62.0	3076	1647	1647	0.299	17.39	14.41	6.70
10	34.7	0.1	34.6	62.0	62.0	3083	1647	1647	0.300	17.41	14.52	6.70
11	38.2	0.1	34.6	62.0	62.0	3083	1647	1647	0.300	17.41	14.52	6.70
12	41.5	0.1	34.6	62.0	62.0	3092	1645	1645	0.303	17.39	14.69	6.67

Sample 10

Interval number	Hydrostatic stress (MPa)	Pore pressure (MPa)	Time of flight (μs)			Wave speed (m/s)			*v*	*E* (GPa)	*K* (GPa)	*G* (GPa)
			P-wave	S1-wave	S2 -Wave	P-wave	S1-wave	S2-wave				
1	3.5	0.1	36.0	63.4	63.4	2789	1560	1560	0.272	15.58	11.42	6.12
2	7.0	0.1	35.6	63.2	63.2	2867	1572	1572	0.285	15.98	12.40	6.22
3	10.5	0.1	35.2	62.8	62.8	2958	1596	1596	0.295	16.61	13.48	6.41
4	14.2	0.1	34.8	62.4	62.4	3037	1621	1621	0.301	17.21	14.39	6.62
5	17.8	0.1	34.4	62.4	62.4	3130	1621	1621	0.317	17.43	15.83	6.62
6	21.0	0.1	34.2	62.4	62.4	3178	1621	1621	0.324	17.52	16.60	6.62
7	24.1	0.1	34.2	62.4	62.4	3178	1621	1621	0.324	17.52	16.60	6.62
8	27.6	0.1	34.0	62.4	62.4	3228	1621	1621	0.331	17.62	17.41	6.62
9	31.1	0.1	34.0	62.4	62.4	3228	1621	1621	0.331	17.62	17.41	6.62
10	34.5	0.1	33.8	62.4	62.4	3270	1624	1624	0.336	17.74	18.06	6.64
11	38.1	0.1	33.8	62.4	62.4	3270	1621	1621	0.337	17.69	18.09	6.62
12	41.7	0.1	33.8	62.4	62.4	3280	1621	1621	0.338	17.71	18.26	6.62

Appendix 2: AVS tests under drained loading condition.

Sample 11

Interval number	Hydrostatic stress (MPa)	Pore pressure (MPa)	Time of flight (µs)			Wave speed (m/s)			*v*	*E* (GPa)	*K* (GPa)	*G* (GPa)
			P-wave	S1-wave	S2 -Wave	P-wave	S1-wave	S2-wave				
1	3.6	0.1	35.8	63.4	63.4	2759	1522	1522	0.281	15.11	11.51	5.90
2	6.9	0.1	35.4	63.2	63.2	2837	1533	1533	0.294	15.49	12.51	5.99
3	10.5	0.1	35.0	62.8	62.8	2920	1557	1557	0.301	16.07	13.47	6.17
4	13.9	0.1	34.4	62.4	62.4	3053	1582	1582	0.317	16.78	15.24	6.37
5	17.4	0.1	34.2	62.4	62.4	3101	1582	1582	0.324	16.87	15.99	6.37
6	20.9	0.1	34.0	61.8	61.8	3150	1620	1620	0.320	17.65	16.34	6.68
7	24.1	0.1	33.8	61.8	61.8	3200	1620	1620	0.328	17.75	17.16	6.68
8	27.7	0.1	33.8	61.8	61.8	3200	1620	1620	0.328	17.75	17.16	6.68
9	31.3	0.1	33.8	61.8	61.8	3205	1618	1618	0.329	17.71	17.27	6.66
10	34.6	0.1	33.6	61.8	61.8	3244	1624	1624	0.333	17.89	17.85	6.71
11	38.0	0.1	33.6	61.8	61.8	3252	1620	1620	0.335	17.85	18.01	6.68
12	41.5	0.1	33.6	61.8	61.8	3252	1620	1620	0.335	17.85	18.01	6.68

Sample 12

Interval number	Hydrostatic stress (MPa)	Pore pressure (MPa)	Time of flight (µs)			Wave speed (m/s)			*v*	*E* (GPa)	*K* (GPa)	*G* (GPa)
			P-wave	S1-wave	S2 -Wave	P-wave	S1-wave	S2-wave				
1	3.4	0.1	36.6	64.0	64.0	2680	1525	1525	0.261	14.99	10.43	5.95
2	6.9	0.1	36.0	63.4	63.4	2789	1560	1560	0.272	15.83	11.60	6.22
3	10.3	0.1	35.4	62.8	62.8	2908	1596	1596	0.284	16.73	12.93	6.51
4	13.9	0.1	35.2	62.4	62.6	2950	1621	1609	0.286	17.15	13.35	6.67
5	17.3	0.1	34.8	62.2	62.4	3037	1634	1621	0.298	17.60	14.55	6.78
6	20.7	0.1	34.6	62.4	62.4	3073	1621	1621	0.307	17.57	15.19	6.72
7	24.3	0.1	34.6	62.4	62.4	3083	1621	1621	0.309	17.60	15.34	6.72
8	27.7	0.1	34.6	62.4	62.4	3083	1621	1621	0.309	17.60	15.34	6.72
9	31.3	0.1	34.6	62.4	62.4	3083	1619	1619	0.310	17.55	15.37	6.70
10	34.7	0.1	34.4	62.4	62.4	3120	1621	1621	0.315	17.68	15.93	6.72
11	38.1	0.1	34.4	62.4	62.4	3130	1621	1621	0.317	17.70	16.08	6.72
12	41.4	0.1	34.4	62.4	62.4	3139	1621	1621	0.318	17.72	16.24	6.72

Appendix 2: AVS tests under drained loading condition.

Sample 13

Interval number	Hydrostatic stress (MPa)	Pore pressure (MPa)	Time of flight (µs)			Wave speed (m/s)			*v*	*E* (GPa)	*K* (GPa)	*G* (GPa)
			P-wave	S1-wave	S2 -Wave	P-wave	S1-wave	S2-wave				
1	3.5	0.1	35.8	63.2	63.2	2621	1457	1457	0.276	13.63	10.16	5.34
2	7.0	0.1	35.6	63.2	63.2	2657	1457	1457	0.285	13.73	10.65	5.34
3	10.5	0.1	35.2	62.6	62.6	2734	1491	1491	0.288	14.41	11.35	5.59
4	13.9	0.1	34.8	62.4	62.4	2815	1503	1503	0.301	14.78	12.36	5.68
5	17.7	0.1	34.6	62.2	62.2	2857	1515	1515	0.305	15.07	12.85	5.77
6	20.7	0.1	34.2	61.0	61.0	2946	1591	1591	0.294	16.48	13.35	6.37
7	24.1	0.1	34.2	61.0	61.0	2946	1591	1591	0.294	16.48	13.35	6.37
8	27.7	0.1	34.0	60.8	60.8	2983	1607	1607	0.296	16.84	13.72	6.50
9	31.3	0.1	34.0	60.8	60.8	2983	1604	1604	0.296	16.79	13.75	6.48
10	34.9	0.1	34.0	60.8	60.8	2992	1604	1604	0.298	16.82	13.90	6.48
11	38.1	0.1	34.0	60.8	60.8	2992	1604	1602	0.299	16.80	13.91	6.47
12	41.4	0.1	33.8	60.6	60.6	3029	1618	1618	0.300	17.13	14.31	6.59

Sample 14

Interval number	Hydrostatic stress (MPa)	Pore pressure (MPa)	Time of flight (µs)			Wave speed (m/s)			*v*	*E* (GPa)	*K* (GPa)	*G* (GPa)
			P-wave	S1-wave	S2 -Wave	P-wave	S1-wave	S2-wave				
1	3.5	0.1	36.4	63.2	63.2	2682	1553	1553	0.248	15.28	10.11	6.12
2	7.0	0.1	36.0	63.2	63.2	2755	1553	1553	0.267	15.52	11.12	6.12
3	10.5	0.1	35.4	62.8	62.8	2872	1577	1577	0.284	16.22	12.54	6.31
4	13.8	0.1	35.0	62.4	62.4	2956	1602	1602	0.292	16.84	13.51	6.52
5	17.3	0.1	34.6	62.4	62.4	3045	1602	1602	0.309	17.06	14.87	6.52
6	20.9	0.1	34.4	62.4	62.4	3092	1602	1602	0.317	17.16	15.59	6.52
7	24.1	0.1	34.2	62.2	62.2	3140	1614	1614	0.320	17.48	16.21	6.62
8	27.7	0.1	34.2	62.2	62.2	3140	1614	1614	0.320	17.48	16.21	6.62
9	31.2	0.1	34.2	62.2	62.2	3149	1614	1614	0.322	17.50	16.37	6.62
10	34.7	0.1	34.0	62.2	62.2	3189	1614	1614	0.328	17.58	17.01	6.62
11	38.1	0.1	34.0	62.2	62.2	3189	1614	1614	0.328	17.58	17.01	6.62
12	41.4	0.1	33.8	62.2	62.2	3230	1614	1614	0.333	17.66	17.67	6.62

Appendix 2: AVS tests under drained loading condition.

Sample 15

Interval number	Hydrostatic stress (MPa)	Pore pressure (MPa)	Time of flight (µs)			Wave speed (m/s)			*v*	*E* (GPa)	*K* (GPa)	*G* (GPa)
			P-wave	S1-wave	S2 -Wave	P-wave	S1-wave	S2-wave				
1	3.5	0.1	36.4	64.0	64.0	2881	1618	1618	0.270	16.80	12.15	6.62
2	7.1	0.1	36.0	63.8	63.8	2959	1630	1630	0.282	17.22	13.18	6.72
3	10.8	0.1	35.8	63.6	63.6	3000	1642	1642	0.286	17.53	13.66	6.82
4	13.9	0.1	35.4	63.4	63.4	3085	1655	1655	0.298	17.97	14.83	6.92
5	17.3	0.1	35.2	63.4	63.4	3121	1655	1655	0.304	18.06	15.38	6.92
6	20.8	0.1	35.2	63.4	63.4	3129	1655	1655	0.306	18.08	15.52	6.92
7	24.2	0.1	35.2	63.4	63.4	3129	1655	1655	0.306	18.08	15.52	6.92
8	27.8	0.1	35.2	63.4	63.4	3129	1655	1655	0.306	18.08	15.52	6.92
9	31.3	0.1	35.2	63.4	63.4	3139	1655	1655	0.307	18.10	15.67	6.92
10	34.6	0.1	35.0	63.4	63.4	3166	1655	1655	0.312	18.16	16.10	6.92
11	38.3	0.1	35.0	63.4	63.4	3175	1655	1655	0.314	18.18	16.25	6.92
12	41.6	0.1	35.0	63.4	63.4	3175	1652	1652	0.314	18.14	16.28	6.90

Sample 16

Interval number	Hydrostatic stress (MPa)	Pore pressure (MPa)	Time of flight (µs)			Wave speed (m/s)			*v*	*E* (GPa)	*K* (GPa)	*G* (GPa)
			P-wave	S1-wave	S2 -Wave	P-wave	S1-wave	S2-wave				
1	3.5	0.1	36.4	63.4	63.4	2848	1636	1636	0.254	16.97	11.49	6.77
2	7.1	0.1	35.8	63.4	63.4	2966	1636	1636	0.281	17.34	13.22	6.77
3	10.9	0.1	35.4	63.4	63.4	3050	1636	1636	0.298	17.57	14.50	6.77
4	13.9	0.1	35.0	63.4	63.4	3130	1636	1636	0.312	17.76	15.75	6.77
5	17.7	0.1	35.0	63.0	63.0	3139	1661	1661	0.305	18.22	15.61	6.98
6	21.0	0.1	34.6	63.0	63.0	3233	1661	1661	0.321	18.43	17.13	6.98
7	24.1	0.1	34.6	63.0	63.0	3233	1661	1661	0.321	18.43	17.13	6.98
8	27.7	0.1	34.6	63.0	63.0	3233	1661	1661	0.321	18.43	17.13	6.98
9	31.2	0.1	34.6	63.0	63.0	3243	1661	1661	0.322	18.45	17.29	6.98
10	34.6	0.1	34.4	63.0	63.0	3282	1661	1661	0.328	18.53	17.94	6.98
11	37.9	0.1	34.4	63.0	63.0	3282	1661	1661	0.328	18.53	17.94	6.98
12	41.7	0.1	34.2	62.4	62.4	3333	1700	1700	0.324	19.37	18.35	7.31

Appendix 2: AVS tests under drained loading condition.

Sample 17

Interval number	Hydrostatic stress (MPa)	Pore pressure (MPa)	Time of flight (µs)			Wave speed (m/s)			*v*	*E* (GPa)	*K* (GPa)	*G* (GPa)
			P-wave	S1-wave	S2 -Wave	P-wave	S1-wave	S2-wave				
1	3.5	0.1	36.4	63.4	63.4	2947	1693	1693	0.254	18.19	12.32	7.26
2	7.0	0.1	35.8	63.0	63.0	3069	1719	1719	0.271	19.03	13.87	7.48
3	10.6	0.1	35.4	62.6	62.6	3147	1746	1746	0.278	19.72	14.79	7.72
4	13.8	0.1	35.0	62.4	62.4	3237	1760	1760	0.290	20.23	16.07	7.84
5	17.3	0.1	34.8	62.4	62.4	3296	1760	1760	0.301	20.40	17.06	7.84
6	20.9	0.1	34.4	62.4	62.4	3397	1760	1760	0.317	20.65	18.76	7.84
7	24.2	0.1	34.4	62.4	62.4	3397	1760	1760	0.317	20.65	18.76	7.84
8	27.7	0.1	34.4	62.4	62.4	3407	1760	1760	0.318	20.67	18.94	7.84
9	31.3	0.1	34.4	62.4	62.4	3407	1757	1757	0.319	20.62	18.97	7.82
10	34.6	0.1	34.2	62.4	62.4	3450	1760	1760	0.324	20.77	19.68	7.84
11	38.0	0.1	34.2	62.4	62.4	3450	1760	1760	0.324	20.77	19.68	7.84
12	41.5	0.1	34.0	62.0	62.0	3493	1788	1788	0.322	21.41	20.10	8.10

Sample 18

Interval number	Hydrostatic stress (MPa)	Pore pressure (MPa)	Time of flight (µs)			Wave speed (m/s)			*v*	*E* (GPa)	*K* (GPa)	*G* (GPa)
			P-wave	S1-wave	S2 -Wave	P-wave	S1-wave	S2-wave				
1	3.5	0.1	36.4	63.6	63.6	3046	1737	1737	0.259	19.26	13.33	7.65
2	7.0	0.1	35.8	63.0	63.0	3172	1777	1777	0.271	20.35	14.84	8.00
3	10.5	0.1	35.4	63.0	63.0	3262	1777	1777	0.289	20.64	16.31	8.00
4	13.9	0.1	34.8	62.4	62.4	3407	1819	1819	0.301	21.82	18.25	8.39
5	17.5	0.1	34.8	62.4	62.4	3418	1819	1819	0.302	21.85	18.42	8.39
6	20.9	0.1	34.2	62.2	62.2	3555	1834	1834	0.319	22.48	20.67	8.52
7	24.1	0.1	34.2	62.2	62.2	3566	1834	1834	0.320	22.50	20.87	8.52
8	27.6	0.1	34.2	62.2	62.2	3566	1834	1834	0.320	22.50	20.87	8.52
9	31.0	0.1	34.2	62.2	62.2	3577	1834	1834	0.322	22.53	21.07	8.52
10	34.7	0.1	34.0	62.2	62.2	3611	1831	1831	0.327	22.55	21.72	8.50
11	38.1	0.1	34.0	62.2	62.2	3622	1834	1834	0.328	22.63	21.89	8.52
12	41.5	0.1	34.0	62.2	62.2	3622	1831	1831	0.328	22.57	21.93	8.50

Appendix 2: AVS tests under drained loading condition.

Sample 19

Interval number	Hydrostatic stress (MPa)	Pore pressure (MPa)	Time of flight (µs)			Wave speed (m/s)			*v*	*E* (GPa)	*K* (GPa)	*G* (GPa)
			P-wave	S1-wave	S2 -Wave	P-wave	S1-wave	S2-wave				
1	3.5	0.1	36.6	63.4	63.4	2810	1636	1636	0.244	16.80	10.93	6.75
2	7.1	0.1	36.0	63.4	63.4	2925	1636	1636	0.272	17.19	12.59	6.75
3	10.3	0.1	35.6	63.4	63.4	3007	1636	1636	0.290	17.42	13.82	6.75
4	13.9	0.1	35.4	63.4	63.4	3050	1636	1636	0.298	17.53	14.47	6.75
5	17.5	0.1	35.0	63.4	63.4	3139	1636	1636	0.314	17.74	15.86	6.75
6	21.0	0.1	34.4	63.0	63.0	3282	1661	1661	0.328	18.49	17.91	6.96
7	24.2	0.1	34.4	63.0	63.0	3282	1661	1661	0.328	18.49	17.91	6.96
8	27.7	0.1	34.4	63.0	63.0	3292	1661	1661	0.329	18.51	18.08	6.96
9	31.2	0.1	34.2	63.0	63.0	3323	1661	1661	0.333	18.57	18.59	6.96
10	34.6	0.1	34.2	63.0	63.0	3333	1661	1661	0.335	18.59	18.76	6.96
11	38.1	0.1	34.0	62.8	62.8	3386	1674	1674	0.338	18.93	19.50	7.07
12	41.9	0.1	34.0	62.8	62.8	3386	1674	1674	0.338	18.93	19.50	7.07

Sample 20

Interval number	Hydrostatic stress (MPa)	Pore pressure (MPa)	Time of flight (µs)			Wave speed (m/s)			*v*	*E* (GPa)	*K* (GPa)	*G* (GPa)
			P-wave	S1-wave	S2 -Wave	P-wave	S1-wave	S2-wave				
1	3.6	0.1	36.2	63.2	63.2	2785	1591	1591	0.258	16.33	11.24	6.49
2	7.1	0.1	35.6	62.8	62.8	2902	1616	1616	0.275	17.08	12.67	6.69
3	10.5	0.1	35.2	62.8	62.8	2977	1616	1616	0.291	17.29	13.80	6.69
4	13.8	0.1	35.0	62.8	62.8	3029	1616	1616	0.301	17.42	14.61	6.69
5	17.3	0.1	34.6	62.8	62.8	3120	1616	1616	0.317	17.63	16.04	6.69
6	20.8	0.1	34.4	62.8	62.8	3168	1616	1616	0.324	17.73	16.81	6.69
7	24.1	0.1	34.2	62.8	62.8	3217	1616	1616	0.331	17.82	17.62	6.69
8	27.7	0.1	34.2	62.8	62.8	3217	1616	1616	0.331	17.82	17.62	6.69
9	31.2	0.1	34.2	62.8	62.8	3217	1616	1616	0.331	17.82	17.62	6.69
10	34.9	0.1	34.2	62.8	62.8	3227	1616	1616	0.333	17.84	17.78	6.69
11	38.2	0.1	34.0	62.6	62.6	3268	1628	1628	0.335	18.15	18.32	6.80
12	41.7	0.1	34.0	62.6	62.6	3268	1628	1628	0.335	18.15	18.32	6.80

Appendix 2: AVS tests under drained loading condition.

Sample 21

Interval number	Hydrostatic stress (MPa)	Pore pressure (MPa)	Time of flight (μs)			Wave speed (m/s)			*v*	*E* (GPa)	*K* (GPa)	*G* (GPa)
			P-wave	S1-wave	S2 -Wave	P-wave	S1-wave	S2-wave				
1	3.6	0.1	36.0	63.4	63.4	2925	1636	1636	0.272	17.06	12.50	6.70
2	6.9	0.1	35.4	62.8	62.8	3050	1674	1674	0.284	18.03	13.94	7.02
3	10.8	0.1	35.0	62.8	62.8	3139	1674	1674	0.301	18.27	15.32	7.02
4	13.8	0.1	34.6	62.4	62.4	3233	1700	1700	0.309	18.96	16.53	7.24
5	17.5	0.1	34.2	62.2	62.2	3333	1714	1714	0.320	19.44	18.02	7.36
6	20.8	0.1	33.8	62.0	62.0	3440	1728	1728	0.331	19.91	19.67	7.48
7	24.2	0.1	33.8	62.0	62.0	3440	1728	1728	0.331	19.91	19.67	7.48
8	27.7	0.1	33.6	62.0	62.0	3485	1728	1728	0.337	20.00	20.45	7.48
9	31.1	0.1	33.6	62.0	62.0	3496	1728	1728	0.338	20.02	20.65	7.48
10	34.9	0.1	33.6	62.0	62.0	3496	1728	1728	0.338	20.02	20.65	7.48
11	38.1	0.1	33.6	62.0	62.0	3507	1728	1728	0.340	20.04	20.85	7.48
12	41.7	0.1	33.4	61.8	61.8	3542	1742	1742	0.341	20.38	21.30	7.60

Sample 22

Interval number	Hydrostatic stress (MPa)	Pore pressure (MPa)	Time of flight (μs)			Wave speed (m/s)			*v*	*E* (GPa)	*K* (GPa)	*G* (GPa)
			P-wave	S1-wave	S2 -Wave	P-wave	S1-wave	S2-wave				
1	3.6	0.1	36.0	63.4	63.4	2891	1617	1617	0.272	16.47	12.07	6.47
2	6.9	0.1	35.4	62.8	62.8	3006	1655	1655	0.283	17.39	13.33	6.78
3	10.8	0.1	35.0	62.6	62.6	3102	1668	1668	0.297	17.86	14.65	6.89
4	13.8	0.1	34.6	62.2	62.2	3186	1694	1694	0.303	18.52	15.66	7.11
5	17.5	0.1	34.4	62.2	62.2	3254	1694	1694	0.314	18.68	16.75	7.11
6	20.8	0.1	34.0	62.2	62.2	3336	1694	1694	0.326	18.85	18.08	7.11
7	24.1	0.1	34.0	62.2	62.2	3346	1694	1694	0.328	18.87	18.26	7.11
8	27.9	0.1	34.0	62.2	62.2	3346	1694	1694	0.328	18.87	18.26	7.11
9	31.3	0.1	33.8	61.8	61.8	3400	1722	1722	0.328	19.49	18.84	7.34
10	34.6	0.1	33.8	61.8	61.8	3400	1722	1722	0.328	19.49	18.84	7.34
11	38.2	0.1	33.8	61.8	61.8	3405	1722	1722	0.328	19.50	18.93	7.34
12	41.6	0.1	33.8	61.8	61.8	3411	1722	1722	0.329	19.51	19.03	7.34

Appendix 2: AVS tests under drained loading condition.

Sample 23

Interval number	Hydrostatic stress (MPa)	Pore pressure (MPa)	Time of flight (μs)			Wave speed (m/s)			*v*	*E* (GPa)	*K* (GPa)	*G* (GPa)
			P-wave	S1-wave	S2 -Wave	P-wave	S1-wave	S2-wave				
1	3.4	0.1	36.0	63.4	63.4	2789	1560	1560	0.272	15.85	11.61	6.23
2	7.1	0.1	35.4	63.4	63.4	2908	1560	1560	0.298	16.17	13.34	6.23
3	10.8	0.1	34.8	62.2	62.2	3037	1634	1634	0.296	17.72	14.49	6.84
4	13.9	0.1	34.4	62.2	62.2	3120	1634	1634	0.311	17.93	15.81	6.84
5	17.7	0.1	34.2	62.2	62.2	3178	1634	1634	0.320	18.05	16.74	6.84
6	20.9	0.1	33.6	62.0	62.0	3323	1647	1647	0.337	18.58	18.99	6.95
7	24.1	0.1	33.6	62.0	62.0	3333	1647	1647	0.338	18.60	19.18	6.95
8	27.7	0.1	33.6	62.0	62.0	3333	1647	1647	0.338	18.60	19.18	6.95
9	31.2	0.1	33.4	61.8	61.8	3377	1661	1661	0.341	18.93	19.78	7.06
10	34.7	0.1	33.4	61.8	61.8	3388	1661	1661	0.342	18.95	19.98	7.06
11	38.2	0.1	33.2	61.4	61.4	3434	1688	1688	0.341	19.56	20.46	7.29
12	41.6	0.1	33.2	61.4	61.4	3434	1688	1688	0.341	19.56	20.46	7.29

Sample 24

Interval number	Hydrostatic stress (MPa)	Pore pressure (MPa)	Time of flight (μs)			Wave speed (m/s)			*v*	*E* (GPa)	*K* (GPa)	*G* (GPa)
			P-wave	S1-wave	S2 -Wave	P-wave	S1-wave	S2-wave				
1	3.6	0.1	36.0	63.4	63.4	2789	1560	1560	0.272	15.84	11.60	6.22
2	6.9	0.1	35.6	63.4	63.4	2867	1560	1560	0.290	16.05	12.73	6.22
3	10.5	0.1	35.2	62.8	62.8	2950	1596	1596	0.293	16.85	13.57	6.52
4	13.9	0.1	35.0	62.8	62.8	2993	1596	1596	0.301	16.96	14.22	6.52
5	17.4	0.1	34.8	62.4	62.4	3037	1621	1621	0.301	17.49	14.63	6.72
6	20.9	0.1	34.4	61.8	61.8	3130	1661	1661	0.304	18.40	15.65	7.06
7	24.2	0.1	34.4	61.8	61.8	3130	1661	1661	0.304	18.40	15.65	7.06
8	27.7	0.1	34.2	61.6	61.6	3168	1674	1674	0.306	18.73	16.12	7.17
9	31.3	0.1	34.2	61.6	61.6	3178	1674	1674	0.308	18.76	16.28	7.17
10	34.9	0.1	34.2	61.6	61.6	3178	1674	1674	0.308	18.76	16.28	7.17
11	38.2	0.1	34.2	61.6	61.6	3188	1674	1674	0.310	18.78	16.44	7.17
12	41.9	0.1	34.0	61.6	61.6	3218	1674	1674	0.314	18.85	16.93	7.17

Appendix 2: AVS tests under drained loading condition.

Sample 25

Interval number	Hydrostatic stress (MPa)	Pore pressure (MPa)	Time of flight (μs)			Wave speed (m/s)			*v*	*E* (GPa)	*K* (GPa)	*G* (GPa)
			P-wave	S1-wave	S2 -Wave	P-wave	S1-wave	S2-wave				
1	3.6	0.1	35.6	63.0	63.0	2797	1545	1545	0.280	16.05	12.18	6.27
2	6.9	0.1	35.2	63.0	63.0	2878	1545	1545	0.297	16.26	13.38	6.27
3	10.5	0.1	34.8	63.0	63.0	2963	1545	1545	0.313	16.46	14.69	6.27
4	13.9	0.1	34.5	62.8	62.8	3021	1557	1557	0.319	16.79	15.47	6.37
5	17.4	0.1	34.2	62.8	62.8	3101	1557	1557	0.331	16.95	16.75	6.37
6	20.9	0.1	34.0	62.8	62.8	3150	1557	1557	0.338	17.04	17.55	6.37
7	24.1	0.1	33.8	62.8	62.8	3200	1557	1557	0.345	17.12	18.39	6.37
8	27.6	0.1	33.8	62.8	62.8	3200	1557	1557	0.345	17.12	18.39	6.37
9	31.2	0.1	33.8	62.8	62.8	3210	1557	1557	0.346	17.14	18.57	6.37
10	34.7	0.1	33.6	62.0	62.0	3263	1607	1607	0.340	18.17	18.90	6.78
11	38.3	0.1	33.4	62.0	62.0	3295	1607	1607	0.344	18.23	19.46	6.78
12	41.4	0.1	33.4	62.0	62.0	3306	1607	1607	0.345	18.24	19.65	6.78

Sample 26

Interval number	Hydrostatic stress (MPa)	Pore pressure (MPa)	Time of flight (μs)			Wave speed (m/s)			*v*	*E* (GPa)	*K* (GPa)	*G* (GPa)
			P-wave	S1-wave	S2 -Wave	P-wave	S1-wave	S2-wave				
1	3.6	0.1	37.2	64.6	64.6	2704	1564	1564	0.249	15.49	10.27	6.20
2	7.1	0.1	36.6	64.6	64.6	2810	1564	1564	0.276	15.83	11.75	6.20
3	10.5	0.1	36.4	64.4	64.4	2848	1576	1576	0.279	16.11	12.16	6.30
4	13.8	0.1	36.2	64.4	64.4	2886	1576	1576	0.288	16.21	12.72	6.30
5	17.3	0.1	36.0	64.4	64.4	2925	1576	1576	0.296	16.31	13.30	6.30
6	20.8	0.1	35.8	64.4	64.4	2966	1576	1576	0.303	16.41	13.90	6.30
7	24.1	0.1	35.6	64.2	64.2	2999	1587	1587	0.305	16.68	14.28	6.39
8	27.7	0.1	35.6	64.2	64.2	3007	1587	1587	0.307	16.70	14.40	6.39
9	31.3	0.1	35.6	64.2	64.2	3015	1587	1587	0.308	16.72	14.53	6.39
10	34.5	0.1	35.4	64.0	64.0	3050	1599	1599	0.310	16.99	14.93	6.48
11	38.2	0.1	35.2	64.0	64.0	3085	1599	1599	0.316	17.07	15.48	6.48
12	41.5	0.1	35.2	64.0	64.0	3102	1599	1599	0.319	17.10	15.75	6.48

Appendix 2: AVS tests under drained loading condition.

Sample 27

Interval number	Hydrostatic stress (MPa)	Pore pressure (MPa)	Time of flight (μs)			Wave speed (m/s)			*v*	*E* (GPa)	*K* (GPa)	*G* (GPa)
			P-wave	S1-wave	S2 -Wave	P-wave	S1-wave	S2-wave				
1	3.6	0.1	36.4	63.8	63.8	2815	1593	1593	0.265	16.47	11.66	6.51
2	7.1	0.1	36.0	63.6	63.6	2891	1605	1605	0.277	16.89	12.65	6.61
3	10.5	0.1	35.6	63.4	63.4	2972	1617	1617	0.290	17.32	13.73	6.71
4	13.8	0.1	35.2	63.0	63.0	3058	1642	1642	0.297	17.96	14.78	6.92
5	17.3	0.1	34.8	62.8	62.8	3148	1655	1655	0.309	18.41	16.08	7.03
6	20.8	0.1	34.4	62.8	62.8	3234	1655	1655	0.323	18.60	17.49	7.03
7	24.1	0.1	34.4	62.8	62.8	3244	1655	1655	0.324	18.62	17.66	7.03
8	27.6	0.1	34.4	62.8	62.8	3254	1655	1655	0.326	18.64	17.82	7.03
9	31.3	0.1	34.4	62.8	62.8	3254	1655	1655	0.326	18.64	17.82	7.03
10	34.6	0.1	34.2	62.8	62.8	3284	1655	1655	0.330	18.70	18.33	7.03
11	38.2	0.1	34.2	62.8	62.8	3305	1655	1655	0.333	18.74	18.68	7.03
12	41.7	0.1	34.2	62.8	62.8	3305	1655	1655	0.333	18.74	18.68	7.03

Sample 28

Interval number	Hydrostatic stress (MPa)	Pore pressure (MPa)	Time of flight (μs)			Wave speed (m/s)			*v*	*E* (GPa)	*K* (GPa)	*G* (GPa)
			P-wave	S1-wave	S2 -Wave	P-wave	S1-wave	S2-wave				
1	3.6	0.1	36.0	63.4	63.4	2857	1598	1598	0.272	16.75	12.27	6.58
2	7.0	0.1	35.4	62.8	62.8	2979	1635	1635	0.284	17.71	13.69	6.89
3	10.5	0.1	35.0	62.6	62.6	3066	1648	1648	0.297	18.16	14.90	7.00
4	13.4	0.1	34.8	62.6	62.6	3120	1648	1648	0.307	18.30	15.77	7.00
5	17.4	0.1	34.4	62.4	62.4	3206	1661	1661	0.317	18.73	17.02	7.11
6	20.7	0.1	34.0	62.2	62.2	3307	1674	1674	0.328	19.19	18.57	7.23
7	24.1	0.1	34.0	62.2	62.2	3307	1674	1674	0.328	19.19	18.57	7.23
8	27.8	0.1	33.8	62.2	62.2	3349	1674	1674	0.333	19.28	19.29	7.23
9	31.2	0.1	33.8	62.2	62.2	3360	1674	1674	0.335	19.30	19.48	7.23
10	34.7	0.1	33.6	62.0	62.0	3404	1688	1688	0.337	19.64	20.08	7.34
11	38.1	0.1	33.6	62.0	62.0	3415	1688	1688	0.338	19.66	20.27	7.34
12	41.4	0.1	33.6	62.0	62.0	3426	1688	1688	0.340	19.68	20.47	7.34

Appendix 2: AVS tests under drained loading condition.

Sample 29

Interval number	Hydrostatic stress (MPa)	Pore pressure (MPa)	Time of flight (µs)			Wave speed (m/s)			*v*	*E* (GPa)	*K* (GPa)	*G* (GPa)
			P-wave	S1-wave	S2 -Wave	P-wave	S1-wave	S2-wave				
1	3.6	0.1	36.8	63.8	63.8	2645	1536	1536	0.245	14.73	9.64	5.91
2	7.1	0.1	36.0	63.6	63.6	2789	1548	1548	0.277	15.33	11.48	6.00
3	10.5	0.1	35.6	63.4	63.4	2867	1560	1560	0.290	15.72	12.47	6.09
4	13.8	0.1	35.2	63.0	63.0	2950	1584	1584	0.297	16.30	13.41	6.28
5	17.3	0.1	34.8	63.0	63.0	3037	1584	1584	0.313	16.50	14.72	6.28
6	20.8	0.1	34.2	62.8	62.8	3178	1596	1596	0.331	16.99	16.79	6.38
7	24.1	0.1	34.0	62.6	62.6	3218	1609	1609	0.333	17.29	17.30	6.48
8	27.7	0.1	34.0	62.6	62.6	3228	1609	1609	0.335	17.30	17.46	6.48
9	31.2	0.1	34.0	62.6	62.6	3228	1609	1609	0.335	17.30	17.46	6.48
10	34.6	0.1	33.8	62.2	62.2	3280	1634	1634	0.335	17.86	18.03	6.69
11	37.9	0.1	33.8	62.2	62.2	3291	1634	1634	0.336	17.88	18.20	6.69
12	41.9	0.1	33.6	62.2	62.2	3333	1634	1634	0.342	17.95	18.91	6.69

Sample 30

Interval number	Hydrostatic stress (MPa)	Pore pressure (MPa)	Time of flight (µs)			Wave speed (m/s)			*v*	*E* (GPa)	*K* (GPa)	*G* (GPa)
			P-wave	S1-wave	S2 -Wave	P-wave	S1-wave	S2-wave				
1	3.6	0.1	36.4	64.2	64.2	2781	1551	1551	0.275	15.13	11.19	5.94
2	6.9	0.1	35.8	64.0	64.0	2897	1562	1562	0.295	15.61	12.68	6.03
3	10.8	0.1	35.2	63.8	63.8	3022	1574	1574	0.314	16.07	14.39	6.12
4	13.8	0.1	34.8	63.8	63.8	3111	1574	1574	0.328	16.25	15.75	6.12
5	17.5	0.1	34.4	63.2	63.2	3206	1610	1610	0.331	17.04	16.85	6.40
6	20.8	0.1	34.0	62.8	62.8	3307	1635	1635	0.338	17.67	18.21	6.60
7	24.1	0.1	34.0	62.6	62.6	3307	1648	1648	0.335	17.90	18.07	6.71
8	27.7	0.1	33.8	62.6	62.6	3360	1648	1648	0.342	17.99	18.94	6.71
9	31.2	0.1	33.8	62.6	62.6	3360	1648	1648	0.342	17.99	18.94	6.71
10	34.6	0.1	33.8	62.6	62.6	3360	1648	1648	0.342	17.99	18.94	6.71
11	38.2	0.1	33.8	62.6	62.6	3360	1648	1648	0.342	17.99	18.94	6.71
12	41.6	0.1	33.6	62.6	62.6	3415	1648	1648	0.348	18.08	19.85	6.71